

PHASE 2 INITIAL BOREHOLE DRILLING AND TESTING, IGNACE AREA

*WP10 – Geological Integration Report for Borehole
IG_BH01*

APM-REP-01332-0260

February 2022

**Nuclear Waste Management Organization
and Golder Associates Ltd.**

nwmo

NUCLEAR WASTE
MANAGEMENT
ORGANIZATION

SOCIÉTÉ DE GESTION
DES DÉCHETS
NUCLÉAIRES

Nuclear Waste Management Organization

22 St. Clair Avenue East, 4th Floor

Toronto, Ontario

M4T 2S3

Canada

Tel: 416-934-9814

Web: www.nwmo.ca

**Phase 2 Initial Borehole Drilling and Testing, Ignace
Area**

**WP10 – Geological Integration Report for Borehole
IG_BH01**

APM-REP-01332-0260

December 2022

**Nuclear Waste Management Organization and Golder
Associates Ltd.**

Document History

Title:	Phase 2 Initial Borehole Drilling and Testing, Ignace Area. WP10 – Geological Integration Report for Borehole IG_BH01		
Report Number:	APM-REP-01332-0260		
Revision:	R1	Date:	December 2022
Author Company(s):	Nuclear Waste Management Organization and Golder Associates Ltd.		
Authored by:	Aaron DesRoches, Lindsay Waffle and Andrew Parmenter (NWMO) and Aynsley Neufeld and Joe Carvalho (Golder Associates Ltd.)		
Verified by:	Andre Vorauer, Mostafa Khorshidi, and Eric Sykes		
Accepted by:	Sarah Hirschorn (Geoscience Director)		

Revision Summary		
Revision Number	Date	Description of Changes/Improvements
R0	2022-02	Initial issue
R1	2022-12	Minor editorial revisions

ABSTRACT

Title: Phase 2 Initial Borehole Drilling and Testing, Ignace Area.
WP10 – Geological Integration Report for Borehole IG_BH01

Report No.: APM-REP-01332-0260

Author(s): Aaron DesRoches, Lindsay Waffle and Andrew Parmenter (NWMO) and
Aynsley Neufeld and Joe Carvalho (Golder Associates Ltd.)

Company: Nuclear Waste Management Organization and Golder Associates Ltd.

Date: December 2022

The Initial Borehole Drilling and Testing project in the Ignace Area, Ontario is part of Phase 2 Geoscientific Preliminary Field Investigations of the Nuclear Waste Management Organization's (NWMO) Adaptive Phased Management (APM) Site Selection Phase. This project involves the drilling and testing of the first of several deep boreholes within the northern portion of the Revell batholith. The first drilled borehole, IG_BH01, is located a direct distance of approximately 21 km southeast of the Wabigoon Lake Ojibway Nation and a direct distance of 43 km northwest of the Town of Ignace. Access to the IG_BH01 drill site is via Highway 17 and primary logging roads. This Geological Integration Report serves as the primary reference of the geological findings from the borehole drilling and testing activities at IG_BH01.

The objective of the Geological Integration Report is to summarize all findings and provide an initial interpretation of the lithological and structural characteristics of the geosphere intersected by borehole IG_BH01, including delineation of rock units and structural units. In addition, distinct intervals of higher fracture frequency identified along the length of the borehole are documented. These components represent the initial geological model for IG_BH01 which can be further used in developing a site-scale 3D geological model.

Findings and uncertainties are summarized at the end of the report. One primary consideration is the understanding that the available information *is from a single borehole*. Whether or not the characteristics of the bedrock interpreted in this report will be representative of characteristics in other boreholes remains uncertain.

TABLE OF CONTENTS

ABSTRACT	iii
1 INTRODUCTION	1
1.1 Technical Objectives and Scope of Report	1
2 Background Information	2
2.1 Geological Setting.....	2
2.2 Background and Overview of Borehole Drilling and Testing.....	5
2.2.1 Drilling Site Description	5
2.3 Borehole Construction Details for IG_BH01.....	8
2.3.1 Borehole Deviation Analysis	9
3 Integrated Geological Interpretation	14
3.1 Data Used for Geological Interpretation	14
3.1.1 Terminology	16
3.2 Geological Results	16
3.2.1 Lithological Interpretation	18
3.2.2 Alteration Interpretation	37
3.2.3 Rock Unit Classification.....	41
3.2.4 Structural Interpretation.....	44
3.2.4.1 Structures.....	46
3.2.4.2 Interpreted Fracture Sets.....	61
3.2.4.3 Fracture Infill Minerals	64
3.2.5 Structural Unit Classification.....	70
3.2.6 High Fracture Frequency Intervals (HFFI)	72
4 Summary of Findings and Uncertainties	85
4.1 Findings	85
4.2 Uncertainties	88
5 References	90
Appendix A: Summary List of Work Packages Completed for IG_BH01	93
Appendix B: Petrography and lithogeochemistry data	95

Appendix C:	Geophysical Near and Far Density Log Correction	105
Appendix D:	Structure log integration methodology	108
Appendix E:	Alteration Log update based on geophysical image log	112
Appendix F:	Summary of Revised Lineation Orientations.....	114
Appendix G:	Stereonets of Fractures by Structural Unit.....	116
Appendix H:	Stereonets of IG_BH01 High Fracture Frequency Intervals (HFFI)	120
Appendix I:	Summary of borehole logs at 1:1,000 scale	124

LIST OF TABLES

Table 1: Details of Casing and Coring Rods used for IG_BH01.....	8
Table 2: Details of Borehole Diameter for IG_BH01	9
Table 3: Summary of Rock Types Encountered in IG_BH01	16
Table 4: Summary average of major oxides in the rock types of IG_BH01. Note that only 5 rock types were sampled for lithogeochemical analysis and there are no results for pegmatite, quartz, and biotite granodiorite-tonalite dykes. Aphanitic and Feldspar-phyric tonalite dykes are combined as they are compositionally the same.....	18
Table 5: Mean geophysical response values for each logged rock type.	33
Table 6: Summary of Classified Rock Units.....	42
Table 7: Summary of structures observed in the borehole.....	44
Table 8: Summary of the Structural Character of Felsic Dykes.....	48
Table 9: Summary of interpreted fracture sets in the borehole. Presents the general description of the orientation with a mean dip and dip direction.	63
Table 10: Position ranges and standard statistics for fracture frequencies captured within the defined structural units (SU) within the borehole.....	71
Table 11. High Fracture Frequency Intervals from IG_BH01	74

LIST OF FIGURES

Figure 1: Location and Geological setting of borehole IG_BH01 in the northern portion of the Revell batholith.	4
Figure 2: Location of the drilling site for borehole IG_BH01.....	6
Figure 3: Drilling location and site layout for IG_BH01.....	7
Figure 4: Aerial view of the drilling site for IG_BH01 – looking northwest.	8
Figure 5: Final IG_BH01 Schematic of construction details; positions are along borehole axis...	9
Figure 6: Closure and bird's eye view of calculated borehole locations for televiewer and gyro surveys. a) Closure profile – distance between calculated borehole position and planned borehole position. b) Plan view – borehole wander on the plane perpendicular to the planned borehole axis.....	10
Figure 7: Tilt and azimuth vs position along borehole for combined magnetic and gyro surveys. Mean and standard deviation for magnetic surveys also shown. a) Tilt (angle with respect to vertical) vs position. b) Azimuth (clockwise angle with respect to True North) vs position.	11
Figure 8: Percent error profile for the azimuth and tilt between the gyro measurements and the mean of the televiewer measurements [$100 \times (\text{Gyro} - \text{Mean of televiewer}) / \text{Gyro}$].	12
Figure 9: Closure and plan view of calculated borehole locations for the gyro survey. a) Closure profile – distance between calculated borehole position and planned borehole position. b) Plan view – borehole wander on the plane perpendicular to the planned borehole axis....	13

- Figure 10: Input datasets used to derive a final lithology log. From left: optical televiewer log, geological core-logged rock types, rock types added to lithology log as a result of review of geophysical logs, four suites of continuous geophysical logs that aid in distinction of rock types, and final lithology log. Due to the low spectral gamma counts, K, U and Th were evaluated using a 10 m window, resulting in a smoothing of their profiles..... 17
- Figure 11: Classification/nomenclature of dominant granitoid phases according to the normalized modal mineral content ($Q + A + P = 100 \text{ Vol}\%$) as determined from investigation of 27 samples taken for lithogeochemical analysis. Average modal mineralogy for each sample was plotted on a simplified ternary Streckeisen diagram after Le Bas and Streckeisen (1991)..... 19
- Figure 12: Plutonic Rock Classification (Debon and Le Fort, 1983). Diagram axes correspond to proportions of K-feldspar and plagioclase to quartz. P is calculated from $(K - (Na+Ca))$, and Q is calculated from $((Si/3) - (K+Na+(2*Ca)/3))$. Parameters calculated as oxide percentages converted to millifications. Crosses show mean composition of each rock type. 20
- Figure 13: Representative examples of biotite granodiorite-tonalite (sample IG_BH01_LG026). a) Hand-sample photograph. b) Billet photograph showing yellow staining of potassium feldspars (billet size is 25 x 40 mm). c) Thin section photomicrograph with rock-forming minerals plagioclase (pl), quartz (qz) and biotite (bt). Sericite (white mica) alteration can be seen in cores of plagioclase crystals; crossed polarizers transmitted light. 21
- Figure 14: Representative examples of biotite tonalite (sample IG_BH01_LG020). a) Hand-sample photograph. b) Billet photograph showing lack of yellow-stained potassium feldspars (billet size is 25 x 40 mm). c) Thin section photomicrograph with rock-forming minerals plagioclase (pl), quartz (qz) and biotite (bt). Minor sericite (white mica) alteration can be seen in cores of plagioclase crystals; crossed polarized transmitted light..... 22
- Figure 15: Representative examples of amphibolite (sample IG_BH01_LG035). a) Hand-sample photograph. b) Billet photograph (billet size is 25 x 40 mm). c) Thin section photomicrograph with main rock-forming minerals albite (ab) and amphibole (am; tremolite-actinolite), along with biotite (brown) and opaque iron-oxide minerals replacing pyrite crystals; plane polarized transmitted light. 24
- Figure 16: Representative examples of feldspar-phyric tonalite dyke (sample IG_BH01_LG024). a) Hand-sample photograph. b) Billet photograph showing yellow staining of alkali feldspar (billet size is 25 x 40 mm). c) Thin section photomicrograph with plagioclase (pl) phenocrysts, in a very fine-grained matrix of quartz and biotite; crossed polarized transmitted light. 26
- Figure 17: Narrow apophyse extending from the margin of an aphanitic tonalite dyke into surrounding biotite granodiorite-tonalite (pencil for scale; approximately 586 m position along borehole)..... 27
- Figure 18: Representative examples of aplite dyke (sample IG_BH01_LG018). a) Hand-sample photograph. b) Billet photograph showing yellow staining of alkali feldspar (billet size is 25 x 40 mm). c) Thin section photomicrograph with rock-forming minerals plagioclase (pl), alkali feldspar (af) and quartz (qz); crossed polarized transmitted light. 28
- Figure 19: Representative examples of pegmatite dyke (sample IG_BH01_LG003). a) Hand-sample photograph showing pegmatite in contact with biotite granodiorite-tonalite. b) Billet photograph showing contact between biotite granodiorite-tonalite (bottom left) and pegmatite (top right) and yellow staining of alkali feldspar (billet size is 25 x 40 mm). c) Thin

- section photomicrograph of pegmatite with large quartz (qz) and alkali feldspar (af) grains; crossed polarized transmitted light..... 29
- Figure 20: Representative examples of quartz dyke (sample IG_BH01_LG011). a) Hand-sample photograph showing contact with biotite granodiorite-tonalite. b) Billet photograph showing yellow staining of alkali feldspar along contact (billet size is 25 x 40 mm). c) Thin section photomicrograph contact showing decrease in grain size and abundant pyrite crystals (opaque, square) at contact between biotite granodiorite-tonalite and quartz dyke. Quartz dyke is at bottom left of thin section image; crossed polarized transmitted light. 31
- Figure 21: Chondrite-normalized rare-earth element (REE) plot (after Taylor and McLennan, 1985) of rock types from IG_BH01 and a representative average of 2.8 Ga low-heavy REE (HREE) tonalite-trondhjemite-granodiorite (TTG) from the Fennoscandian shield (black squares; Halla, 2018). Y-axis shows concentrations (expressed as logarithm to the base 10 of the value) of REE (x-axis, by atomic number) in IG_BH01 samples normalized to a reference Chondrite standard. REE patterns of biotite granodiorite-tonalite, biotite tonalite, feldspar-phyric tonalite dykes, and biotite granodiorite-tonalite dykes demonstrate steep fractionation and significant depletion of HREE. Aplite dykes demonstrate a less steep fractionation and negative europium anomalies, suggesting they from are from a later stage, evolved granite source. 32
- Figure 22: Violin plots show the distribution of geophysical log responses associated with the logged rock types. Each violin shows the distribution of the data values with the median (thick dashed line), and quartiles (thin dashed lines) marked. Rock types are ordered based on total data counts from left to right in each graph. 36
- Figure 23: Distribution of Neutron and Density Values of all Rock Types encountered in IG_BH01. Colored points represent mean values of the geophysical response and the error bars represent standard deviation..... 37
- Figure 24: Alteration types and distribution along the borehole based on geological core logging and analysis of the optical televiewer log resulting in a final alteration log. A2 indicates intervals with slight alteration and A3 indicates intervals with moderate alteration. 39
- Figure 25: Examples of the different types of alteration observed, a) Hematization (43 m), b) Potassic (455 m), c) Silicification (553 m), d) Chloritization (896 m), e) Bleaching (42 m), f) Sericitization (650 m). 40
- Figure 26: Examples of mineral-scale alteration observed in petrographic thin sections of the biotite granodiorite-tonalite. a) Chloritized biotite crystals and sericitized plagioclase adjacent to zoned, unaltered plagioclase at 223.25 m along borehole (viewed under crossed polarized transmitted light). b) Sericitized plagioclase crystals and chloritized biotite at 582.95 m (viewed under plane polarized transmitted light). 41
- Figure 27: Summary of final logged lithology, alteration and key geophysical logs presented alongside interpreted rock units for IG_BH01. Due to the low spectral gamma counts, K, U and Th were evaluated using a 10 m window, resulting in a smoothing of their profiles. ... 43
- Figure 28: Equal Area Lower Hemisphere Projections (stereonet) showing poles to planar structural measurements, unweighted (n = 1860). 45
- Figure 29: Equal Area Lower Hemisphere Projections (stereonet) showing a summary of the poles for planar structural measurements. Top: all data – contours, unweighted (n = 1860). Bottom: all data – contours, Terzaghi-weighted. 46

- Figure 30: Stereonet showing poles and unweighted contours for Igneous Primary Structures (IPS; n = 43). Open symbol identifies broken Igneous Primary Structure (IPS-BR) and filled symbols identify partially intact/intact Igneous Primary Structures (IPS-PIN/IN). 47
- Figure 31: Stereonet showing poles and unweighted contours for biotite tonalite contacts (n = 26). Filled symbols identify partially intact/intact contacts (CO-PIN/IN). 47
- Figure 32: Stereonet showing poles and unweighted contours for amphibolite contacts (n = 26). Open symbols identify broken contacts (CO-BR) and filled symbols identify partially intact/intact contacts (CO-PIN/IN). 48
- Figure 33: Stereonet showing the distribution of poles for logged felsic dykes (n = 48), including, biotite granodiorite-tonalite dykes (n = 6), aphanitic tonalite dykes (n = 2), feldspar-phyric tonalite dykes (n = 10), aplite dykes (n = 18), pegmatite dykes (n = 8), and quartz dykes (n = 4). 49
- Figure 34: Examples of primary igneous and ductile structure. a) Biotite rich horizon interpreted as primary igneous layering, in biotite granodiorite-tonalite (949 m along borehole). b) Biotite-defined foliation trending at a moderate angle to the core axis, parallel to the white dashed line, and wrapping into a narrow quartz-rich shear zone oriented at a high angle to the core axis near left side of photo, in biotite granodiorite-tonalite (670 m along borehole). c) Shear zone developed at moderate angle to core axis within and along the margin of amphibolite at its contact with biotite granodiorite-tonalite (659 m along borehole). 50
- Figure 35: Summary log showing the frequency per metre of brittle structures (left) in comparison to stick plots that show the distribution of all brittle structures (Joints – JN, Veins – VN and Faults - FLT) and all ductile structures (Shear Zones – SHR and Foliation – FO). 51
- Figure 36: Stereonets showing orientation information for Foliation (FO). Top: All data – poles and contours, unweighted (n = 65). Filled symbols identify partially intact/intact Foliation (FO-PIN/IN). Bottom: All Foliation data, Terzaghi-weighted contours (n = 123). 52
- Figure 37: Stereonets showing orientation information for Shear Zones (SHR). Top: All data – poles and contours, unweighted (n = 48). Open symbols identify broken Shear Zones (SHR-BR) and filled symbols identify partially intact/intact Shear Zones (SHR-PIN/IN). Bottom: All Shear Zone data, Terzaghi-weighted contours (n = 73). 53
- Figure 38: Examples of brittle structures observed in IG_BH01: a) broken, clean, hairline (no visible geological aperture), joint, in biotite granodiorite-tonalite (358 m), b) broken joint with soft gouge-like infill and mm-scale geological aperture, in amphibolite (793 m), c) intact mm-scale calcite vein (middle of photo) adjacent, and to the left of one partially intact joint and one completely broken joint, in amphibolite (656 m), d) intact cm-scale quartz vein, in biotite tonalite (235 m), e) broken, hairline (no visible geological aperture) fault with associated cm-scale halo of silicification, in biotite granodiorite-tonalite, f) lineation defined by aligned quartz (parallel to black arrow) on broken fault plane, in biotite granodiorite-tonalite (431 m). 54
- Figure 39: Stereonets showing orientation information for Joints (JN). Top: All data – poles and contours, unweighted (n = 1249). Open symbols identify broken Joints (JN-BR) and filled symbols identify partially intact/intact Joints (JN-PIN/IN). Bottom: All Joint data, Terzaghi-weighted contours (n = 2331). 56
- Figure 40: Stereonets showing orientation information for all Veins (VN). Top: All data – poles and contours, unweighted (n = 339). Open symbols identify broken Veins (VN-BR) and

filled symbols identify partially intact/intact Veins (VN-PIN/IN). Bottom: All Vein data, Terzaghi-weighted contours (n = 590).	57
Figure 41: Stereonets showing orientation information for Faults (FLT). All data – poles (n = 16). Open symbols identify broken Faults (FLT-BR) and filled symbols identify partially intact/intact Faults (FLT-PIN/IN). Poles to faults with weak and uncertain lineations are circled.	58
Figure 42: Stereonet showing all lineations by their rake on fault planes (black, n = 13) and shear planes (red, n = 7).	59
Figure 43: Stereonet plot showing poles to all fracture planes logged as broken during geological core logging, with unweighted contours.	60
Figure 44: Stereonet plot showing poles to all fracture planes logged as intact or partially intact, with unweighted contours.	60
Figure 45: Stereonets of all oriented fractures, including all joints, veins and faults. Top: All fractures – poles, unweighted (n = 1604). Identified pole clusters are colour-coded to highlight their distribution. Middle: All fractures – contours (n = 1604), unweighted. Bottom: All fractures – contours, Terzaghi-weighted (n = 3056). Middle and bottom stereonet are overlain by final fracture set interpretation. See text and Table 9 for additional summary.	62
Figure 46: Summary log showing the frequency per metre of all brittle structures (left) in comparison to stick plots that show the distribution of all fractures assigned to defined fracture sets 1, 2, 3a/3b combined and 4a/4b combined, as well as unassigned random fractures.	64
Figure 47: Summary log showing the frequency per metre (Fracture Freq.) of all brittle structures (left) in comparison to stick plots that show the distribution of the most common infill mineral phases including quartz (Qz), chlorite (Chl), iron oxide stain (Fe), epidote (Ep), calcite (Ca), a granitic (Gt) or pegmatitic (Pg) assemblage that includes some combination of alkali-feldspar (Afs) with quartz, plagioclase and biotite, and, fractures that exhibit either clay (Cl), broken rock (Br) or soft gouge (Go_So).	65
Figure 48: Stereonet plot showing poles to all fracture planes logged with quartz +/- chlorite, biotite, phlogopite, muscovite, epidote, iron oxide staining, or calcite.	66
Figure 49: Stereonet plot showing poles to all fracture planes logged with chlorite.	66
Figure 50: Stereonet plot showing poles to all fracture planes logged with iron staining.	67
Figure 51: Stereonet plot showing poles to all fracture planes logged with calcite.	67
Figure 52: Stereonet plot showing poles to all fracture planes logged with epidote.	68
Figure 53: Stereonet plot showing poles to all fracture planes logged with granitic infill, including alkali-feldspar +/- quartz, plagioclase and biotite.	68
Figure 54: Stereonet plot showing poles to all fracture planes logged with clay, broken rock, or soft gouge.	69
Figure 55: Stereonet showing poles to all fractures logged as having no identifiable mineral infill phase. Fractures logged in 'viewer' datasets only, geological 'core' logging only, or identified in 'both' datasets, are distinguished.	69
Figure 56: Per metre fracture frequency histogram (left) and cumulative fracture frequency curve (right) showing vertical distribution of all logged joints, faults, and veins along the borehole. The cumulative fracture frequency curve shows the changes in slope where boundaries in	

structural units (SU) are defined. Structural units and their top and bottom positions along borehole are labelled on the figure.....	71
Figure 57. High fracture frequency intervals (HFFI) interpreted based on fracture intensity from borehole fracture frequency log. Five high fracture frequency intervals are outlined by their yellow bands. The red dashed line represents the peak location.	73
Figure 58. Terzaghi-weighted stereonet plot of fractures (JN, VN, FLT) within high fracture frequency interval 1 (HFFI_1) from 18.0 – 40.67 m. Two peaks are defined, a major peak with a mean orientation of 128/75 and a minor peak with a mean orientation of 165/41 (DipDirection/Dip).	75
Figure 59. Core from an interval of HFFI_1 (23.98 – 35.55 m). Biotite granodiorite-tonalite with intersecting shallowly- and steeply-dipping fractures creating sections of broken core. The area of increased fracture frequency at the top of the interval is associated with visible, pink-coloured alteration, logged as hematization.	76
Figure 60. Core from an interval of HFFI_2 (547.24 – 558.90 m). Biotite granodiorite-tonalite with one feldspar-phyric tonalite dyke at 548.47 m. Silicification is logged around the dyke and is visible in the photo as darker grey patches. Fractures are subhorizontal and fairly well spaced.....	77
Figure 61. Core from an interval of HFFI_3 (a: 642.38 – 654.48 m; b: 654.48 – 666.32 m). Biotite granodiorite-tonalite with visible pink and white alteration associated with the amphibolite occurrences (a & b). The amphibolite contacts and structures associated with the amphibolites (shear, some joints, etc.) are gently inclined. The two fracture peaks identified in the interval are both steeply inclined, one dipping south and the other dipping west. These fractures are visible especially in (a) and where they intersect the shallower structures the core is visibly broken up.	78
Figure 62. Core from an interval of HFFI_4 (a: 774.30 – 786.50 m; b: 786.35 – 798.56 m). Small feldspar-phyric tonalite dykes and amphibolite are visible. The fractures are well spaced, with a slight increase around the subordinate rock types.	80
Figure 63. Core from HFFI_5 (965.21 – 976.73 m). Biotite granodiorite-tonalite at the top of the interval and the first amphibolite occurrence, with sub-vertical contacts dipping towards the southwest. Increasing fracture and alteration (logged as potassic) intensity approaching the amphibolite, returning to well-spaced fractures in the unaltered biotite granodiorite-tonalite.	81
Figure 64: Lineament traces near IG_BH01 interpreted from LiDAR DEM and airborne geophysics data (DesRoches et al., 2018). Lineament traces dominantly trend north-northwest with some shorter lineaments trending northeast. Note that the heavy black line near the upper right corner of the image is a Wabigoon dyke.	83
Figure 65: Rose diagram of the lineaments (N = 40) around IG_BH01 (see Figure 64) interpreted from LiDAR DEM and airborne geophysics data (DesRoches et al., 2018). Lineament orientations are plotted using a bin size of 10 degrees.	84
Figure 66. Rose diagrams of the borehole logged fracture orientations using a minimum dip angle of 45 degrees, and bin size of 5 degrees. a) Unweighted (N = 1604); b) Terzaghi-weighted to account for directional bias of the borehole path (weighted N = 3056).	84
Figure 67: Summary log of geological information for IG_BH01, including (from left to right), final log of lithology, classification of rock units, per metre fracture frequency, and structural units, representing the 1-dimensional geological model for IG_BH01.	86

1 INTRODUCTION

The Initial Borehole Drilling and Testing project in the Ignace Area, Ontario is part of Phase 2 Geoscientific Preliminary Field Investigations of the Nuclear Waste Management Organization's (NWMO) Adaptive Phased Management (APM) Site Selection Phase.

Following the first stage of the Phase 2 Initial General Field Studies summarized by Golder (2015) and in collaboration with the community, an area located in the northern portion of the Revell batholith was selected by the NWMO for further investigation through an initial borehole drilling campaign which involves the drilling and testing of several deep boreholes. A five-by-five-kilometre region located at the surface within this part of the batholith defines the lateral extents of the 'Revell site' being investigated. The boundaries of this region also extend vertically for one and a half kilometres into the subsurface to define the three-dimensional volume for future site-scale modelling activities. The location of the first 1000 m deep and vertically oriented borehole, IG_BH01, with respect to the Revell site, is shown in Figure 1 and Figure 2.

The first drilled borehole, IG_BH01, is located a direct distance of approximately 21 km southeast of the Wabigoon Lake Ojibway Nation and a direct distance of 43 km northwest of the Town of Ignace. Access to the IG_BH01 drill site is via Highway 17 and primary logging roads (Figure 1). This single borehole integration report serves as the primary reference of the geological findings from the borehole drilling and testing activities at IG_BH01.

The project fieldwork was carried out by a team led by Golder Associates Ltd. (Golder) on behalf of the NWMO. The overall program, described in the Initial Borehole Characterization Plan (Golder, 2017) includes activities divided into work packages related to: the mobilization and set up of the borehole drilling site, the recovery and logging of the bedrock core, drilling water management and groundwater sampling, borehole geophysical and hydraulic testing, laboratory testing, and on-going monitoring activities at the borehole. All activities are documented in work package (WP) data reports that describe test methods, collected data, and calculations, where applicable. The full list of work packages and associated data reports is included in Appendix A.

This report, which represents the tenth work package (WP10 Integration and Synthesis), presents an integrated summary of geological and geophysical information collected primarily during the completion of three work packages, including, WP02: Borehole Drilling and Coring (Golder, 2018b), WP03: Geological and Geotechnical Core Logging, Photography and Sampling (Golder, 2018c) and WP05: Geophysical Well Logging and Interpretation (Golder, 2019a).

1.1 Technical Objectives and Scope of Report

The objective of this Geological Integration report is to evaluate relevant data and provide an interpretation of the lithological and structural characteristics of the geosphere intersected by borehole IG_BH01. This initial interpretation will be revised as further boreholes are drilled to form a holistic interpretation for the geosphere.

Additional information related to developing an understanding of the petrophysical and transport properties of the bedrock of the Revell site, as well as the geomechanical, hydrogeological, geochemical, and thermal properties will be reported on separately and integrated into a Descriptive Geosphere Site Model (DGSM) report. The DGSM report will summarize the additional borehole- and laboratory-derived data related to all of the additional topics listed above. The DGSM report will present this information along with a geological model that integrates the WP10 results for each of the boreholes. The information presented in this report, which focuses on IG_BH01, represents the first step in this integration process.

The scope of this Single Borehole Data Integration report is summarized in the following sections:

- Section 1 provides the report introduction and includes the summary of technical objectives and scope of the sections in the report.
- Section 2 first briefly describes the geological setting for the area around the borehole location and then provides an overview of the borehole drilling and testing activity. This includes a brief site description, a summary of the borehole construction, and deviation surveys of the borehole.
- Section 3 presents the integrated summaries of the lithological, alteration and structural characteristics of the bedrock intersected by the borehole (Section 3.2). Then, using this information, an initial geological model, with interpretation of rock units and structural units for the borehole, is presented.
- Section 4 summarizes the findings and addresses uncertainties.
- Appendix A lists all Work Packages and Work Package report names produced as part of the full suite of activities associated with IG_BH01.
- Appendix B presents the petrographic, modal mineralogy, and lithogeochemical data, which are summarized in Section 3.
- Appendix C presents a table of values summarizing the correction applied to the geophysical near and far density log.
- Appendix D contains the methodology for integrating the un-oriented structural dataset generated during WP03 with the televiewer geophysical logs collected during WP05 to produce a final log of oriented structures. The integrated structural dataset is presented in Section 3.
- Appendix E presents the alteration log update based on the interpretation of altered intervals from the optical televiewer image log.
- Appendix F presents the lineation dataset, with integrated trend and plunge data re-assessed as rake measurements.
- Appendix G presents lower hemisphere equal area projections (stereonet) summarizing the brittle fractures for each structural unit (SU) in the borehole, defined in Section 3.2.5.
- Appendix H presents lower hemisphere equal area projections (stereonet) summarizing the structural orientation information for all high fracture frequency intervals (HFFI) in the borehole, defined in Section 3.2.6.
- Appendix I presents a summary plot of the borehole results presented in the report at a 1:1000 scale.

2 BACKGROUND INFORMATION

2.1 Geological Setting

The approximately 2.7-billion-year-old Revell batholith is located in the western part of the Wabigoon Subprovince of the Archean Superior Province. The batholith is roughly elliptical in shape trending northwest, is approximately 40 km in length, 15 km in width, and covers an area of approximately 455 km². Based on initial geophysical modelling, the batholith is approximately 2 km to 3 km thick through the center of the northern portion (SGL, 2015). The batholith is surrounded by supracrustal rocks of the Raleigh Lake (to the north and east) and Bending Lake (to the southwest) greenstone belts (Figure 1).

Four main rock units are identified in the supracrustal rock group: mafic metavolcanic rocks, intermediate to felsic metavolcanic rocks, metasedimentary rocks, and mafic intrusive rocks (Figure 1). Sedimentation within the supracrustal rock assemblage was largely synvolcanic, although sediment deposition in the Bending Lake area may have continued past the volcanic period (Stone, 2009; Stone, 2010a; Stone, 2010b). All supracrustal rocks are affected, to varying degrees, by penetrative brittle-ductile to ductile deformation under greenschist- to amphibolite-facies metamorphic conditions (Blackburn and Hinz, 1996; Stone et al., 1998). In some locations, primary features, such as pillow basalt or bedding in sedimentary rocks are preserved, in other locations, primary relationships are completely masked by penetrative deformation. Uranium-lead (U-Pb) geochronological analysis of the supracrustal rocks produced ages that range between 2734.6 +/- 1.1 Ma and 2725 +/- 5.0 Ma (Stone et al., 2010).

Three main plutonic rock units comprise the Revell batholith (Figure 1), including, from oldest to youngest: a Biotite Tonalite to Granodiorite suite, a Hornblende Tonalite to Granodiorite suite, and a Biotite Granite to Granodiorite suite. Plutonic rocks of the Biotite Tonalite to Granodiorite suite occur along the southwestern and northeastern margins of the Revell batholith. The principal type of rock within this suite is a white to grey, medium-grained, variably massive to foliated or weakly gneissic, biotite tonalite to granodiorite. One sample of foliated and medium-grained biotite tonalite produced a U-Pb age of 2734.2 +/- 0.8 Ma (Stone et al., 2010). The Hornblende Tonalite to Granodiorite suite occurs in two irregularly shaped zones surrounding the central core of the Revell batholith. Rocks of the Hornblende Tonalite to Granodiorite suite range compositionally from tonalite through granodiorite to granite and also include significant proportions of quartz diorite and quartz monzodiorite. One sample of coarse-grained grey mesocratic hornblende tonalite produced a U-Pb age of 2732.3 +/- 0.8 Ma (Stone et al., 2010). Rocks of the Biotite Granite to Granodiorite suite underlie most of the northern, central and southern portions of the Revell batholith. Rocks of this suite are typically coarse-grained, massive to weakly foliated, and white to pink in colour. The Biotite Granite to Granodiorite suite ranges compositionally from granite through granodiorite to tonalite. A distinct potassium (K)-Feldspar Megacrystic Granite phase of the Biotite Granite to Granodiorite suite occurs as an oval-shaped body in the central portion of the Revell batholith. One sample of coarse-grained, pink, massive K-feldspar megacrystic biotite granite produced a U-Pb age of 2694.0 +/- 0.9 Ma (Stone et al., 2010).

Borehole IG_BH01 is within an investigation area centred in the northern portion of the Revell batholith. Bedrock exposure in the area is generally very good due to minimal overburden, few water bodies, and relatively recent forestry activities. Ground elevations generally range from 400 to 450 m above sea level. The ground surface broadly slopes towards the northwest as indicated by the flow direction of the main rivers in the area. Local water courses generally tend to flow to the southwest towards Mennin Lake.

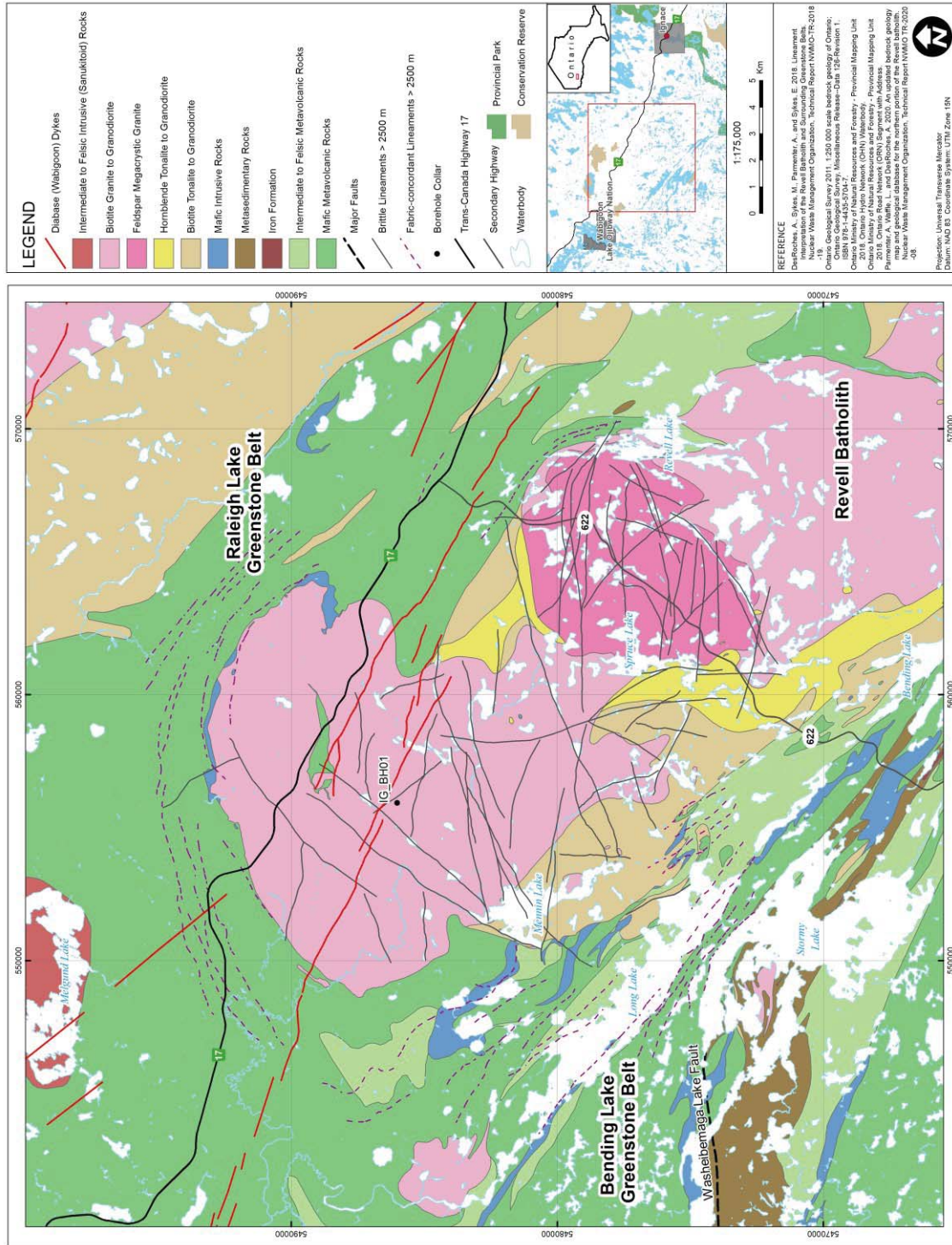


Figure 1: Location and Geological setting of borehole IG_BH01 in the northern portion of the Revell batholith.

The bedrock surrounding IG_BH01 is composed mainly of massive to weakly foliated felsic intrusive rocks that vary in composition between granodiorite and tonalite, and together form a relatively homogeneous intrusive complex. Bedrock identified as tonalite transitions gradationally into granodiorite and no distinct contact relationships between these two rock types are typically observed (SRK and Golder, 2015; Golder and PGW, 2017). Massive to weakly foliated granite is identified at the ground surface to the southeast of the investigation area. The granite is observed to intrude into the granodiorite-tonalite bedrock, indicating it is distinct from, and younger than, the intrusive complex (Golder and PGW, 2017).

West-northwest trending mafic dykes interpreted from aeromagnetic data extend across the northern portion of the Revell batholith and into the surrounding greenstone belts (DesRoches et al., 2018). One mafic dyke occurrence in the investigation area is approximately 15-20 m wide Wabigoon dyke swarm. One sample from the same Wabigoon swarm produced a U-Pb age of 1887 \pm 13 Ma (Stone et al., 2010), indicating that these mafic dykes are Proterozoic in age. It is assumed based on surface measurements that these mafic dykes are sub-vertical (Golder and PGW, 2017).

Long, narrow valleys are located along the western and southern limits of the investigation (Figure 1). All of these mafic dykes have a similar character and are interpreted to be part of the area (Figure 2). These local valleys host creeks and small lakes that drain to the southwest and may represent the surface expression of structural features that extend into the bedrock. A broad valley is located along the eastern limits of the investigation area and hosts a more continuous, un-named water body that flows to the south. The linear and segmented nature of this waterbody's shorelines may also represent the surface expression of structural features that extend into the bedrock.

Regional observations from mapping have indicated that structural features are widely spaced (typical 30 to 500 cm spacing range) and dominantly comprised of sub-vertical joints with two main orientations, northeast and northwest trending. Interpreted bedrock lineaments generally follow these same dominant orientations in the northern portion of the Revell batholith (Figure 1; DesRoches et al., 2018). Minor subhorizontal joints have been observed with minimal alteration, suggesting they are younger and perhaps related to glacial unloading. One mapped regional-scale fault, the Washeibemaga Lake fault, trends east and is located to the west of the Revell batholith (Figure 1). Additional details of the lithological units and structures found at surface within the investigation area are reported in Golder and PGW (2017).

2.2 Background and Overview of Borehole Drilling and Testing

2.2.1 Drilling Site Description

The drilling site for borehole IG_BH01 is located adjacent to Dyment Road where it intersects an old, overgrown logging road (dashed line in Figure 2), near the centre of the Revell site. The drilling site is approximately 100 m in the N-S direction, 40 m in the E-W direction, at its widest point, and has an area of 3,500 m² (Figure 3). The borehole is located at the northern end of the drilling site.

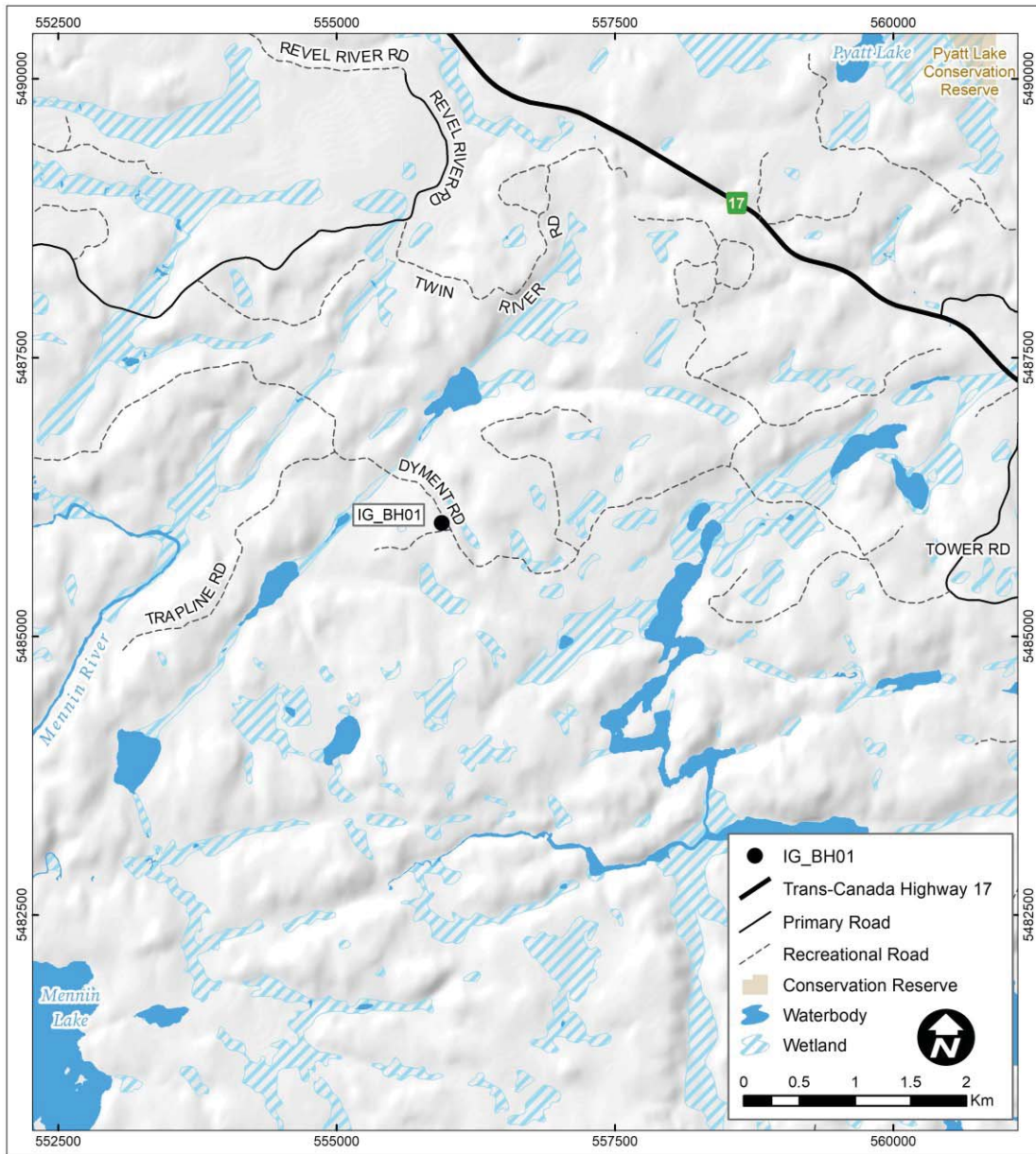


Figure 2: Location of the drilling site for borehole IG_BH01.

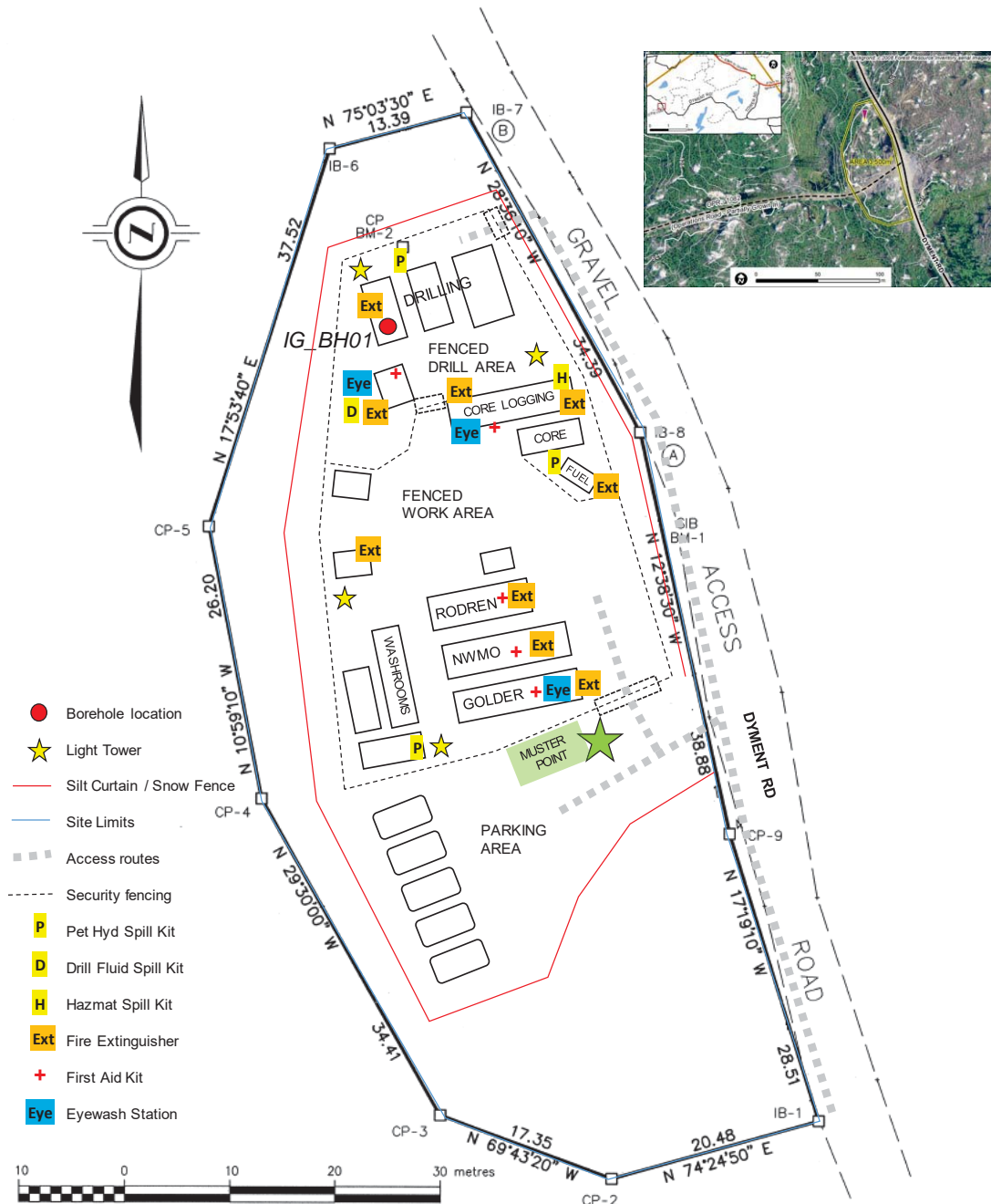


Figure 3: Drilling location and site layout for IG_BH01.

The drilling site was constructed to minimize the need for ground clearing and reduce the effects of erosion from water runoff. Factors which influenced the selection of the location of borehole IG_BH01 included distance from major surface lineaments, closeness to existing roads and minimal overburden thickness. The majority of the site was rock outcrop, and a compacted aggregate pad was constructed to level off the area where the drill rig would be located. An oblique aerial view of the drilling site is shown in Figure 4.



Figure 4: Aerial view of the drilling site for IG_BH01 – looking northwest.

2.3 Borehole Construction Details for IG_BH01

IG_BH01 was drilled vertically using a diamond drill with two sets of casing installed in the upper 69 m of the borehole to ensure borehole stability and reduce mixing of surface and deep groundwaters. The borehole construction is shown in the borehole schematic (Figure 5). The down-axis position along the borehole is measured in metres from surface.

PWT conductor casing was installed and cemented approximately 1.35 m into the bedrock to prevent drill fluid from escaping through the fractured upper bedrock. No overburden was encountered or recovered during the casing installation as bedrock was present at surface.

The borehole was drilled to 100 m and evaluated to determine a position to install the HWT casing. The borehole was reamed to the desired length of 69 m in preparation for installing HWT casing.

The casing was cemented in place using a high sulphate resistant cement (LaFarge) and the cement was left to cure for 36 hours. Drilling and coring activities resumed for the remainder of the borehole down to a drilled position along borehole of 1001.18 m. The final IG_BH01 casing diameters and positions, borehole and core diameters are shown in Table 1 and Table 2.

Table 1: Details of Casing and Coring Rods used for IG_BH01.

Casing Type	Outer Diameter (mm)	Inner Diameter (mm)	Position (m)
Conductor (PWT) Casing	139.7	127.0	1.35
Surface (HWT) Casing	114.3	101.6	69.0
HQ3 Drill Bit	96.0 ¹	61.1 ²	N/A

¹Open borehole diameter. ²HQ3 core diameter size.

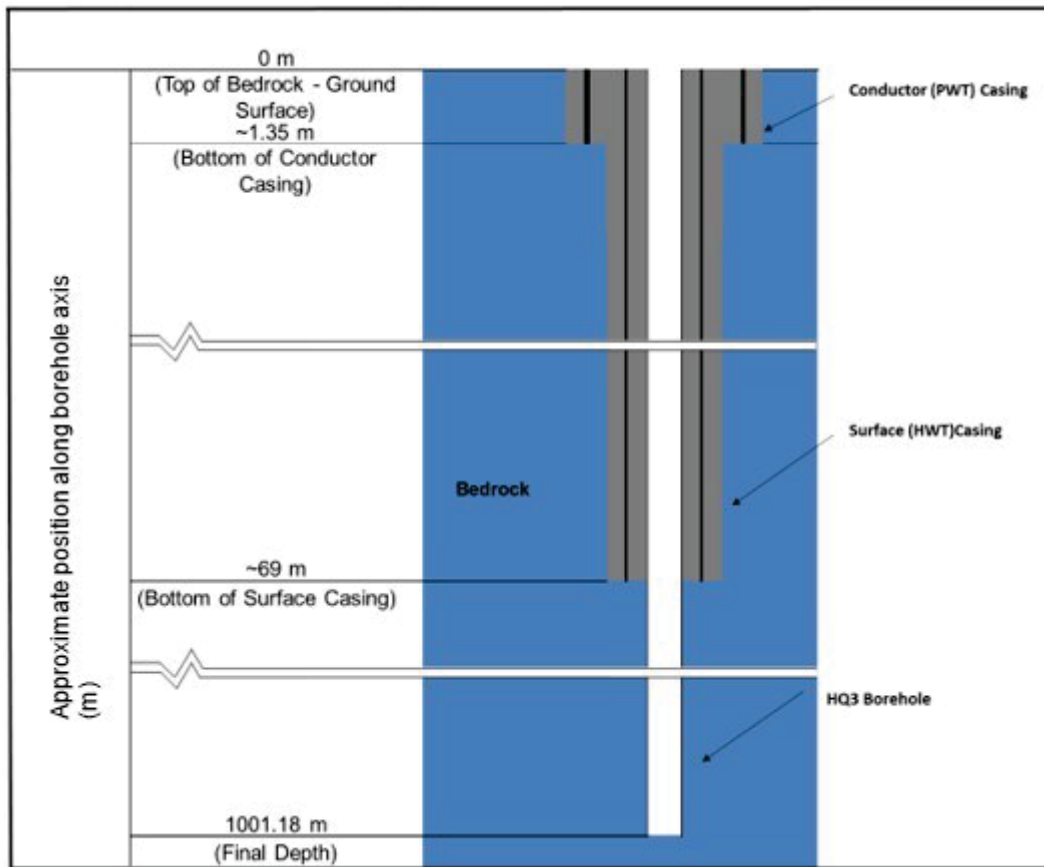


Figure 5: Final IG_BH01 Schematic of construction details; positions are along borehole axis.

Table 2: Details of Borehole Diameter for IG_BH01

Position from (m)	Position to (m)	Diameter Type	Borehole Diameter (mm)
0	1.35	PW Casing Shoe	143.76
1.35	69	HW Casing Shoe	117.65
69	1001.18	HQ Drill Bit	96

2.3.1 Borehole Deviation Analysis

Borehole IG_BH01 was planned to be drilled vertically (inclination = -90°) with no correction made for deviation as the drilling progressed. Two gyro surveys were conducted; one at 50 m intervals during drilling (downhole – multiple probe trips) to monitor deviation during drilling, and the other at 10 m intervals at the end of drilling (up hole – single trip; Golder, 2018b). During the geophysical logging, six televiwer surveys were conducted to measure a continuous profile of borehole deviation using an onboard 3-axis magnetometer and accelerometer. Surveys included four optical televiwer surveys (two downhole and two uphole) and two acoustic televiwer surveys (one downhole and one uphole). The televiwer surveys provided continuous inclination and declination data at ~ 2 mm intervals (Golder, 2019a).

In all cases, the borehole positioning calculation method used was the Minimum Curvature Method. Of the common borehole positioning methods, the Minimum Curvature method yields the most accurate location of the borehole (API, 1985). Each survey yielded a borehole path, which was used to assess the uncertainty in the borehole position (Figure 6).

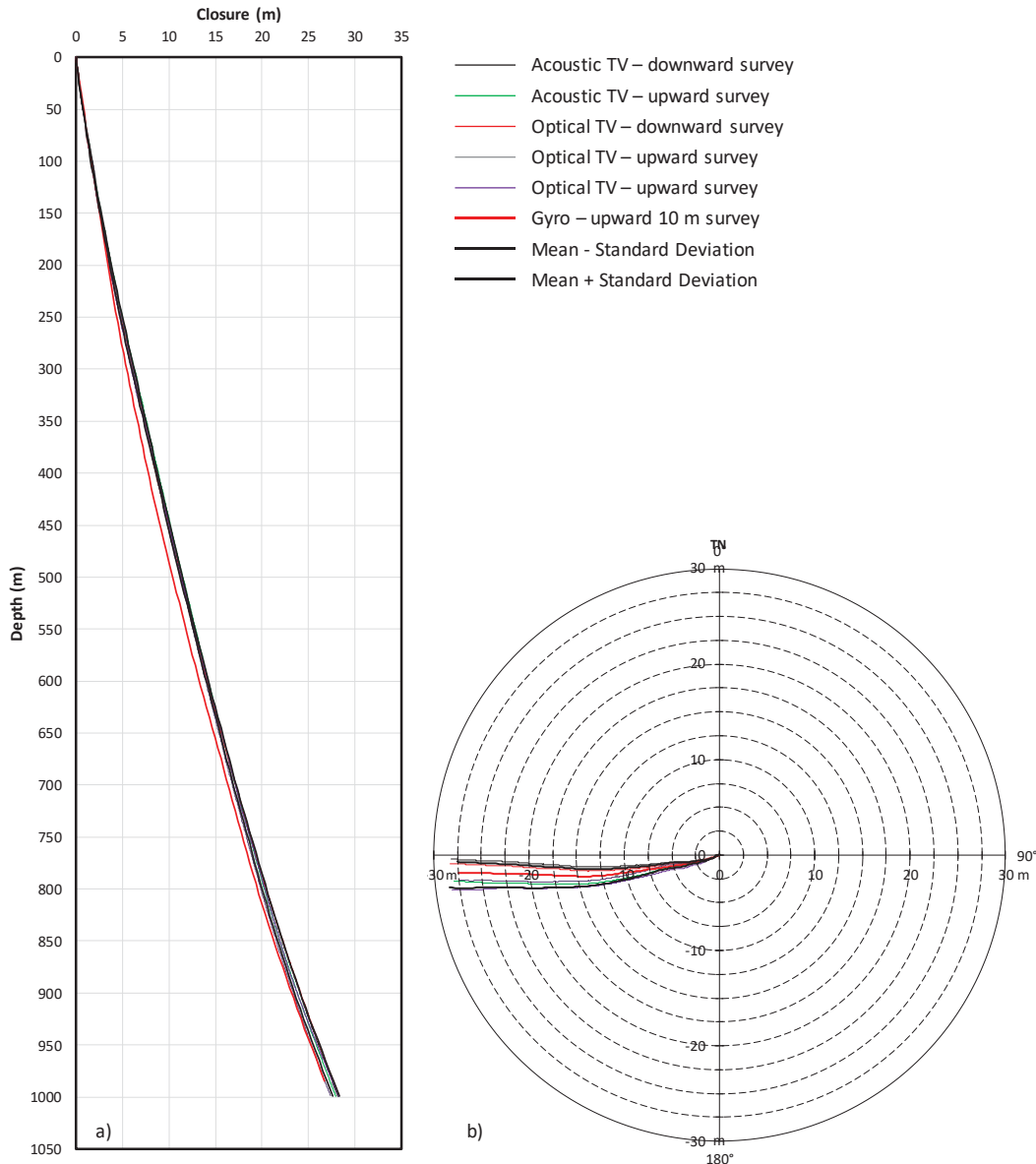


Figure 6: Closure and bird's eye view of calculated borehole locations for televiewer and gyro surveys. a) Closure profile – distance between calculated borehole position and planned borehole position. b) Plan view – borehole wander on the plane perpendicular to the planned borehole axis.

When the borehole positions from the televiewer surveys were plotted, it was observed that one of the optical televiewer downhole surveys resulted in a path that deviated from the others (outside of the mean ± 1 standard deviation envelope) and it was excluded from further analyses. The plan view (Figure 6b) shows the downward and upward surveys cluster in two groups, and the gyro survey bisects the groups. The grouping of the televiewer paths could be due to the different tensions in the cable between lowering the tool and pulling the tool upwards, and the fact that the televievers are never stationary (continuous measurement).

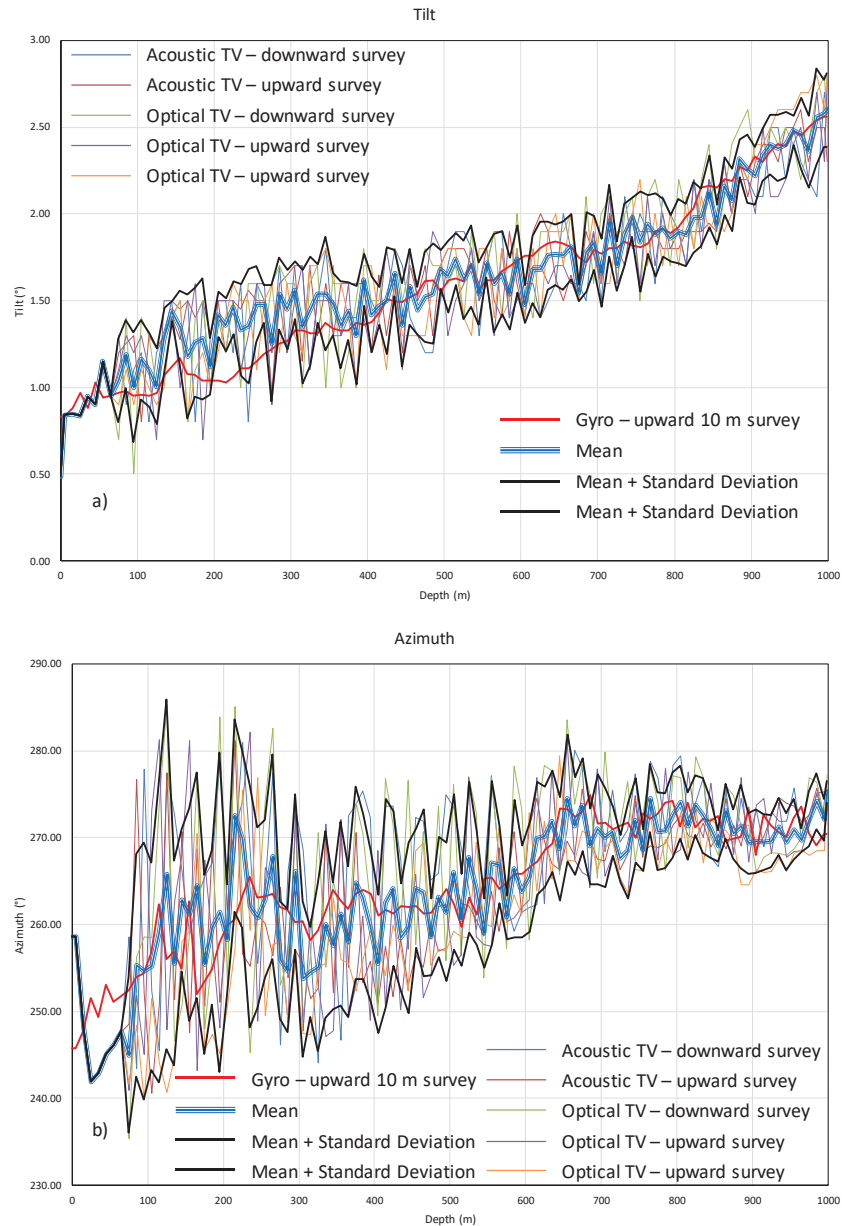


Figure 7: Tilt and azimuth vs position along borehole for combined magnetic and gyro surveys. Mean and standard deviation for magnetic surveys also shown. a) Tilt (angle with respect to vertical) vs position. b) Azimuth (clockwise angle with respect to True North) vs position.

Figure 7 shows the azimuth and the tilt of the televiwer surveys and the 10 m spaced gyro survey. The measurements for the two gyro surveys were reasonably consistent with differences in tilt less than 0.15° and azimuths within 5° , with the exception of a few stations. The gyro survey with stations 10 m apart was compared with the televiwer surveys. To facilitate the comparison, the televiwer survey profiles were sampled at 10 m intervals for a direct comparison with the gyro survey. Due to the steel casing, the majority of the televiwer surveys were terminated at the base of the casing and are missing data from the first 69 m. Therefore, a single televiwer survey, conducted prior to grouting the casing, was used for the first 69 m.

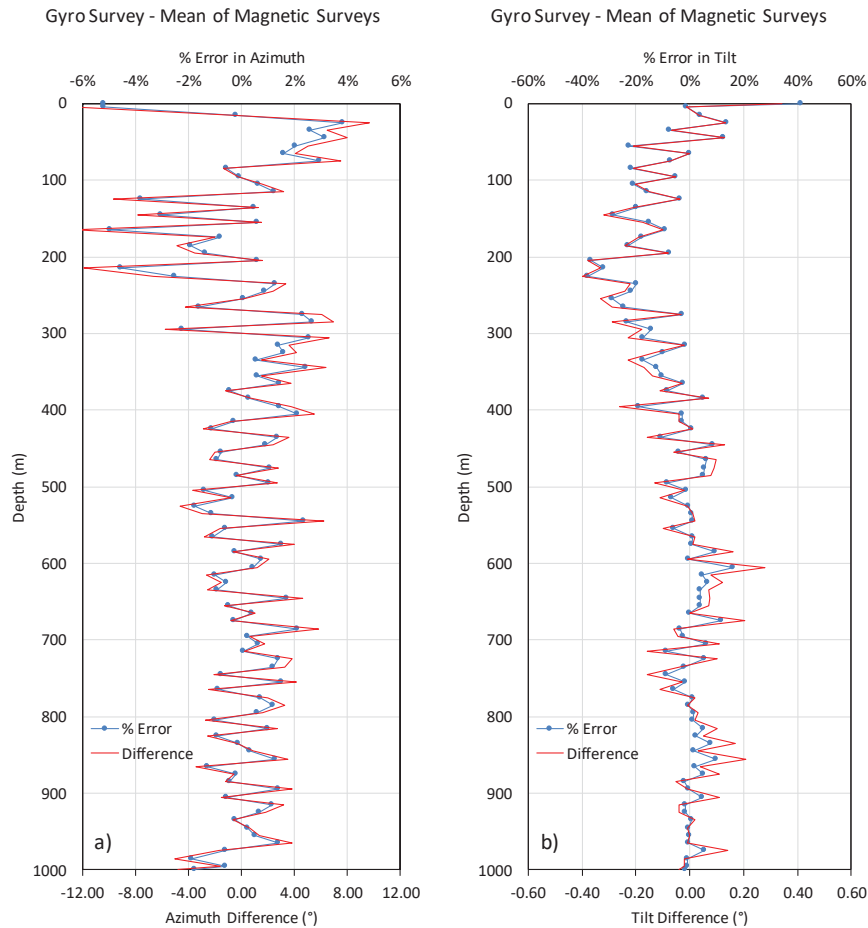


Figure 8: Percent error profile for the azimuth and tilt between the gyro measurements and the mean of the televiewer measurements [$100 \times (\text{Gyro} - \text{Mean of televiewer}) / \text{Gyro}$].

For comparison, Figure 8 shows the percent error in azimuth and tilt measurements along the length of the borehole. Analysis indicates that the error in azimuth is $0.07\% \pm 1.7\%$ and the error in tilt is $-4\% \pm 11.9\%$. The azimuth of the gyro survey plots close to the mean of all the surveys. The tilt of the gyro survey indicates that the hole is steeper at the top than the average of that of the magnetic surveys, but it has a smoother trend.

The three components of the location of the borehole, namely, easting, northing, and true vertical depth, were compared between the Gyro survey (10 m stations) and the mean of all televiewer surveys. The televiewer surveys provided an estimate of the magnitude of the error, as well as an average for comparison with the gyro survey. The Reflex EZ-Gyro instrument is considered more accurate than the televievers and has been shown to be consistent with the average of the televiewer surveys. The comparison indicates that the largest uncertainty between the measurements is in the northing direction and is approximately 1.2 m (standard deviation for the televiewer surveys) at the end of the borehole. The uncertainty in the easting direction is approximately 0.5 m (standard deviation for the televiewer surveys). The uncertainty in the true vertical depth is about 0.15 m (standard deviation for the televiewer surveys).

Based on the analysis provided, and the stationary nature of the gyroscopic measurement, results from the gyroscopic survey recorded at 10 m intervals in the borehole are considered to accurately represent the borehole geometry, with a narrow standard deviation when compared to the televiewer logged deviation results.

Therefore, the borehole orientation measured by the Gyro survey, as shown in Figure 9, is the most accurate representation of the borehole path. The borehole is collared at 555943.35 E, 5486016.45 N, and Elevation 430.72 masl, deviates from the planned vertical orientation between 1° and 2° in the westerly direction, and terminates at 555915.94 E, 5486014.57 N, and Elevation - 570.14 masl. The true vertical depth of the borehole is 1000.86 mbgs and terminates 27.41 m to the west and 1.88 m to the south of the collar. Note that location and thickness values for lithology, alteration, structures, etc. throughout the remainder of this report are calculated from positions along borehole axis, measured in metres (unless otherwise indicated).

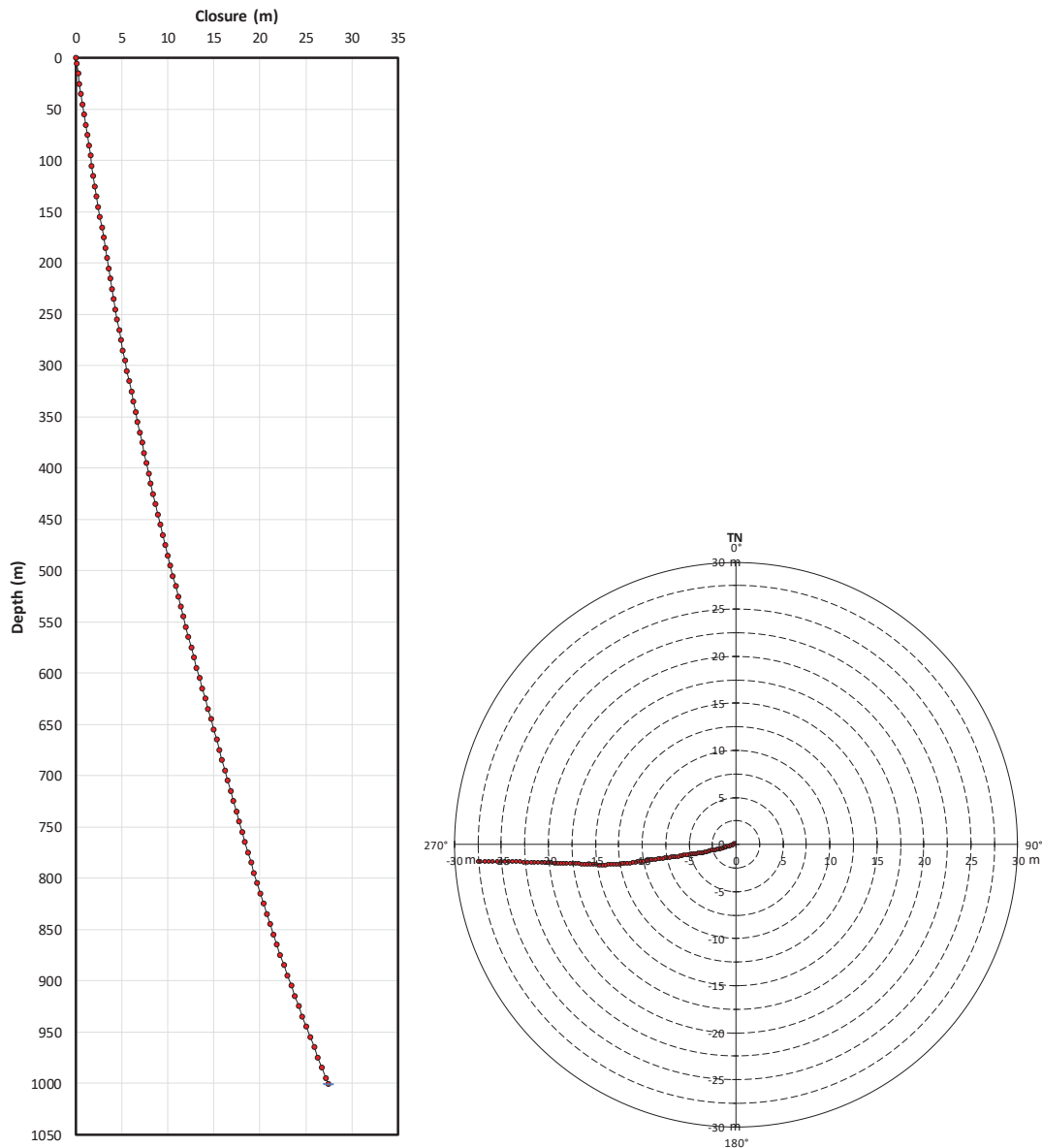


Figure 9: Closure and plan view of calculated borehole locations for the gyro survey. a) Closure profile – distance between calculated borehole position and planned borehole position. b) Plan view – borehole wander on the plane perpendicular to the planned borehole axis.

3 INTEGRATED GEOLOGICAL INTERPRETATION

The following section presents an integrated geological interpretation for IG_BH01 using the data collected during both geological core (WP03) and geophysical (WP05) logging activities, as well as relevant data from the laboratory analyses of core samples. The data sources and terminology used in order to develop the geological interpretation presented herein are described first in Section 3.1. The lithological interpretation, including final lithology and alteration logs is presented in Sections 3.2.1 and 3.2.2, respectively, resulting in the development of an integrated rock unit model described in Section 3.2.3. A structural interpretation is presented in Section 3.2.4, resulting in a structural unit model described in Section 3.2.5, and a description of identified high fracture frequency intervals in Section 3.2.6.

3.1 Data Used for Geological Interpretation

The bedrock lithology, alteration, and structural features were logged continuously over a total borehole length of 1001.18 m (Golder, 2018c). This initial analysis was largely based on visual inspection of the core to describe the unique rock and alteration types and associated characteristics including texture, fabric, and grain size. Variations in bedrock radiometric components were evaluated with the use of a handheld gamma-ray spectrometer, measured once per three metre core run, to help distinguish between the various granitoid phases encountered.

Structural features in the borehole were initially collected by geological core logging to evaluate unique structure types, mineral infillings, and other associated characteristics. Orientations of the logged structures were initially measured relative to an arbitrary reference line drawn along the length of the core axis.

Following completion of the drilling and logging activities, continuous borehole geophysical logs were acquired and the results from some of these logs were used to enhance the analysis of lithology, alteration and structure (Golder, 2019a). The orientations of logged structures based on arbitrary references lines were corrected through analysis of the continuous downhole optical and acoustic televiewer surveys, following the method described in Appendix D.

Geological core logging data determined to be relevant to geological interpretation include the following, as presented in the geological and geotechnical core logging report (Golder, 2018c):

- Lithology
 - Rock Class & Rock Type
 - Rock Fabric
 - Textures (Igneous, Metamorphic)
 - Grain Size (Ground Mass, Phenocryst/Porphyroblast)
 - Defining Minerals
 - Colours & Intensity
- Alteration
 - State
 - Mineral Assemblage
- Weathering
 - State
- Structure
 - Position Along Borehole
 - Type
 - Broken/Intact/Partially Intact
 - Sub-Type

- Infilling or Defining Mineral Details
- Rock Wall Strength
- Shape
- Roughness
- Dip and Dip-Direction
- Alpha, Beta, Gamma, and Delta Angles
- Geological Aperture
- Width (where applicable)

Note that geological aperture is an estimated measurement of the open space between two adjacent fracture surfaces determined visually during geological core logging, during interpretation of downhole televiewer logs, or during the integration of data from these two sources. For our purposes, geological apertures are estimated values only because there are multiple possible sources of uncertainty in how a reported aperture value relates to the true aperture of a fracture identified as broken. There are uncertainties related to measurement inaccuracy, including where the opening is very small, where the opposing fracture planes are not parallel or fit poorly together, or due to limits in televiewer resolution. In addition, effects due to drilling or decompression may create or enhance the visible open space identified as aperture. Finally, aperture measured in core or on a borehole wall is only a local aperture that is not necessarily representative over the entire fracture.

To further enhance the bedrock lithology, alteration, and structure along the length of the borehole, the following geophysical log results were determined to be most relevant:

- Optical Televiewer
- Acoustic Televiewer
- Natural Gamma
- Spectral Gamma
- Gamma-Gamma Density
- Neutron

All geophysical logging results are summarized in a separate geophysical logging report (Golder, 2019a). Prior to interpreting the geophysical log responses associated with rock types from the borehole, minor positional adjustments were made to the geophysical log data to match log responses to key lithological markers identified in geological core logging, such as amphibolites which produce strong anomalies in density and neutron logs. Positional adjustments, when made, were typically less than 10 cm.

To further increase the lithological understanding of IG_BH01, 45 core samples were collected for whole-rock major and trace element litho-geochemistry as well as qualitative (mineral identification) and quantitative (modal mineralogy) thin section analysis. Samples were crushed, sieved, and separated for three different analyses. A portion of each sample was subjected to a lithium metaborate/tetraborate fusion, with the resulting bead digested in a weak nitric acid solution. Analyses were carried out by inductively coupled plasma optical emission spectrometry (ICP-OES) and inductively coupled plasma mass spectrometry (ICP-MS). The second portion of each sample was subjected to multi-acid digestion and analysis by ICP-MS and the third portion was sent for Instrumental Neutron Activation Analysis (INAA). Results from these analyses are integrated below to present a final interpretation of the lithological and alteration characteristics of IG_BH01. The litho-geochemical data are included in Appendix B.

3.1.1 Terminology

Several terms are introduced throughout this section to aid in describing the integration process. This includes:

- Rock Unit - A borehole length comprising a dominant rock type and/or a combination of rock types (and, if applicable, alteration and weathering types) that are considered distinct from adjacent parts of the borehole. A minimum unit thickness of five (5) m is used herein to define each rock unit. Each rock unit is uniquely labelled and can be repeated with a sublabel at different positions along borehole if appropriate.
- Structural Unit - A borehole length comprising a relatively uniform per metre fracture frequency that is distinct from adjacent parts of the borehole. Each structural unit is uniquely labelled and can be repeated with a sublabel at different positions along borehole if appropriate.
- Rock Type - A rock having a unique, identifiable set of characteristics.
- High Fracture Frequency Interval - A cluster of fractures (i.e., faults, joints and or veins) that exceeds a minimum relative fracture frequency threshold along a distinct borehole length.

3.2 Geological Results

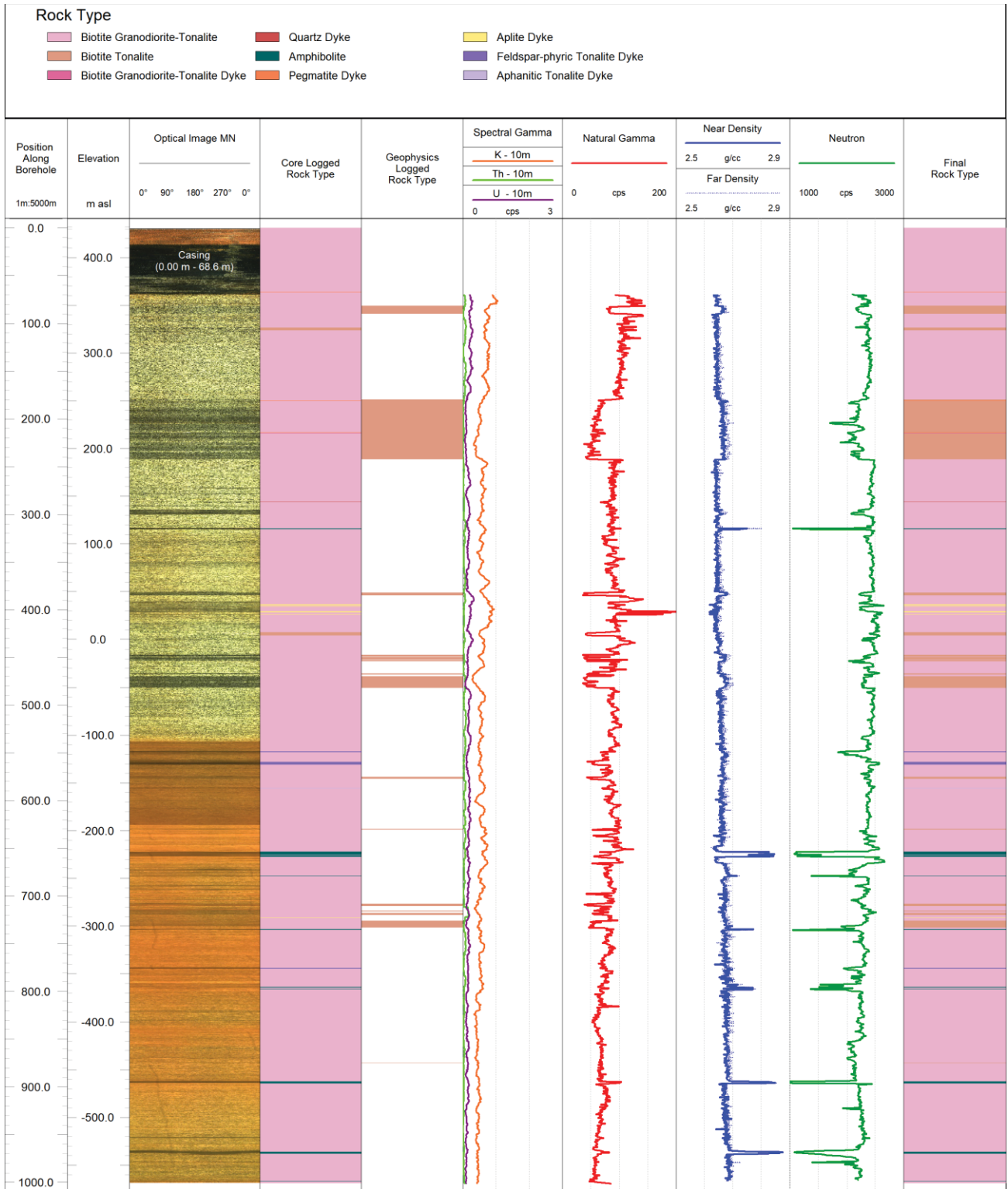
This section presents the results from the integration of the geological core logging (WP03) and geophysical logging (WP05) datasets along with integration of the results from an additional 45 samples selected for both petrographic and lithochemical analysis. Through the process of data integration, a total of nine distinct rock types are identified for IG_BH01 (Table 3). A final log of lithology is presented which shows their distribution along the length of the borehole (Figure 10).

Table 3: Summary of Rock Types Encountered in IG_BH01

Rock Type	Texture	Fabric	Grain Size (mm)	Total Logged Length (m)	% of Recovered Core
Biotite granodiorite-tonalite	Equigranular	Massive to weakly foliated	0.1-5	864.40	86.3
Biotite tonalite	Equigranular	Massive	0.1-5	114.22	11.4
Amphibolite	Equigranular	Foliated to massive	<1	12.39	1.2
Feldspar-phyric tonalite dyke	Porphyritic	Foliated to massive	<0.5* 1-3.5**	4.83	0.5
Aplite dyke	Equigranular	Massive	<1	3.27	<0.5
Pegmatite dyke	Inequigranular	Massive	5-50	0.65	<0.1
Aphanitic tonalite dyke	Equigranular	Foliated	<1	0.43	<0.1
Quartz dyke	Equigranular	Massive	5-10	0.37	<0.1
Biotite granodiorite-tonalite dyke	Equigranular	Massive	0.1-5	0.62	<0.1

*Groundmass

**Phenocrysts



*Note: orange colour appearance of lower 460 m of televiewer image is affected by the borehole fluid turbidity.

Figure 10: Input datasets used to derive a final lithology log. From left: optical televiewer log, geological core-logged rock types, rock types added to lithology log as a result of review of geophysical logs, four suites of continuous geophysical logs that aid in distinction of rock types, and final lithology log. Due to the low spectral gamma counts, K, U and Th were evaluated using a 10 m window, resulting in a smoothing of their profiles.

3.2.1 Lithological Interpretation

The main rock types intersected by borehole IG_BH01 include a biotite granodiorite-tonalite and a similar, but compositionally distinct, biotite tonalite. Subordinate rock types identified in IG_BH01 include distinct metre-scale packages of amphibolite and several suites of sub-metre thick dykes of varying felsic composition (Table 3 and Table 4). This final interpretation of the rock types encountered in IG_BH01, shown in Figure 10, presents an updated understanding relative to the information that was initially reported in the WP03 data report (Golder, 2018c). A short summary of this evolution of understanding is included along with the lithological descriptions below that summarize the main characteristics of the rock types identified in IG_BH01.

Table 4: Summary average of major oxides in the rock types of IG_BH01. Note that only 5 rock types were sampled for lithochemical analysis and there are no results for pegmatite, quartz, and biotite granodiorite-tonalite dykes. Aphanitic and Feldspar-phyric tonalite dykes are combined as they are compositionally the same.

Rock Type	Major Oxide Composition (average, %)									
	SiO ₂	Al ₂ O ₃	Fe ₂ O ₃	MnO	MgO	CaO	Na ₂ O	K ₂ O	TiO ₂	P ₂ O ₅
Biotite granodiorite-tonalite	73.06	13.72	2.50	0.03	0.50	2.33	4.22	2.07	0.22	0.06
Biotite tonalite	69.01	15.69	3.36	0.04	0.80	3.43	4.78	1.50	0.36	0.10
Amphibolite	48.16	11.78	9.29	0.15	10.77	9.66	2.00	2.81	0.66	0.30
Aphanitic and Feldspar-phyric tonalite dykes	70.49	15.08	3.07	0.04	0.78	3.19	4.46	1.77	0.38	0.10
Aplite dyke	75.32	13.39	0.98	0.04	0.06	0.62	3.82	5.24	0.04	0.02

Main Rock Types

The bedrock intersected by IG_BH01 is dominated by a medium-grained granitoid rock, with biotite as the primary mafic mineral. This granitoid rock represents a total of 97.8 % of the recovered core. The general consistency in character of the recovered core with the bedrock identified on the ground surface indicates that the biotite granodiorite-tonalite encountered in IG_BH01 is part of the same granodiorite-tonalite bedrock unit that was mapped at ground surface in the vicinity of the borehole (Golder and PGW, 2017).

Gamma ray spectrometry measurements taken during geological core logging suggested that the granitoid rock was tonalitic in composition, using a % potassium (K) cut-off of < 1.7 % to identify rock as tonalite versus > 1.7 % to identify granodiorite. Overall, the results straddled the boundary between tonalite and granodiorite end members and therefore the rock was uniformly logged as 'biotite tonalite' for simplicity. A darker coloured and slightly finer-grained variation of the 'biotite tonalite' was also identified during the logging. This darker coloured variant was interpreted as being primarily due to an apparent increase in biotite content, and so these sections were identified as 'biotite-rich tonalite', a mappable unit compositionally similar to, but distinct from, 'biotite tonalite'. The contacts between these two granitoid rocks vary from sharp to gradational along the length of the borehole. Contacts between them were not always clearly distinguishable during the run-by-run logging. However, upon inspection of the optical televiewer image, in conjunction with reviewing photographs of the recovered core, the distribution of the darker 'biotite-rich tonalite' became more apparent as distinct, decimetre- to metre-scale intervals, and in one occurrence an approximately 60-metre-thick interval, primarily in the upper half of the borehole.

Subsequent petrographic and lithogeochemical investigation, including modal mineral analysis of 27 samples of the granitoid, indicate that the rock identified during geological core logging as 'biotite tonalite' is indeed not uniformly tonalitic. The granitoid exhibits a range in composition that spreads across the granodiorite-tonalite boundary on a QAP ternary diagram, as suspected (Figure 11).

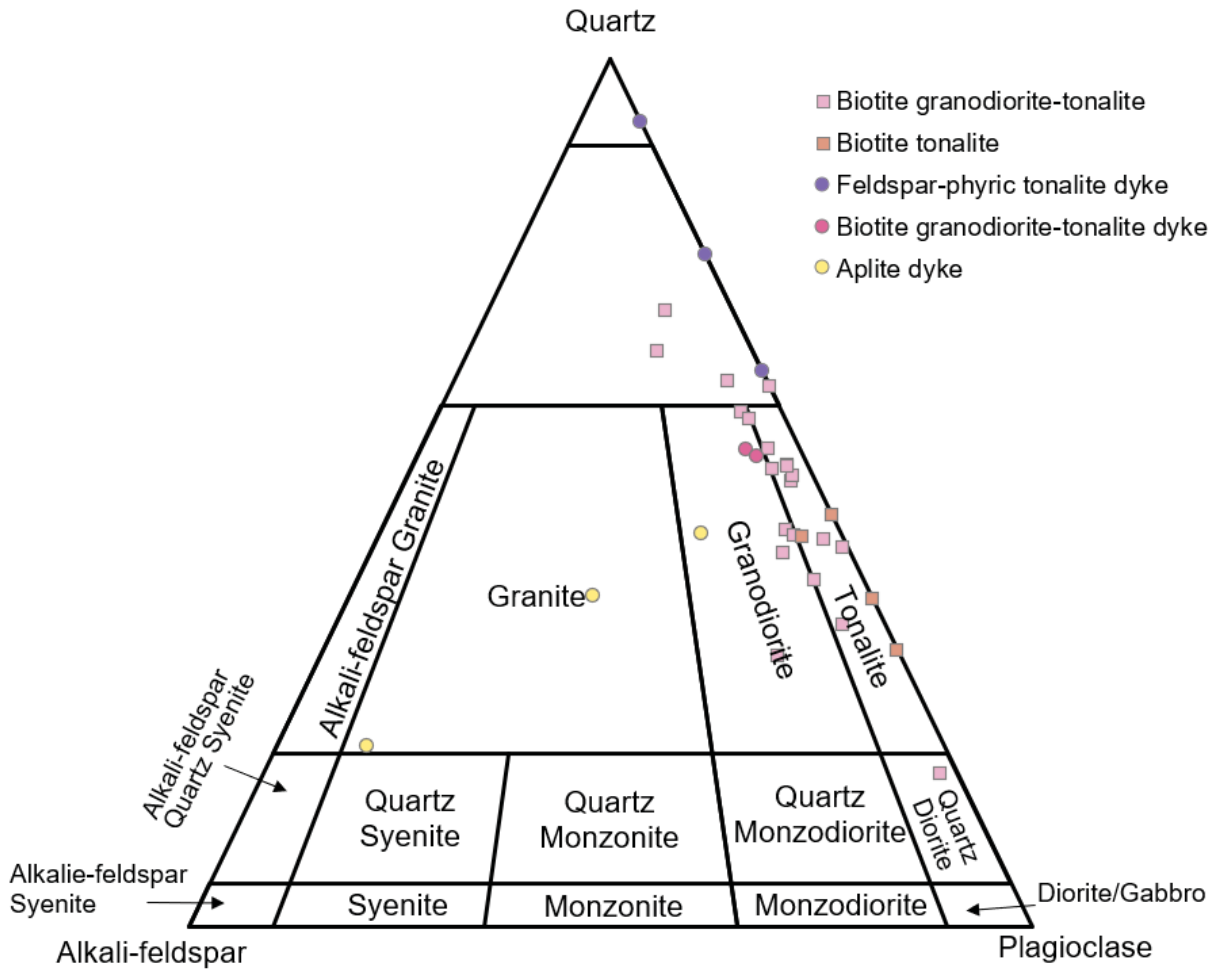


Figure 11: Classification/nomenclature of dominant granitoid phases according to the normalized modal mineral content (Q + A + P = 100 Vol%) as determined from investigation of 27 samples taken for lithogeochemical analysis. Average modal mineralogy for each sample was plotted on a simplified ternary Streckeisen diagram after Le Bas and Streckeisen (1991).

A similar result is produced when the lithogeochemical data (Table 4) for the granitoid phases are plotted on a plutonic rock classification diagram (Figure 12; Debon and Le Fort, 1983). As such, this rock is identified herein as a 'biotite granodiorite-tonalite'.

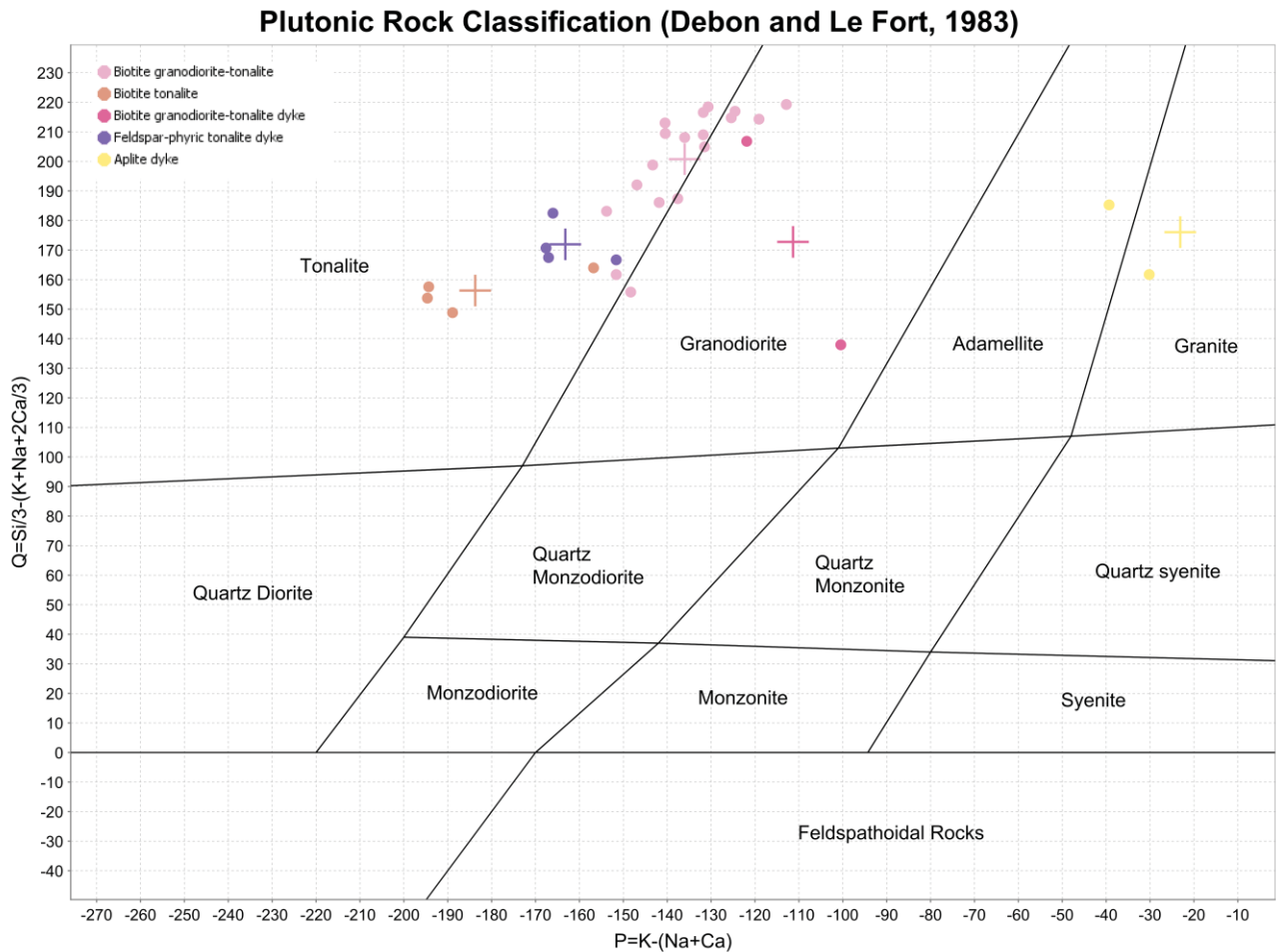


Figure 12: Plutonic Rock Classification (Debon and Le Fort, 1983). Diagram axes correspond to proportions of K-feldspar and plagioclase to quartz. P is calculated from $(K - (Na + Ca))$, and Q is calculated from $((Si/3) - (K + Na + (2 \cdot Ca)/3))$. Parameters calculated as oxide percentages converted to millifications. Crosses show mean composition of each rock type.

The petrographic and lithochemical analyses of the rock initially logged as 'biotite-rich tonalite' confirm the smaller grain size, and a slight increase in biotite content. However, the most important observation from this additional analysis is that this subunit is very poor in alkali feldspar (Table 4). These 'biotite-rich tonalite' rocks plot uniformly in the tonalite field on both the QAP and plutonic rock classification diagrams (Figure 11 and Figure 12, respectively). As such, this rock is identified herein as a 'biotite tonalite', which is a distinct endmember of the biotite granodiorite-tonalite. As information is obtained from future boreholes this distinction will continue to be evaluated. The lithochemical data and modal mineral composition of the samples, determined semi-quantitatively using polished thin sections, is presented in Appendix B:.

Biotite granodiorite-tonalite: The biotite granodiorite-tonalite unit is pale to medium white-grey and equigranular with mineral size tending towards the upper range of medium-grained (0.3-3.5 mm average) for all mineral phases (Figure 13). Its main mineral phases are quartz, plagioclase, and biotite, with the latter comprising 5-10 % of the matrix. This rock is predominantly massive although a weak biotite-defined foliation becomes locally apparent below approximately 400 m along borehole.

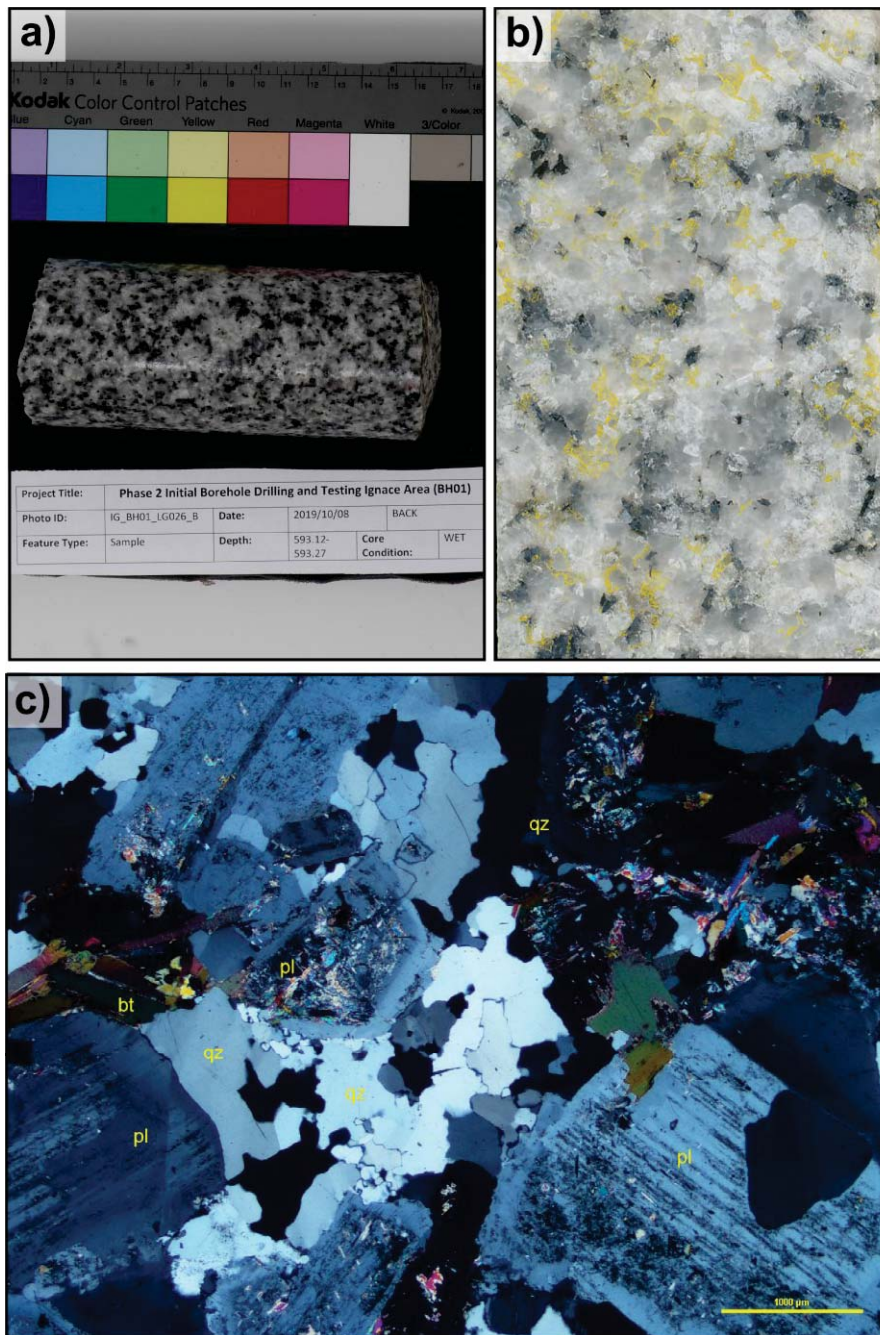


Figure 13: Representative examples of biotite granodiorite-tonalite (sample IG_BH01_LG026). a) Hand-sample photograph. b) Billet photograph showing yellow staining of potassium feldspars (billet size is 25 x 40 mm). c) Thin section photomicrograph with rock-forming minerals plagioclase (pl), quartz (qz) and biotite (bt). Sericite (white mica) alteration can be seen in cores of plagioclase crystals; crossed polarizers transmitted light.

Biotite tonalite: The biotite tonalite is pale to medium white-grey and equigranular with mineral size tending towards the lower range of medium grained (0.1-2 mm average; Figure 14). The biotite tonalite unit exhibits an equigranular and massive fabric. The main mineral phases are quartz, plagioclase, and biotite, with the latter comprising 8-13 % of the matrix.

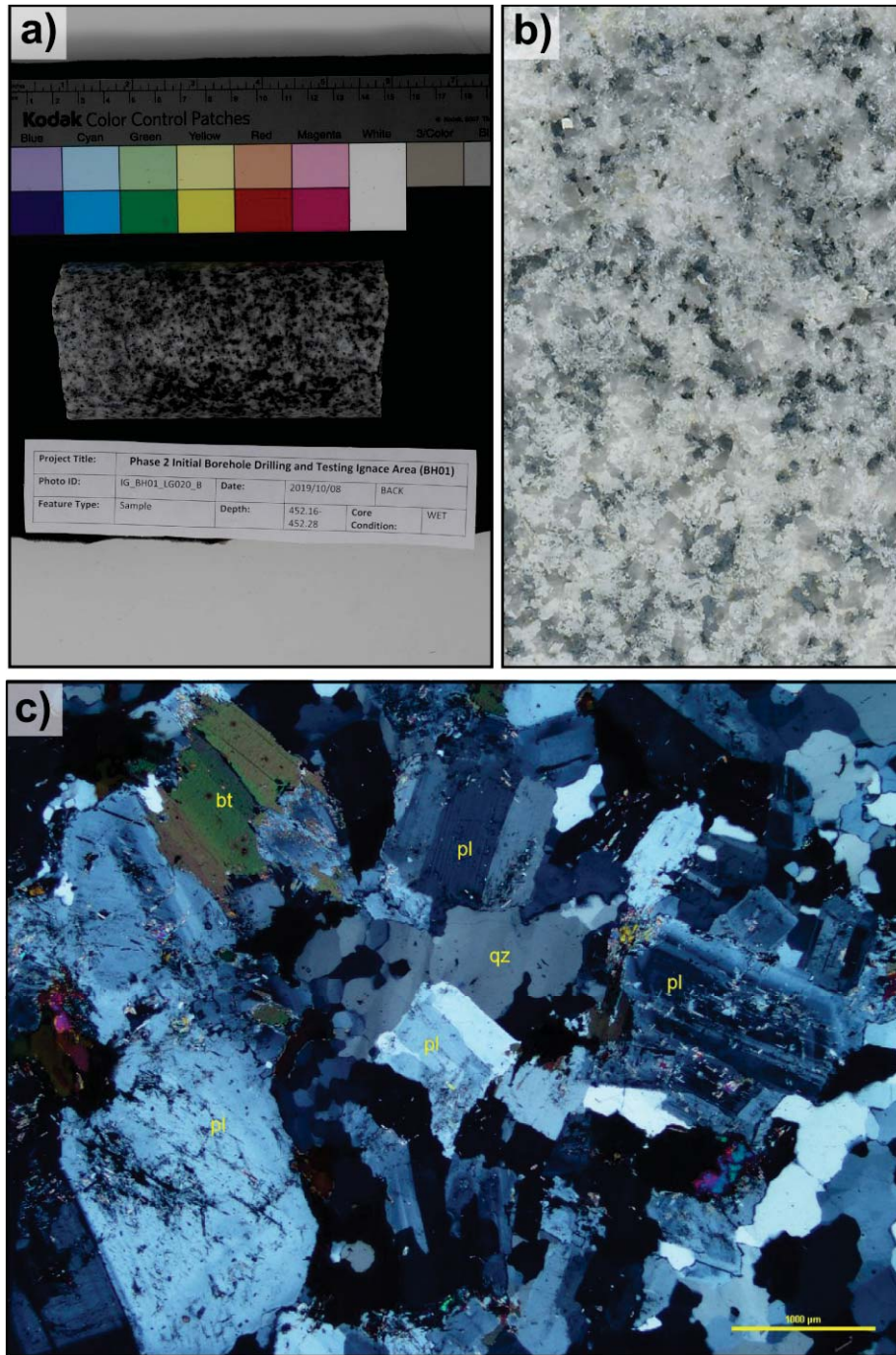


Figure 14: Representative examples of biotite tonalite (sample IG_BH01_LG020). a) Hand-sample photograph. b) Billet photograph showing lack of yellow-stained potassium feldspars (billet size is 25 x 40 mm). c) Thin section photomicrograph with rock-forming minerals plagioclase (pl), quartz (qz) and biotite (bt). Minor sericite (white mica) alteration can be seen in cores of plagioclase crystals; crossed polarized transmitted light.

The reclassification of some biotite granodiorite-tonalite intervals to biotite tonalite represents the main component of information added from WP05 and lithogeochemistry to create the final lithology log (Figure 10). The revised lithological identification reduces the quantity of biotite granodiorite-tonalite to 864.40 m (86.3 %) of the total recovered core length from the originally logged 975.11 m (97.4 %). The intersected length of biotite tonalite was revised from the 3.51 m (<1 %) to 114.22 m (11.4 %). The biotite tonalite layers are also coincident with distinct signatures in the natural gamma ray, gamma-gamma density, and neutron logs, providing additional basis for their distinction from the biotite granodiorite-tonalite beyond their visual characteristics (Figure 10).

Subordinate Rock Types

In IG_BH01, the subordinate rock types encountered (amphibolite, aphanitic tonalite dykes, feldspar-phyric tonalite dykes, quartz dykes, aplite dykes, pegmatite dykes, and biotite granodiorite-tonalite dykes) represent a combined total of 2.2 % of the recovered core (Table 3).

Amphibolite: Thirteen occurrences of amphibolite were logged in IG_BH01, accounting for 12.39 m (1.2 %) of the total recovered core (Table 3). It is unclear whether the amphibolite units are dykes or xenoliths from the surrounding greenstone belts, or a combination, because primary contact relationships such as chilled margins are obscured by penetrative deformation localized along the amphibolite contacts. Based on the mineral assemblage and evidence of low-grade metamorphism, they will be referred to as *amphibolites* in this report and this term will be refined as more information is received from future boreholes and testing. The amphibolites range in width from 0.26 m to 2.62 m. One amphibolite was identified at approximately 314 m along borehole, while the remainder of the occurrences were observed below 650 m along borehole (Figure 10). The identified amphibolites consistently exhibit sharp increases in density values and decreases in neutron values relative to the host biotite granodiorite-tonalite. Amphibolites are dark grey-green, equigranular, and usually fine-grained (<1 mm; Figure 15). The mineral assemblages include albite, tremolite/actinolite, plagioclase, biotite, chlorite, and epidote, +/- accessory titanite, calcite, and iron oxides. Lithogeochemistry shows an increase in iron and magnesium and a decrease in silica relative to the felsic units, which is expected in a mafic unit (Table 4).

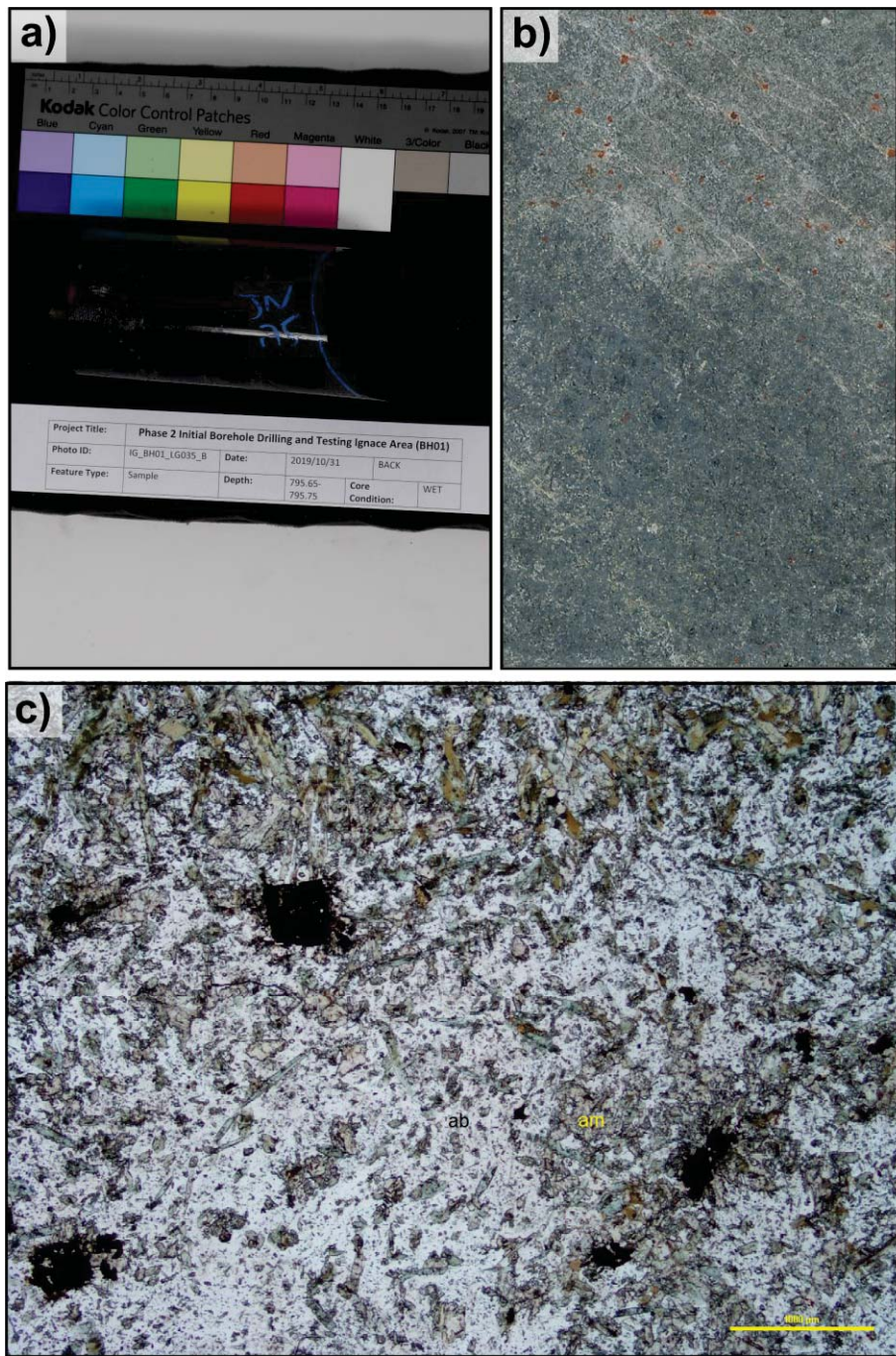


Figure 15: Representative examples of amphibolite (sample IG_BH01_LG035). a) Hand-sample photograph. b) Billet photograph (billet size is 25 x 40 mm). c) Thin section photomicrograph with main rock-forming minerals albite (ab) and amphibole (am; tremolite-actinolite), along with biotite (brown) and opaque iron-oxide minerals replacing pyrite crystals; plane polarized transmitted light.

Amphibolite contacts with the adjacent biotite granodiorite-tonalite are consistently sharp and exhibit a well-defined foliation; just over half of the contacts are broken (14/26; 54 %). As will be discussed later in the summary of structural information (Section 3.2.4), the contacts between individual amphibolite occurrences and the adjacent biotite granodiorite-tonalite primarily dip shallowly-moderately towards the north-northwest. Within the amphibolite occurrences themselves,

transitions between massive and strongly foliated domains are common and often observed to be sharp.

The internal foliation is generally observed to align with the orientation of the contacts. A decimetre- to metre-scale hematite +/- potassic alteration halo commonly envelops the amphibolite in the surrounding biotite granodiorite-tonalite. In addition, some fracture surfaces within the amphibolites are coated by chlorite.

Aphanitic and feldspar-phyric tonalite dykes: A suite of distinct felsic dykes was logged in seven occurrences between 500 – 1000 m along borehole (Figure 10). The dykes range in width from 0.19 m to 2.92 m and have a combined total length of 5.26 m, representing 0.5 % of the recovered core (Table 3). These dykes are characteristically dark grey-black with an aphanitic matrix (Figure 16). In one instance, a narrow apophyse of matrix material intrudes the surrounding rock, consistent with the interpretation that these are dykes (Figure 17). Petrographic analysis identified the mineral composition of the dykes as quartz, plagioclase, and biotite with minor alkali feldspar. Five of the occurrences also exhibit distinct, medium-grained albite phenocrysts within a matrix that is otherwise compositionally and texturally similar to the other two occurrences (Figure 16). During logging, these dykes were termed felsic or feldspar-phyric felsic dykes. Petrographic and lithogeochemical analyses of four samples from this suite of felsic dykes plot entirely within the tonalite field on the plutonic classification diagram (Figure 12 and Table 4). Based on this additional information, these names have been refined to aphanitic tonalite and feldspar-phyric tonalite dykes.

All of the aphanitic tonalite and feldspar-phyric tonalite dykes exhibit sharp contacts with the adjacent biotite granodiorite-tonalite and, in some occurrences, a well-defined foliation is also present. In thin section, this foliation is a weak to moderate schistosity defined by the alignment of biotite and quartz. Contacts were primarily intact with only a small number of occurrences (2/14; 14 %) identified as broken. Internally, these aphanitic tonalite and feldspar-phyric tonalite dykes vary between massive and foliated (schistose). Both the dyke contacts and internal foliation are predominantly oriented at a high angle to the core axis, suggesting a shallowly dipping orientation.

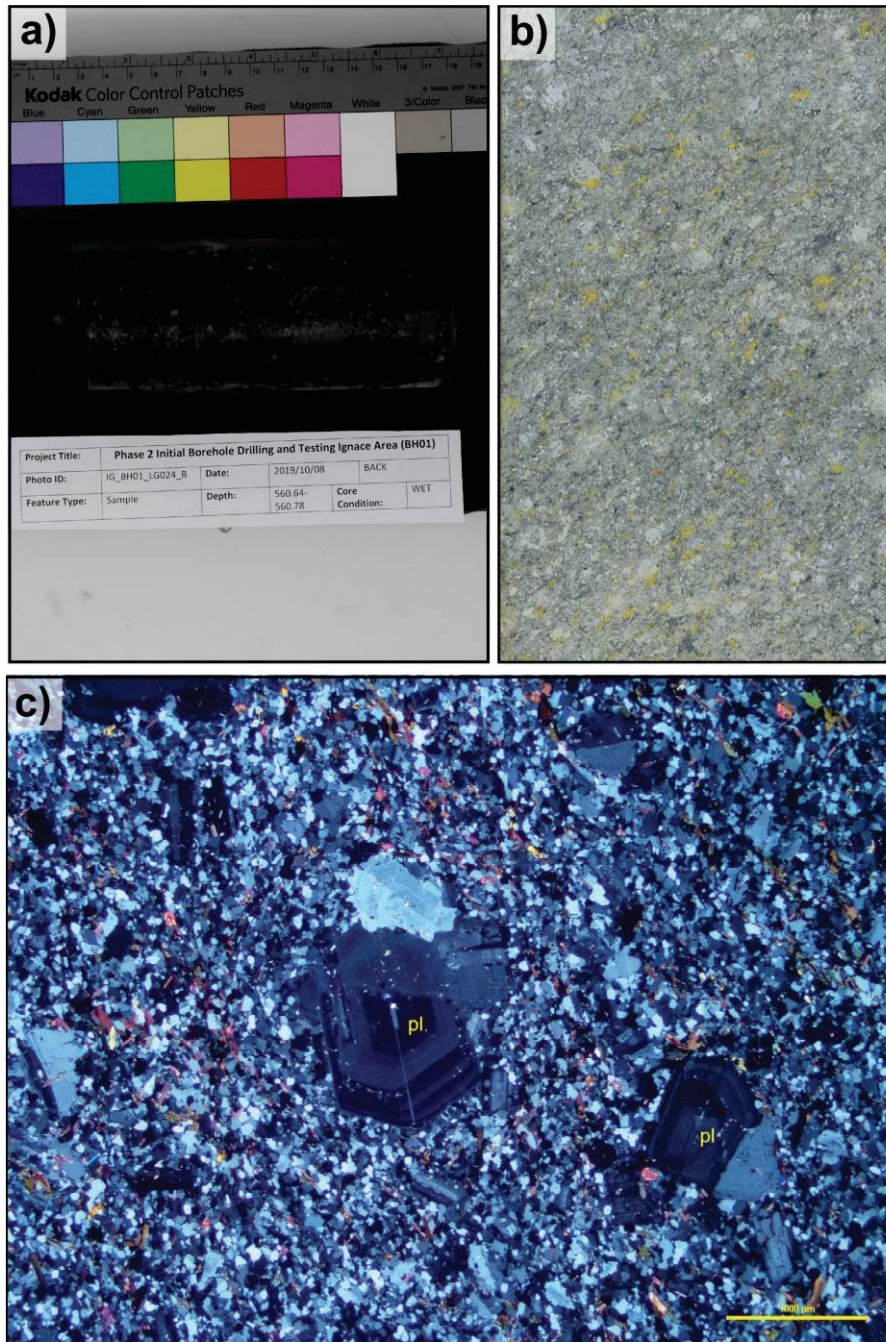


Figure 16: Representative examples of feldspar-phyric tonalite dyke (sample IG_BH01_LG024). a) Hand-sample photograph. b) Billet photograph showing yellow staining of alkali feldspar (billet size is 25 x 40 mm). c) Thin section photomicrograph with plagioclase (pl) phenocrysts, in a very fine-grained matrix of quartz and biotite; crossed polarized transmitted light.



Figure 17: Narrow apophyse extending from the margin of an aphanitic tonalite dyke into surrounding biotite granodiorite-tonalite (pencil for scale; approximately 586 m position along borehole).

Aplite dykes: Aplite dykes, ranging in width between 0.1 m and 0.84 m, were observed in nine occurrences, and represent a combined total length of 3.27 m (<0.5 %) of the recovered core (Table 3). They are primarily clustered between 390 m and 410 m along borehole (Figure 10). The aplite dykes are light white-grey, equigranular and very fine-grained to aphanitic (<1 mm). The aplite dykes are granitic in composition (Figure 12 and Table 4) with main mineral phases of plagioclase, potassium feldspar, quartz and minor biotite (Figure 18). Contact between the aplite dykes and the adjacent biotite granodiorite-tonalite are consistently sharp and intact, and oriented at a relatively low angle to the core axis.

Pegmatite Dykes: Pegmatite dykes, ranging in width from 0.12 m to 0.21 m, were observed in four occurrences and represent a combined total length of 0.65 m (<0.1 %) of the recovered core (Table 3). Pegmatite dykes are mostly found in the upper 250 m of the borehole (Figure 10). These dykes are light grey-pink, massive, and inequigranular with distinct, very coarse-grained (10-50 mm), square-edged, K-feldspar crystals within a coarse-grained (5-10 mm) matrix of quartz and plagioclase (Figure 23). The pegmatite dykes exhibit gradational to sharp and consistently intact contacts with the adjacent granodiorite-tonalite. The contacts are consistently oriented at a low angle to the core axis.

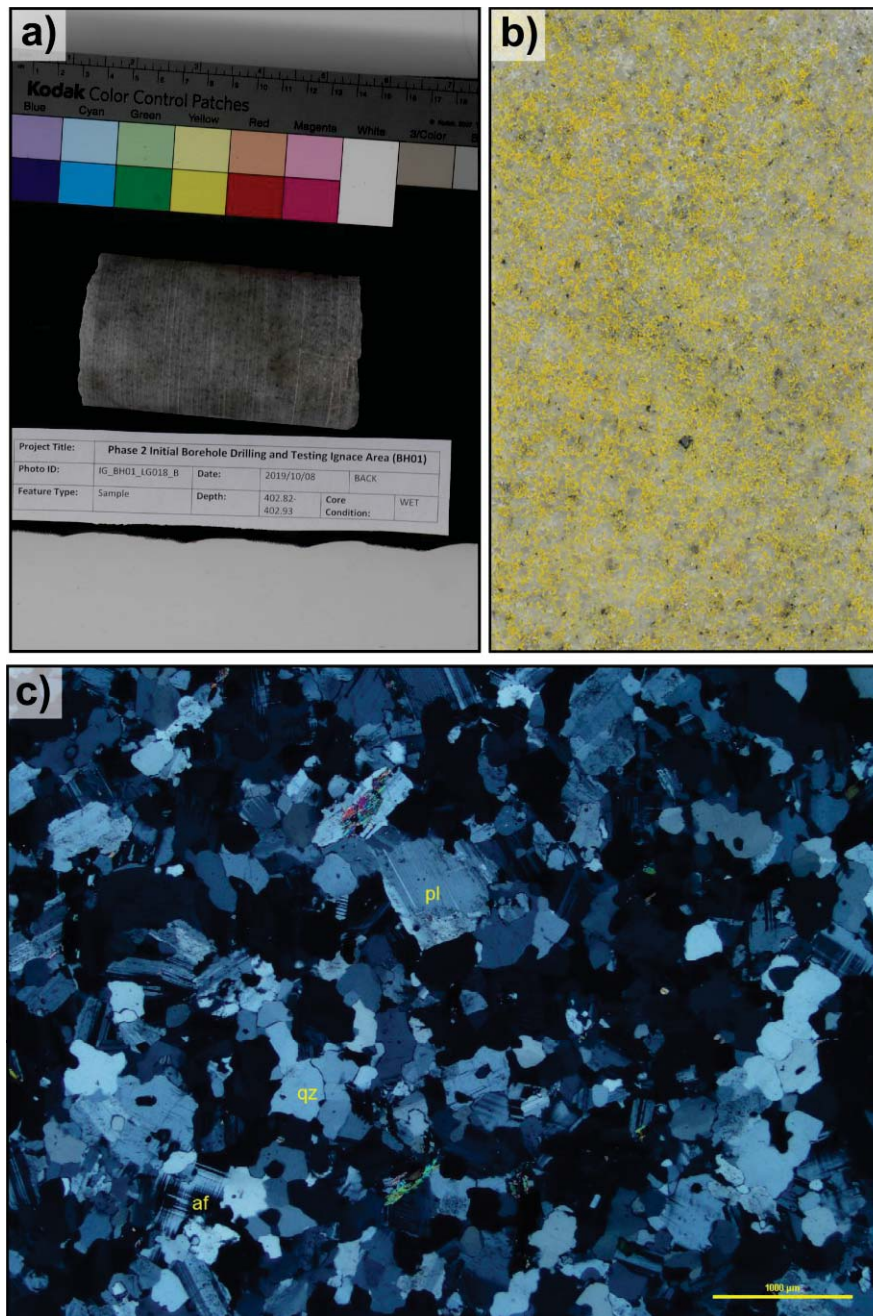


Figure 18: Representative examples of aplite dyke (sample IG_BH01_LG018). a) Hand-sample photograph. b) Billet photograph showing yellow staining of alkali feldspar (billet size is 25 x 40 mm). c) Thin section photomicrograph with rock-forming minerals plagioclase (pl), alkali feldspar (af) and quartz (qz); crossed polarized transmitted light.

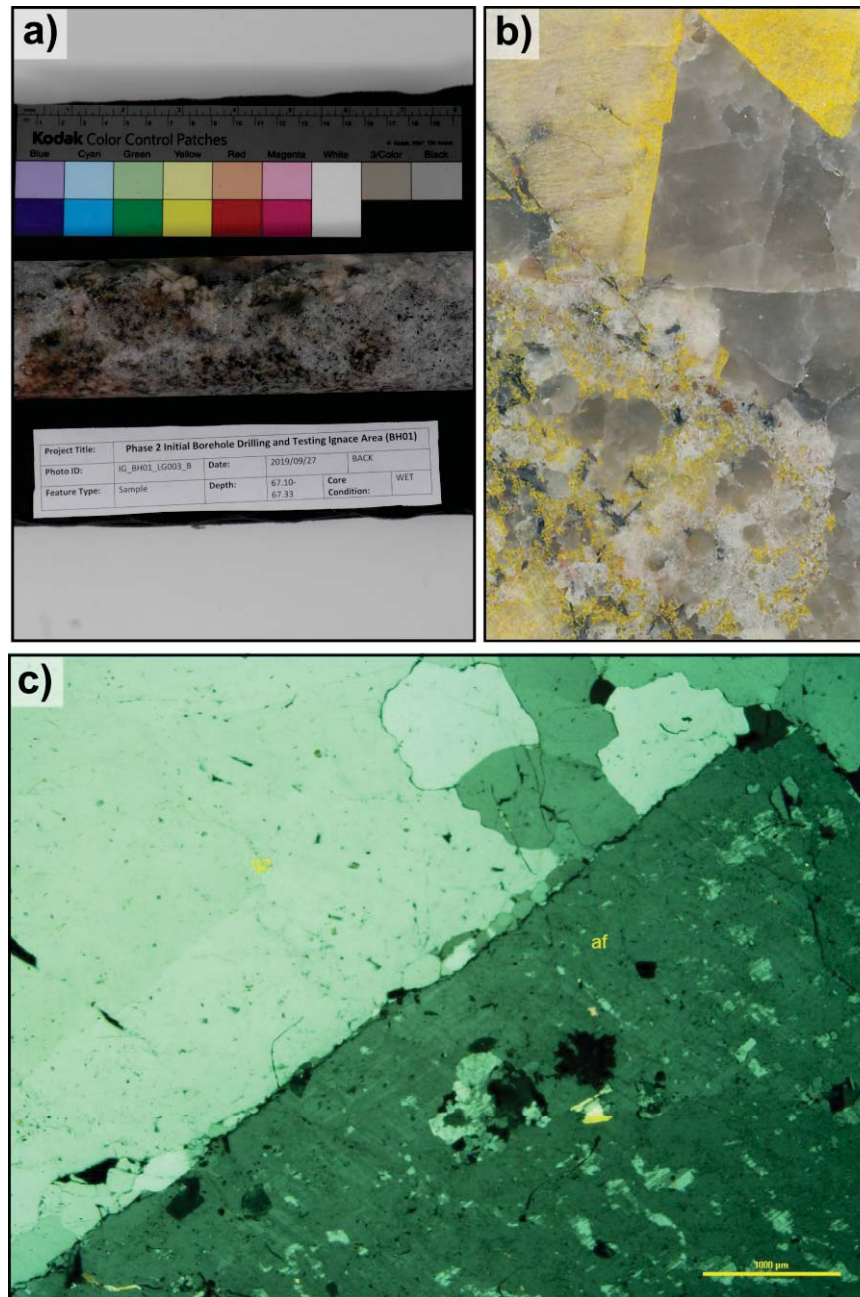


Figure 19: Representative examples of pegmatite dyke (sample IG_BH01_LG003). a) Hand-sample photograph showing pegmatite in contact with biotite granodiorite-tonalite. b) Billet photograph showing contact between biotite granodiorite-tonalite (bottom left) and pegmatite (top right) and yellow staining of alkali feldspar (billet size is 25 x 40 mm). c) Thin section photomicrograph of pegmatite with large quartz (qz) and alkali feldspar (af) grains; crossed polarized transmitted light.

Biotite granodiorite-tonalite dykes: Three biotite granodiorite-tonalite dykes, with widths between 0.15 m and 0.24 m and representing a total of 0.62 m (less than 0.1 %) of total recovered core (Table 3), were observed in the recovered core at 214, 234, and 953 m along borehole (Figure 10). These occurrences are identified as dykes herein as they appear to crosscut the main bedrock units. In addition, two analysed samples of these dykes plot furthest into the granodiorite field on the plutonic rock classification diagram (Figure 12). However, the name biotite granodiorite-tonalite is being kept for this report as two samples are not conclusive of their true genesis. This

interpretation will continue to be assessed as additional information becomes available. These dykes are light grey-off white, massive, equigranular and coarse-grained (5-10 mm), with a similar composition to the main biotite granodiorite-tonalite complex, albeit with more visible albite (Figure 19). These dykes exhibit sharp and consistently intact contacts with the adjacent biotite granodiorite-tonalite and are oriented at moderate to low angles relative to the core axis. They have been identified as dykes based on visible intrusive contacts and narrow width.

Quartz dykes: Two quartz dykes, with widths of 0.13 m and 0.24 m for a total of 0.37 m (representing less than 0.1 % of total recovered core; Table 3), were observed in the recovered core between 275 m and 300 m along borehole (Figure 10). These dykes are white, massive and medium-grained (5-10 mm) and composed almost entirely of quartz with some minor occurrences of pyrite (Figure 20). The quartz dyke occurrences exhibit sharp, intact contacts with the adjacent biotite granodiorite-tonalite. These contacts are oriented at low angles relative to the core axis. These quartz dykes are likely hydrothermal veins (pyrite is strongly suggestive of this), but the current geological core logging procedure is to identify anything over 5 cm as a dyke or separate rock type and anything under 5 cm as a vein. This approach will be re-evaluated for future boreholes, but for consistency in this report these larger quartz bodies will be referred to as dykes.

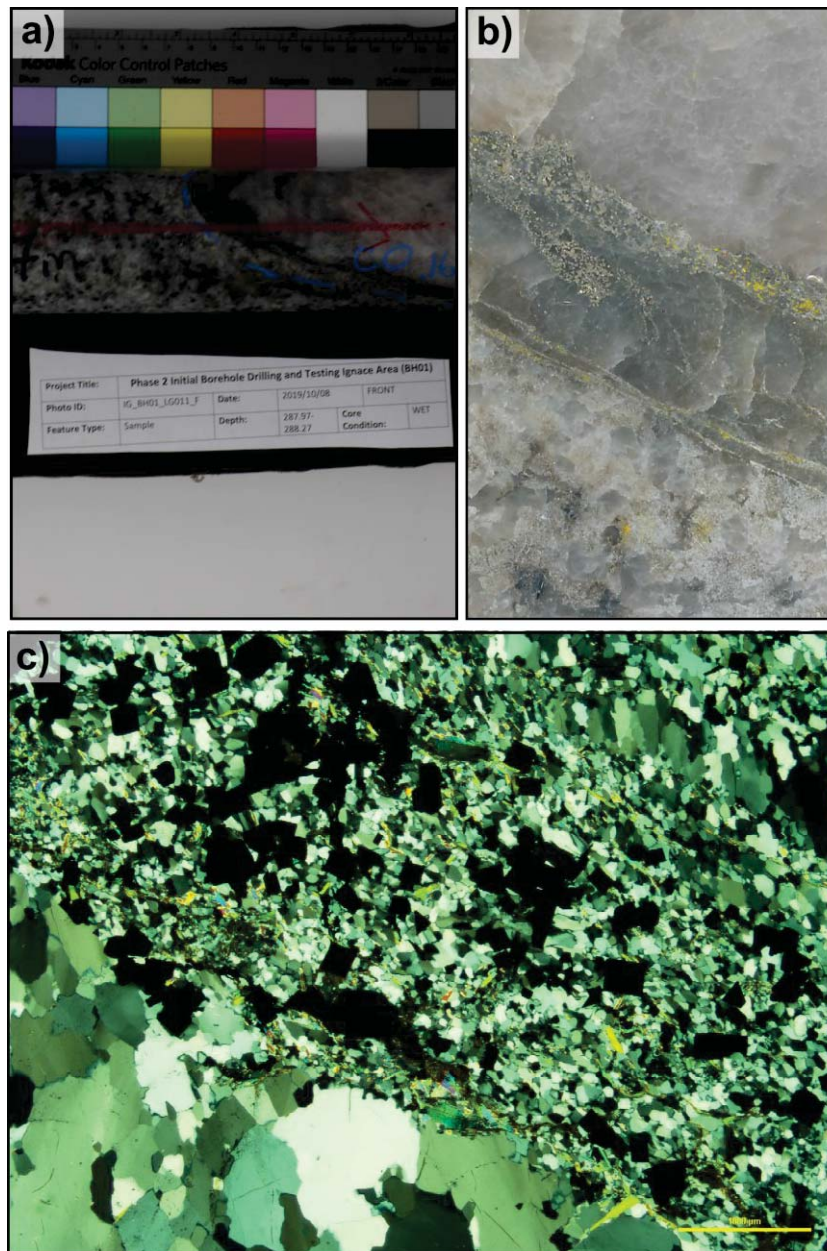


Figure 20: Representative examples of quartz dyke (sample IG_BH01_LG011). a) Hand-sample photograph showing contact with biotite granodiorite-tonalite. b) Billet photograph showing yellow staining of alkali feldspar along contact (billet size is 25 x 40 mm). c) Thin section photomicrograph contact showing decrease in grain size and abundant pyrite crystals (opaque, square) at contact between biotite granodiorite-tonalite and quartz dyke. Quartz dyke is at bottom left of thin section image; crossed polarized transmitted light.

Summary of rare-earth element data for biotite granodiorite-tonalite and biotite tonalite

Rare-earth element (REE) data, collected as part of the lithogeochemistry analysis, are plotted for all rock units with the exception of the pegmatite and quartz dykes (Figure 21). Concentrations (expressed as logarithm to the base 10 of the value) of REE (shown on the x-axis, by atomic number) in these samples are normalized to a reference Chondrite standard. The chondrite-normalized pattern of the biotite granodiorite-tonalite, biotite tonalite, feldspar-phyric tonalite dykes, and biotite granodiorite-tonalite dykes is steeply fractionated [average $(La/Yb)_{28} = 76.8$] with significant depletion of heavy rare-earth elements (HREE; average $(Gd/Er)_{28} = 3.4$). IG_BH01

samples plot with other Neoproterozoic low-HREE granitoids of the tonalite-trondhjemite-granodiorite (TTG) suite, which carry a basaltic crust signature (Halla, 2018 and references therein). The origin of low-HREE TTGs is thought to be high-pressure melting of deep, thick oceanic crust during subduction. One reason for a depletion of HREE is residual garnets retaining the HREE in the source basalt (Halla et al., 2009). The amphibolites are less steeply fractionated [average $(La/Yb)_{10} = 31.9$] with significant depletion of HREE [average $(Gd/Er)_{10} = 3.5$]. The aplite dykes are moderately fractionated [average $(La/Yb)_3 = 52.5$] and have negative europium anomalies, suggesting they are from a later stage, evolved granite source. The similar pattern of all rock types (with the exception of the aplite dykes) indicates a possible common magmatic source. This suggests that the amphibolites may represent mafic dykes that intruded into the granodiorite-tonalite synchronous with either granitoid emplacement or regional deformation.

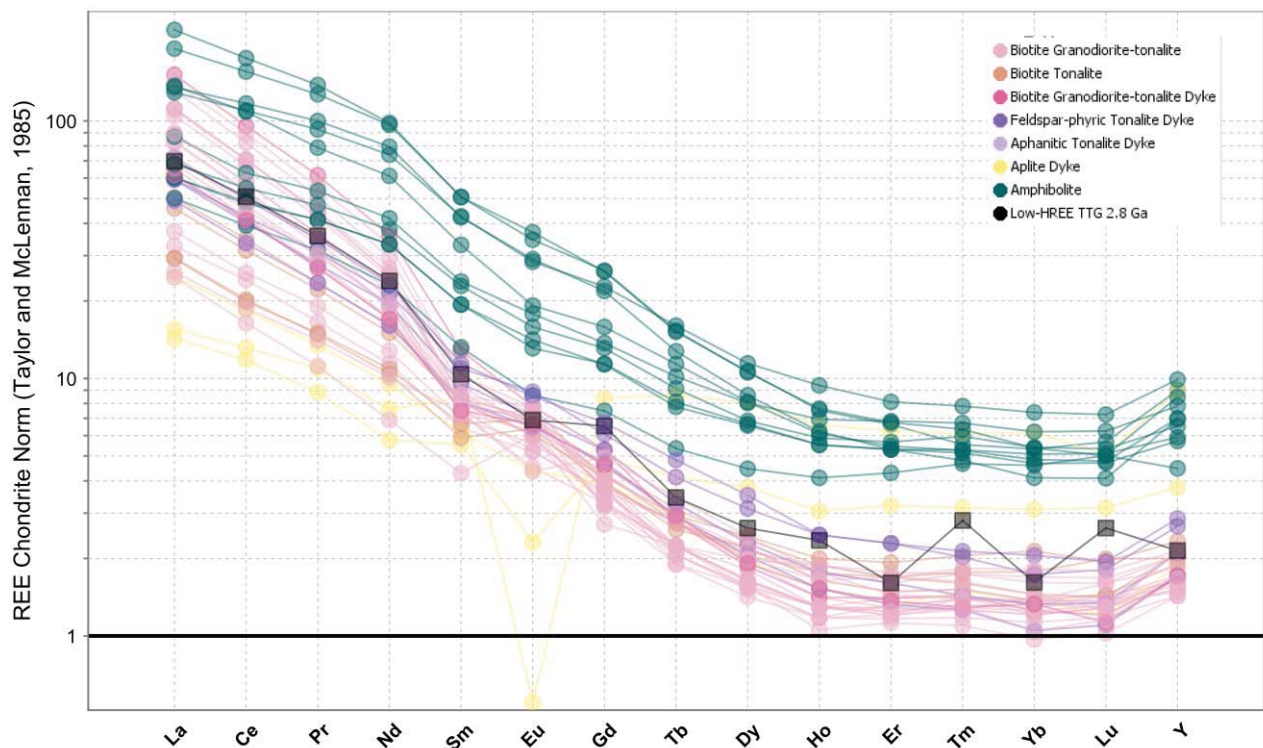


Figure 21: Chondrite-normalized rare-earth element (REE) plot (after Taylor and McLennan, 1985) of rock types from IG_BH01 and a representative average of 2.8 Ga low-heavy REE (HREE) tonalite-trondhjemite-granodiorite (TTG) from the Fennoscandian shield (black squares; Halla, 2018). Y-axis shows concentrations (expressed as logarithm to the base 10 of the value) of REE (x-axis, by atomic number) in IG_BH01 samples normalized to a reference Chondrite standard. REE patterns of biotite granodiorite-tonalite, biotite tonalite, feldspar-phyrlic tonalite dykes, and biotite granodiorite-tonalite dykes demonstrate steep fractionation and significant depletion of HREE. Aplite dykes demonstrate a less steep fractionation and negative europium anomalies, suggesting they are from a later stage, evolved granite source.

Summary of geophysical characteristics of the identified rock types

A suite of geophysical logs, including natural gamma, spectral gamma, gamma-gamma density and neutron logs are widely used both for identifying rock types and delineating contacts (e.g., Keys, 1997). The physics governing these selected logs is well-suited for distinguishing lithological contacts and subtle boundaries between the rocks described herein. Such subtle boundaries could reflect sharp or gradational changes in mineralogical composition, such that any variability not observed in the initial stage of geological core logging could be identified by assessment in

comparison with these geophysical logs (Figure 22). The discussion below describes in more detail the particular usefulness of each of these geophysical logs in helping to characterize bedrock lithology, in general, and then applies this information to analyse further the specific rock types encountered in the borehole. A summary table of mean geophysical responses for each logged rock type is included in Table 5. The full suite of geophysical logs collected for IG_BH01 is described in the WP05 data report (Golder, 2019a).

Table 5: Mean geophysical response values for each logged rock type.

Rock Type (N=number of points)	Natural Gamma (cps)	Neutron* (cps)	Density** (g/cm ³)	K (cps)	Th (cps)	U (cps)
<i>Amphibolite (N=233)</i>	79.66	1126.87	2.81	0.54	0.05	0.14
<i>Aplite Dyke (N=64)</i>	160.43	2520.64	2.63	0.82	0.04	0.22
<i>Biotite Granodiorite-Tonalite (N=15822)</i>	84.59	2329.66	2.66	0.57	0.04	0.16
<i>Biotite Granodiorite-Tonalite Dyke (N=17)</i>	62.77	2167.60	2.66	0.45	0.03	0.13
<i>Biotite Tonalite (N=2273)</i>	58.47	2220.14	2.67	0.48	0.03	0.12
<i>Feldspar-phyric Tonalite Dyke (N=101)</i>	61.41	2322.84	2.67	0.50	0.03	0.13
<i>Aphanitic Tonalite Dyke (N=9)</i>	67.34	2428.83	2.67	0.66	0.07	0.19
<i>Pegmatite Dyke (N=9)</i>	79.49	2145.05	2.66	0.52	0.03	0.11
<i>Quartz Dyke (N=8)</i>	62.71	2352.44	2.65	0.55	0.03	0.17

* long spacing neutron sensor values are presented.

** mean gamma-gamma density values, from near and far measurements, are presented.

The natural gamma log quantifies the amount of radioactive isotopes occurring naturally within the bedrock, which typically corresponds to mineralogy. However, it does not identify the responsible radioisotopes. The spectral gamma log differentiates the relative amount of radioisotopes, such as potassium, uranium and thorium (presented in counts per second - cps). Although natural gamma and spectral gamma logs do not correlate directly to specific rock types, their relative variabilities along the length of the borehole were used to assess mineralogical variation that would indicate changes in rock type.

Data measured from both the gamma-gamma density and neutron logs were used to quantify petrophysical properties of the bedrock (e.g., bulk rock density), and were correlated to specific rock types. Measurement of these logs are, however, sensitive to variations in pore space in the bedrock. The gamma-gamma log measures at a near and far sensor the backscatter and attenuation of gamma photons emitted from the logging gamma source where the measured response is converted to bulk density through calibration prior to recording data.

The neutron log uses a neutron source and detector to measure the relative neutron counts in the bedrock along the borehole wall. Most neutron interactions can be inversely related to hydrogen ion concentrations in the bedrock, such that, responses can be on one hand related to water content or porosity of the bedrock (e.g., Daniels et al., 1984; Keys, 1997). On the other hand, mainly in very low porosity rocks, neutron counts can be significantly influenced by relative changes in bedrock mineralogy, primarily the presence of hydrous minerals (e.g., biotite, amphiboles, and chlorite).

Although electrical resistivity, single point resistance and induction logs can be used as a diagnostic tool to interpret rock types and contacts, within the rocks identified in this borehole, there is no indication of there being changes associated with varying rock types. Variations in resistivity or electrical resistance may be largely correlated to changes in fracture frequency and changes in secondary porosity (e.g., fracture porosity).

Description of borehole geophysical data acquisition and processing are detailed in Golder (2019a). Data underwent filtering and positional corrections, and for this analysis the data have been exported at a uniform spacing of 5 cm along the length of the borehole from bottom of casing to end of borehole. Continuously measured natural gamma, spectral gamma, neutron, and density responses are presented in Figure 10 and were used to highlight spatial variations in physical bedrock properties along the borehole. By comparing the laboratory reported density values from 46 samples to the continuous geophysical density logs it was determined that the geophysical logs, on average, overestimated the density values for the borehole by approximately 3 percent. A correction factor was determined by averaging the differences between each laboratory measurement and the field measurement at the corresponding position, for both the near and far density logs (see Appendix C). The geophysical density logs were corrected using the correction factor to reduce the geophysical log values by 3 percent (i.e., $DENSITY_{corrected} = DENSITY_{measured} / 1.03$), therefore making the profile consistent with the measured laboratory values.

For analysis, a mean density profile was calculated based on the average of the corrected near and far density values along the length of the borehole. The resulting corrected (and uncorrected) density logs show a gradual increase in density with increasing position along borehole. This gradual density increase is characterized by an increase of 0.036 g/cm^3 over the length of the open borehole (930 m). At this point, it is expected that this gradient is a characteristic of the bedrock, and the cause of this systematic increase will continue to be investigated as additional borehole geophysical data is collected.

The biotite granodiorite-tonalite and biotite tonalite phases make up the majority of the measured geophysical response values and can be attributed as the base-line values for the bedrock. Any deviations away from this response tend to be associated with various factors, including changes in rock type and associated mineralogy, presence of fractures and associated infillings, and presence of alteration types and associated intensities.

For the most part, data extracted for biotite granodiorite-tonalite and biotite tonalite phases are subtly differentiated based on the variability of their natural gamma, density and neutron responses. The biotite tonalite units consistently have reduced natural gamma, higher mean bulk density, and lower neutron responses compared to the biotite granodiorite-tonalite (Figure 10). As noted in the rock descriptions above, the main difference between these two rock types is that the biotite tonalite is consistently poorer in alkali feldspar content, which can provide a simple explanation for its reduced gamma response. In addition, reduction in the neutron response in the biotite tonalite phase could possibly be interpreted as an increase in apparent porosity of this unit. Such an increase in porosity could either be associated with primary structure (e.g., inter-grain pore space), or secondary porosity associated with fracturing. Alternatively, an increase in the amounts of hydrous minerals in the bedrock could be responsible for a reduction in the neutron counts. Although increased concentrations of hydrous minerals were not identified in the petrography of the four biotite tonalite samples, this possibility will be explored in future boreholes. This alternative interpretation is also consistent with reduced neutron responses measured on biotite-rich granites from the Lac Du Bonnet batholith (Brown et al., 1989).

Overall, natural gamma, neutron, and density distributions shown in Figure 22 display considerable similarities between all felsic rocks, except the aplite dykes, and petrophysical and whole rock litho-geochemistry analyses from future boreholes will be used to further refine understanding of these units. The aplite dykes produce a distinct natural gamma response with the mean value typically 2 to 3 times higher than values measured for other rock types (Figure 22). Using data measured from the spectral gamma probe, this distinct response for the aplite dykes can be differentiated into elevated presence of potassium (increased potassium feldspar noted in litho-geochemistry and petrography, detailed in Section 3.2.1) and slightly elevated uranium

compared to the other rock types. Despite being slightly elevated in potassium and uranium, the total measured amounts are still exceptionally low.

The amphibolite occurrences in the borehole are responsible for sharp reductions in neutron counts and increases in bulk density relative to the host biotite granodiorite-tonalite. The increased bulk density of amphibolites can be directly related to the presence of tremolite-actinolite which is a relatively dense mineral, especially in comparison to the main mineral phases comprising the felsic units (i.e., plagioclase, alkali feldspar and quartz). The reduced neutron counts of the amphibolites can possibly be associated with an increase in apparent primary porosity, however, it is more likely related to secondary (e.g., fracture) porosity or the hydrous nature of their mineral assemblage.

The remaining logged rock types (i.e., biotite granodiorite-tonalite dykes, aphanitic and feldspar-phyrlic tonalite dykes, pegmatite dykes, and quartz dykes) are characterized by natural gamma ray, neutron and density responses that are similar to each other and to the host biotite granodiorite-tonalite complex.

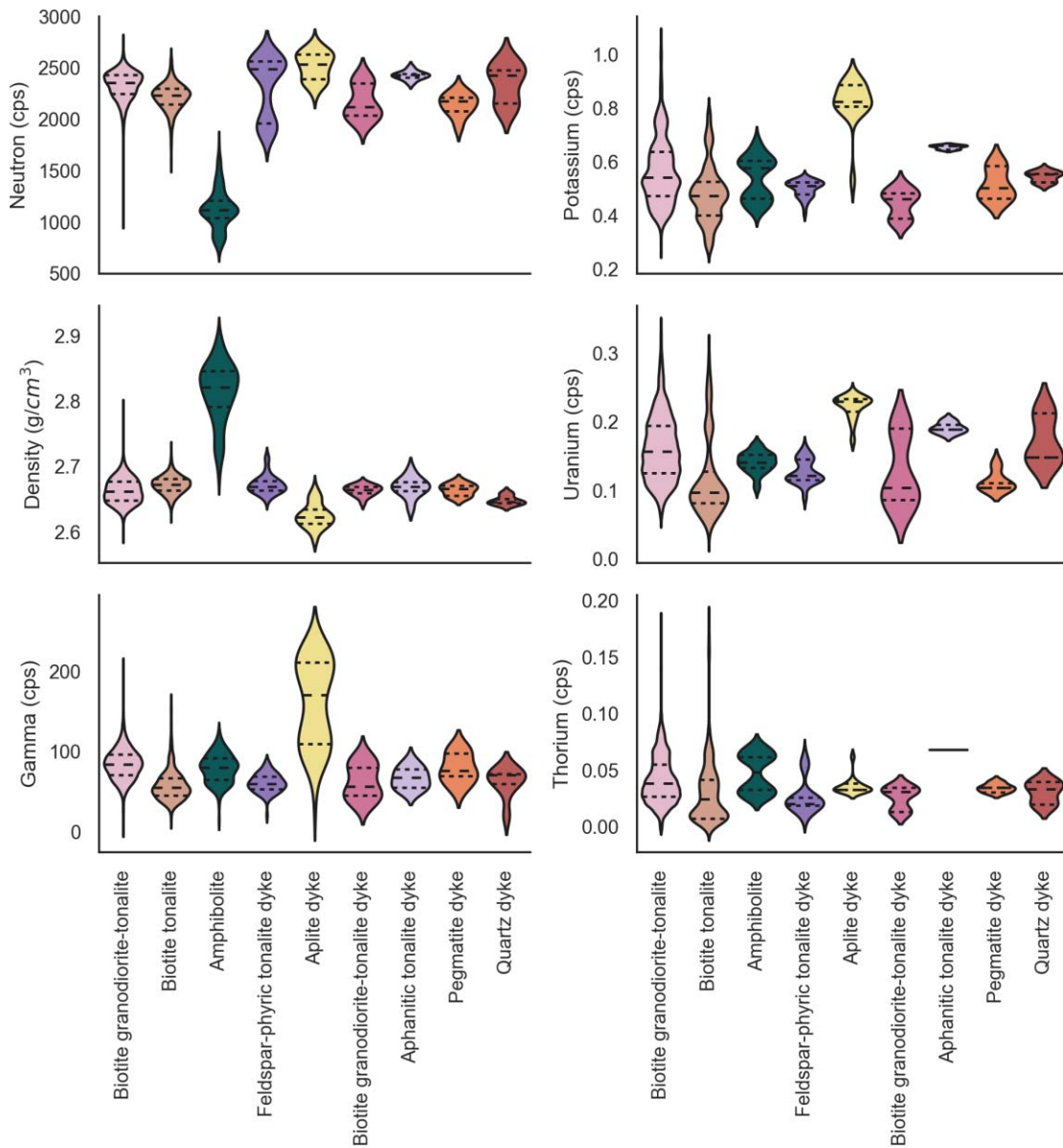


Figure 22: Violin plots show the distribution of geophysical log responses associated with the logged rock types. Each violin shows the distribution of the data values with the median (thick dashed line), and quartiles (thin dashed lines) marked. Rock types are ordered based on total data counts from left to right in each graph.

The distribution of Neutron, Density, Natural Gamma and Potassium values are presented in Figure 23 showing the cross-correlation between the selected geophysical log data and corresponding rock types. Scattered data points are plotted for the entire length of the borehole at 5 cm intervals. The larger data points represent mean centroid values of the geophysical responses and the error bars represent the standard deviation.

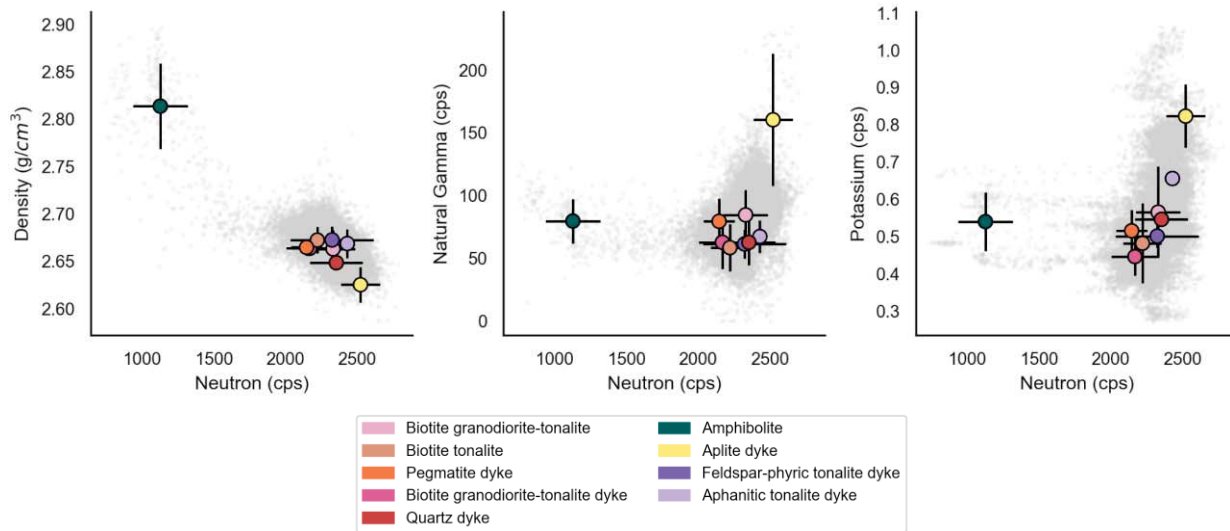


Figure 23: Distribution of Neutron and Density Values of all Rock Types encountered in IG_BH01. Colored points represent mean values of the geophysical response and the error bars represent standard deviation.

Overall, the distributions of biotite granodiorite-tonalite, biotite tonalite, pegmatite, feldspar-phyric tonalite dykes, aphanitic tonalite dykes, and quartz dykes largely overlap making distinguishing between them using geophysical comparison plots alone difficult. However, the aplite dykes are characterized by a high natural gamma and low bulk density values which is apparent in the natural and spectral gamma borehole logs (Figure 10). Amphibolites are uniquely characterized by low natural gamma and neutron counts, and high bulk densities and can be distinguished from the other felsic units in all cross-plots (Figure 23). Most of the density values over approximately 2.75 g/cm³ are attributed to amphibolites.

3.2.2 Alteration Interpretation

The descriptions for each alteration type encountered in IG_BH01 are included below and in the final alteration log shown in Figure 24. Descriptions of alterations observed through geological core logging are also included in the WP03 report (Golder 2018c). The final alteration log displays the summary of the data integrated to define the log, including the WP03 alteration log and the additions from assessment of the optical televiewer log. Core photographs of all the identified alteration types are presented in Figure 25. In addition to the macroscopically identified alteration types, mineral-scale alteration features from the petrographic analysis are summarized and present thin section images in Figure 26.

Six alteration types were observed during geological core logging based on the alteration mineral assemblages identified, including: hematization, potassic alteration, silicification, chloritization, bleaching, and sericitization. This initial visual assessment assigned 84.76 m (8.4 %) of the recovered core as slightly altered (A2), where the alteration is generally confined to fractures and with little or no penetration of the alteration beyond the fracture plane. 13.79 m (1.4 %) was assigned as moderately altered (A3), where the alteration may penetrate into the wallrock and create an envelope or halo of alteration around a fracture (Figure 29). No occurrences of highly altered rock were identified. Locally along the length of the borehole, the optical televiewer log, in

combination with the continuous borehole geophysical logs, highlighted additional intervals interpreted to be associated with subtle changes in physical rock properties that could be attributed to alteration (see Appendix E: for details on this process). For the most part, this association was based on the bedrock appearance in the optical televiewer such that the changes in colour were improved compared to geological core logging. This interpretation added an additional 11.23 m (1.1 %) of slightly to moderately altered rock, including 6.91 m of silicification, 2.77 m of potassic alteration, 1.06 m of bleaching, and 0.49 m of hematization to the final alteration log (Figure 24). The total metreage identified for each alteration type reported below includes the sum of occurrences identified from both the geological core logging and the additional amount added based on assessment of the televiewer logs, representing a total of 109.78 m (11 %) of the recovered core by length. Overall, there is an increased occurrence of features associated with alteration below approximately 600 m along borehole (Figure 24).

Hematization was observed in 63 discrete intervals and is the most prevalent alteration type encountered with the majority occurring in the upper 50 m. A total of 63.40 m (6.0 %) of the borehole was logged with some degree of hematite alteration. The distribution of hematization ranged from hairline alteration, typically occurring around fractures and logged with no observable width, to broader intervals up to 3.72 m in width. It is characterized by red, brown, or rusty staining of the rock and/or coating around mineral grains (Figure 25a). Hematization was also commonly developed in proximity to logged amphibolite units.

Potassic alteration was identified in 87 occurrences, representing a total of 20.65 m (2.1 %) of the recovered core by length. Individual occurrences of potassic alteration range in width from hairline to 2.97 m. Potassic alteration was only observed below 400 m, with an increase in prevalence between 700 m and 900 m along borehole. The mineral assemblage defining potassic alteration is alkali feldspar and/or biotite, possible minor sericite, chlorite, and quartz (Figure 25b).

Silicification was identified in 43 occurrences representing a total of 18.75 m (1.9 %) of the recovered core. This alteration is characterized by a light to medium grey discolouration of the bedrock and associated reduction in the clarity of the original texture of the biotite granodiorite-tonalite (Figure 25c). There is a slight increase in silicification within the lower half of the borehole relative to the upper half. Individual occurrences range in width from 0.01 to 4.71 m. Some intervals logged as silicification may be albitization or an aluminous alteration; there is an ongoing project to further characterize the alteration styles and will refine the naming for subsequent boreholes.

Chloritization was identified in three occurrences, ranging in width from hairline zones to 1.5 m, and representing a total of 2.01 m (<1 %) of the recovered core. The appearance of grey-green chlorite was the main diagnostic characteristic of this alteration type and in all occurrences the bedrock was described as slightly altered (Figure 25d). All logged occurrences of chloritization are below 600 m and they are mainly identified within, or along the contacts of, the amphibolites. Based on petrographic analysis, some of the biotite crystals are partially or totally replaced by chlorite and/or epidote (Figure 26).

Bleaching was observed to slightly alter the biotite granodiorite-tonalite in eleven occurrences, ranging from hairline zones logged with no width to 1.06 m in width, and representing a total of 4.33 m (<1 %) of the recovered core. Bleaching is identified by a whitening of the altered bedrock (Figure 25e) and is likely an aluminous or sericitic alteration (again, ongoing characterization of alteration types is occurring and this term will be revised for future boreholes). Bleaching was observed both near surface above 100 m and below 700 m along borehole.

Sericitization was observed to slightly alter the biotite granodiorite-tonalite in two occurrences, ranging in width from 0.30 to 0.34 m and representing a combined total length of 0.64 m (<<1 %) of the recovered core. Sericitization imparts a grey colour to the altered rock (Figure 25f). It was

observed between 650 m and 700 m along borehole. Based on petrographic analysis, there is evidence of microscopic sericite alteration, represented by replacement of plagioclase cores by fine-grained white mica, in the biotite granodiorite-tonalite (Figure 26).

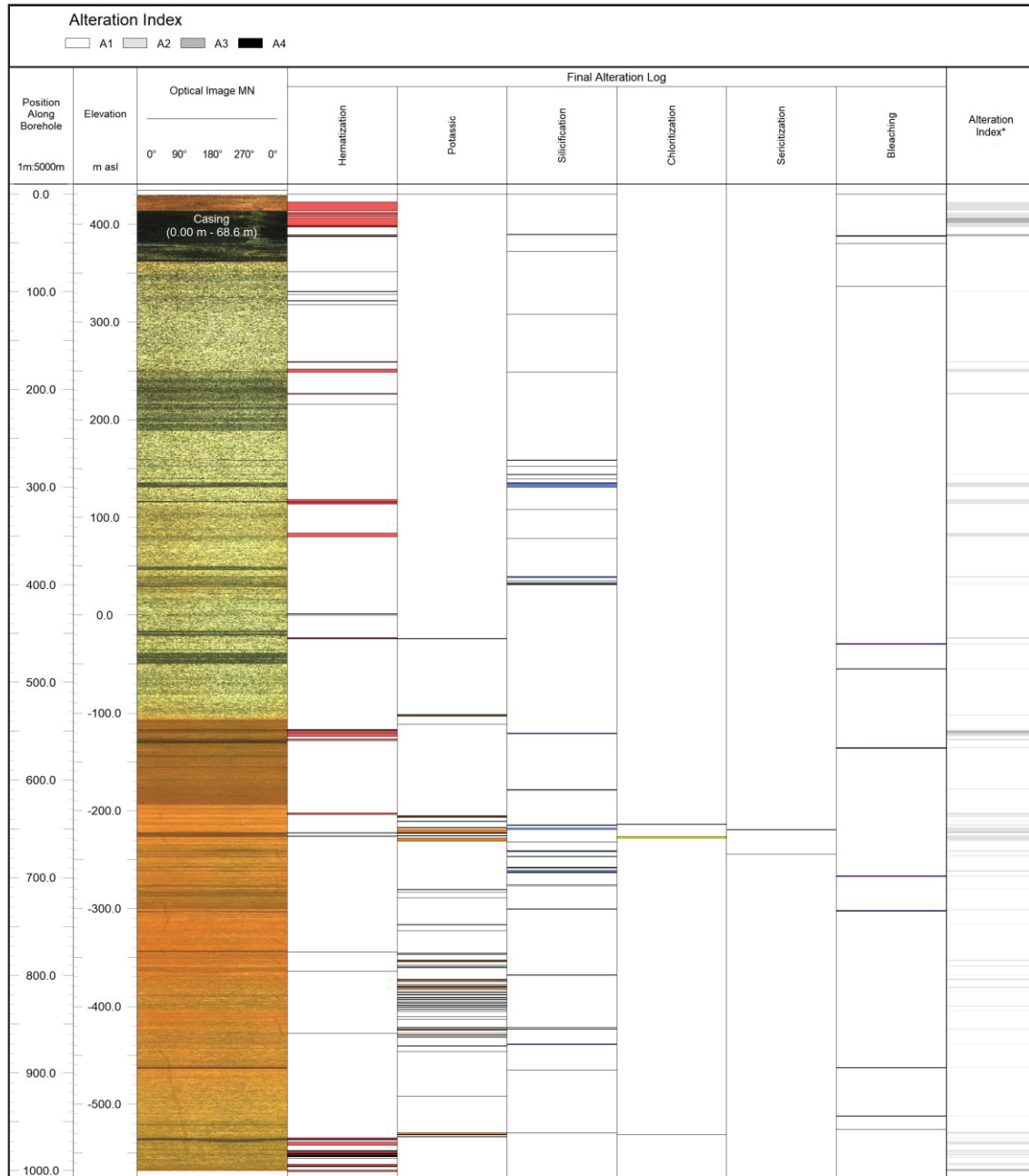


Figure 24: Alteration types and distribution along the borehole based on geological core logging and analysis of the optical televiewer log resulting in a final alteration log. A2 indicates intervals with slight alteration and A3 indicates intervals with moderate alteration.

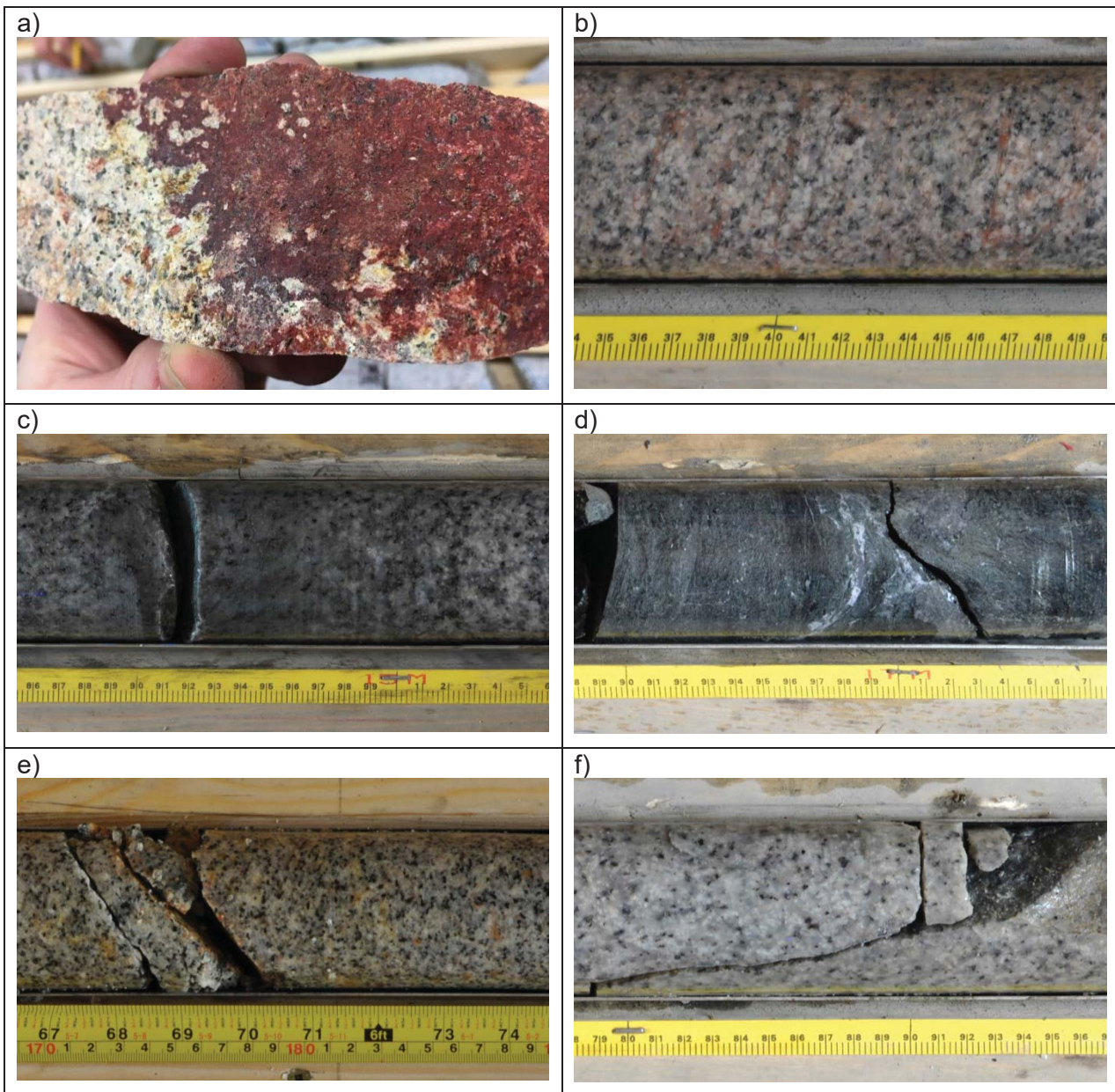


Figure 25: Examples of the different types of alteration observed, a) Hematization (43 m), b) Potassic (455 m), c) Silicification (553 m), d) Chloritization (896 m), e) Bleaching (42 m), f) Sericitization (650 m).

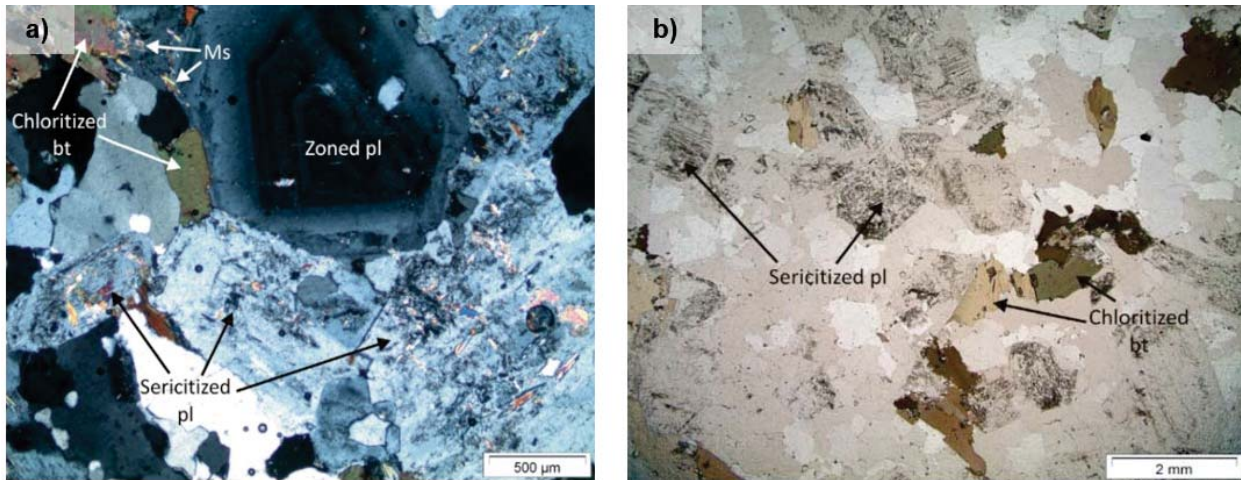


Figure 26: Examples of mineral-scale alteration observed in petrographic thin sections of the biotite granodiorite-tonalite. a) Chloritized biotite crystals and sericitized plagioclase adjacent to zoned, unaltered plagioclase at 223.25 m along borehole (viewed under crossed polarized transmitted light). b) Sericitized plagioclase crystals and chloritized biotite at 582.95 m (viewed under plane polarized transmitted light).

3.2.3 Rock Unit Classification

Rock units (RU) are defined primarily on the basis of dominant rock type encountered within the borehole and the degree of subordinate rock types encountered in the interval. The core logged rock types, combined with key continuous geophysical datasets were used to distinguish distinct rock types within each RU, and defining the top and bottom interval positions. A minimum thickness of five metres was used to identify RUs.

Based on the distribution of the three dominant rock types identified and catalogued in the lithology log, including (in order of dominance): (1) biotite granodiorite-tonalite, (2) biotite tonalite, and (3) amphibolite, a total of four RUs are defined within the borehole (Figure 27). Rock units RU1a and RU1b are dominated by biotite granodiorite-tonalite, exhibit similar geophysical signatures, and include few occurrences of subordinate rock types. RU2 represents the only interval dominated by biotite tonalite over a considerable thickness. RU3 is characterized by the repeated occurrence of amphibolite. Table 6 presents a summary of the final RU interpretations and the characteristics of each RU are described in further detail below.

Rock unit 1a (RU1a) extends from the ground surface (0 m) to 180.01 m along borehole. This interval predominantly consists of biotite granodiorite-tonalite, with a single pegmatite dyke and thin biotite tonalite intervals. The biotite tonalite intervals consistently exhibit sharp and intact, and near-horizontal, upper and lower contacts with the biotite granodiorite-tonalite. Throughout RU1 the biotite granodiorite-tonalite is massive, light grey to white in colour, and predominantly medium-grained. With the exception of the upper 70 m of the borehole, where casing is installed, the density, gamma and neutron logs exhibit relatively uniform profiles through this unit. The bottom of RU1a is marked by a sharp reduction in natural and spectral gamma counts, a subtle increase in bulk density, and a reduction in the neutron counts.

Rock unit 2 (RU2) extends from 180.01 m to 242.50 m along borehole. This section of the borehole is distinguished as a unique RU based on a grain-size reduction and an apparent increase in biotite content, such that the interval is mainly comprised of biotite tonalite. This interval is mainly massive, equigranular and medium-grained (though on the lower end of the medium grain-size range relative to the biotite granodiorite-tonalite). Although the upper transition with RU1a appears sharp in the geophysical logs, in the core it is gradational over a one to two metre section of the core. Natural gamma and density values are relatively consistent throughout the interval; however, neutron counts show a reduction compared to the other RUs, and values show substantial variability. The

variability in neutron counts is expected to result from an increase in hydrogen content, however, the physical explanation may correspond to either an increase in primary or secondary porosity or a change in the concentration of hydrous minerals. The overall slight decrease in grain size and change in mineralogy from the biotite granodiorite-tonalite to biotite tonalite (decrease in alkali feldspar, slight increase in biotite) coincides with the observed increase in mean density and reduced gamma and neutron counts. Two cm-scale, coarse-grained pegmatite dykes and two cm-scale, medium-grained biotite granodiorite-tonalite dykes were also identified in RU2. The lower boundary of RU2 is sharp and dips steeply towards the southeast (72° towards 136°).

Rock unit 1b (RU1b) extends from 242.50 m to 653.71 m along borehole, and is composed primarily of biotite granodiorite-tonalite, and occurrences of quartz dykes, aplite dykes, massive to strongly foliated feldspar-phyric tonalite dykes, one amphibolite (at ~315 m), and several m-scale biotite tonalite intervals. The subordinate units account for 7.70 m of the 411.21 m interval (1.87 %). The biotite granodiorite-tonalite is predominantly medium-grained and massive throughout this RU, though locally a weak biotite foliation is present. The bottom of RU1b is marked by a sharp contact between the biotite granodiorite-tonalite (above) and a shallowly-dipping (35° towards 342°) m-scale, foliated amphibolite (below).

Rock unit 3 (RU3) extends from 653.71 m to 1001.18 m along borehole. RU3 is composed of medium-grained, massive, biotite granodiorite-tonalite that is light grey to white in colour, and intervals of amphibolite, aplite dykes, pegmatite dykes, and feldspar-phyric tonalite dykes. Locally, the biotite granodiorite-tonalite exhibits a weak foliation defined by aligned biotite, and some variability in grain size (from fine- to medium-grained). The amphibolite units, which distinguish this RU, are dark green to grey in colour, fine-grained, and massive to strongly foliated. The density log shows distinct peaks coincident with the amphibolite, and a sharp reduction in the neutron count is also evident. Foliation in the amphibolite is commonly concentrated along the contacts with the surrounding granodiorite-tonalite. The amphibolite contacts primarily dip shallowly to moderately towards the north-northwest in all occurrences except for one. In the latter occurrence, at 969 m along borehole, the contact between the amphibolite and surrounding rock dips steeply towards the southwest. The amphibolites of RU3 exhibit similar distinct geophysical characteristics to the amphibolite at 315 m. With the exception of the amphibolite units, density log values through this unit exhibit a uniform trend of slight density increase with increasing position along borehole. Gamma and neutron logs exhibit a relatively high degree of variability. The base of RU3 coincides with the deepest extent of recovered core and the bottom of the borehole.

Table 6: Summary of Classified Rock Units

Position Range (m)	Dominant Rock Type	Rock Unit (RU)
0 – 180.01	Biotite granodiorite-tonalite	RU1a
180.01 – 242.50	Biotite tonalite	RU2
242.50 – 653.71	Biotite granodiorite-tonalite	RU1b
653.71 – 1001.18	Biotite granodiorite-tonalite with amphibolite	RU3

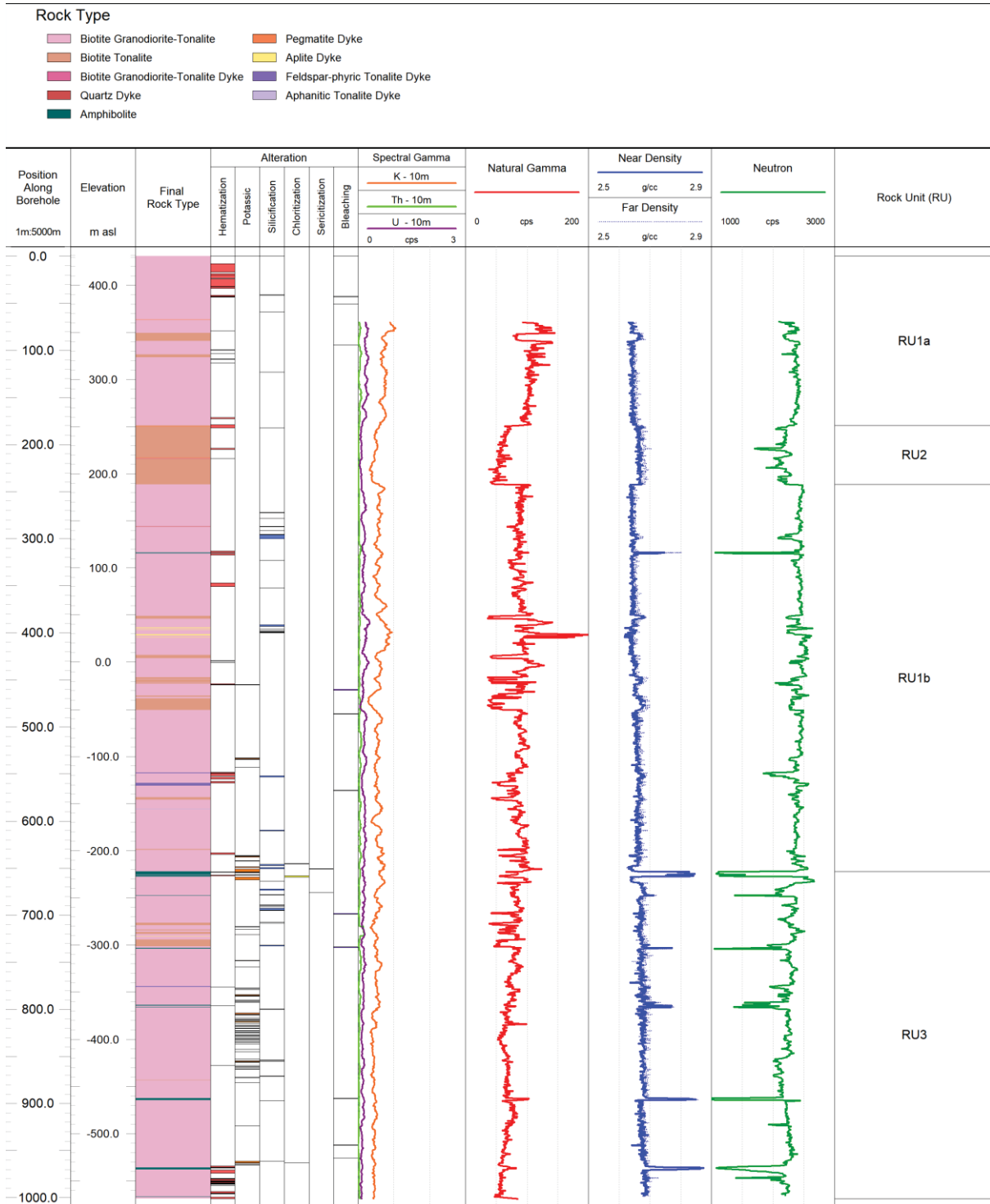


Figure 27: Summary of final logged lithology, alteration and key geophysical logs presented alongside interpreted rock units for IG_BH01. Due to the low spectral gamma counts, K, U and Th were evaluated using a 10 m window, resulting in a smoothing of their profiles.

The main uncertainty associated with this initial rock unit model is whether or not additional borehole information will fit within this same framework or if a different picture of the bedrock will emerge. However, RU3, comprising multiple similarly oriented amphibolite units dipping, on average, moderately towards the north-northwest, may have distinct enough characteristics to allow it to be correlated to similar rock units in adjacent boreholes.

3.2.4 Structural Interpretation

A description and interpretation of bedrock structural features measured along the borehole are presented in this section. Structural measurements include both geological and geotechnical characteristics from core logging and geophysical televiewer logging datasets and are integrated into a final structure log. The final structure log includes a total of 1964 structures, including 840 that were logged and observed only by geological core logging, 837 structures that were logged both in geological core logging and televiewer logging, and 287 structures that were logged and observed only by televiewer. An additional 435 non-natural mechanical breaks were identified during geological core logging which have already been separated from the dataset presented below.

During geological core logging, structures were oriented relative to an arbitrary reference line drawn along the length of the axis of each core run. The methodology for assigning true dip and dip direction to each logged structure, integrating the geological core logging information with the orientation information extracted from the televiewer log datasets, is presented in Appendix D. During this process of structure integration, 96 % of the features, representing 1860 planar features and 23 linear structures, were oriented and assigned true dip and dip direction (true trend and plunge for linear structures). The remaining (un-oriented) structures could not be assigned a true dip or dip direction as a result of being located within sections of the core that could not be corrected with the televiewer information. Oriented structural data are plotted by structure type and shown on equal area, lower-hemisphere stereographic projections (stereonet) throughout this section. Table 7 provides a summary of the results from the integration, presented by unique structure type.

Table 7: Summary of structures observed in the borehole.

Structure Type	Number of Oriented Structure			Total	Un-oriented Occurrences (Core Logged Only)	Total Structures Logged
	Core Logged Only	Both (Core and Televiewer)	Televiewer Logged Only			
Joint (JN)	513	582	154	1249	55	1304 ³
Vein (VN)	130	120	89	339	7	346
Contact (CO)	24	74	2	100	14 (4) ¹	114
Foliation (FO)	16	12	37	65	1	66
Igneous Primary Structure (IPS)	18	20	5	43	0	43 ³
Shear Zones (SHR)	31	17	0	48	4	52 ³
Lineation (LIN) ²	23	0	0	23	0	23
Fault (FLT)	4	12	0	16	0	16
Total	759	837	287	1883	81	1964

¹ 10 un-oriented contacts were added based on the integration.

² LIN identification in logging datasets refers to the parent structure on which the lineations occur. Lineations are only observed and measured in geological core logging, by observing the structure surface.

³ The approach for capturing geological contact and lineation information was revised prior to logging of boreholes IG_BH02 and IG_BH03. For consistency, the final IG_BH01 structure log included in the NWMO AcQuire database was updated after completion of the reporting and analysis presented herein. This revision includes the addition of 15 Joints (N = 1319) and four Shear Zones (N = 56). The updated Shear Zone dataset includes replacement of one Igneous Primary Structure (N = 42).

Because this borehole has a near-vertical trajectory (planned inclination = -90°), steeply dipping structures will be under-represented and purely vertical structures will be nearly absent (e.g., Terzaghi, 1965). To acknowledge this bias and begin to explore the implications of it, the presentation below includes Terzaghi-weighted contoured stereonet along with the unweighted data for all structures except for oriented lithological contacts. The legend associated with each of the weighted stereonet indicates the number of features expected based on the Terzaghi weighting. The minimum bias angle applied for this analysis, using the software DIPS© (Version 7)

by Rocscience, is 15° . A summary of orientation information for all 1860 naturally occurring planar structures is presented in Figure 28. In comparing the unweighted and Terzaghi-weighted contours, in Figure 29, it is clear that the latter emphasizes the pole clusters of steepest dipping structures oriented at a low angle to the core axis, reducing the dominance of the shallowest dipping structures oriented at a high angle to the core axis.

More recently, advanced procedures for addressing orientation bias have been reported in the literature (e.g., Davy et al., 2006). However, such alternative approaches require not yet available information such as fractures size-distribution for each orientation set. The use of such methods will be made possible, and justified, as additional borehole and surface structural information become available.

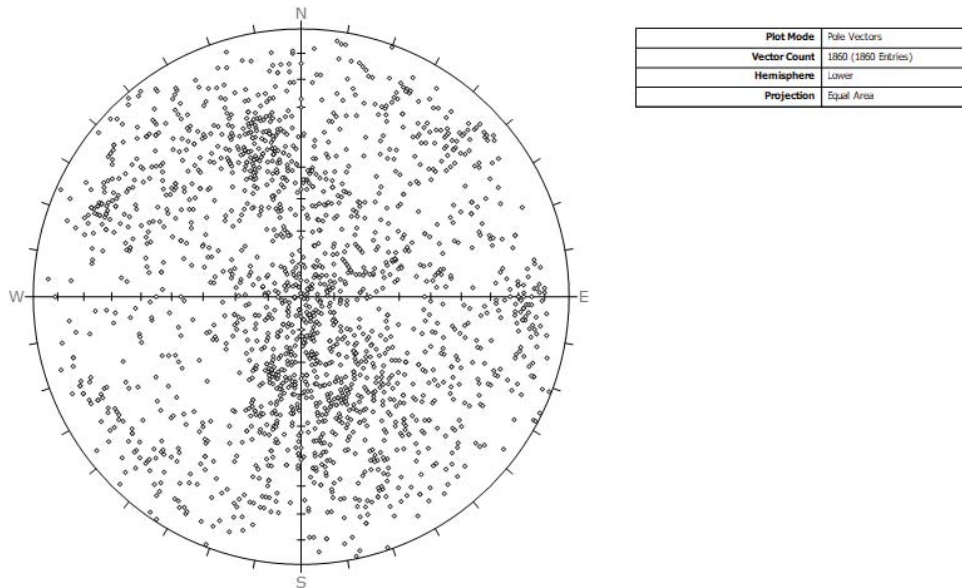


Figure 28: Equal Area Lower Hemisphere Projections (stereonets) showing poles to planar structural measurements, unweighted (n = 1860).

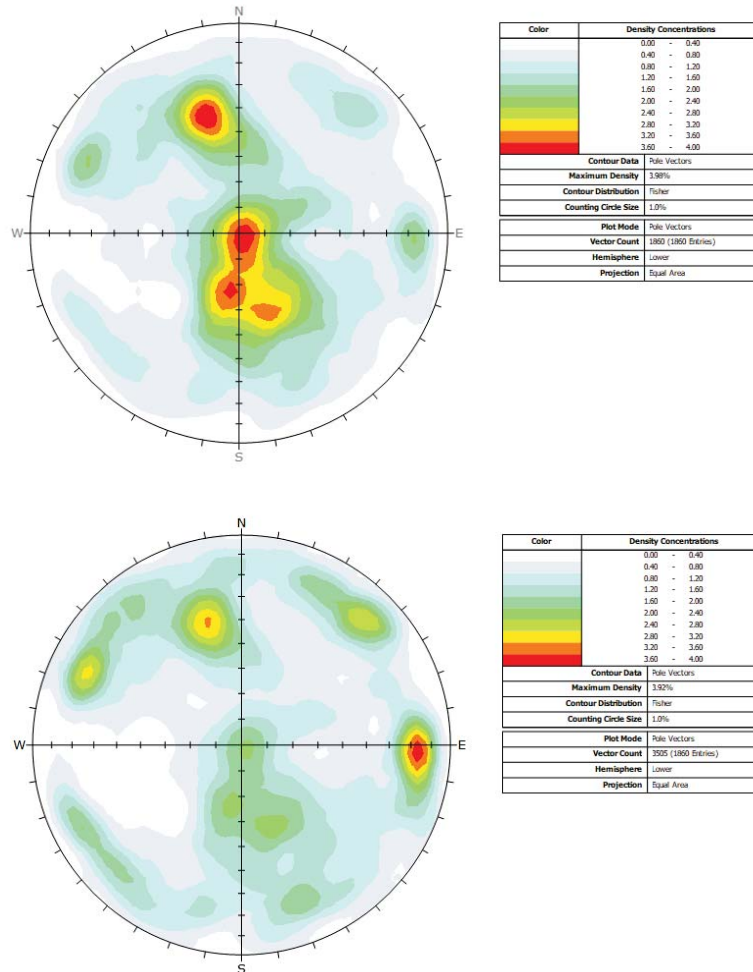


Figure 29: Equal Area Lower Hemisphere Projections (stereonet) showing a summary of the poles for planar structural measurements. Top: all data – contours, unweighted (n = 1860). Bottom: all data – contours, Terzaghi-weighted.

3.2.4.1 Structures

The structural information presented below includes discussion of features logged as igneous primary structures, contacts, ductile structures, brittle structures, including joints, veins and faults, and linear structures.

Igneous Primary Structures

Igneous primary structures include features interpreted to have originated with the formation or emplacement of the igneous rock. For IG_BH01 this includes a total of 43 occurrences identified as primary igneous layering. These features are generally characterized by sharp to gradational changes in grain size or biotite mineral concentrations. The features may be layering or mafic schlieren but are identified generally as igneous primary structures at this stage. All occurrences, except for one, were observed as intact and all occurrences were successfully oriented. One feature in the core identified as primary igneous layering is shown in Figure 34a. The true nature of all features logged as igneous primary structures will continue to be assessed as additional information from future boreholes becomes available. Figure 30 presents the stereographic

projection of all igneous primary structures, showing significant scatter in their orientations and a few minor pole clusters generally emphasizing gentle to moderate dips.

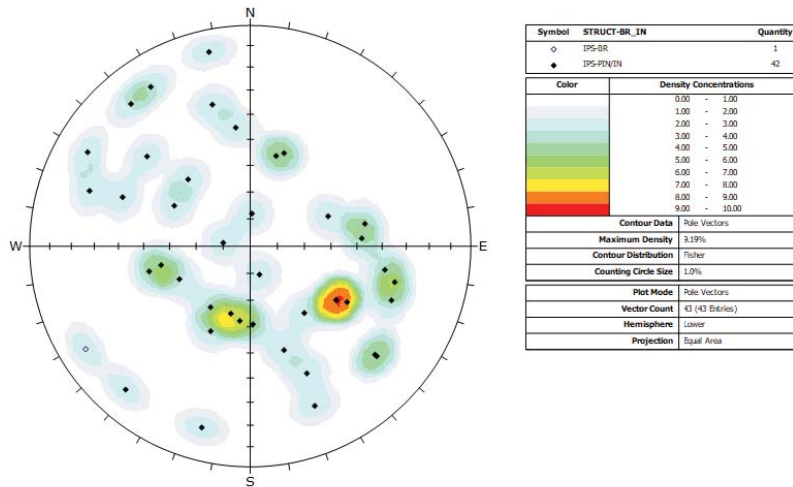


Figure 30: Stereonet showing poles and unweighted contours for Igneous Primary Structures (IPS; n = 43). Open symbol identifies broken Igneous Primary Structure (IPS-BR) and filled symbols identify partially intact/intact Igneous Primary Structures (IPS-PIN/IN).

Contacts

Top and bottom contact orientations were logged for each change in rock type wherever the boundary was sharp enough to confidently identify a contact plane. The majority of the logged contacts represent boundaries between occurrences of biotite granodiorite-tonalite and subordinate rock types. Out of a total of 114 logged contacts, 100 of these could be oriented.

A total of 26 biotite tonalite contacts with the adjacent biotite granodiorite-tonalite were oriented (Figure 31), all of which were logged as intact. Although there is some scatter in the data, the majority of the poles plot in either the northwest or southeast quadrants defining gently to moderately inclined contacts that dip to the southeast or northwest, respectively.

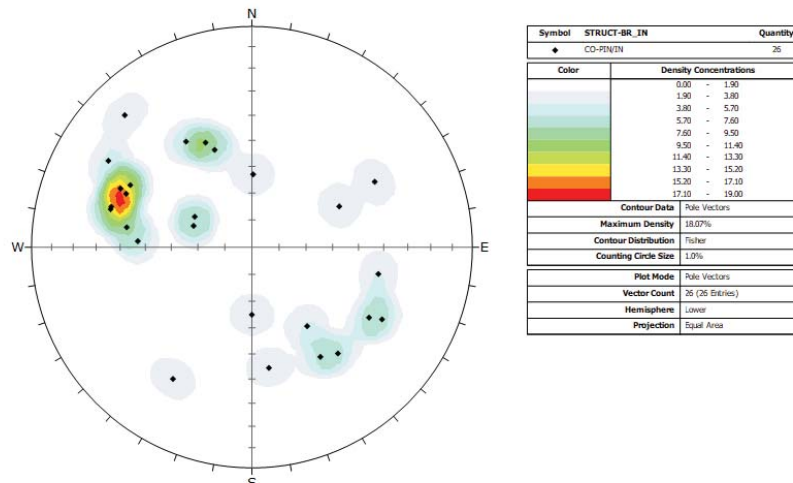


Figure 31: Stereonet showing poles and unweighted contours for biotite tonalite contacts (n = 26). Filled symbols identify partially intact/intact contacts (CO-PIN/IN).

A total of 26 amphibolite contacts were oriented (Figure 32), including 14 instances logged as broken. One dominant pole cluster indicates that the majority of amphibolite contacts are gently to moderately inclined and dip towards the north-northwest. One amphibolite occurrence, at 968 m along borehole, exhibits two sub-parallel contacts that dip steeply towards the southwest. All amphibolite contacts exhibit evidence of penetrative ductile to brittle-ductile deformation obscuring any indication of their primary relationship with the surrounding bedrock. The deformation manifests as cm- to dm-scale localized shear zones that are developed along, and sub-parallel to, their contacts. A comparison of the amphibolite contact orientations and shear zone orientations, the latter shown in Figure 37, highlights this relationship.

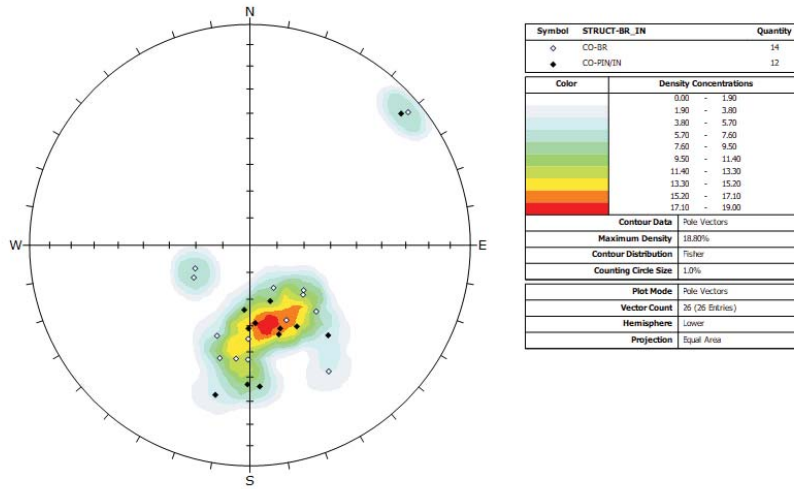


Figure 32: Stereonet showing poles and unweighted contours for amphibolite contacts (n = 26). Open symbols identify broken contacts (CO-BR) and filled symbols identify partially intact/intact contacts (CO-PIN/IN).

The contact orientations for all felsic phases interpreted as dykes are shown in Figure 33 and their structural characteristics are summarized in Table 8. Overall, felsic dyke contacts are all intact except for one broken aplite dyke contact. Dyke contacts are gently to steeply inclined and exhibit variable dip directions that are predominantly towards the north.

Table 8: Summary of the Structural Character of Felsic Dykes

Dyke Type	# of occurrences	Contacts: # broken/# intact	Attitude(s)
Biotite granodiorite-tonalite	3	0/6	Varying orientations, moderately inclined
Aphanitic tonalite	1	0/2	Northeast-dipping, gently inclined
Feldspar-phyrlic tonalite	5	0/10	Varying orientations, gently to moderately inclined
Aplite	9	1/17	Primarily north-dipping, moderately to steeply inclined
Pegmatite	4	0/8	North, east or west-dipping, steeply inclined
Quartz	2	0/4	North and west-dipping, moderately to steeply inclined

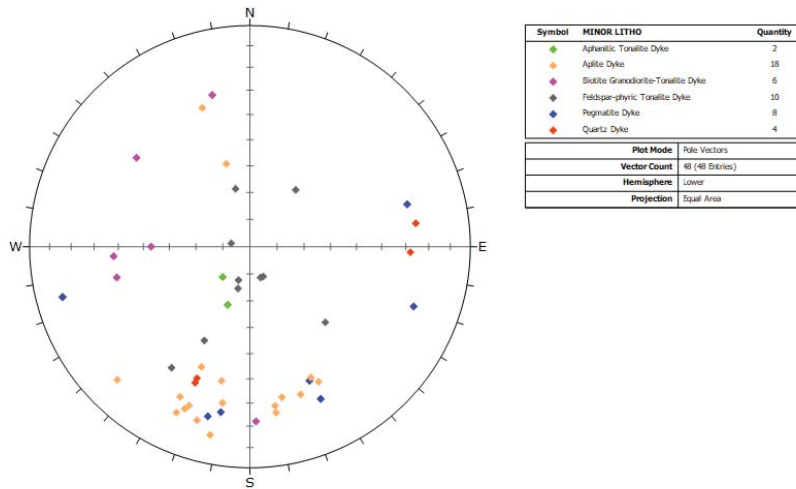


Figure 33: Stereonet showing the distribution of poles for logged felsic dykes (n = 48), including, biotite granodiorite-tonalite dykes (n = 6), aphanitic tonalite dykes (n= 2), feldspar-phyric tonalite dykes (n = 10), aplite dykes (n = 18), pegmatite dykes (n = 8), and quartz dykes (n = 4).

Ductile Structures

Ductile structures identified in IG_BH01 include foliation (FO) and shear zones (SHR). Examples of these structures are shown in Figure 34b and Figure 34c. Stick plots indicating the distribution of the ductile structures are included in Figure 35. Figure 35 also includes the overall per metre fracture frequency and stick plots for all brittle structures logged in the borehole. The brittle structures will be described in detail after presentation of the ductile structures.

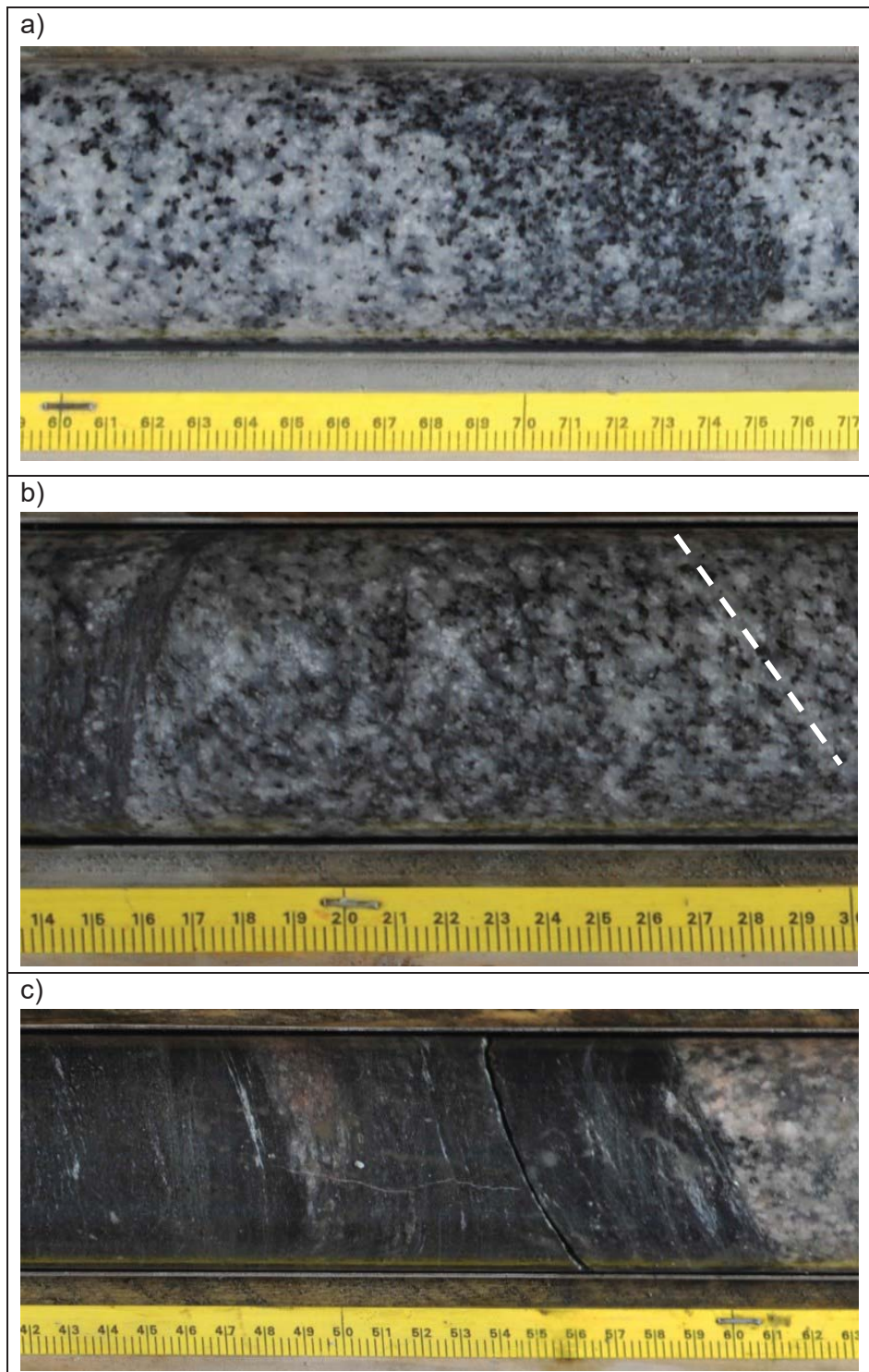


Figure 34: Examples of primary igneous and ductile structure. a) Biotite rich horizon interpreted as primary igneous layering, in biotite granodiorite-tonalite (949 m along borehole). b) Biotite-defined foliation trending at a moderate angle to the core axis, parallel to the white dashed line, and wrapping into a narrow quartz-rich shear zone oriented at a high angle to the core axis near left side of photo, in biotite granodiorite-tonalite (670 m along borehole). c) Shear zone developed at moderate angle to core axis within and along the margin of amphibolite at its contact with biotite granodiorite-tonalite (659 m along borehole).

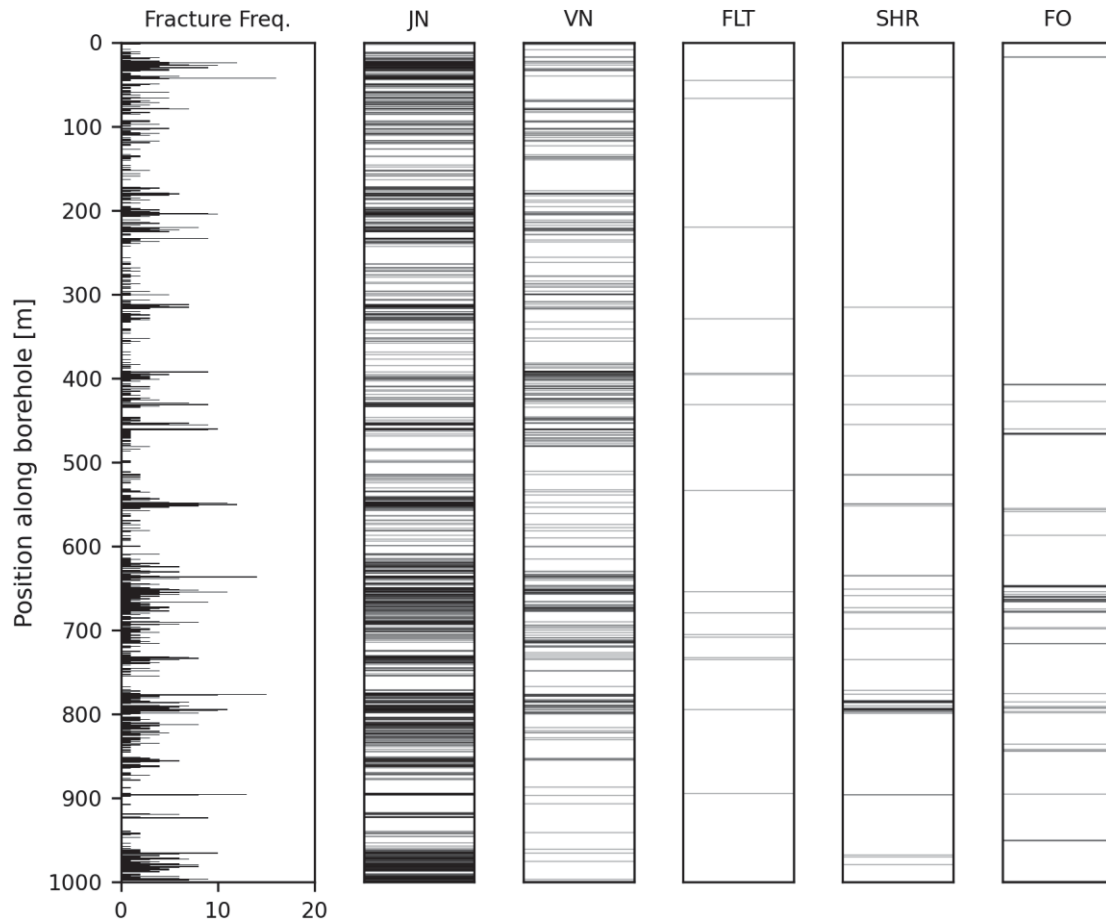


Figure 35: Summary log showing the frequency per metre of brittle structures (left) in comparison to stick plots that show the distribution of all brittle structures (Joints – JN, Veins – VN and Faults - FLT) and all ductile structures (Shear Zones – SHR and Foliation – FO).

Foliation was logged where preferential orientation of mineral grains was observed. A total of 66 occurrences were recorded, and the majority of occurrences were observed below 400 m along borehole, with evidence of a slightly denser cluster of foliations between 650 m and 700 m along borehole (Figure 35). The foliation is described as weakly developed and is characterized by the preferred alignment of biotite. An example of well-developed foliation is shown in Figure 34b. It is observed as uniformly intact in both geological core logging and televiewer logs, with more success identifying the weak alignment through televiewer logging. Figure 36 presents the stereonet of foliation orientations. All occurrences except for one were successfully oriented. There is scatter in the distribution of foliation poles, however one dominant pole cluster in the unweighted dataset defines a steeply inclined foliation plane that dips north-northwest. The Terzaghi-weighted contours emphasize the same pole cluster. Less prominent pole clusters in the unweighted dataset define steeply inclined foliation occurrences that dip southeast and gently to moderately inclined occurrences that dip southwest.

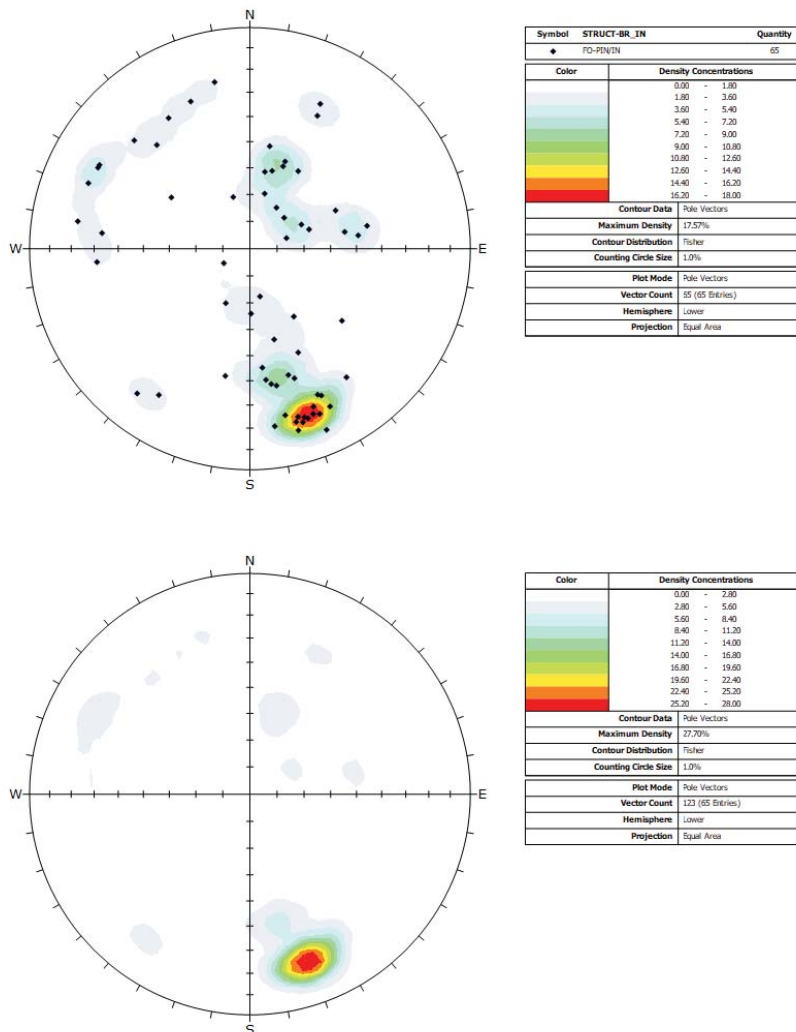


Figure 36: Stereonets showing orientation information for Foliation (FO). Top: All data – poles and contours, unweighted (n = 65). Filled symbols identify partially intact/intact Foliation (FO-PIN/IN). Bottom: All Foliation data, Terzaghi-weighted contours (n = 123).

A total of 52 shear zones were logged in BH01. These structures were initially identified during geological core logging as either ductile or brittle-ductile shear zones. In the assessment of the entire shear zone dataset, it was determined that all occurrences more likely represent a continuum of ductile to brittle deformation. Therefore, the presentation herein integrates all occurrences simply as a single shear zone dataset. Typical shear zone examples are shown in Figure 34b and Figure 34c. The majority are identified in geological core logging only (67 %), with the remaining shear zones identified in both geological core logging and televiewer logs (33 %); 48 of the 52 (92 %) shear zones were successfully oriented. The shear zones were observed to primarily be intact or partially intact; with only three occurrences logged as broken. They range in width from hairline to 12 cm. The most common mineral phase associated with shear zones is quartz, with lesser associations of chlorite, epidote, hematite, pyroxene, and hornblende. They are commonly observed along the contacts of amphibolite occurrences and, in some cases, feldspar-phyrlic felsic dykes. Some occurrences are also identified within the biotite granodiorite-tonalite. The stick plot of shear zone occurrences highlights that they are primarily identified below 400 m, and the majority occur between 650 m and 800 m (Figure 35). Figure 37 presents the unweighted and weighted stereonet for all oriented shear zones. One prominent pole cluster in the unweighted dataset

defines gently to moderately inclined shear zones that dip north-northwest. A second pole cluster, which is emphasized by the Terzaghi weighting, defines steeply inclined shear zones that dip southwest.

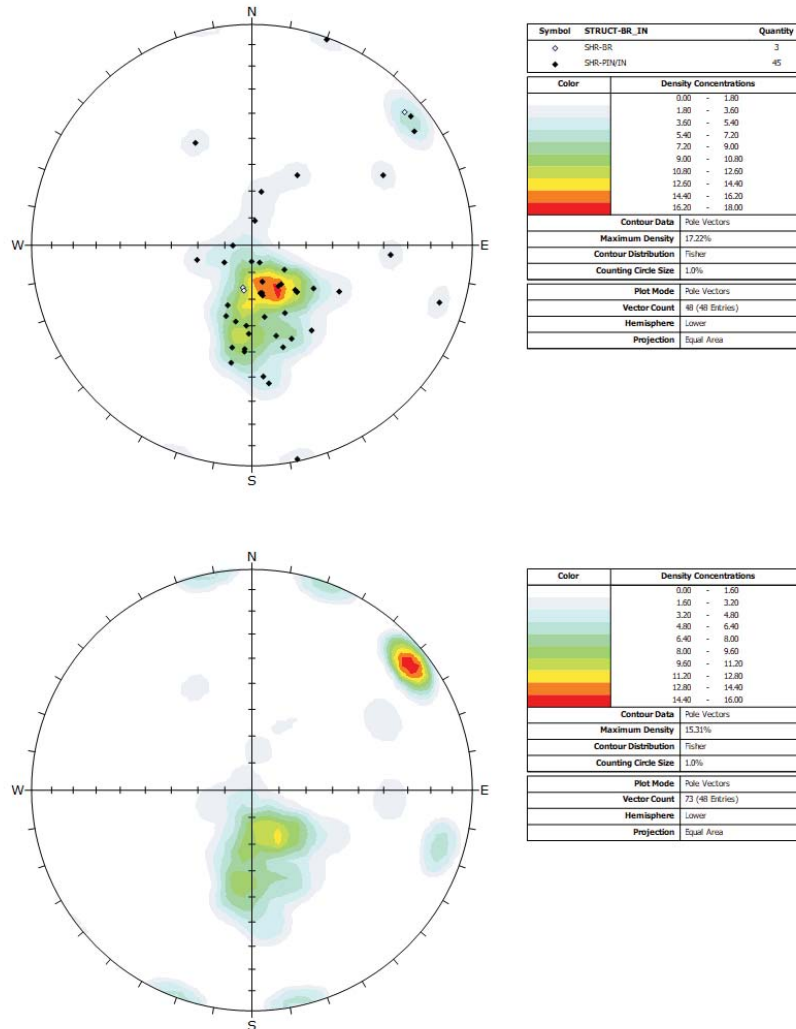


Figure 37: Stereonets showing orientation information for Shear Zones (SHR). Top: All data – poles and contours, unweighted (n = 48). Open symbols identify broken Shear Zones (SHR-BR) and filled symbols identify partially intact/intact Shear Zones (SHR-PIN/IN). Bottom: All Shear Zone data, Terzaghi-weighted contours (n = 73).

Brittle Structures

This section describes the brittle structures, including all joints (JN), veins (VN), and faults (FLT), representing the group of features collectively identified as fractures. A summary of the per metre fracture frequency for all brittle structures, as well as stick plots detailing their distribution in the borehole, is included in Figure 35. Typical examples of brittle structures identified in the borehole are included in Figure 38.

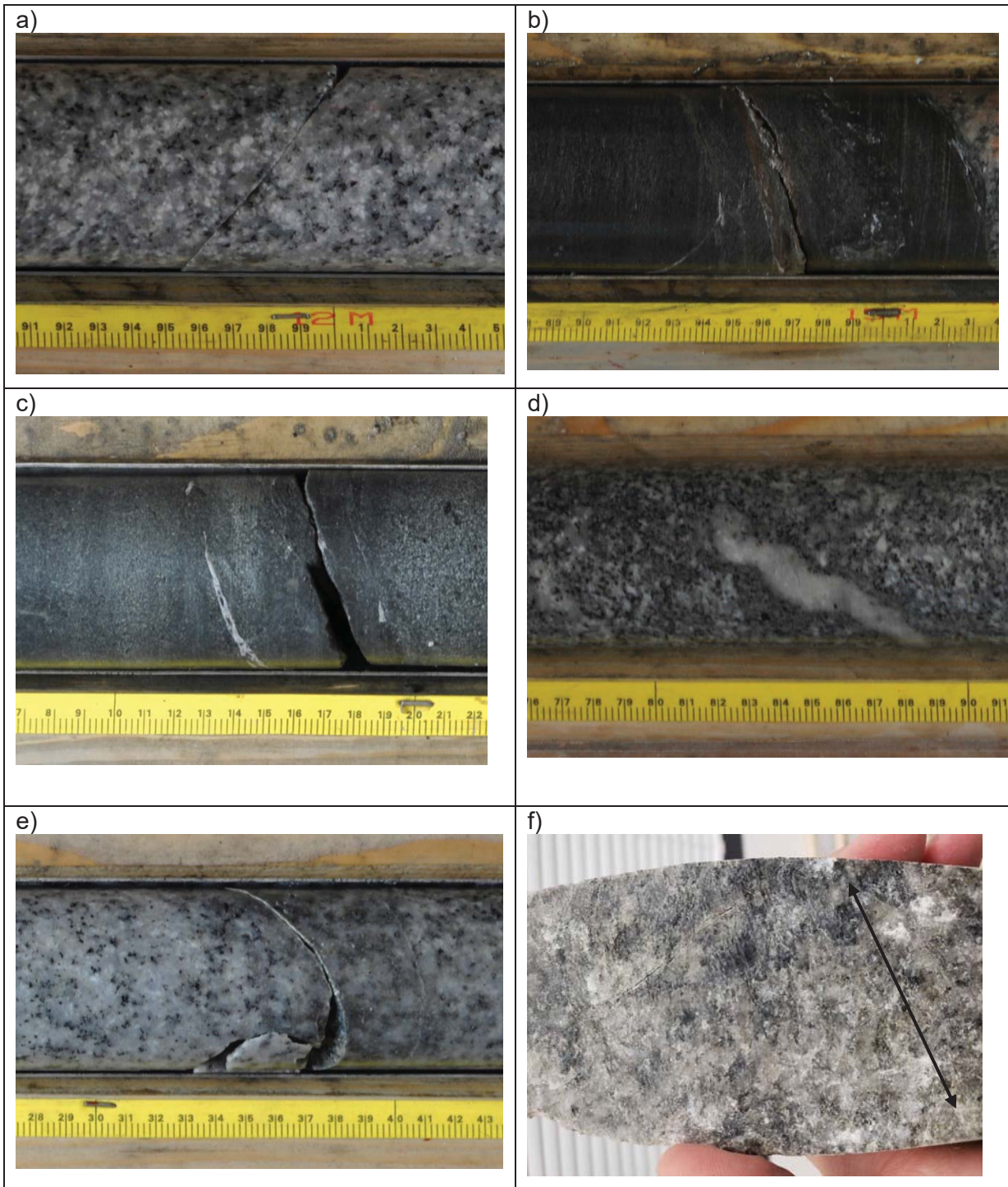


Figure 38: Examples of brittle structures observed in IG_BH01: a) broken, clean, hairline (no visible geological aperture), joint, in biotite granodiorite-tonalite (358 m), b) broken joint with soft gouge-like infill and mm-scale geological aperture, in amphibolite (793 m), c) intact mm-scale calcite vein (middle of photo) adjacent, and to the left of one partially intact joint and one completely broken joint, in biotite tonalite (235 m), d) intact cm-scale quartz vein, in biotite granodiorite-tonalite (656 m), e) broken, hairline (no visible geological aperture) fault with associated cm-scale halo of silicification, in biotite granodiorite-tonalite, f) lineation defined by aligned quartz (parallel to black arrow) on broken fault plane, in biotite granodiorite-tonalite (431 m).

A total of 1304 joints were logged in IG_BH01. They are distributed along the entire length of the borehole and since they dominate the total brittle structure dataset the peaks in the per metre fracture frequency correlate well with the clusters evident in the stick plot of all joints (Figure 35). A total of 545 of the 1304 joints (42 %), were logged as broken, while the remaining 759 (58 %) were logged as intact or partially intact. The majority of the joints (1259/1304; 97 %) exhibit no geological aperture, meaning that any natural aperture, if present, was too small to identify visually. In the remaining 45 occurrences, mm to cm-scale geological apertures (maximum of 27 mm) were observed. Where joints were logged as broken during geological core logging, and did not exhibit any geological aperture, the adjacent broken core pieces were able to be fit back together without any visual evidence of an opening along the fracture plane. In these instances, it is possible that the break was mechanically induced as a result of the drilling process along a joint that was otherwise intact in situ.

Joint surfaces were logged as clean, with no associated mineral infill, in 561 occurrences (43 %), while the remaining 743 (57 %) included observation of staining, slight alteration, or coating with a hairline (<1 mm width) infill. The common mineral phases associated with the joints were quartz, chlorite, iron oxide (hematite), calcite, and epidote.

Typical examples of joints are shown in Figure 38a: one broken joint with a soft gouge-like infill and mm-scale geological aperture in amphibolite (Figure 38b); and one example of a partially intact joint adjacent to a broken joint in amphibolite (Figure 38c). The majority of identified joints were logged in both geological and televiewer logs (582; 45 %) or geological core logging only (568; 44 %), with the remaining joints identified in televiewer logs only (154; 12 %); 1249 of 1304 (96 %) joints were successfully oriented. Figure 39 presents the unweighted and weighted stereonet for all oriented joints. The unweighted pole clusters emphasize subhorizontal to moderately inclined joints dipping north-northwest to north and moderately inclined joints dipping southeast to south. Less prominent pole clusters also define steeply inclined joints dipping southwest, west and east-southeast. These latter, less prominent pole clusters, and another broad pole cluster in the southwest quadrant, are emphasized in the Terzaghi-weighted joint dataset suggesting that they may represent subsets of vertical, northwest- and north- to north-northeast-striking, joint sets.

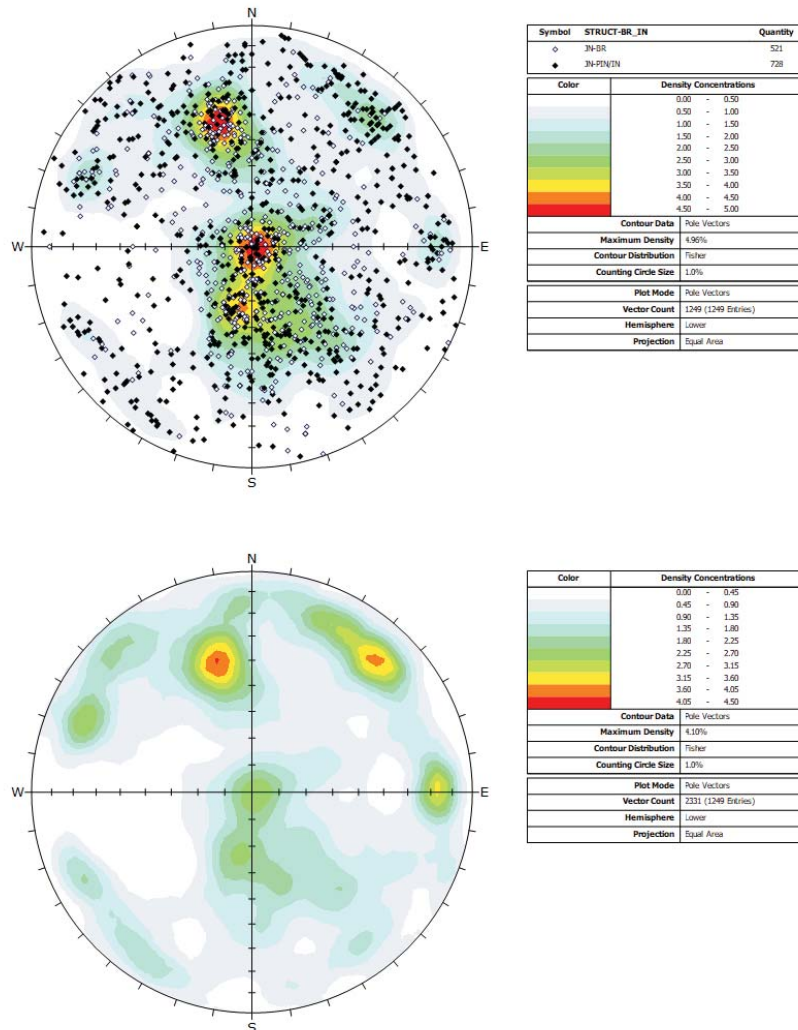


Figure 39: Stereonets showing orientation information for Joints (JN). Top: All data – poles and contours, unweighted (n = 1249). Open symbols identify broken Joints (JN-BR) and filled symbols identify partially intact/intact Joints (JN-PIN/IN). Bottom: All Joint data, Terzaghi-weighted contours (n = 2331).

A total of 346 veins were logged in IG_BH01, distributed along the entire length of the borehole. The majority of the veins (332; 96 %) were logged as intact or partially intact and the remaining 14 vein occurrences were logged as broken. The stick plot of vein occurrences highlights the observation that veins are identified along the entire length of the borehole, including higher density intervals between 400 and 450 m and between 650 and 800 m (Figure 35). A total of 257 veins (74 %) were identified in geological core logging and therefore confidently associated with mineral phases. A total of 89 veins (26 %) were identified only in the televiewer dataset. In the latter occurrences, the infilling mineral could not be determined with certainty. The main mineral infilling phases identified include, quartz in 146 veins (42 %, Figure 38d), followed by a ‘granitic’ assemblage of alkali feldspar +/- plagioclase +/- biotite +/- quartz with lesser muscovite +/- phlogopite in 70 occurrences (20 %), chlorite in 17 veins (5 %) and calcite in 15 veins (4 %, Figure 38c). Logged vein thicknesses range between hairline (sub-mm) and 5 cm. A total of 339 of 346 (98 %) veins were successfully oriented. Figure 40 presents the unweighted and weighted stereonet for all oriented veins. The poles scatter broadly across the stereonet, with one main pole cluster indicating veins that are steeply inclined and dip to the west. Lesser pole clusters indicate gently to moderately inclined veins that dip north-northwest and south-southeast, and steeply inclined veins

that dip broadly southeast and northeast. The poles to the steeply inclined veins are also emphasized in the Terzaghi-weighted dataset.

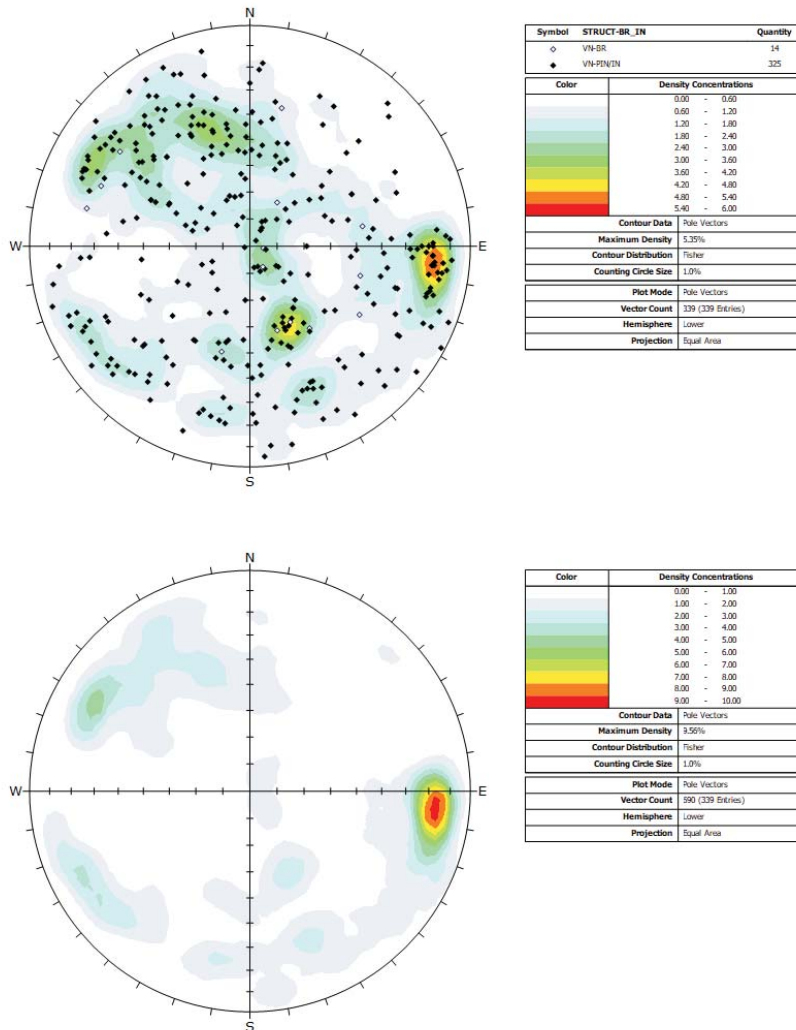


Figure 40: Stereonets showing orientation information for all Veins (VN). Top: All data – poles and contours, unweighted (n = 339). Open symbols identify broken Veins (VN-BR) and filled symbols identify partially intact/intact Veins (VN-PIN/IN). Bottom: All Vein data, Terzaghi-weighted contours (n = 590).

Faults include features interpreted to have resulted from brittle deformation and exhibit some evidence of displacement. A total of 16 faults were logged in IG_BH01. The stick plot highlights the observation that faults are distributed along the entire length of the borehole, with a subtle cluster evident between approximately 650 and 750 m along borehole (Figure 35). The main diagnostic criterion used to identify a fault in the recovered core is the presence of slickenlines on the fault surfaces. The majority of the logged faults (15/16; 94 %) were broken, allowing the full plane to be observed. In one occurrence the fault was partially intact such that a portion of the plane was exposed. In 15 (94 %) of the logged faults, the surface was recorded as a hairline structure with no geological aperture. One fault was logged with 1 mm geological aperture. The common mineral phases identified on fault surfaces were chlorite, clay and epidote, quartz, and an iron oxide stain. A typical example of a fault is shown in Figure 38e, highlighting the observation that faults in IG_BH01 are very narrow and discrete structures with only slight evidence of damage in the rock surrounding the fault plane (in this case, a silicification halo around the fault). Figure 38f shows a

fault plane with slickenlines defined by quartz. In this occurrence, the lineation plunges shallowly in the fault plane suggesting near horizontal (transcurrent) movement. Additional information related to the orientation of lineations is included in the next subsection.

Twelve of the faults were identified in both geological and televiewer logging (75 %), with the remaining four faults observed in geological core logging only (25 %). All faults were successfully oriented. Figure 41 presents the unweighted stereonet for all faults. The fault dataset defines gently to steeply inclined north to northwest dipping faults, as well as steeply inclined faults that dip west and northeast, and moderately to steeply inclined faults that dip east. During a re-examination of the fault planes to measure the rake of each associated logged lineation, it was found that three of the faults originally identified had only faint lineations of unclear orientations. The poles to these three occurrences are circled in the stereonet.

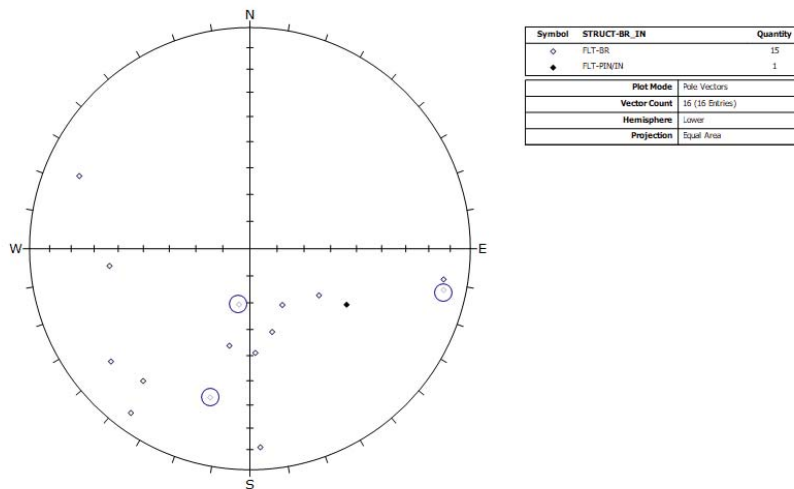


Figure 41: Stereonets showing orientation information for Faults (FLT). All data – poles (n = 16). Open symbols identify broken Faults (FLT-BR) and filled symbols identify partially intact/intact Faults (FLT-PIN/IN). Poles to faults with weak and uncertain lineations are circled.

Lineations

A total of 23 lineations were identified during geological core logging, including 16 occurrences identified on faults and seven occurrences associated with shear zones. Lineations were identified by the alignment of minerals on fault and shear planes, and their gamma and delta angles were determined by measurement relative to the arbitrary reference line drawn along the core axis. When plotting each corrected lineation, i.e., its true trend and plunge, the field estimation of gamma and delta introduced enough error to cause the lineations to plot off of their associated great circles (planes). To correct the plotting error from the field estimation of the gamma and delta angles, each lineation was re-assessed visually and their rake (ranging between 0° to 180°) on the plane was measured. The rake is the angle between the lineation and the strike line of the plane in which the lineation is found, following the right-hand rule convention. In this process 13 of the 16 fault lineations were clearly re-identified on their respective surfaces and a rake was measured. The remaining three lineations were too weak to clearly define a single orientation for a confident re-measurement of their rake. All seven lineation occurrences originally identified on shear planes were re-assigned rake values. The rake values for both the fault and shear planes were then converted to final trends and plunges for each lineation. A summary of the results for lineations identified on both fault and shear planes are presented in Figure 42. The complete uncorrected

(trend, plunge) and corrected (rake, trend-corrected, plunge-corrected) lineation dataset is presented in Appendix F.

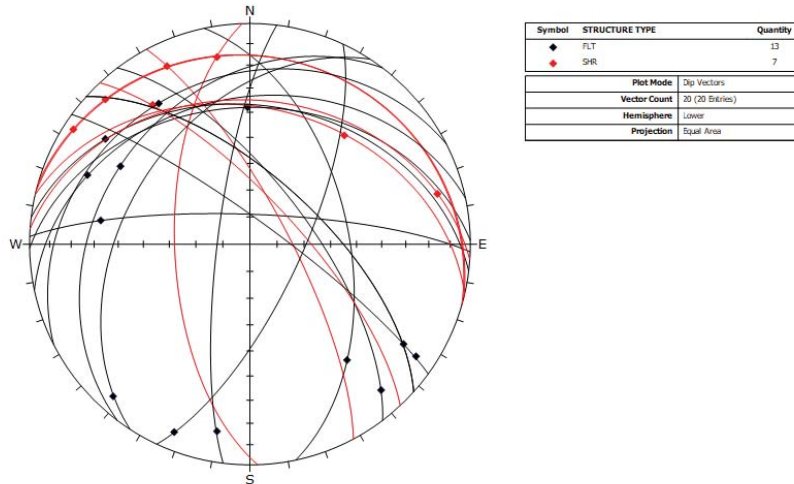


Figure 42: Stereonet showing all lineations by their rake on fault planes (black, n = 13) and shear planes (red, n = 7).

All lineations, regardless of the orientation of their associated fault or shear plane, exhibit gentle to moderate plunges (Figure 42). The majority of the lineations plunge towards the northwest on gently to moderately inclined northwest- to north-dipping planes, or towards the southeast on steeply inclined planes that dip northeast. Two southwest-plunging lineations are associated with steeply inclined fault planes that dip west and east-southeast. A third lineation that plunges in the same direction is associated with a gently inclined fault plane that dips northwest. Two lineations that plunge northeast are associated with moderately inclined shear planes that dip north. Preferentially oriented chlorite, epidote or quartz define these lineations.

Overall, the dataset of planes and lineations, though small, provides good indication that dip-slip motion predominates on gently to moderately inclined northwest to north dipping planes and nearly-transcurrent motion predominates on steeply inclined planes. Structures identified as faults and shear zones during geological core logging generally exhibit a similar history of motion, most prominently in a northwest-southeast direction.

Broken vs Intact or Partially Intact Structures

During the geological core logging, naturally occurring fractures were categorized as being broken (BR) when the core was physically broken into separate pieces at the location of the logged structure. Otherwise, they were categorized as intact (IN) or partially intact (PIN) where complete or partial cohesion was maintained along the planer logged structure. Of the 1604 oriented fractures, 550 (34 %) were logged as broken (Figure 43) and 1054 (66 %) were logged as intact or partially intact (Figure 44). This categorization is based on a visual assessment of core condition when the core is removed from the barrel and initially examined. As mentioned earlier in the discussion of joints, which includes the majority of broken fractures, most of the adjacent broken fracture planes could be physically fit back together with no visible geological aperture. Therefore, the broken characteristic alone does not imply any direct relationship to the potential for a fracture to be hydraulically conductive. This categorization also does not include any judgement on whether or not the drilling activity itself may have induced the broken character. The primary difference between the distribution of poles to fractures logged as broken versus intact (or partially intact),

comparing Figure 43 with Figure 44, is that steeper dipping structures are less likely to have been logged as broken.

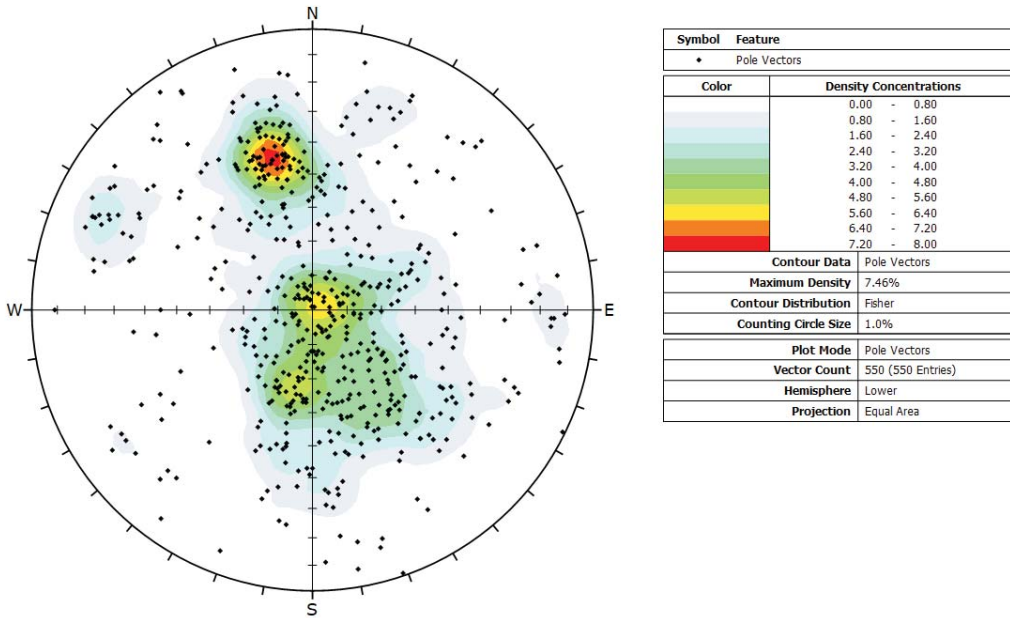


Figure 43: Stereonet plot showing poles to all fracture planes logged as broken during geological core logging, with unweighted contours.

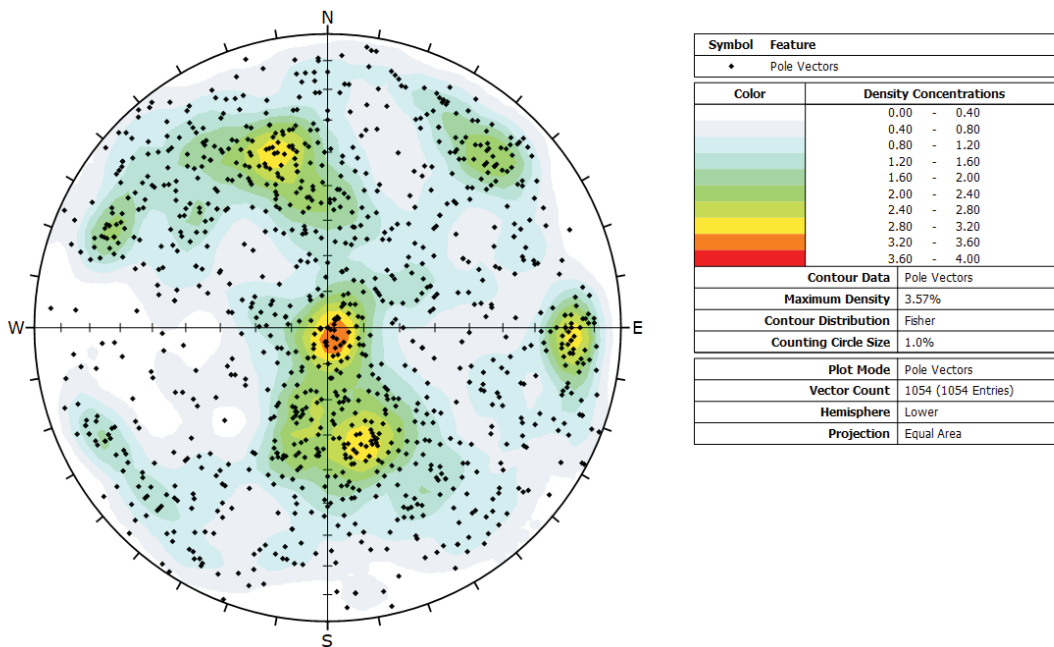


Figure 44: Stereonet plot showing poles to all fracture planes logged as intact or partially intact, with unweighted contours.

3.2.4.2 Interpreted Fracture Sets

Figure 45 presents the distribution of fracture poles and contoured stereographic distribution of poles to all logged fractures (joints, veins, faults, $n = 1604$) in order to assess for the presence of visible pole clusters that may define fracture sets in IG_BH01. These identified fracture sets can be compared with fracture sets identified in other boreholes, and also with surface mapped fracture and interpreted fracture (lineament) orientations, to provide guidance in developing three-dimensional fracture network models. Shear zones have not been included in this assessment.

Based on visual assessment of pole clusters and using a contour density cut-off of 1 % from the Terzaghi-weighted dataset as a guide, six clusters labelled (i) to (vi) were initially identified in IG_BH01. Expert judgement was also employed to refine boundaries between pole clusters. These clusters are outlined on the stereonet of unweighted poles to all fractures (upper stereonet plot in Figure 45), and include:

- a large pole cluster that overlaps the centre of the stereonet to define a subhorizontally-oriented to moderately inclined, north- to north-northwest-dipping fracture set (Cluster i - grey symbols in Figure 48, top stereonet);
- a pole cluster that defines a moderately to steeply inclined fracture set dipping south- to south-southeast (Cluster ii - red symbols in Figure 48, top stereonet);
- a pole cluster that defines a steeply inclined fracture set dipping west- to west-northwest (Cluster iii - green symbols in Figure 48, top stereonet);
- a pole cluster that defines a steeply inclined fracture set dipping southeast (Cluster iv - orange symbols in Figure 48, top stereonet);
- a pole cluster that defines a steeply inclined fracture set dipping northeast (Cluster v - blue symbols in Figure 48, top stereonet); and
- a pole cluster that defines a steeply inclined fracture set dipping southwest (Cluster vi - purple symbols in Figure 48, top stereonet).

The remaining unclustered poles are not assigned to any particular possible fracture set and are therefore assigned to an additional random set.

The same six pole clusters are also outlined on the unweighted and Terzaghi-weighted contour plots (middle and bottom images in Figure 48, respectively). The Terzaghi-weighted plot de-emphasizes the shallower-dipping pole clusters and emphasizes the steeply inclined pole clusters, as expected for a vertical borehole (Figure 45). Notably, the Terzaghi-weighted contours, relative to the unweighted contours, extend closer to the perimeter of the stereonet than the unweighted contours, providing some indication that the steeply inclined and oppositely-dipping pole clusters, (iii and iv) and (v and vi), potentially represent members of the same near-vertical to vertically-oriented fracture sets. Given that IG_BH01 is near vertical and near vertical to vertical fractures were poorly sampled during drilling, this is considered to be a suitable working hypothesis.

As a final interpretation of fracture sets for IG_BH01, pole cluster (i) is assigned to Fracture Set 1 defined by subhorizontally-oriented to moderately inclined, north- to north-northwest-dipping fractures, pole cluster (ii) is assigned to Fracture Set 2 defined by moderately to steeply inclined, south- to south-southeast-dipping fractures, pole clusters (iii) and (iv) are assigned to Fracture Set 3, which includes steeply inclined, west- to west-northwest-dipping fractures (subset 3a) and steeply inclined, south-southeast-dipping fractures (subset 3b), pole cluster (v) and (vi) are assigned to Fracture Set 4, which includes steeply inclined, northeast-dipping fractures (subset 4a) and steeply inclined, southwest-dipping fractures (subset 4b). These final fracture set IDs are labelled on the unweighted and Terzaghi-weighted contour plots in Figure 45 and summarized in Table 9.

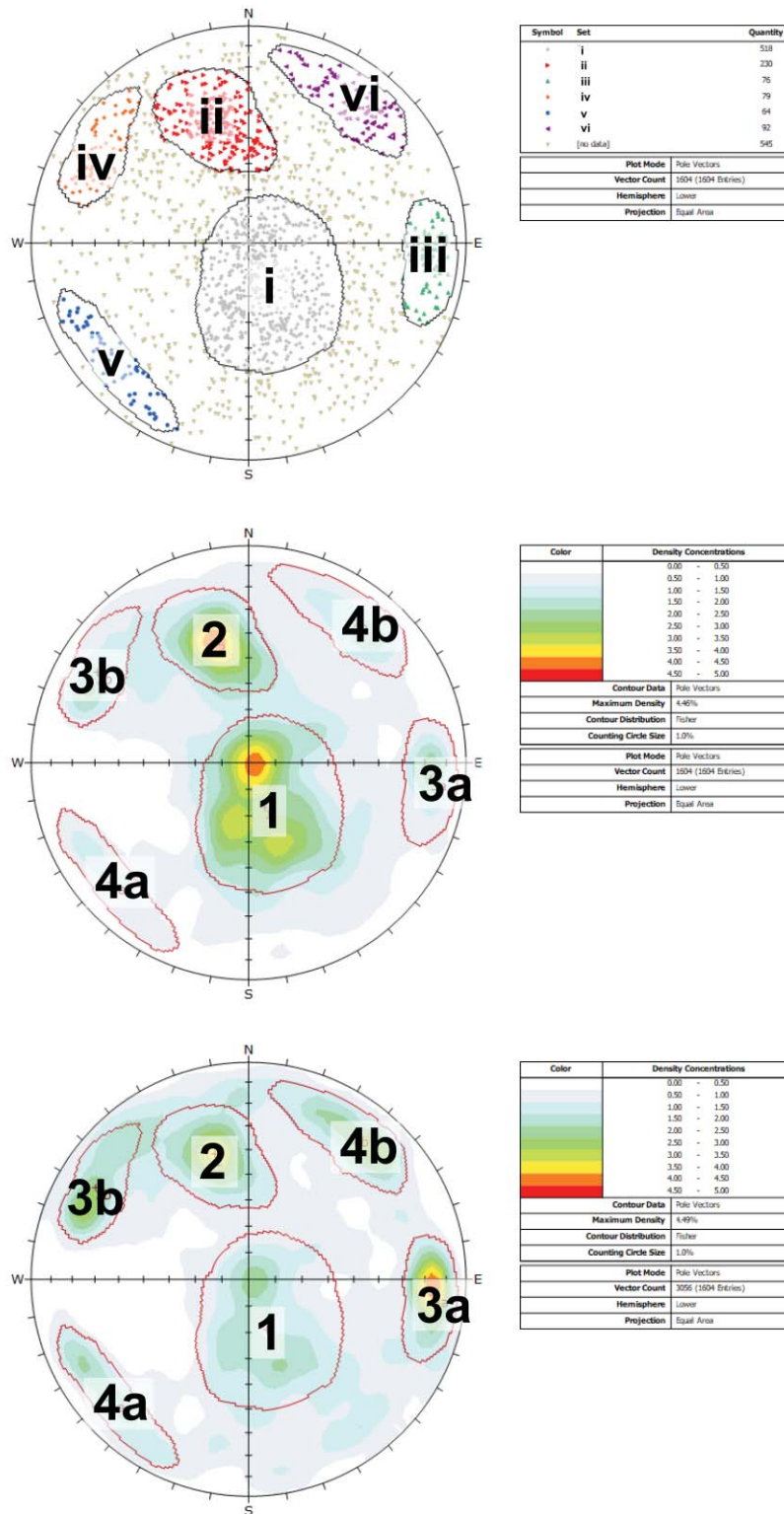


Figure 45: Stereonets of all oriented fractures, including all joints, veins and faults. Top: All fractures – poles, unweighted (n = 1604). Identified pole clusters are colour-coded to highlight their distribution. Middle: All fractures – contours (n = 1604), unweighted. Bottom: All fractures – contours, Terzaghi-weighted (n = 3056). Middle and bottom stereonet are overlain by final fracture set interpretation. See text and Table 9 for additional summary.

Table 9: Summary of interpreted fracture sets in the borehole. Presents the general description of the orientation with a mean dip and dip direction.

Fracture Set ID	Orientation	Mean Dip / Dip Direction	Fracture Count
1	Subhorizontal to moderately inclined set, dipping north to north-northwest.	20 / 340	518
2	Moderately to steeply Inclined, dipping south-southeast	50 / 165	230
3a	Steeply dipping set, dipping west to west-northwest.	74 / 275	76
3b	Steeply dipping set, dipping southeast.	71 / 121	79
4a	Steeply dipping set, dipping northeast.	74 / 049	64
4b	Steeply dipping set, dipping southwest.	71 / 216	92

Regarding the relationship between fracture sets and ductile structures, foliation is predominantly steeply inclined and dips towards the north-northwest, with the majority of poles falling outside of Fracture Set 1. The majority of shear zones are subhorizontal to inclined, dipping to the north-northwest (Fracture Set 1; Figure 37), while a small number are steeply inclined and dip southeast (Fracture Set 4b). One steeply inclined shear zone dips west (Fracture Set 3a; Figure 37). The similarity of orientation between the brittle fracture sets and the ductile structures suggests that pre-existing ductile fabrics exerted some control on the development of brittle structures in the rock mass, in particular Fracture Set 1.

Regarding the relationship between fracture sets and brittle structures, the large number of joints relative to veins and faults is consistent with the presence of joints in all identified fracture sets (Figure 39). Poles to veins cluster prominently in Fracture Sets 3a and 3b, and less so in Fracture Set 2, Fracture Set 4a and Fracture Set 1 (Figure 40). Poles to faults cluster prominently in Fracture Sets 3a and 3b, and less so in Fracture Set 1 and Fracture Set 4a (Figure 41). The majority of amphibolite contacts fall within Fracture Set 1 (Figure 32).

Stick plots of the distribution of each fracture assigned to a fracture set, as well as unassigned random fractures, are plotted adjacent to the per metre fracture frequency of IG_BH01 in Figure 46. This presentation aids in assessing the degree of clustering evident by fracture set. Fracture Set 1 are prominent along the entire length of the borehole, including at the very top and bottom of the borehole. The tightest cluster of Fracture Set 1 occurs at ca. 550 m and a slight increase in frequency is also evident between 600 and 800 m. Overall, the clearest Fracture Set 1 clusters appear to spatially coincide with peaks in the fracture frequency curve. There is also a notable absence of Fracture Set 1 between ca. 450 and 550 m along borehole. Fracture Set 2 is identified along the entire length of the borehole with the highest fracture frequency evident in the upper 250 m. Below 250 m, the frequency of Fracture Set 2 is generally low except for a slight increase between ca. 650 and 850 m along borehole. Combined Fracture Sets 3a and 3b are sparsely distributed in the upper 500 m of the borehole, with large gaps in occurrence common and with a slightly increased fracture frequency in the lower 500 m of the borehole, particularly around 700 m along borehole. Fractures assigned to combined Fracture Sets 4a and 4b are the most sparsely distributed. They exhibit a consistently low fracture frequency in the upper 800 m of the borehole. Immediately below this is a single broad zone of increased frequency of Fracture Sets 4a and 4b, followed immediately by a wide gap in their distribution. Fracture Sets 3a/3b and 4a/4b are near vertical, so their sparse distribution may be a result of borehole orientation bias.

Overall, it is difficult to define clear fracture clusters in any of Fracture Sets 2, 3a/3b or 4a/4b. The set of unassigned random fractures (545/1604; 34 %) is prominent along the entire length of the borehole with a slightly increased frequency in the upper 50 m, at approximately 650 m, and near the bottom of the borehole below 950 m.

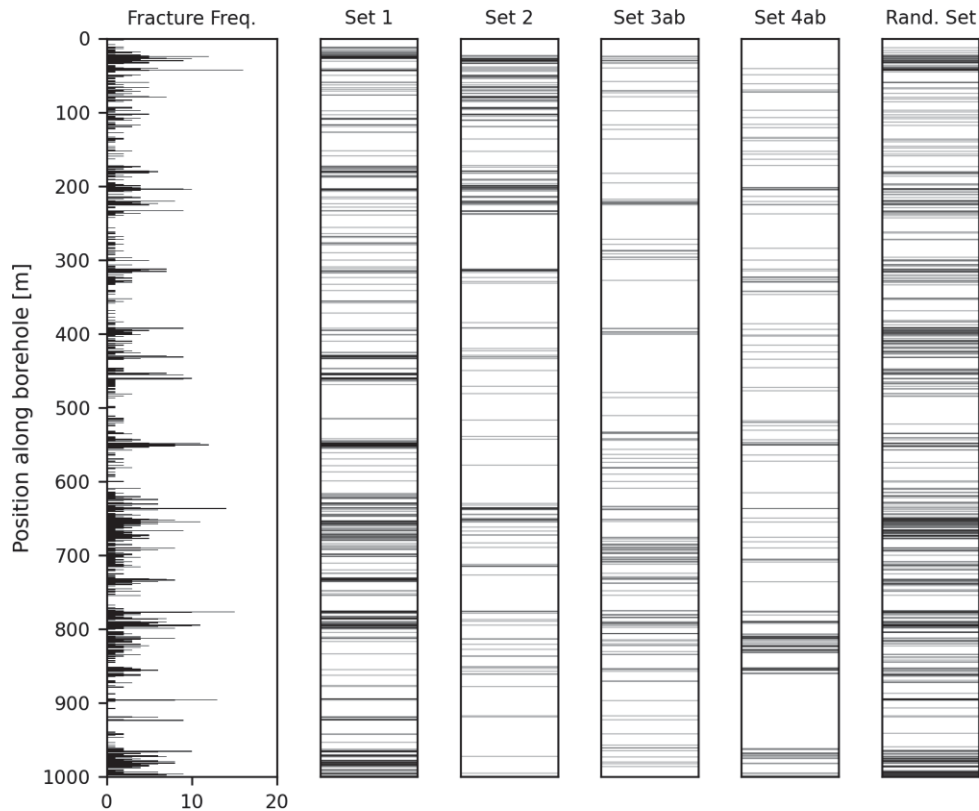


Figure 46: Summary log showing the frequency per metre of all brittle structures (left) in comparison to stick plots that show the distribution of all fractures assigned to defined fracture sets 1, 2, 3a/3b combined and 4a/4b combined, as well as unassigned random fractures.

It is understood that there is some uncertainty in the present assessment, including whether fracture sets can or should be defined, and whether each of the two similarly-striking but oppositely-dipping Fracture Sets 3a/3b and 4a/4b should be treated as endmembers of the same sub-vertical fracture set. As additional boreholes are drilled, including angled boreholes in multiple directions, this initial interpretation of fracture sets presented above will be refined.

3.2.4.3 Fracture Infill Minerals

Fracture infill or secondary minerals are observed in association with all fracture types in IG_BH01, and include surface staining or hairline infilling in joints, mineral lineations on fault surfaces, and vein infilling. Of the 1604 logged fractures, 1024 (64 %) were identified during geological core logging to host infilling minerals. The most prominent infill mineral phase identified in IG_BH01 is quartz, which occurs both as the sole mineral phase and in association with some occurrences of chlorite, iron oxide stain, calcite, and epidote. The discussion below focuses on the orientation and distribution of these mineral phases. Stick plots of the distribution of each of these infill mineral types are plotted adjacent to the per metre fracture frequency of IG_BH01 in Figure 47.

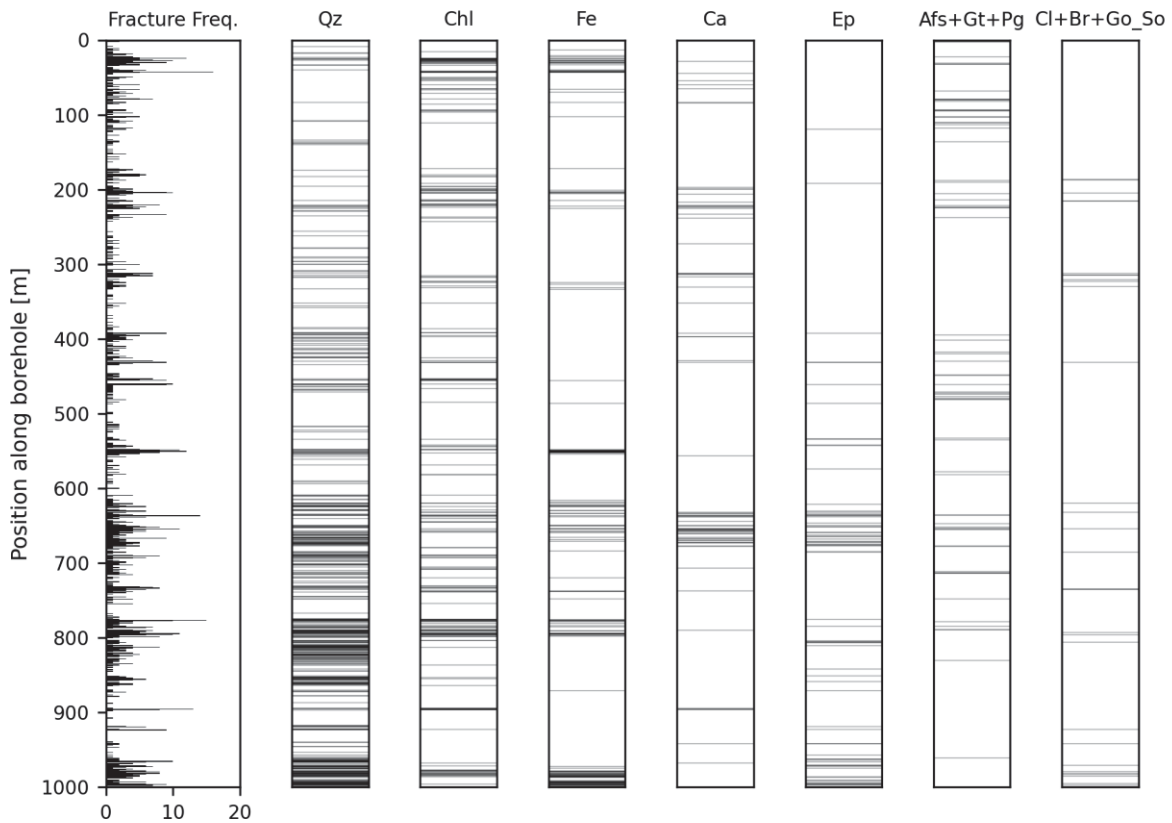


Figure 47: Summary log showing the frequency per metre (Fracture Freq.) of all brittle structures (left) in comparison to stick plots that show the distribution of the most common infill mineral phases including quartz (Qz), chlorite (Chl), iron oxide stain (Fe), epidote (Ep), calcite (Ca), a granitic (Gt) or pegmatitic (Pg) assemblage that includes some combination of alkali-feldspar (Afs) with quartz, plagioclase and biotite, and, fractures that exhibit either clay (Cl), broken rock (Br) or soft gouge (Go_So).

Quartz +/- chlorite, biotite, phlogopite, muscovite, epidote, iron oxide stain, or calcite was logged in 507 of the 1604 (32 %) oriented fractures. Prominent pole clusters of quartz +/- accessory mineral-filled fractures fall within fracture set 1 and fracture set 4b (Figure 48). Fractures with quartz +/- accessory mineral infill are sparse in the upper 550 m of the borehole. The frequency of quartz infill increases markedly in the lower 450 m of the borehole, following the peaks evident in the fracture frequency curve (Figure 47).

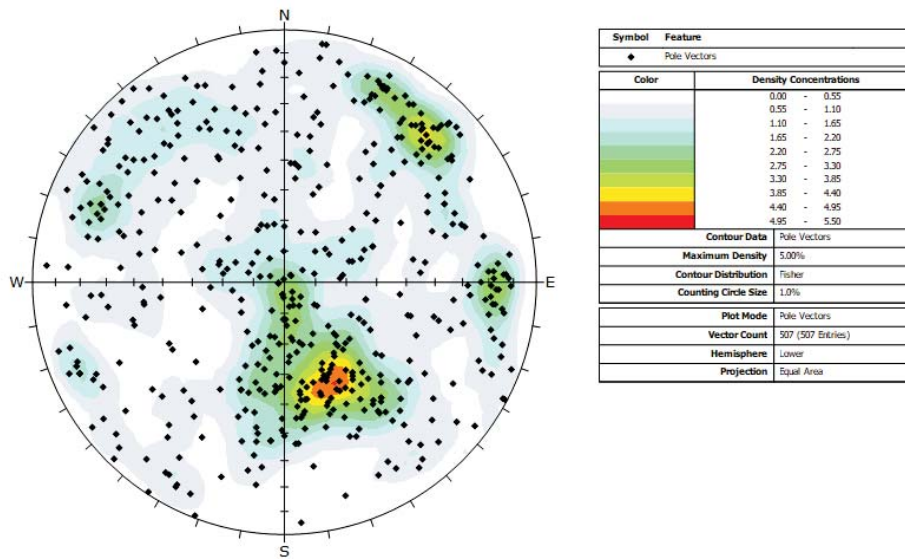


Figure 48: Stereonet plot showing poles to all fracture planes logged with quartz +/- chlorite, biotite, phlogopite, muscovite, epidote, iron oxide staining, or calcite.

Chlorite is identified as an infill mineral phase in 231 of the 1604 (14 %) oriented fractures and the distribution of the poles to these fractures exhibit one prominent cluster that can be attributed to fracture set 2 (Figure 49). The distribution of chlorite-filled fractures varies along the borehole with slight concentrations above 100 m, around 200 m, and broadly between approximately 600 – 800 m (Figure 47).

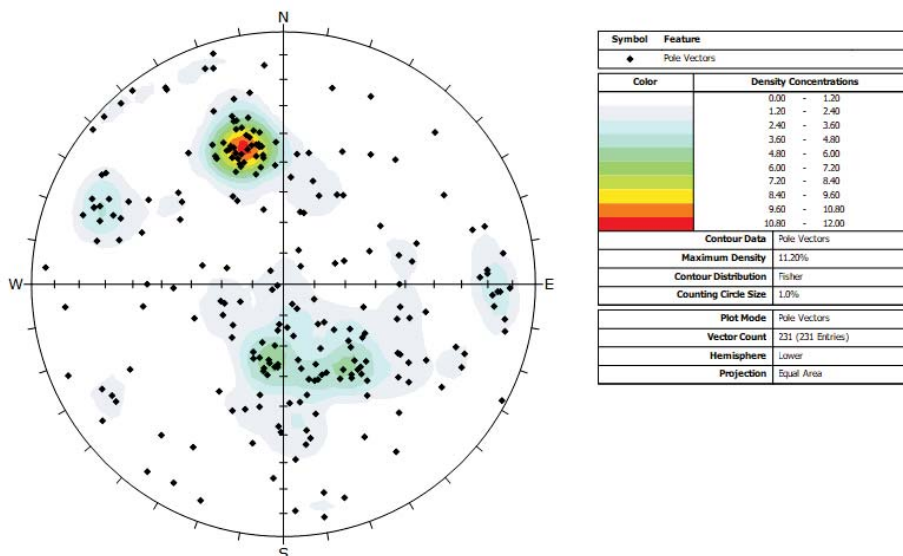


Figure 49: Stereonet plot showing poles to all fracture planes logged with chlorite.

An iron oxide mineral, potentially hematite, is present primarily as a stain on the surfaces of 176 of the 1604 (11 %) oriented fractures (Figure 50). One prominent pole cluster of iron oxide-filled fractures fall within fracture set 1 and a less prominent pole cluster overlaps with the region of fracture set 2. The distribution of iron oxide-stained fractures is heterogeneous along the borehole with a slightly higher frequency evident in the upper 50 m of the borehole, at 550 m, and near the very bottom of the borehole (Figure 47).

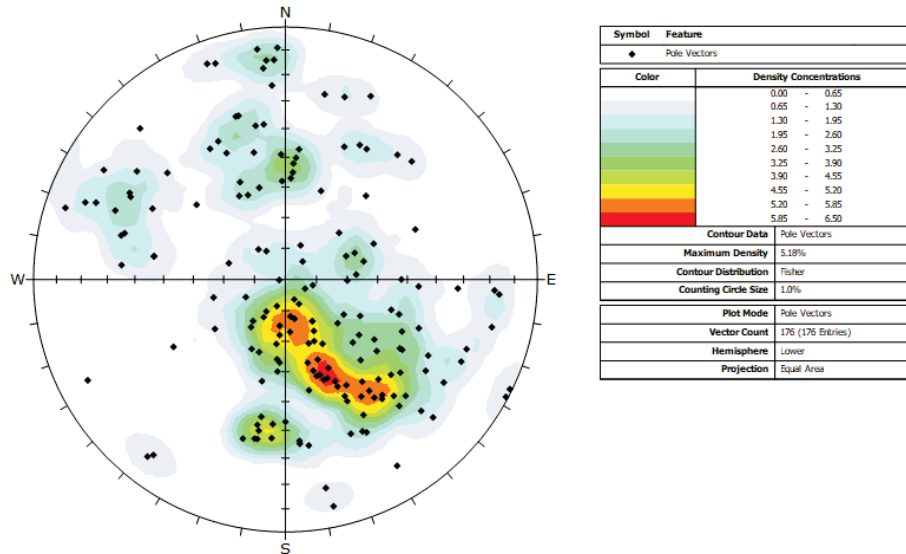


Figure 50: Stereonet plot showing poles to all fracture planes logged with iron staining.

Calcite is identified as a mineral infill phase on 75 of the 1604 (5 %) oriented fractures. The distribution of the poles to calcite-filled fractures exhibits one prominent cluster coincident with fracture set 2 (Figure 51). These calcite-filled fractures primarily cluster along the borehole between approximately 200 and 300 m and around 650 m (Figure 47).

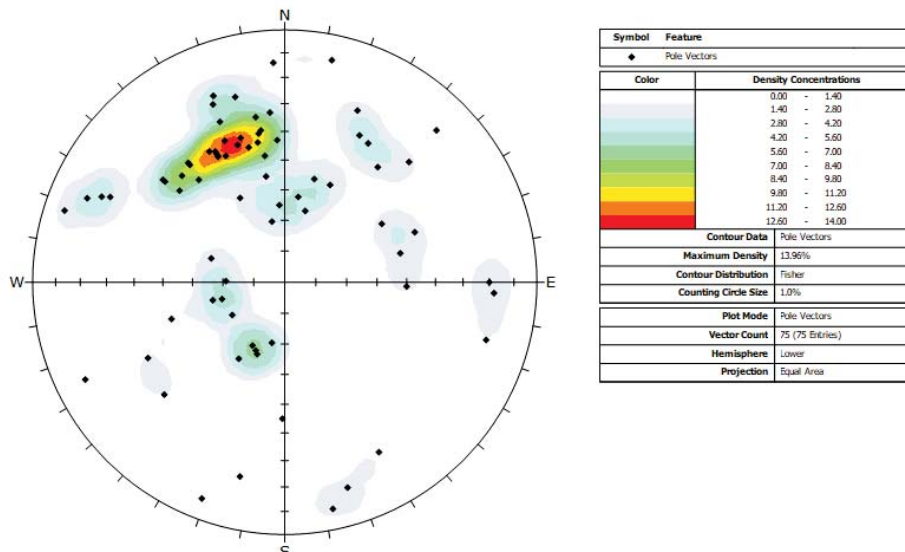


Figure 51: Stereonet plot showing poles to all fracture planes logged with calcite.

Epidote is identified as a mineral infill phase on 74 of the 1604 (5 %) oriented fractures. The distribution of poles to epidote-filled fractures exhibits one prominent pole cluster that coincides with fracture set 3b and two less prominent pole clusters that coincide with fracture set 1 and fracture set 3a (Figure 52). Epidote is nearly absent in fractures logged in the upper 400 m of the borehole and only slightly more common at greater depth, except for one interval of increased frequency of occurrence at around 650 m along borehole (Figure 47).

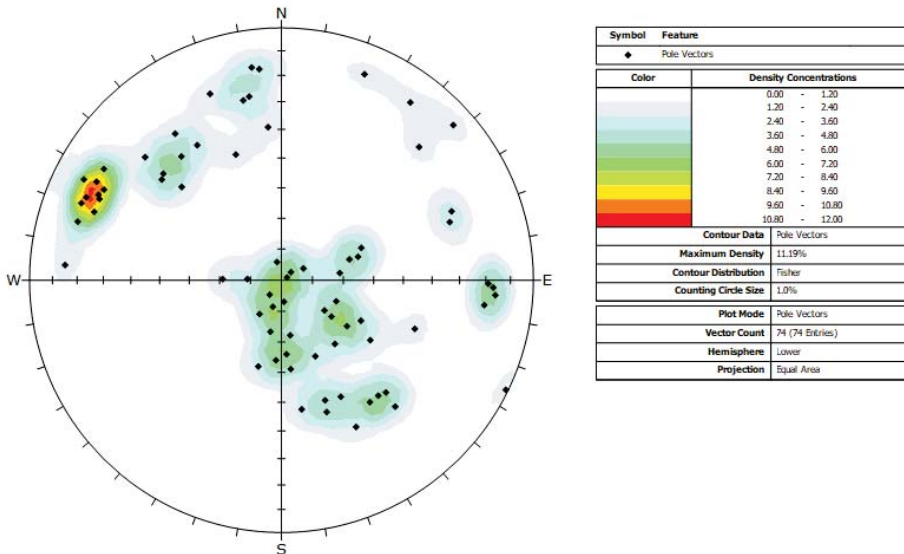


Figure 52: Stereonet plot showing poles to all fracture planes logged with epidote.

A granitic infill assemblage characterized by alkali-feldspar +/- quartz, plagioclase and biotite, and lesser muscovite +/- phlogopite, including some coarser-grained pegmatitic occurrences, is identified in 70 of the 1604 (4 %) oriented fractures. The distribution of the poles to these fractures exhibits one prominent cluster coincident with fracture set 2 (Figure 53).

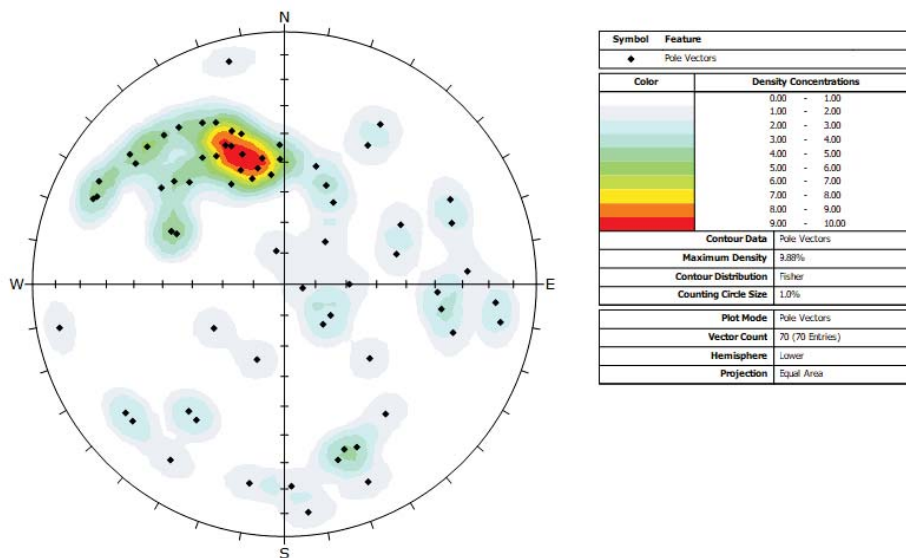


Figure 53: Stereonet plot showing poles to all fracture planes logged with granitic infill, including alkali-feldspar +/- quartz, plagioclase and biotite.

Additional infilling mineral types were identified on 31 of 1604 oriented fractures (2 %), including occurrences of clay infilling in 14 fractures, broken rock fragments interpreted as infilling fractures in 11 occurrences, and infill identified as soft gouge identified in six occurrences. The majority of the poles to all three of these groups overlap with fracture set 1 (Figure 54).

A total of 580 fractures (36 %) have no associated infill mineral phase assigned to them. This includes 243 fractures that were only identified in the televiewer datasets and could not confidently be assessed for infill mineral type, even if present (Figure 55). The poles to fractures with no assigned infill minerals exhibit one prominent cluster in the centre of the stereonet highlighting the dominance of subhorizontal fractures (fracture set 1). A less prominent pole cluster defines moderately inclined fractures dipping south-southeast (fracture set 2). Both of these pole clusters include fractures identified only in televiewer logging, fractures only identified in geological core logging, and fractures identified in both stages of logging.

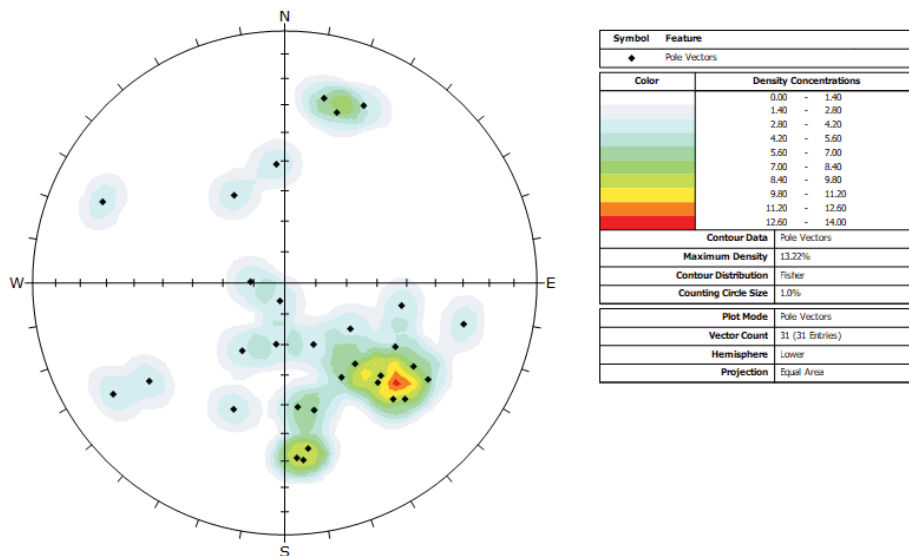


Figure 54: Stereonet plot showing poles to all fracture planes logged with clay, broken rock, or soft gouge.

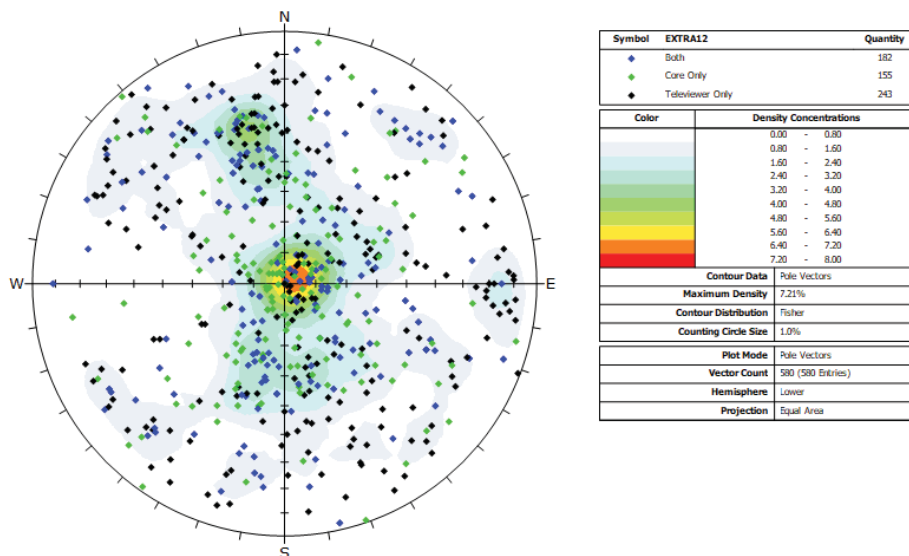


Figure 55: Stereonet showing poles to all fractures logged as having no identifiable mineral infill phase. Fractures logged in 'televiewer' datasets only, geological 'core' logging only, or identified in 'both' datasets, are distinguished.

3.2.5 Structural Unit Classification

Structural units (SU) have been defined to capture the general variation in fracture frequency along the length of the borehole. Boundaries between structural units were defined primarily on the basis of broad changes in slope visible in the cumulative fracture frequency curve. This curve was derived using the fracture dataset (i.e., joints, veins, and faults, including broken and intact/partially intact structures) and is presented in Figure 56. The per metre mean fracture frequency, derived using the same dataset, is also reported as an additional indicator of these same general trends. A total of five SUs are defined for IG_BH01 (Figure 56). Stereonets of fracture orientation data for each defined SU are presented in Appendix G:

Structural unit 1 (SU1) extends from the ground surface (0 m) to 44.06 m along borehole (Figure 56). This unit exhibits a relatively shallow slope in the cumulative fracture frequency curve corresponding to a relatively higher degree of fracturing of the bedrock than the adjacent, deeper, SU2. The average fractures per metre in this unit is 3.11, however, fracture frequency is not consistent throughout the unit, and ranges from metre long intervals completely devoid of fractures and intervals up to 16 fractures per metre. There are 128 oriented fractures in SU1, including 117 joints and 11 veins (Appendix G). The distributions of the poles to these fractures overlap with Fracture Sets 2 and 3a, and to a lesser extent Fracture Set 1.

Structural unit 2 (SU2) is a 575 m interval that extends from 44.06 m to 619.45 m along borehole and is defined by a relatively steep slope in the cumulative fracture frequency corresponding to a lower degree of fracturing of the bedrock compared to the adjacent SU's above and below (Figure 56). This interval has an average fracture frequency of 1.21 fractures per metre and exhibits some local variability in counts ranging between 0 and 12 fractures per metre. There are 680 oriented fractures in SU2, including 477 joints, 195 veins, and 8 faults (Appendix G). The distributions of the poles to these fractures overlap with all defined Fracture Sets, though only a small cluster of poles overlaps with Fracture Set 4b.

Structural unit 3 (SU3) extends from 619.45 m to 862.68 m along borehole (Figure 56) and shows a relatively shallow slope, compared to SU2, in the cumulative fracture frequency curve corresponding to a relatively higher degree of fracturing of the bedrock. The slope of the curve corresponds to an average fracture frequency of 2.43 fractures per metre with local variability within the unit ranging between 0 and 15 fractures per metre. There are 567 oriented fractures in SU3, including 436 joints, 195 veins, and 8 faults (Appendix G). The distributions of the poles to these fractures overlap with all defined Fracture Sets, though only a small cluster of poles overlaps with Fracture Set 4b.

Structural unit 4 (SU4) extends from 862.68 m to 961.20 m along borehole (Figure 56). Both the fracture frequency and cumulative frequency curves show this interval has a low degree of fracturing with an average fracture frequency of 0.74 fractures per metre. The unit is mostly free of fracturing; however, there is still variability of the fracture frequency ranging between 0 and 13 fractures per metre. The distributions of the poles to these fractures overlap with all defined Fracture Sets, though only a small cluster of poles overlaps with Fracture Set 4b. There are 61 oriented fractures in SU4, including 55 joints, 5 veins, and 1 fault (Appendix G). The distributions of the poles to these fractures overlap with Fracture Sets 3a and 3b, and to a lesser extent Fracture Set 1.

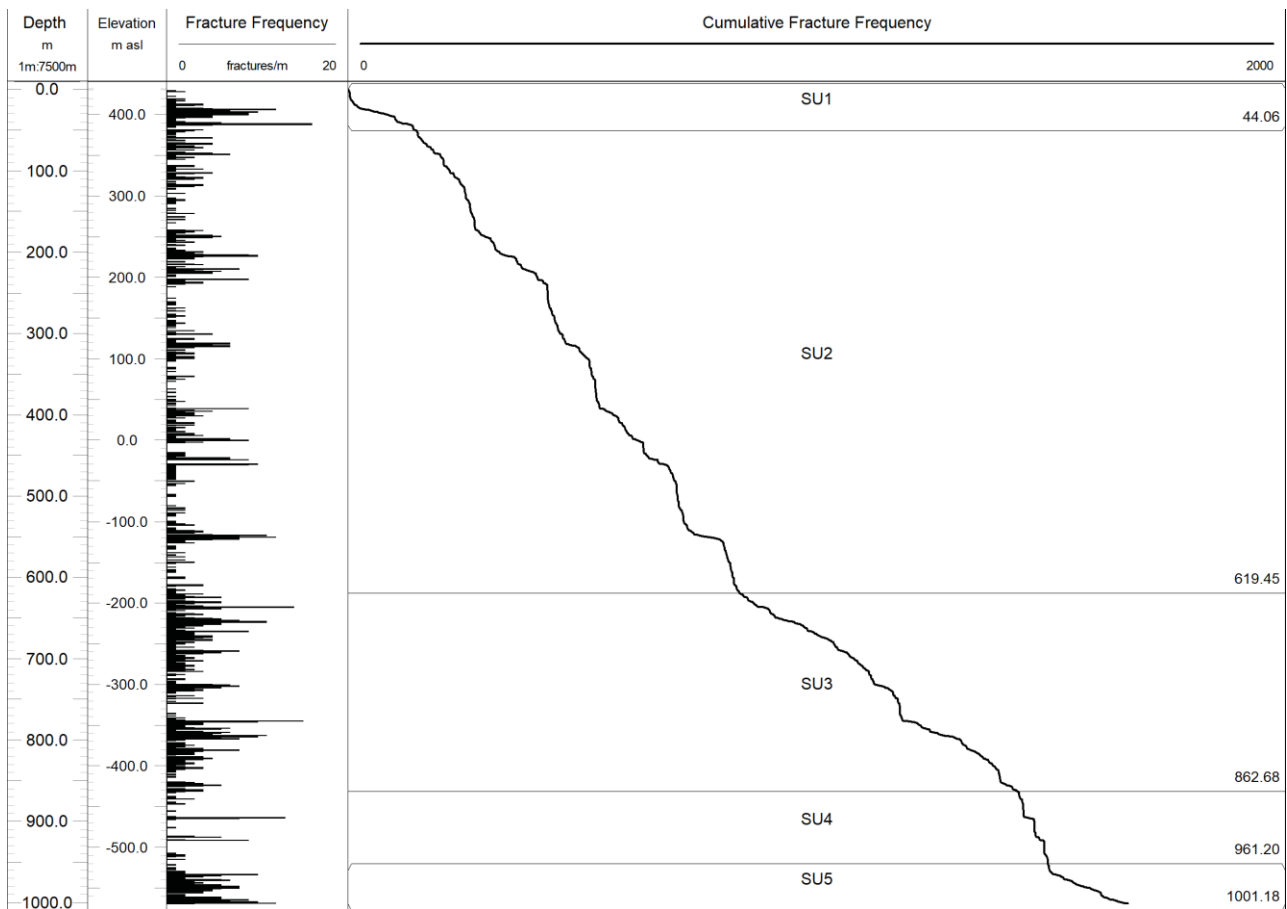


Figure 56: Per metre fracture frequency histogram (left) and cumulative fracture frequency curve (right) showing vertical distribution of all logged joints, faults, and veins along the borehole. The cumulative fracture frequency curve shows the changes in slope where boundaries in structural units (SU) are defined. Structural units and their top and bottom positions along borehole are labelled on the figure.

The final structural unit (SU5) is defined from 961.20 m to the bottom of the borehole at 1001.18 m (Figure 56). This unit has the highest average fracture frequency at 4.15 fractures per metre and displays a fairly uniform distribution within the interval. The change in the slope of the cumulative fracture frequency curve is well defined where interval is marked by a shallow slope characterized by a higher degree of fracturing of the bedrock. The fracture frequency is fairly consistent within the unit, ranging between 0 and 12 fractures per metre. There are 168 oriented fractures in SU5, including 144 joints and 4 veins (Appendix G). The distributions of the poles to these fractures overlap with Fracture Set 4b, and the more steeply inclined end of Fracture Set 1.

Table 10: Position ranges and standard statistics for fracture frequencies captured within the defined structural units (SU) within the borehole.

	<i>SU1</i>	<i>SU2</i>	<i>SU3</i>	<i>SU4</i>	<i>SU5</i>
<i>Position Range (m)</i>	0 – 44.06	44.06 – 619.45	619.45 – 862.68	862.68 – 961.20	961.20 – 1001.18
<i>Thickness (m)</i>	44.06	575.39	243.23	98.52	39.98
<i>Min (/m)</i>	0.00	0.00	0.00	0.00	0.00
<i>Max (/m)</i>	16.00	12.00	15.00	13.00	12.00
<i>Average (/m)</i>	3.11	1.21	2.43	0.74	4.15
<i>Standard Deviation (/m)</i>	3.56	1.89	2.51	1.93	2.98

As with the rock units defined previously, the criteria for defining the interpreted structural units for IG_BH01 may be modified once additional fracture data is collected in future boreholes. The framework presented here represents an interpretation based on general broad trends in the available data.

3.2.6 High Fracture Frequency Intervals (HFFI)

Along with the broad changes in fracture frequency that are used to define the SU's described above, additional more discrete intervals of increased fracture frequency were also identified in IG_BH01. These occurrences are referred to as high fracture frequency intervals (HFFI's) and are defined as a cluster of fractures (i.e., faults, joints and or veins) that exceeds a minimum relative fracture intensity threshold along a distinct borehole length (see below for details of IG_BH01). The spatial distribution of fractures and their intensity over the length of the borehole provide meaningful justification for defining HFFI's within the subsurface. Within the boreholes, the HFFI's are primarily dominated by fractures that share similar orientations within a single fracture set (i.e., fracture corridor) or by fractures in a range of orientations (i.e., fracture swarm), and locally may also include few minor ductile shear zones, though ductile structures were not included in the statistical analysis used to define the HFFI's. Fracture summaries presented in the previous sections provide details on fracture sets, fracture types, and fracture mineral infilling which may contribute to the characterization of the HFFI's. At the end of this section, an attempt is made to broadly correlate the identified HFFI's with lineaments trends that were interpreted based on remote sensing data on the ground surface in proximity to IG_BH01.

HFFI's were defined using a semi-automated approach applied to the borehole fracture frequency per metre log. To visualize contiguous zones of increased fracture intensity, the fracture frequency distribution was smoothed with a uniformly weighted moving average filter using the "uniform_filter1d" function from the SciPy processing package in Python (Virtanen et al. 2020). This filter is equivalent to a moving mean and is commonly applied to time-series data to smooth high-frequency data and enable detection of broader responses. This filter preserves the low-frequency components of the input data while high-frequency components are attenuated. The magnitude of the filter is defined by the uniform window size (w), which controls the degree of smoothing applied. In this study, a step size and window size of 1 m and 15 m, respectively, was defined.

The HFFI's are defined using the smoothed fracture frequency curve using two peak detection algorithms, "find_peaks" and "peak_widths" from the SciPy processing package (Virtanen et al. 2020). The peak detection algorithm finds all local maxima by simple comparison of neighboring values. A peak is defined as a local maximum where any sample whose two direct neighbours have a smaller amplitude. The difference in magnitude with the neighbouring values is defined by a threshold value in the algorithm, such as the peak prominence. The prominence of a peak measures the magnitude of the peak relative to the neighbouring values and is defined as the vertical distance between the peak and its lowest neighbouring value. Using the smoothed fracture frequency curve as input data, the peak prominence threshold was set at four for this study.

Once peaks are defined, the peak widths are based on the anomaly width at a specified distance between the peak maxima and the lowest neighbouring value (i.e., along the prominence height). In this study, a relative height of 0.5 is used at a threshold to extract the width of the peak.

Figure 57 presents the HFFI results from the fracture frequency data in IG_BH01. Based on the smoothed fracture frequency data and the peak detection analysis, position ranges and widths of five HFFI's have been defined. Figure 57 shows the cumulative counts of fractures along the length of the borehole and displays the fracture frequency per metre and the filtered fracture frequency. The cumulative curve, along with these data plots show evidence of discrete intervals of increased fracture intensity. Stick plots of joints, veins and faults display the location of each individual fracture type along the borehole length. A summary of the HFFI's for IG_BH01 are presented in

Table 11, including dominant fracture orientation(s), rock type(s) present, fracture set association, alteration, and fracture infill characteristics.

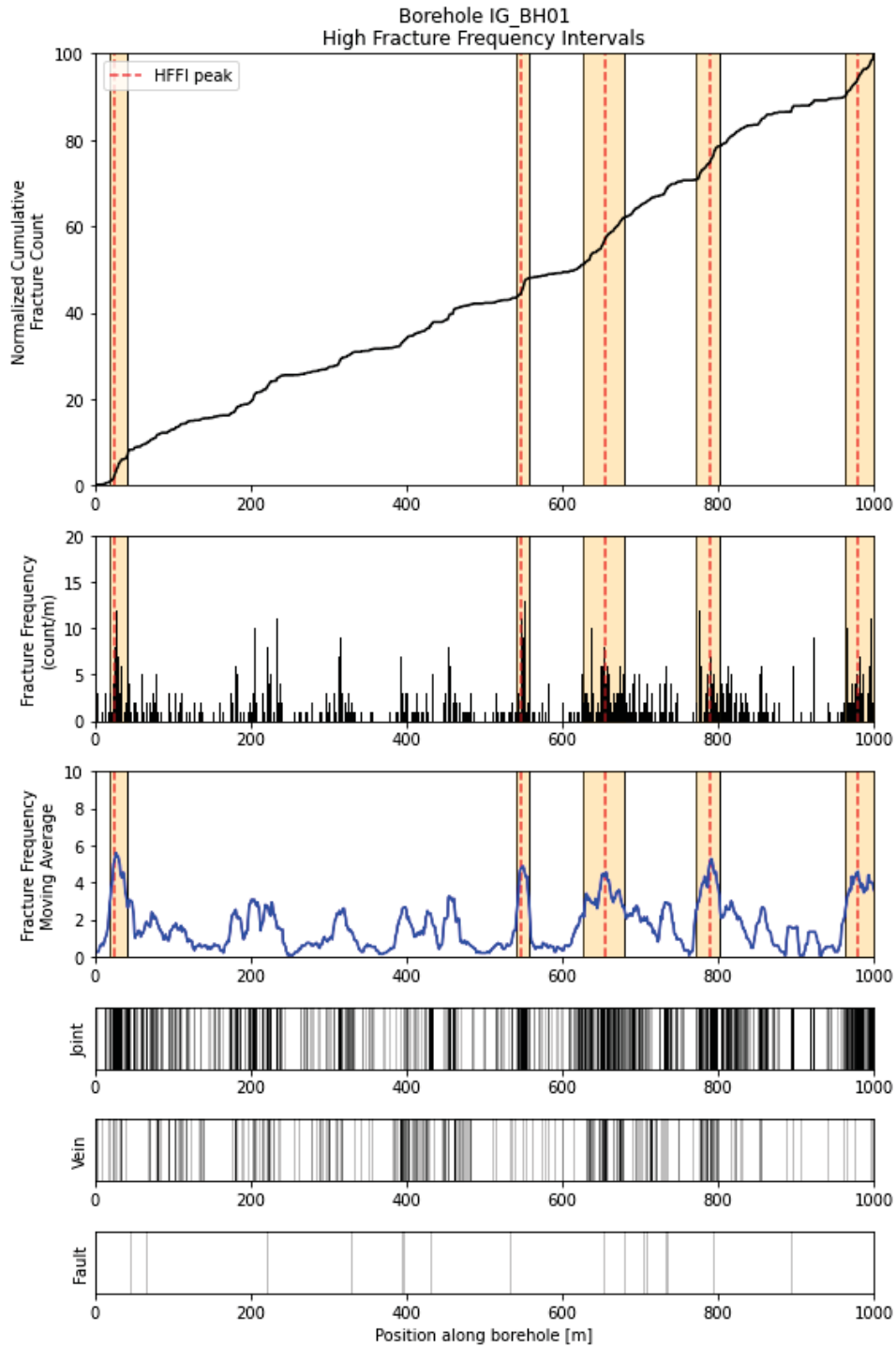


Figure 57. High fracture frequency intervals (HFFI) interpreted based on fracture intensity from borehole fracture frequency log. Five high fracture frequency intervals are outlined by their yellow bands. The red dashed line represents the peak location.

Although the results presented in Figure 57 are visually verified to be ideal candidates for HFFI interpretation, changing the peak detection algorithm input parameters can result in other possible HFFI outcomes. For example, reducing the peak prominence threshold or the applied window size in the smoothing function results in an increase in the number of peaks identified from the data. Conversely, increase these parameters reduces the number of peaks identified. Similarly, adjusting the peak height parameter used in the peak width algorithm works to either increase or decrease the width of the identified interval, however the peak location remains the same. Despite these possible uncertainties, the approach used here attempted to optimize the peak picking parameters through trial and error in order to visually match the identified peaks to the obvious increases in fracture frequency observed in the data. The application of this approach can then be applied to other boreholes, therefore reducing interpreter bias and subjectivity in the identification of HFFI's in the boreholes.

Table 11. High Fracture Frequency Intervals from IG_BH01

High Fracture Frequency Interval (HFFI)	Top Position (m)	Bottom Position (m)	Width (m)	Dominant Fracture Set Orientations* (major; minor (STR TYPE))	Rock Type, Alteration, Infill
IG_BH01_HFFI_1	18.00	40.67	22.67	128/75 (JN, VN); 165/41 (JN)	The entire interval is biotite granodiorite-tonalite with four intervals of hematization. Fracture sets are almost entirely defined by joints with only few veins. Chlorite, iron oxide, and quartz are the most common infill types. Quartz infill is logged in structures that define the dominant fracture orientation (128/75) while chlorite and iron oxide are logged in structures that define the minor fracture orientation (165/41).
IG_BH01_HFFI_2	541.00	557.27	16.27	008/13 (JN)	Biotite granodiorite-tonalite with one feldspar-phyric tonalite dyke. Hematization, silicification, and one interval of potassic alteration. Iron oxide, quartz, and chlorite are the most common infill types and all three are associated with fractures in the dominant orientation (008/13).
IG_BH01_HFFI_3	627.50	679.75	52.25	172/70 (JN, VN); 277/74 (VN, JN)	Biotite granodiorite-tonalite with one interval of biotite tonalite and four amphibolite intervals. Potassic alteration, silicification, chloritization, hematization, and sericitization are all logged. The amphibolite contacts dip gently toward the north-northwest and are not clustered with the major or minor fracture orientations identified. Quartz, epidote, and chlorite infill are logged in fractures in the main fracture orientation (172/70). Quartz, epidote, biotite, and iron oxide infill are logged in the fractures in the secondary fracture orientation (277/74). The most common infill types logged are quartz, calcite, epidote, chlorite, and iron oxides.
IG_BH01_HFFI_4	772.40	801.75	29.35	112/65 (JN, VN); 330/33 (JN, VN)	Biotite granodiorite-tonalite with one interval of biotite tonalite, one aplite dyke, four amphibolites, and three feldspar-phyric tonalite dykes. Potassic alteration, hematization, and one interval of silicification are logged. The contacts of the subordinate rock types broadly cluster with the minor fracture orientation (330/33). Quartz and chlorite infill are logged in fractures in the major and minor fracture orientations and are the most common logged infill types in the interval.
IG_BH01_HFFI_5	962.25	1001.18	38.93	359/52 (JN) 324/45 (JN)	Biotite granodiorite-tonalite with three intervals of amphibolite. Hematization is the dominant alteration type logged, with minor potassic alteration and chloritization. Two of the amphibolites have contacts oriented with the major fracture orientations (dipping moderately towards the north-northwest) and the third is sub-vertical, dipping towards the southwest. Quartz is the dominant logged infill type by far, followed by iron oxide, chlorite, and a few occurrences of epidote.

*DipDirection/Dip convention

For each HFFI, fracture (including joints, veins, and faults) orientations are plotted on stereonet to further evaluate the orientation distributions and define one or more orientations that are characteristic of the interval (e.g., HFFI_1 in Figure 58, see Appendix H: for stereonet of all defined HFFI's). Figure 58 presents a Terzaghi-weighted stereonet for HFFI_1 containing 94 fractures (joints and veins). Dominant orientations in Table 11 are interpreted manually as the peaks defined by the Terzaghi-weighted pole density maxima. The resulting fracture orientations from within the HFFI's can provide input into modelling such zones as surfaces in deterministic fracture network models.

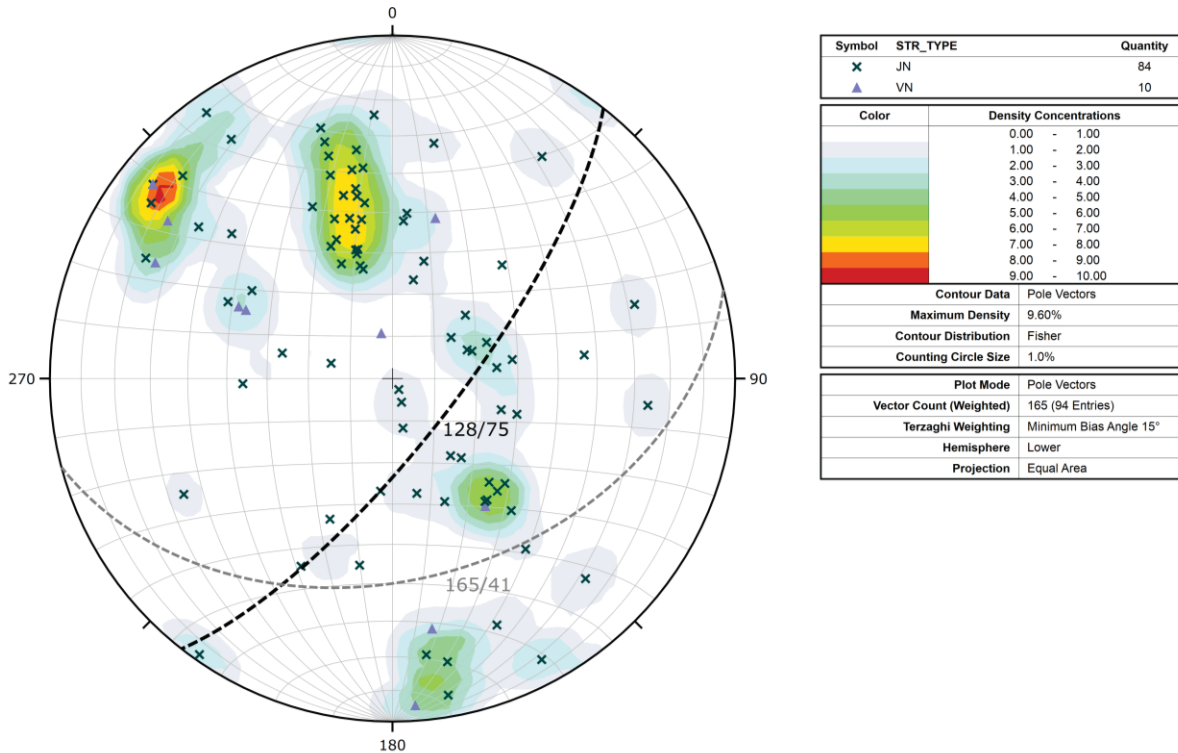


Figure 58. Terzaghi-weighted stereonet plot of fractures (JN, VN, FLT) within high fracture frequency interval 1 (HFFI_1) from 18.0 – 40.67 m. Two peaks are defined, a major peak with a mean orientation of 128/75 and a minor peak with a mean orientation of 165/41 (DipDirection/Dip).

HFFI_1 (18.00 – 40.67 m)

HFFI_1 is entirely composed of biotite granodiorite-tonalite. There are visible, pink-coloured alteration halos (logged as hematization) around fractures (Figure 59). The fractures in this interval are predominantly joints and two peaks are defined: a major peak (based on Terzaghi weighting) that dips steeply southeast (128/75) and a minor peak that dips moderately south-southeast (165/41). The intersection of these relatively steep joints with the moderately dipping joints creates intervals of broken core and appear to localize the alteration (Figure 59). Quartz infill is logged in association with the steeply-dipping fractures while chlorite and iron oxide, which are the most common infill types in this interval, are logged in association with the moderately-dipping minor fracture peak.



Figure 59. Core from an interval of HFFI_1 (23.98 – 35.55 m). Biotite granodiorite-tonalite with intersecting shallowly- and steeply-dipping fractures creating sections of broken core. The area of increased fracture frequency at the top of the interval is associated with visible, pink-coloured alteration, logged as hematization.

HFFI_2 (541.00 – 557.27 m)

HFFI_2 is predominantly biotite granodiorite-tonalite with one feldspar-phyric tonalite dyke that is 0.86 m thick. Logged alteration is mainly hematization with minor silicification and potassic alteration. The fractures in this interval are fairly well spaced and are mainly subhorizontal or gently inclined and dipping north (008/13). Alteration is associated with the fractures and the feldspar-phyric tonalite dyke, which can be seen in Figure 60. The contacts of the dyke are also gently inclined and dipping north, clustered with the fracture peak in this interval (see Appendix H:). Three shear zones are logged in HFFI_2, two are oriented with the main fracture peak and one is moderately inclined and dips southwest. The dominant fracture infill type logged is iron oxide, with minor quartz and chlorite. All three infill types are logged in association with fractures in the main orientation peak.



Figure 60. Core from an interval of HFFI_2 (547.24 – 558.90 m). Biotite granodiorite-tonalite with one feldspar-phryic tonalite dyke at 548.47 m. Silicification is logged around the dyke and is visible in the photo as darker grey patches. Fractures are subhorizontal and fairly well spaced.

HFFI_3 (627.50 – 679.75 m)

HFFI_3 is biotite granodiorite-tonalite with one interval of biotite tonalite and four amphibolite occurrences with top contacts at 653.71 m, 654.4 m, 657.4 m, and 679.05 m along the borehole and a total length of 5.04 m. Alteration in this interval is dominantly potassic with chloritization, silicification, sericitization and one instance of hematization. Alteration is mainly associated with the amphibolite (Figure 61). All of the amphibolite contacts are gently inclined and dip north-northwest, which is not identified as a fracture peak due to the spread in orientations. However, many of the joints, veins, and the only two faults logged in the interval are also gently inclined and dip north-northwest (see Appendix H:). There are seven shear zones in this HFFI, four are gently inclined and dip north-northwest, one is oriented with the minor fracture peak (277/74) and the other two are steeply inclined and not associated with an identified peak. The most common infill types in HFFI_3 are quartz, calcite, epidote, chlorite, and iron oxide. There are no specific infill types associated with the major and minor fracture peaks in this interval; there is one instance of soft gouge logged in association with a joint in amphibolite at 654.22 m, and it is gently inclined and dips north-northwest, aligned with the amphibolite contacts.

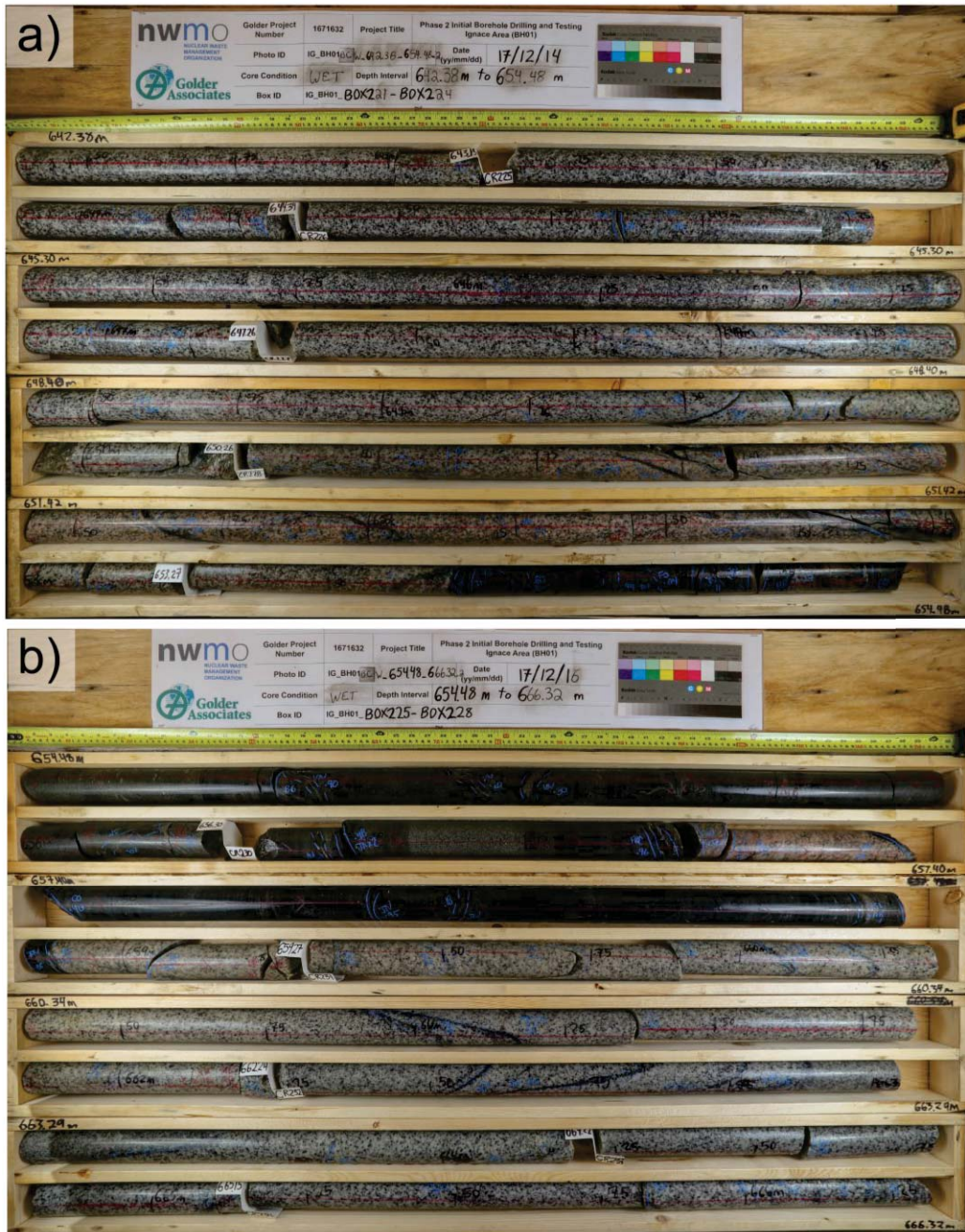


Figure 61. Core from an interval of HFFI_3 (a: 642.38 – 654.48 m; b: 654.48 – 666.32 m). Biotite granodiorite-tonalite with visible pink and white alteration associated with the amphibolite occurrences (a & b). The amphibolite contacts and structures associated with the amphibolites (shear, some joints, etc.) are gently inclined. The two fracture peaks identified in the interval are both steeply inclined, one dipping south and the other dipping west. These fractures are visible especially in (a) and where they intersect the shallower structures the core is visibly broken up.

HFFI_4 (772.40 – 801.75 m)

HFFI_4 starts in biotite granodiorite-tonalite and has three feldspar-phyric tonalite dykes near the top of the interval at 775.69, 776.44, and 778.35 m, along the borehole and totaling 1.05 m in length. Deeper in the interval there are three amphibolite units at 792.82, 795.53, and 797.43 m

along the borehole and totaling 0.88 m in length (Figure 62). Alteration in HFFI_4 is predominantly logged as potassic with two intervals of hematization and one of silicification. The main fracture peak is steeply inclined, dips east-southeast and is defined mainly by joints. The minor fracture peak, defined by veins and joints, has a greater spread in orientations but is generally gently inclined and dips northwest (see Appendix H:). Most of the contacts of the subordinate rock types are clustered with the gently inclined minor fracture peak that dips northwest. There are 25 shear zones logged in HFFI_4 and all of them are gently inclined and dip northwest, associated with the amphibolite contacts and the minor fracture peak. The most common secondary infills logged in this interval are quartz and chlorite. There are two instances of soft gouge, one logged in associated with a joint in amphibolite at 792.83 m and the other associated with the upper contact of an amphibolite at 795.53 m. Both are gently inclined and dip north-northwest, approximately coincident with the minor fracture peak orientation.

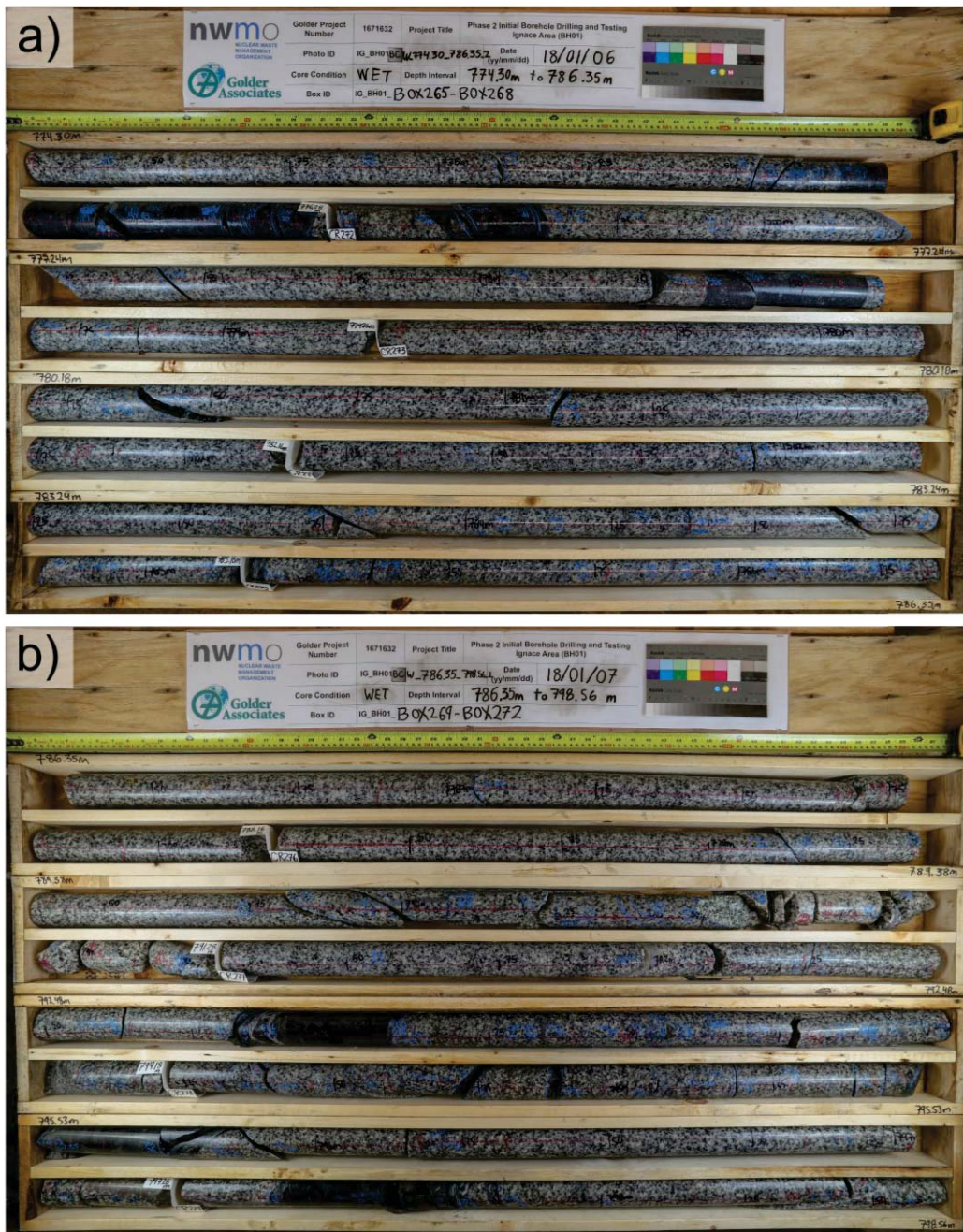


Figure 62. Core from an interval of HFFI_4 (a: 774.30 – 786.50 m; b: 786.35 – 798.56 m). Small feldspar-phyric tonalite dykes and amphibolite are visible. The fractures are well spaced, with a slight increase around the subordinate rock types.

HFFI_5 (962.25 – 1001.18 m)

The last high fracture frequency interval (HFFI_5) encompasses the end of the borehole and is biotite granodiorite-tonalite with three amphibolites totaling 3.35 m in length with top contacts at 967.85, 978.76, and 998.82 m along the borehole, respectively. There are two dominant fracture peaks in this interval, the peaks overlap but there are distinct maxima that dip moderately towards the north and northwest (see Appendix H:). The peaks are almost entirely defined by joints. Contacts of the lower two amphibolites are gently inclined and dip north-northwest, coincident with

the main fracture peaks, and. The upper amphibolite (967.85 m) is sub-vertical, dipping towards the southwest (Figure 63). Four shear intervals are logged in HFFI_5, two are oriented with the main fracture peaks dipping north-northwest and two are associated with the upper amphibolite, steeply dipping southwest. Quartz is the dominant infill type in this interval by far, followed by iron oxide, chlorite, and a few occurrences of epidote. Soft gouge is logged in three structures, all joints, one in an amphibolite and the other two in biotite granodiorite-tonalite. Two occurrences of soft gouge and oriented with the main fracture peaks; the third (and deepest) occurrence is moderately dipping south-southwest not associated with any fracture cluster.



Figure 63. Core from HFFI_5 (965.21 – 976.73 m). Biotite granodiorite-tonalite at the top of the interval and the first amphibolite occurrence, with sub-vertical contacts dipping towards the southwest. Increasing fracture and alteration (logged as potassic) intensity approaching the amphibolite, returning to well-spaced fractures in the unaltered biotite granodiorite-tonalite.

Comparison of Fracture Orientations to Local Lineament Network

Fracture orientations in the borehole display some correlation to the dominant trend of nearby lineaments that were interpreted using remote sensing data (DesRoches et al., 2018). Figure 64 displays the interpreted structural lineaments in proximity to IG_BH01. Northeast and north-northwest trends are most prominent in the rose diagram of lineament orientations (Figure 65). The north-northwest trend exhibits a broad but well-defined peak characterized predominantly by narrow and short lineaments visible on Figure 64. To the northeast of the surface collar location of IG_BH01 a set of north-northwest trending lineaments occur which are characterized by a maximum trace length of approximately 4 km. The northeast trending lineaments are mainly characterized by shorter trace lengths, with the exception of one longer lineament to the northwest of the IG_BH01 collar location, which has a trace length greater than 8 km.

Rose diagrams for both unweighted and Terzaghi-weighted borehole-logged fractures, with a minimum dip angle of 45°, display some similarities to the lineament trends (Figure 66). The unweighted fractures show main peaks trending northwest, north-northeast, and east-northeast, as

well as a subordinate northerly trend. The applied Terzaghi-weighting tends to increase the intensity of northwest, north, and north-northeast, trends and slightly decrease the presence of the east-northeast trend. Notwithstanding the broad spread in fracture orientations, the northwest trending and north to east-northeast trending peaks in the borehole data are visible in the lineament traces near IG_BH01.

Comparing the lineament trends in proximity to IG_BH01 with those of the interpreted fracture sets, and main structural orientations in the HFFI's, highlights further the similarity in orientations. The northeast trending lineaments are generally consistent with the strike of Fracture Set 3 and the dominant structural orientation in HFFI 1, and slightly oblique to Fracture Set 2 and the dominant structural orientation in HFFI 4. The north-northwest trending lineaments are slightly oblique to the northwest trend of Fracture Set 4, and one peak orientation of shear zones. The east-trending lineament also overlaps the cluster of poles defining Fracture Set 2. All of these borehole-interpreted fracture sets, and the shear zones, are subvertical to steeply inclined, except for Fracture Set 2, which is moderately inclined.

It is worth noting that the northeast trending lineaments parallel the dominant direction of glacial advance and retreat across the region. It is uncertain therefore whether all northeast trending interpreted lineaments reflect structurally significant features of the bedrock or if some are instead a product of glacial erosion. However, the understanding that the steeply inclined and northeast striking Fracture Set 3b is present along the length of the borehole suggests that at least some of these lineaments do represent real bedrock structures.

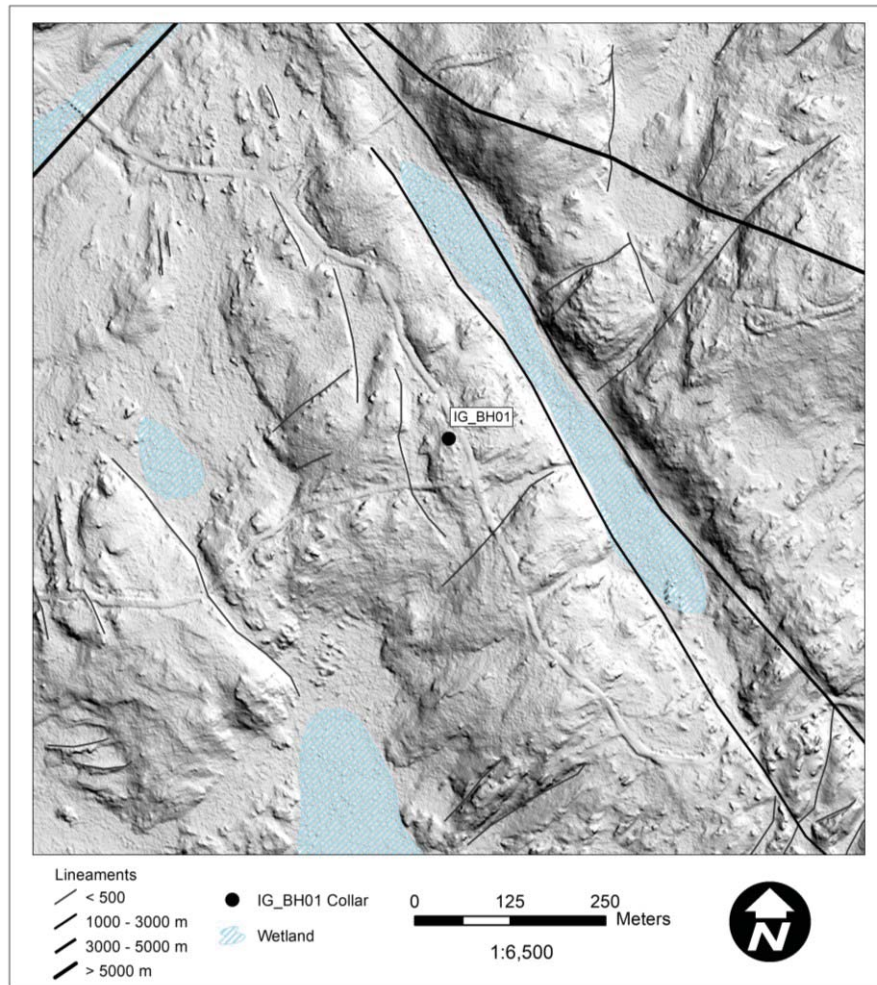


Figure 64: Lineament traces near IG_BH01 interpreted from LiDAR DEM and airborne geophysics data (DesRoches et al., 2018). Lineament traces dominantly trend north-northwest with some shorter lineaments trending northeast. Note that the heavy black line near the upper right corner of the image is a Wabigoon dyke.

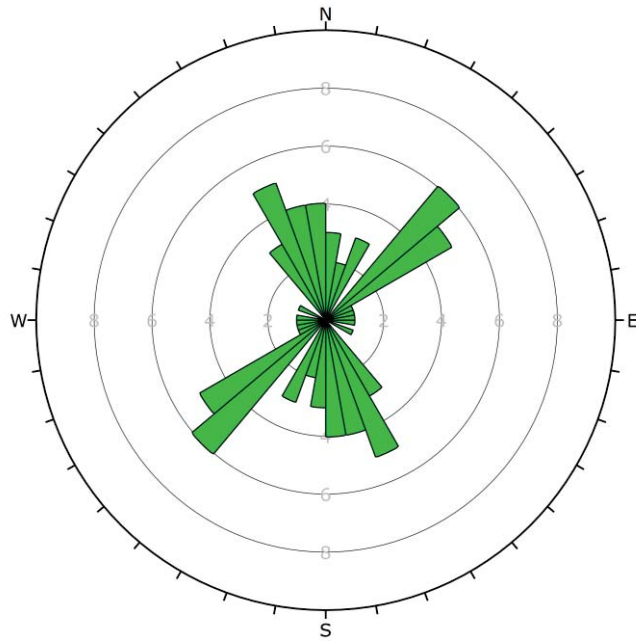


Figure 65: Rose diagram of the lineaments ($N = 40$) around IG_BH01 (see Figure 64) interpreted from LiDAR DEM and airborne geophysics data (DesRoches et al., 2018). Lineament orientations are plotted using a bin size of 10 degrees.

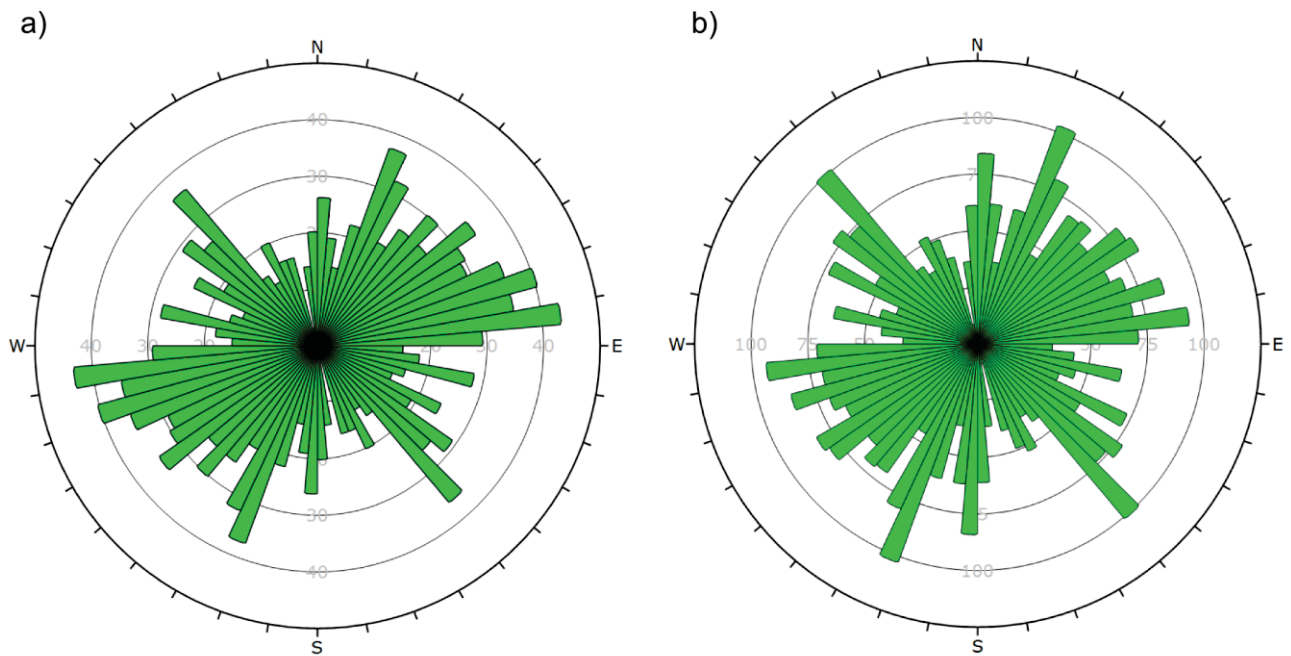


Figure 66. Rose diagrams of the borehole logged fracture orientations using a minimum dip angle of 45 degrees, and bin size of 5 degrees. a) Unweighted ($N = 1604$); b) Terzaghi-weighted to account for directional bias of the borehole path (weighted $N = 3056$).

4 SUMMARY OF FINDINGS AND UNCERTAINTIES

4.1 Findings

The geological findings are based on the geological information available to date, which are summarized in this report. One primary consideration is the understanding that the available information *is from a single, near-vertical, borehole*. Whether or not the characteristics of the bedrock interpreted in this report will be representative of characteristics in other boreholes remains uncertain. However, the level of uncertainty related to the overall understanding of the bedrock across the study area will decrease as information from multiple boreholes is acquired and integrated together. A simplified summary of the geological model for IG_BH01 is presented below showing the final lithology log, rock units, per metre fracture frequency and structural units (Figure 67).

The bedrock intersected by IG_BH01 is homogeneous and dominated by a medium-grained rock of tonalitic to granodioritic composition, representing a total of 97.8 % of the recovered core. Optical and acoustic televiewer, natural and spectral gamma, gamma-gamma density and neutron geophysical logs provided additional evidence to distinguish subordinate rock types from the main rock types in this crystalline rock environment. The integration of visual geological core logging and geophysical logging was useful for developing the final interpretation of lithology and alteration and was critical for assigning true orientations to the logged structures.

The lithochemical and petrographic datasets provided mineral and rock chemistry information used to distinguish subtle variations between the felsic igneous rocks encountered in the borehole. Some of these distinctions were not evident based on the geological and geophysical core logging alone. The majority of the felsic igneous rocks encountered share a similar mineralogy, ranging in composition between tonalite and granodiorite, except for a suite of aplitic dykes of more granitic composition and some quartz dykes.

Amphibolite was the most common subordinate rock type identified during borehole drilling. Amphibolite occurrences were predominantly observed within the lower half of the borehole as narrow (m-scale) units. Contact orientations for the amphibolites within this zone are gently to moderately dipping towards the north-northwest. The distinct character and orientation of the amphibolite units suggests that such a zone may be traceable to other boreholes.

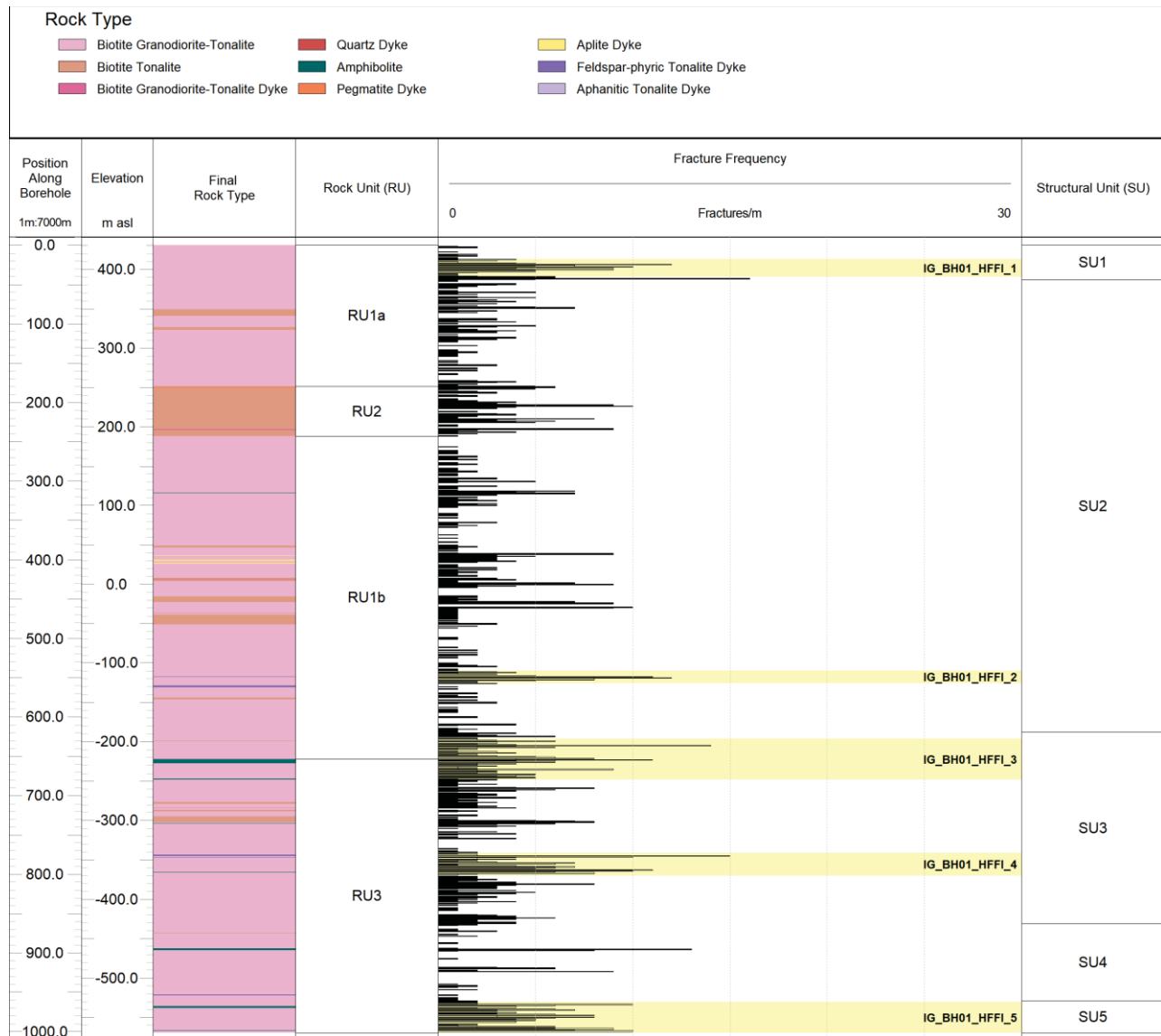


Figure 67: Summary log of geological information for IG_BH01, including (from left to right), final log of lithology, classification of rock units, per metre fracture frequency, and structural units, representing the 1-dimensional geological model for IG_BH01.

Overall, the degree of alteration of the bedrock intersected by IG_BH01 appears to be low. Six alteration types (potassic, chloritization, hematization, sericitization, silicification, and bleaching) were identified during geological and geophysical logging. The majority of logged alteration was identified below 400 m along borehole, with the exception of hematization/iron staining which occurs locally along the entire length of the borehole with increased presence at the top and bottom. Petrographic analysis highlighted a common, but weak sericitization of plagioclase that was not evident from the geological core logging.

Based on broad changes in lithology along the length of the borehole four rock units were defined. The weak intensity of the alteration was not considered to be a useful characteristic for distinguishing the rock units. The majority of the borehole has a massive texture, with some

subordinate rock types dominantly hosting ductile fabric (foliation and shear zones). The presence or absence of ductile fabric was not considered to be a useful characteristic for defining rock units.

The structures identified in the borehole included features associated with ductile and brittle deformation processes. Shear zones exhibit characteristics of both brittle and ductile deformation processes, including the local presence of fractures, primarily in association with amphibolite occurrences. Shear zones are predominantly gently dipping towards the north-northwest, and only slightly shallower dipping than the amphibolite contacts. An associated foliation, defined by biotite, is predominantly weak and steeply dipping in a similar direction as the shear zones. The majority of the identified occurrences of ductile structures, including foliation and shear zones, are below 400 m along borehole.

The complete fracture dataset appears to indicate the presence of four fracture sets:

- a gently to moderately inclined north to northwest-dipping set (Set 1);
- a moderately inclined south-southeast-dipping set (Set 2); and
- two sub-vertical sets, one trending north-north-easterly with subsets dipping towards the west-northwest (Set 3a) and southeast (Set 3b) and one trending northwesterly with subsets dipping towards the northeast (Set 4a) and southwest (4b). These sub-vertical sets and defined subsets require corroboration from future boreholes to verify their relationship.

Joints are overwhelmingly the most common fracture type identified in the borehole, followed by veins and faults. Faults are consistently very narrow, identified mainly by the presence of slickenlines, and exhibit only slight evidence of damage in the rock surrounding the fault plane. Set 1 fractures overlap in orientation with the shear zones.

Overall, the dataset of planes and lineations, though small, provides good indication that dip-slip motion predominates on gently to moderately inclined northwest to north dipping planes and nearly-transcurrent motion predominates on steeply inclined planes. Structures identified as faults and shear zones during geological core logging generally exhibit a similar history of motion, most prominently in a northwest-southeast direction. It is unknown at this point what the shortening and extension directions were, and whether the observed planes and lineations formed contemporaneously under the same stress regime or at different times under different orientations of applied stress. Future boreholes and surface mapping campaigns will attempt to clarify these outstanding questions.

The borehole was subdivided into five structural units based on variation in fracture frequency log and slope of the cumulative fracture frequency curve. The subdivision resulted in average fracture frequencies for the structural units ranging between 0.7 and 4.2 fractures per metre.

Five high fracture frequency intervals (HFFI's) were defined along the borehole using a semi-automated approach applied to the borehole fracture frequency per metre log. The intervals range in width from just over 16 m to just over 52 m. One HFFI was identified at around 30 m along the borehole, with the additional four HFFI's all occurring in the lower half of the borehole around 550 m, 650 m, 785 m, and 980 m. All HFFI's, except the one at 30 m, include at least one subordinate rock type occurrence other than biotite granodiorite-tonalite. The most common subordinate rock types represented are the aphanitic or feldspar-phyric tonalite dykes, and amphibolite.

Logged structures, defined fracture sets, and HFFI's, in the borehole display some correlation to the dominant lineament trends in proximity to the borehole. The northeast trending lineaments are generally consistent with the strike of Fracture Set 3 and the dominant structural orientation in HFFI 1, and slightly oblique to Fracture Set 2 and the dominant structural orientation in HFFI 4. The north-northwest trending lineaments are slightly oblique to the northwest trend of Fracture Set 4, and one peak orientation of shear zones. The east-trending lineament also overlaps the cluster of

poles defining Fracture Set 2. All of these borehole-interpreted fracture sets, and the shear zones, are subvertical to steeply inclined, except for Fracture Set 2, which is moderately inclined.

Considering all of the geological observations described throughout the report, several key summary points are highlighted below. These observations align with a developing understanding that the region below approximately 600 to 650 m along borehole has a different character than the rock above it, including that:

- there is a cluster of shear zones and foliation between approximately 650 and 800 m,
- there is a cluster of veins between approximately 650 and 800 m,
- there is a cluster of faults between approximately 650 and 750 m,
- hydrothermal alteration is most prevalent below approximately 600 m, and
- amphibolite, which occurs primarily below 650 m, shows evidence of ductile strain and brittle deformation internally and along its contacts, as well as evidence of hematization and chloritization.

This 650 m and deeper bedrock interval is distinguished in the rock unit and structural unit zonation models as RU3 and SU3-SU4-SU5, respectively. From a lithological point of view, RU3 exhibits the highest degree of lithological heterogeneity when compared with the rock types observed in the other rock units interpreted in IG_BH01. However, the apparent relative heterogeneity must be weighed against the understanding that overall, the bedrock encountered in IG_BH01 is relatively homogeneous. From a structural point of view, these observations suggest that there is localization of ductile strain and brittle deformation in this deep bedrock zone. This increased structural complexity is commonly, but not solely, observed proximal to amphibolite occurrences and indicates some fluid flow in the geological history was focused along these lithological discontinuities.

The significance of this deep bedrock zone, and the other geological relationships identified here, will continue to be explored as additional information is gathered from future surface and subsurface investigations, including the drilling of additional boreholes and two-dimensional and vertical seismic profiling.

4.2 Uncertainties

With subsurface information available from only one borehole, many geological uncertainties remain. With respect to lithology, key uncertainties include whether the biotite tonalite rock is a distinct and mappable rock type beyond IG_BH01, or if it simply represents a local compositional variation of an otherwise homogenous granodioritic to tonalitic bedrock. In addition, the nature of the amphibolite occurrences is still unclear. Are these deformed mafic dykes or vestiges of greenstone belt material? Contact relationships are unclear due to localization of strain at the amphibolite margins, and lithogeochemistry results are so far inconclusive. The distribution of the amphibolite and the other subordinate rock types in three-dimensions beyond IG_BH01 is also a remaining uncertainty.

With respect to structure, a Terzaghi-weighting was applied to correct for borehole orientation bias. It is understood that there are other techniques available. Further exploration of the best approach to account for the borehole orientation bias will be investigated as additional data becomes available, including data from differently oriented angled boreholes. Whether or not the drilling activity itself, or stress relief, may have induced the broken character of logged fractures remains an uncertainty. The true nature of logged televiewer-only and core-only structures also remains uncertain. There is additional uncertainty in distribution of fracture lengths, as well as the density and mean orientation of steeply dipping structures. There is also uncertainty as to whether the steeply-dipping and NE and NW striking fractures, sets 3a and 3b and sets 4a and 4b, respectively, represent shallower dipping members of under-represented sub-vertical to vertical fracture sets. In

particular, sets 3a and 3b are not exactly parallel in strike suggesting that they may not represent one single fracture set. In addition, the timing and number of stages of fracture development (and re-activation), mineral infilling and alteration, and the resulting implications for the geological history of the area remain uncertain.

The subset of identified fractures that are likely to be hydraulically conductive also remains uncertain. This is especially important in understanding the significance of logged geological apertures. As mentioned above, geological apertures are estimated values only because there are multiple possible sources of uncertainty in how a reported aperture value relates to the true aperture of a fracture identified as broken. There are uncertainties related to measurement inaccuracy, including where the opening is very small, where the opposing fracture planes are not parallel or fit poorly together, or due to limits in televiewer resolution. In addition, effects due to drilling or decompression may create or enhance the visible open space identified as aperture. Finally, aperture measured in core or on a borehole wall is only a local aperture that is not necessarily representative over the entire fracture length. There are also cases where fractures are logged as broken but exhibit no measurable geological aperture. Additional analysis of the observed structures in the acoustic and optical televiewer datasets, including fractures and their characteristics (e.g., broken vs intact nature, mineral infilling, orientation), will aim to reduce these uncertainties.

Finally, the absolute dimensions of the rock units and structural units presented above were defined based on a subjective and non-unique approach. With the same data inputs, alternative approaches may have defined more or less units and ultimately produced a different geological model for the borehole. A statistically robust method was used to define high fracture frequency intervals along the borehole. However, the approach is still non-unique. Different analytical approaches may produce a different result. Furthermore, the broader geological significance of these intervals, identified along a single borehole, remains uncertain.

5 REFERENCES

- American Petroleum Institute (API), 1985. Directional Drilling Survey Calculation Methods and Terminology (Bulletin No. D20). Dallas, TX.
- Blackburn, C.E., Hinz, P., 1996. Kenora Resident Geologist's District (Open File Report No. 5958), Report of Activities 1996, Resident Geologists. Ontario Geological Survey.
- Brown, A., Soonawala, N.M., Everitt, R.A., Kamineni, D.C., 1989. Geology and geophysics of the Underground Research Laboratory site, Lac du Bonnet batholith, Manitoba. *Canadian Journal of Earth Sciences* 26, 404–425.
- Daniels, J.J., Olhoeft, G.R., Scott, J.H., 1984. Interpretation of core and well log physical property data from drill hole UPH-3, Stephenson County, Illinois (USGS Numbered Series No. 82–941). United States Geological Survey.
- Davy, P., Darcel, C., Bour, O., Munier, R., De Dreuzy, J.-R., 2006. A note on the angular correction applied to fracture intensity profiles along drill core. *Journal of Geophysical Research: Solid Earth* 111, B11408. <https://doi.org/10.1029/2005JB004121>
- DesRoches, A., Sykes, M., Parmenter, A., Sykes, E., 2018. Lineament Interpretation of the Revell Batholith and Surrounding Greenstone Belts (No. NWMO-TR-2018-19). Nuclear Waste Management Organization.
- Debon, F., Le Fort, P., 1983. A chemical and mineralogical classification of common plutonic rocks and associations. *Earth and Environmental Science Transactions of the Royal Society of Edinburgh* 73, 135–149.
- Glazner, A.F., Bartley, J.M., Coleman, D.S., 2019. A More Informative Way to Name Plutonic Rocks. *GSA Today* 29. <https://doi.org/10.1130/GSATG384A.1>
- Golder Associates Ltd., 2013. Phase 1 Geoscientific Desktop Preliminary Assessment of Potential Suitability for Siting a Deep Geological Repository for Canada's Used Nuclear Fuel: Township of Ignace, Ontario (No. APM-REP-06144-0011). Nuclear Waste Management Organization.
- Golder Associates Ltd., 2015. Phase 2 Geoscientific Preliminary Assessment, Findings from Initial Field Studies: Township of Ignace, Ontario (No. APM-REP-06145-0001). Nuclear Waste Management Organization.
- Golder Associates Ltd., 2017. Phase 2 Initial Borehole Drilling and Testing, Ignace Area: Initial Borehole Characterization Plan for IG_BH01 (No. APM-PLAN-01332-0242). Nuclear Waste Management Organization.
- Golder Associates Ltd., 2018a. Phase 2 Initial Borehole Drilling and Testing, Ignace Area: WP4B Data Report - Geomechanical Testing of Core for IG_BH01 (No. APM-REP-01332-0232). Nuclear Waste Management Organization.
- Golder Associates Ltd., 2018b. Phase 2 Initial Borehole Drilling and Testing, Ignace Area: WP2 Data Report - Borehole Drilling and Coring for IG_BH01 (No. APM-REP-01332-0229). Nuclear Waste Management Organization.
- Golder Associates Ltd., 2018c. Phase 2 Initial Borehole Drilling and Testing, Ignace Area: WP3 Data Report - Geological and Geotechnical Core Logging, Photography and Sampling for IG_BH01 (No. APM-REP-01332-0230). Nuclear Waste Management Organization.
- Golder Associates Ltd., 2018d. Phase 2 Initial Borehole Drilling and Testing, Ignace Area. WP7 Data Report - Opportunistic Groundwater Sampling for IG_BH01 (No. APM-REP-01332-0236). Nuclear Waste Management Organization.
- Golder Associates Ltd., 2019a. Phase 2 Initial Borehole Drilling and Testing, Ignace Area: WP5 Data Report - Geophysical Well Logging for IG_BH01 (No. APM-REP-01332-0234).

- Golder Associates Ltd., 2019b. Phase 2 Initial Borehole Drilling and Testing, Ignace Area: WP4C Data Report - Porewater Extraction and Analysis and Petrographic Analysis for IG_BH01 (No. APM-REP-01332-0233). Nuclear Waste Management Organization.
- Golder Associates Ltd., 2019c. Phase 2 Initial Borehole Drilling and Testing, Ignace Area. WP6 Data Report – Hydraulic Testing for IG_BH01 (No. APM-REP-01332-0235). Nuclear Waste Management Organization.
- Golder Associates Ltd., 2019d. Phase 2 Initial Borehole Drilling and Testing, Ignace Area. WP9 Data Report – Westbay MP38 Casing Completion for IG_BH01 (No. APM-REP-01332-0237). Nuclear Waste Management Organization.
- Golder Associates Ltd., 2020a. Phase 2 Initial Borehole Drilling and Testing, Ignace Area. WP4a Data Report – Petrophysical Testing of Core for IG_BH01 (No. APM-REP-01332-0231). Nuclear Waste Management Organization.
- Golder Associates Ltd., Paterson Grant and Watson, Ltd., 2017. Phase 2 Geoscientific Preliminary Assessment: Geological Mapping, Township of Ignace and Area, Ontario (No. APM-REP-01332-0225). Nuclear Waste Management Organization.
- Halla, J., 2018. Highlights on Geochemical Changes in Archaean Granitoids and Their Implications for Early Earth Geodynamics. *Geosciences* 8, 353. <https://doi.org/10.3390/geosciences8090353>
- Halla, J., van Hunen, J., Heilimo, E., Hölttä, P., 2009. Geochemical and numerical constraints on Neoproterozoic plate tectonics. *Precambrian Research* 174, 155–162. <https://doi.org/10.1016/j.precamres.2009.07.008>
- Irvine, T.N., Baragar, W.R.A., 1971. A Guide to the Chemical Classification of the Common Volcanic Rocks. *Can. J. Earth Sci.* 8, 523–548. <https://doi.org/10.1139/e71-055>
- Jensen, L.S., 1976. A new cation plot for classifying subalkalic volcanic rocks (Misc. Paper No. 66). Ontario Division of Mines.
- Jensen, L.S., Pyke, D.R., 1982. Komatiites in the Ontario Portion of the Abitibi belt, in: *Komatiites*. George Allen and Unwin, London, pp. 147–157.
- Keys, W.S., 1997. *A Practical Guide to Borehole Geophysics in Environmental Investigations*. CRC Press.
- Kuno, H., 1968. Differentiation of basalt magmas, in: *Poldervaart Treatise on Rocks of Basaltic Composition*. pp. 623–688.
- Le Bas, M.J., Streckeisen, A.L., 1991. The IUGS systematics of igneous rocks. *Journal of the Geological Society* 148, 825–833. <https://doi.org/10.1144/gsjgs.148.5.0825>
- Parmenter, A., Waffle, L., DesRoches, A. 2020. Bedrock geology of the Revell batholith and surrounding greenstone belts (No. NWMO-TR-2020-08). Nuclear Waste Management Organization.
- Sander Geophysics Limited (SGL), 2015. Phase 2 Geoscientific Preliminary Assessment, Acquisition, Processing and Interpretation of High-Resolution Airborne Geophysical Data (No. APM-REP-06145-0002). Nuclear Waste Management Organization.
- SRK Consulting, Inc., Golder Associates Ltd., 2015. Phase 2 Geoscientific Preliminary Assessment, Observation of General Geological Features, Township of Ignace, Ontario (No. APM-REP-06145-0004). Nuclear Waste Management Organization.
- Stone, D., 2010a. Geology of the Stormy Lake Area, Northwestern Ontario, Project Unit 09-003 (Open File Report No. 6260), Summary of Field Work and Other Activities 2010. Ontario Geological Survey, Sudbury, Canada.
- Stone, D., 2010b. Precambrian geology of the central Wabigoon Subprovince area, northwestern Ontario (Open File Report No. 5422). Ontario Geological Survey.
- Stone, D., 2009. Geology of the Bending Lake Area, Northwestern Ontario (Open File Report No. 6240), Summary of Field Work and Other Activities 2009. Ontario Geological Survey, Sudbury, Canada.

- Stone, D., Davis, D.W., Hamilton, M.A., Falcon, A., 2010. Interpretation of 2009 Geochronology in the Central Wabigoon Subprovince and Bending Lake Areas, Northwestern Ontario, Project Unit 09-003 (Open File Report No. 6260), Summary of Field Work and Other Activities 2010. Ontario Geological Survey.
- Stone, D., Halle, J., Chaloux, E., 1998. Geology of the Ignace and Pekagoning Lake Areas, Central Wabigoon Subprovince (Misc. Paper No. 169), Summary of Field Work and Other Activities 1998. Ontario Geological Survey.
- Taylor, S.R., McLennan, S.M., 1985. The continental crust: Its composition and evolution. United States.
- Terzaghi, R.D., 1965. Sources of Error in Joint Surveys. *Géotechnique* 15, 287–304.
<https://doi.org/10.1680/geot.1965.15.3.287>
- Virtanen, P. et al. 2020. SciPy 1.0--Fundamental Algorithms for Scientific Computing in Python. *Nature Methods*, 17, 261–272.

**Appendix A: Summary List of Work
Packages Completed for IG_BH01**

WP Number	WP Name	Report Reference
WP01	Site Infrastructure and Access Road Construction	No report
WP02	Borehole Drilling and Coring	Golder, 2018b
WP03	Geological and Geotechnical Core Logging, Photography and Sampling	Golder, 2018c
WP04a	Petrophysical Testing of Core	Golder, 2020a
WP04b	Geomechanical Testing of Core	Golder, 2018a
WP04c	Porewater Extraction and Analysis and Petrographic Analysis	Golder, 2019b
WP05	Geophysical Well Logging and Interpretation	Golder, 2019a
WP06	Hydraulic Testing	Golder, 2019c
WP07	Opportunistic Groundwater Sampling and Testing	Golder, 2018d
WP08	Temporary Well Sealing	No report
WP09	Westbay MP38 Multi-Level Groundwater Monitoring System Installation	Golder, 2019d

**Appendix B: Petrography and
lithogeochemistry data**

Petrography

Semi-quantitative optical petrography was completed by Activation Laboratories in Thunder Bay, Ontario (LGXXX). Modal mineralogy was determined using a known scale grid and visually determining area coverage of minerals in the sample. Note that only rock types plotted on the QAP diagram (Figure 11) are listed. PLA = plagioclase feldspar; QTZ = quartz; AFS = alkali feldspar.

Modal mineralogy (original and normalized) presented as percentages, determined semi-quantitatively using polished thin sections.

Sample ID	From (position along borehole; m)	To (position along borehole; m)	Mineral %			Total	Mineral %			Total	Final Rock Type
			PLA	QTZ	AFS		PLA	QTZ	AFS		
IG_BH01_LG001	1.60	1.82	53	39	5.75	97.75	54.2	39.9	5.9	100	Biotite granodiorite-tonalite
IG_BH01_LG002	24.71	24.83	57	33	4.75	94.75	60.2	34.8	5.0	100	Biotite granodiorite-tonalite
IG_BH01_LG003a	67.10	67.33	26	15	7	48	54.2	31.3	14.6	100	Biotite granodiorite-tonalite
IG_BH01_LG004	80.77	80.90	22	65	11	98	22.4	66.3	11.2	100	Biotite granodiorite-tonalite
IG_BH01_LG005	131.88	131.97	21	71	8	100	21.0	71.0	8.0	100	Biotite granodiorite-tonalite
IG_BH01_LG006	170.10	170.29	49	43	8	100	49.0	43.0	8.0	100	Biotite granodiorite-tonalite
IG_BH01_LG007	201.60	201.73	47	42	4.5	93.5	50.3	44.9	4.8	100	Biotite tonalite
IG_BH01_LG008a	214.10	214.23	57	12.5	1.5	71	80.3	17.6	2.1	100	Biotite granodiorite-tonalite
IG_BH01_LG009	227.27	227.35	62	29	0.1	91.1	68.1	31.8	0.1	100	Biotite tonalite
IG_BH01_LG010	234.07	234.22	36	51	6	93	38.7	54.8	6.5	100	Biotite granodiorite-tonalite
IG_BH01_LG011a	287.97	288.27	23	18	0.25	41.25	55.8	43.6	0.6	100	Biotite granodiorite-tonalite
IG_BH01_LG012	298.11	298.32	34	56	0	90	37.8	62.2	0.0	100	Biotite granodiorite-tonalite
IG_BH01_LG015	335.11	335.30	31	60	4.5	95.5	32.5	62.8	4.7	100	Biotite granodiorite-tonalite
IG_BH01_LG019	443.22	443.30	33	54.5	4.5	92	35.9	59.2	4.9	100	Biotite granodiorite-tonalite
IG_BH01_LG020	452.16	452.28	56	34	0	90	62.2	37.8	0.0	100	Biotite tonalite
IG_BH01_LG021	470.11	470.22	46	41.5	0	87.5	52.6	47.4	0.0	100	Biotite tonalite
IG_BH01_LG022	529.93	530.02	42	40	5.5	87.5	48.0	45.7	6.3	100	Biotite granodiorite-tonalite
IG_BH01_LG026	593.12	593.27	51	43	2.25	96.25	53.0	44.7	2.3	100	Biotite granodiorite-tonalite
IG_BH01_LG027	636.09	636.20	48	44	5.5	97.5	49.2	45.1	5.6	100	Biotite granodiorite-tonalite
IG_BH01_LG029	659.05	659.25	43	53	4.5	100.5	42.8	52.7	4.5	100	Biotite granodiorite-tonalite
IG_BH01_LG030	701.13	701.25	39	52	3.5	94.5	41.3	55.0	3.7	100	Biotite granodiorite-tonalite
IG_BH01_LG032	752.30	752.35	35	55	4	94	37.2	58.5	4.3	100	Biotite granodiorite-tonalite
IG_BH01_LG037	841.99	842.11	41	46	2.5	89.5	45.8	51.4	2.8	100	Biotite granodiorite-tonalite
IG_BH01_LG039	901.98	902.16	43	49	2.25	94.25	45.6	52.0	2.4	100	Biotite granodiorite-tonalite
IG_BH01_LG040	950.02	950.13	41	49	2.25	92.25	44.4	53.1	2.4	100	Biotite granodiorite-tonalite
IG_BH01_LG041a	953.41	953.62	10.5	12.5	0.6	23.6	44.5	53.0	2.5	100	Biotite granodiorite-tonalite
IG_BH01_LG044	995.04	995.15	42.5	49	0.35	91.85	46.3	53.3	0.4	100	Biotite granodiorite-tonalite

Litho geochemistry

All analyses performed by Activation Laboratories Ltd. in Thunder Bay or Ancaster, Ontario. In addition to the results included below, 28 certified reference materials (to measure accuracy), 7 duplicates (to measure precision), and 8 method blanks (to monitor contamination) were analysed by Actlabs to ensure overall quality control in the litho geochemical analyses. Certified reference material measurements averaged within 10% of certified values (>90% accuracy). Duplicate sample measurements averaged within 7% of original measured values (>93% precision), and the method blanks all returned measurements below detection limit (no discernable contamination).

Litho geochemical results of various tests carried out by Activation Laboratories. For details on each analysis performed, see Section 3.2.1.

Report Number: A19-14907																							
Report Date: 16/03/2020																							
Analyte Symbol	From (position along borehole; m)	To (position along borehole; m)	Au	As	Br	Cr	Cs	Co	Ce	Eu	Hf	Ir	La	Lu	Mo	Nd	Rb	Sb	Se	Sm	Ta	Th	
Unit Symbol			ppb	ppm	ppm	ppm	ppm	ppm	ppm	ppm	ppm	ppm	ppb	ppm	ppm	ppm	ppm	ppm	ppm	ppm	ppm	ppm	ppm
Detection Limit			2	0.5	0.5	5	1	1	3	0.2	1	5	0.5	0.05	5	5	5	20	0.2	3	0.1	0.5	0.2
Analysis Method			INAA	INAA	INAA	INAA	INAA	INAA	INAA	INAA	INAA	INAA	INAA	INAA	INAA	INAA	INAA	INAA	INAA	INAA	INAA	INAA	INAA
IG_BH01_LG001	1.6	1.82	< 2	< 0.5	< 0.5	< 5	< 1	3	26	0.2	4	< 5	13.5	< 0.05	< 5	< 5	50	< 0.2	< 3	1.4	< 0.5	3.6	
IG_BH01_LG002	24.71	24.83	< 2	< 0.5	< 0.5	< 5	< 1	5	23	0.3	3	< 5	12.1	< 0.05	< 5	< 5	< 20	0.4	< 3	1.3	< 0.5	3.5	
IG_BH01_LG003	67.1	67.33	< 2	< 0.5	< 0.5	< 5	< 1	1	25	< 0.2	3	< 5	15.6	< 0.05	< 5	8	100	< 0.2	< 3	1.2	< 0.5	4.5	
IG_BH01_LG004	80.77	80.9	6	0.9	< 0.5	< 5	3	< 1	35	< 0.2	3	< 5	21.4	< 0.05	< 5	9	80	< 0.2	< 3	1.5	< 0.5	9.2	
IG_BH01_LG005	131.88	131.97	< 2	0.6	< 0.5	< 5	< 1	< 1	52	< 0.2	2	< 5	29.5	< 0.05	< 5	10	50	< 0.2	< 3	1.5	< 0.5	6.9	
IG_BH01_LG006	170.1	170.29	< 2	3.1	< 0.5	< 5	1	2	62	< 0.2	3	< 5	39	< 0.05	< 5	14	50	< 0.2	< 3	2	< 0.5	9.7	
IG_BH01_LG007	201.6	201.73	4	2	< 0.5	8	< 1	7	33	< 0.2	3	< 5	17.9	< 0.05	< 5	6	50	< 0.2	< 3	1.7	< 0.5	3.7	
IG_BH01_LG008	214.1	214.23	< 2	1	< 0.5	< 5	2	2	26	< 0.2	4	< 5	15.4	< 0.05	< 5	6	70	< 0.2	< 3	1.1	< 0.5	3.8	
IG_BH01_LG009	227.27	227.35	< 2	2.3	< 0.5	< 5	4	7	28	< 0.2	4	< 5	16.6	< 0.05	< 5	< 5	< 20	< 0.2	< 3	1.5	< 0.5	3.6	
IG_BH01_LG010	234.07	234.22	< 2	0.8	< 0.5	< 5	1	< 1	90	0.6	4	< 5	53.9	< 0.05	< 5	20	100	< 0.2	< 3	2.7	< 0.5	13	
IG_BH01_LG011	287.97	288.27	< 2	0.9	< 0.5	< 5	< 1	1	43	< 0.2	2	< 5	24.5	< 0.05	< 5	14	20	< 0.2	< 3	1.4	< 0.5	7.2	
IG_BH01_LG012	298.11	298.32	< 2	0.9	< 0.5	7	3	2	52	< 0.2	3	< 5	31	< 0.05	< 5	11	100	< 0.2	< 3	1.5	< 0.5	7.6	
IG_BH01_LG013	299.95	300.13	< 2	< 0.5	< 0.5	< 5	2	2	36	< 0.2	2	< 5	23	< 0.05	< 5	10	80	< 0.2	< 3	1.2	< 0.5	6	
IG_BH01_LG014	315.04	315.12	< 2	< 0.5	< 0.5	258	< 1	35	180	2.6	3	< 5	85.8	< 0.05	< 5	62	< 20	< 0.2	< 3	11.1	< 0.5	13.5	
IG_BH01_LG015	335.11	335.3	< 2	< 0.5	< 0.5	< 5	2	< 1	53	< 0.2	3	< 5	31.3	< 0.05	< 5	12	70	< 0.2	< 3	1.6	< 0.5	7.9	
IG_BH01_LG016	394.98	395.13	< 2	< 0.5	< 0.5	< 5	3	< 1	19	< 0.2	3	< 5	9.4	< 0.05	< 5	8	120	< 0.2	< 3	1.3	< 0.5	5.6	

IG_BH01_LG017	400.37	400.53	< 2	< 0.5	< 0.5	< 5	< 1	< 1	13	< 0.2	2	< 5	6.1	0.07	6	< 5	160	< 0.2	< 3	1.3	< 0.5	4.9
IG_BH01_LG018	402.82	402.93	< 2	< 0.5	< 0.5	< 5	4	< 1	17	< 0.2	4	< 5	5.7	0.15	8	< 5	200	< 0.2	< 3	1.7	1.1	5.5
IG_BH01_LG019	443.22	443.3	< 2	1.4	< 0.5	< 5	3	< 1	67	0.3	3	< 5	40.3	< 0.05	< 5	10	100	0.3	< 3	1.7	< 0.5	7.1
IG_BH01_LG020	452.16	452.28	< 2	< 0.5	< 0.5	< 5	< 1	9	21	< 0.2	4	< 5	11	< 0.05	< 5	< 5	< 20	< 0.2	< 3	1.4	< 0.5	1.8
IG_BH01_LG021	470.11	470.22	< 2	< 0.5	< 0.5	< 5	1	8	19	< 0.2	4	< 5	11.1	< 0.05	< 5	8	< 20	< 0.2	< 3	1.3	< 0.5	2.3
IG_BH01_LG022	529.93	530.02	< 2	0.7	4.4	< 5	< 1	5	66	0.3	5	< 5	41	< 0.05	< 5	19	40	< 0.2	< 3	1.7	< 0.5	8.1
IG_BH01_LG023	549.15	549.33	< 2	0.8	< 0.5	10	3	8	39	0.4	4	< 5	22.5	< 0.05	< 5	12	60	< 0.2	< 3	2.3	< 0.5	4.5
IG_BH01_LG024	560.64	560.78	< 2	< 0.5	< 0.5	7	4	2	32	0.5	4	< 5	18.6	< 0.05	< 5	12	< 20	< 0.2	< 3	1.7	< 0.5	3.9
IG_BH01_LG025	587.04	587.2	< 2	< 0.5	< 0.5	15	< 1	8	34	0.5	3	< 5	21.4	< 0.05	< 5	12	< 20	< 0.2	< 3	1.9	< 0.5	4.3
IG_BH01_LG026	593.12	593.27	< 2	< 0.5	< 0.5	< 5	1	3	76	0.5	3	< 5	47.5	< 0.05	< 5	17	30	< 0.2	< 3	2.1	< 0.5	9.6
IG_BH01_LG027	636.09	636.2	< 2	< 0.5	< 0.5	< 5	< 1	< 1	16	< 0.2	3	< 5	9.4	< 0.05	< 5	< 5	< 20	0.2	< 3	0.9	< 0.5	3.1
IG_BH01_LG028	656.32	656.48	< 2	0.7	< 0.5	168	3	34	97	2.4	4	< 5	48	< 0.05	< 5	35	40	< 0.2	< 3	8.6	< 0.5	7.1
IG_BH01_LG029	659.05	659.25	< 2	< 0.5	< 0.5	< 5	< 1	< 1	20	< 0.2	2	< 5	10	< 0.05	< 5	< 5	40	0.3	< 3	1.4	< 0.5	4.7
IG_BH01_LG030	701.13	701.25	< 2	2.1	< 0.5	< 5	2	2	56	0.4	4	< 5	36.8	< 0.05	< 5	12	< 20	< 0.2	< 3	1.7	< 0.5	6.8
IG_BH01_LG031	735.09	735.33	< 2	2.5	< 0.5	898	15	48	42	0.7	2	< 5	19.5	< 0.05	< 5	16	190	< 0.2	< 3	3	< 0.5	2.9
IG_BH01_LG032	752.3	752.35	< 2	1	< 0.5	11	1	3	85	0.6	5	< 5	52.9	< 0.05	< 5	17	100	< 0.2	< 3	2.3	< 0.5	9.1
IG_BH01_LG033	776.2	776.28	< 2	0.7	< 0.5	13	3	3	44	0.5	4	< 5	25.2	< 0.05	< 5	9	< 20	< 0.2	< 3	2.5	< 0.5	5.2
IG_BH01_LG034	792.92	793.03	4	< 0.5	< 0.5	893	5	46	45	0.7	2	< 5	21.2	< 0.05	< 5	18	130	< 0.2	< 3	4.1	< 0.5	2.7
IG_BH01_LG035	795.65	795.75	< 2	< 0.5	< 0.5	455	3	38	55	1.1	2	< 5	29.6	< 0.05	< 5	24	60	0.3	< 3	5.1	< 0.5	3.4
IG_BH01_LG036	797.48	797.62	< 2	< 0.5	< 0.5	959	5	48	44	0.8	1	< 5	19.5	< 0.05	< 5	15	170	< 0.2	< 3	4	< 0.5	3.6
IG_BH01_LG037	841.99	842.11	< 2	< 0.5	18.4	13	< 1	3	41	0.3	4	< 5	26.1	< 0.05	< 5	9	20	< 0.2	< 3	1.7	< 0.5	5.1
IG_BH01_LG038	895.67	895.97	< 2	< 0.5	< 0.5	8	< 1	6	36	0.4	4	< 5	21.8	< 0.05	< 5	8	30	< 0.2	< 3	1.5	< 0.5	5.3
IG_BH01_LG039	901.98	902.16	< 2	< 0.5	< 0.5	399	2	37	129	2	3	< 5	63	< 0.05	< 5	53	50	< 0.2	< 3	10.6	< 0.5	8.5
IG_BH01_LG040	950.02	950.13	< 2	< 0.5	< 0.5	9	< 1	7	41	0.4	4	< 5	22.7	< 0.05	< 5	7	30	< 0.2	< 3	1.8	< 0.5	5.2
IG_BH01_LG041	953.41	953.62	< 2	< 0.5	< 0.5	8	< 1	< 1	37	0.3	3	< 5	20.7	< 0.05	< 5	9	50	< 0.2	< 3	1.8	< 0.5	5.7
IG_BH01_LG042	968.28	968.44	< 2	1.5	< 0.5	1170	13	54	106	1.9	2	< 5	46.3	< 0.05	< 5	49	110	< 0.2	< 3	9.3	< 0.5	5.5
IG_BH01_LG043	978.81	978.9	< 2	1.9	4.1	443	< 1	41	97	1	< 1	< 5	46.9	< 0.05	< 5	34	30	< 0.2	< 3	6.9	< 0.5	3
IG_BH01_LG044	995.04	995.15	< 2	< 0.5	< 0.5	18	< 1	4	62	0.7	4	< 5	36.8	< 0.05	< 5	15	110	< 0.2	< 3	2.4	< 0.5	8.1
IG_BH01_LG045	999.1	999.29	< 2	< 0.5	< 0.5	905	6	47	54	0.9	2	< 5	26.8	< 0.05	< 5	16	< 20	< 0.2	< 3	5.4	< 0.5	4

Analyte Symbol	Tb	U	W	Yb	Mass	SiO2	Al2O3	Fe2O3(T)	MnO	MgO	CaO	Na2O	K2O	TiO2	P2O5	Total	Sc	Be	V	Cr	Co	Ga	Ge
Unit Symbol	ppm	ppm	ppm	ppm	g	%	%	%	%	%	%	%	%	%	%	%	ppm	ppm	ppm	ppm	ppm	ppm	ppm
Detection Limit	0.5	0.5	1	0.2		0.01	0.01	0.01	0.001	0.01	0.01	0.01	0.01	0.001	0.01	0.01	1	1	5	20	1	1	0.5
Analysis Method	INAA	INAA	INAA	INAA	INAA	FUS-ICP	FUS-ICP	FUS-ICP	FUS-ICP	FUS-ICP	FUS-ICP	FUS-ICP	FUS-ICP	FUS-ICP	FUS-ICP	FUS-ICP	FUS-ICP	FUS-ICP	FUS-ICP	FUS-MS	FUS-MS	FUS-MS	FUS-MS
IG_BH01_LG001	< 0.5	< 0.5	< 1	< 0.2	30.9	70.18	15.35	2.69	0.04	0.62	2.6	4.72	2.37	0.268	0.06	99.39	3	1	27	< 20	5	20	0.8
IG_BH01_LG002	< 0.5	0.7	< 1	0.4	30	71	15.84	2.69	0.037	0.59	2.6	4.75	2.26	0.269	0.07	100.8	4	1	26	< 20	4	21	0.8
IG_BH01_LG003	< 0.5	0.9	< 1	< 0.2	29.4	68.7	15.07	2.34	0.028	0.5	1.25	3.89	5.55	0.204	0.05	98.64	2	< 1	17	< 20	4	18	0.9
IG_BH01_LG004	< 0.5	0.9	< 1	< 0.2	28.7	75.67	12.53	1.61	0.027	0.23	1.62	4.11	2.29	0.098	0.04	98.61	2	2	< 5	< 20	1	17	1.1
IG_BH01_LG005	< 0.5	2.6	< 1	< 0.2	31.9	75.89	13.46	2.04	0.032	0.29	1.85	4.24	2.13	0.142	0.02	100.6	1	2	7	< 20	< 1	16	< 0.5
IG_BH01_LG006	< 0.5	< 0.5	< 1	< 0.2	28.7	74.16	13.3	2.12	0.031	0.37	2.06	4.23	1.95	0.158	0.03	98.89	2	1	7	< 20	2	18	0.8
IG_BH01_LG007	< 0.5	< 0.5	< 1	< 0.2	29.4	69.39	15.2	3.29	0.046	0.78	3.07	4.44	1.94	0.336	0.1	99	5	2	32	< 20	2	22	< 0.5
IG_BH01_LG008	< 0.5	1.9	< 1	0.4	29.7	67.04	17.28	2.85	0.04	0.6	2.56	5.43	3.15	0.269	0.04	100.7	3	2	25	< 20	4	23	0.8
IG_BH01_LG009	< 0.5	< 0.5	< 1	< 0.2	27.8	68.81	16.03	3.31	0.042	0.7	3.25	5.04	1.49	0.328	0.1	99.64	4	2	29	< 20	6	23	0.8
IG_BH01_LG010	< 0.5	1.1	< 1	< 0.2	28.6	69.37	15.63	2.33	0.03	0.38	2.09	4.42	3.74	0.175	0.06	98.71	2	< 1	12	< 20	2	19	1
IG_BH01_LG011	< 0.5	0.9	< 1	< 0.2	29.6	78.11	11.05	2.19	0.025	0.22	1.52	3.5	1.9	0.11	0.02	99.58	1	1	< 5	< 20	2	14	0.9
IG_BH01_LG012	< 0.5	3	< 1	< 0.2	29.3	74.13	12.63	1.84	0.027	0.26	1.84	4.05	2.09	0.124	0.03	98.93	1	1	6	< 20	2	18	0.9
IG_BH01_LG013	< 0.5	2.2	< 1	< 0.2	30.2	81.66	8.74	1.56	0.02	0.18	1.26	2.71	1.44	0.092	0.03	99.19	1	< 1	7	< 20	2	13	1
IG_BH01_LG014	< 0.5	2.4	< 1	1.3	29.3	52.38	14.85	7.75	0.14	8.51	8.04	4.07	0.89	0.672	0.49	100.5	17	3	140	310	26	17	< 0.5
IG_BH01_LG015	< 0.5	2.4	< 1	< 0.2	30.8	75.04	13.03	2.13	0.03	0.33	1.99	4.15	2.07	0.14	0.03	99.35	2	1	7	< 20	2	18	0.9
IG_BH01_LG016	< 0.5	4.7	< 1	< 0.2	30.8	75.5	13.49	0.95	0.014	0.08	0.69	3.36	5.71	0.036	0.01	100	< 1	1	< 5	< 20	1	19	1.2
IG_BH01_LG017	< 0.5	8.4	< 1	0.6	30.2	76.51	13.16	1.04	0.02	0.06	0.75	3.97	4.81	0.039	< 0.01	100.7	< 1	2	6	< 20	< 1	20	< 0.5
IG_BH01_LG018	< 0.5	14.8	< 1	1.4	31.6	73.94	13.51	0.94	0.087	0.05	0.43	4.12	5.2	0.03	0.02	98.52	3	1	< 5	< 20	< 1	25	2
IG_BH01_LG019	< 0.5	3.6	< 1	< 0.2	31.5	73.92	13.37	2.05	0.027	0.33	2.12	4.24	2.03	0.165	0.04	98.67	2	1	9	< 20	2	18	1
IG_BH01_LG020	< 0.5	< 0.5	< 1	0.2	33.1	68.39	15.97	3.41	0.038	0.84	3.72	4.8	1.25	0.384	0.09	99.41	5	1	37	< 20	6	21	0.7
IG_BH01_LG021	< 0.5	< 0.5	< 1	0.4	34.6	69.44	15.57	3.41	0.038	0.88	3.69	4.84	1.3	0.372	0.1	100.1	5	1	41	< 20	7	22	0.7
IG_BH01_LG022	< 0.5	1.6	< 1	< 0.2	33.9	73.89	13.05	2.34	0.028	0.45	2.45	4.1	1.67	0.223	0.06	98.6	2	1	14	< 20	3	18	0.8
IG_BH01_LG023	< 0.5	0.7	< 1	0.5	29.9	69.79	15.07	3.3	0.039	0.81	3.14	4.32	2.06	0.447	0.12	100.7	4	1	31	< 20	6	20	0.8
IG_BH01_LG024	< 0.5	< 0.5	< 1	< 0.2	31.4	71.63	15.47	2.57	0.031	0.61	3.22	4.42	1.6	0.293	0.08	100.2	3	1	23	< 20	4	20	0.8
IG_BH01_LG025	< 0.5	0.7	< 1	< 0.2	31.2	70.2	15.15	3.1	0.038	0.89	3.34	4.49	1.76	0.33	0.09	99.75	4	1	33	20	6	21	0.9

IG_BH01_LG026	< 0.5	1.7	< 1	< 0.2	30.7	75.11	13.35	2.59	0.034	0.48	2.36	4.01	1.92	0.24	0.08	100.6	2	2	16	< 20	< 1	16	< 0.5
IG_BH01_LG027	< 0.5	1.9	< 1	0.3	30.4	74.6	13.68	1.41	0.025	0.29	1.94	4.66	1.96	0.11	0.05	99.14	1	2	11	< 20	< 1	18	< 0.5
IG_BH01_LG028	< 0.5	0.9	< 1	1.5	31.3	54.05	14.02	8.69	0.117	6.6	7.64	2.87	2.68	0.978	0.38	99.99	19	2	168	190	34	19	1.2
IG_BH01_LG029	< 0.5	0.9	< 1	< 0.2	30.5	74	14.19	1.29	0.023	0.22	1.91	4.71	2.28	0.088	0.03	99.2	2	1	9	< 20	1	19	1
IG_BH01_LG030	< 0.5	< 0.5	< 1	< 0.2	28.9	73.29	13.73	3.09	0.038	0.67	2.76	3.96	1.72	0.317	0.09	100.2	2	1	24	< 20	5	18	0.7
IG_BH01_LG031	< 0.5	< 0.5	< 1	1.1	22.8	47.18	10.22	9.22	0.156	10.98	9.14	0.17	5.38	0.557	0.17	99.81	30	1	193	1040	47	12	1.6
IG_BH01_LG032	< 0.5	1.7	< 1	< 0.2	27.1	72.67	13.38	3.33	0.039	0.71	2.65	3.91	1.76	0.32	0.08	99.24	2	1	24	< 20	5	19	0.9
IG_BH01_LG033	< 0.5	< 0.5	< 1	0.5	29.8	70.34	14.61	3.31	0.039	0.82	3.06	4.59	1.65	0.443	0.12	100.2	4	2	34	< 20	6	21	0.9
IG_BH01_LG034	< 0.5	0.8	< 1	1.1	28.6	47.66	10.63	9.64	0.168	12.04	9.53	0.89	4	0.577	0.16	99.74	33	1	203	1110	49	14	1.6
IG_BH01_LG035	< 0.5	< 0.5	< 1	1.3	29.3	49.87	13.68	9.93	0.154	8.53	9.96	2.91	1.87	0.732	0.22	100.4	27	1	227	590	42	17	1.6
IG_BH01_LG036	< 0.5	< 0.5	< 1	0.9	26	46.08	11.07	10.94	0.175	13.09	8.62	1.13	3.58	0.582	0.17	98.12	35	1	206	1270	54	17	1.5
IG_BH01_LG037	< 0.5	< 0.5	< 1	< 0.2	27.2	70.24	14.09	3.49	0.043	0.86	3.07	4.17	1.67	0.337	0.1	98.49	3	1	29	< 20	6	19	0.8
IG_BH01_LG038	< 0.5	3.2	< 1	0.3	29.9	72.22	13.47	3.15	0.042	0.69	2.68	4.1	1.8	0.299	0.07	98.89	2	1	23	< 20	5	19	1
IG_BH01_LG039	< 0.5	1.5	< 1	1.2	25.2	49.84	13.3	8.05	0.127	10.93	9.37	2.87	2.22	0.649	0.48	100.3	21	2	139	520	41	17	1.2
IG_BH01_LG040	< 0.5	< 0.5	< 1	< 0.2	30.7	70.83	13.81	3.56	0.044	0.86	2.93	4.04	1.68	0.335	0.1	98.52	3	1	29	< 20	6	18	0.7
IG_BH01_LG041	< 0.5	0.8	< 1	< 0.2	29.8	74.68	13.46	2.49	0.039	0.45	2.18	4.1	2.32	0.201	0.06	100.2	2	1	26	< 20	< 1	17	< 0.5
IG_BH01_LG042	< 0.5	2.3	< 1	1	25.5	43.91	9.2	9.43	0.169	16.82	9.47	0.64	3.49	0.636	0.37	98.66	26	2	139	1460	58	13	1.4
IG_BH01_LG043	< 0.5	< 0.5	< 1	1	24.6	41.51	9.69	9.45	0.152	9.12	14.39	1.69	2.41	0.627	0.32	99.9	26	3	179	550	42	12	1.2
IG_BH01_LG044	< 0.5	< 0.5	< 1	0.3	25.1	72.51	13.07	3.67	0.05	0.95	2.8	3.63	1.66	0.377	0.12	99.38	3	2	29	< 20	3	19	< 0.5
IG_BH01_LG045	< 0.5	1.1	< 1	1.2	29	49.1	11.13	9.76	0.164	11.03	10.47	2.71	1.53	0.607	0.19	99.87	33	2	223	1040	46	13	1.4

Analyte Symbol	As	Rb	Sr	Y	Zr	Nb	Mo	In	Sn	Sb	Cs	Ba	La	Ce	Pr	Nd	Sm	Eu	Gd	Tb	Dy	Ho	Er	Tm
Unit Symbol	ppm	ppm	ppm	ppm	ppm	ppm	ppm	ppm	ppm	ppm	ppm	ppm	ppm	ppm	ppm	ppm	ppm	ppm	ppm	ppm	ppm	ppm	ppm	ppm
Detection Limit	5	1	2	0.5	1	0.2	2	0.1	1	0.2	0.1	2	0.05	0.05	0.01	0.05	0.01	0.005	0.01	0.01	0.01	0.01	0.01	0.005
Analysis Method	FUS-MS	FUS-MS	FUS-ICP	FUS-MS	FUS-ICP	FUS-MS	FUS-MS	FUS-MS	FUS-MS	FUS-MS	FUS-MS	FUS-ICP	FUS-MS											
IG_BH01_LG001	< 5	60	297	4.3	95	2	< 2	< 0.1	1	< 0.2	1.6	556	13.7	24.6	2.61	9.1	1.61	0.486	1.18	0.16	0.81	0.16	0.44	0.062
IG_BH01_LG002	< 5	55	312	4.3	100	2.1	< 2	< 0.1	1	< 0.2	1.4	513	12	23.1	2.27	8.1	1.48	0.452	1.12	0.16	0.83	0.15	0.4	0.062
IG_BH01_LG003	< 5	93	206	3.6	60	2.5	< 2	< 0.1	1	< 0.2	1	1606	15.5	26.4	2.54	8.88	1.28	0.344	1.02	0.14	0.72	0.13	0.34	0.047
IG_BH01_LG004	< 5	71	161	3.6	58	3.3	< 2	< 0.1	1	< 0.2	2.3	405	22.8	39.7	3.72	12.1	1.74	0.455	1.09	0.13	0.62	0.11	0.35	0.05
IG_BH01_LG005	< 5	64	187	3.3	84	3.8	< 2	< 0.1	1	< 0.2	1.6	424	30.3	50.7	4.49	13.3	1.7	0.546	0.99	0.12	0.6	0.11	0.3	0.05
IG_BH01_LG006	< 5	62	197	3.5	83	3.6	< 2	< 0.1	1	< 0.2	1.2	403	40.5	67.6	6.13	19.1	2.17	0.553	1.31	0.16	0.74	0.12	0.32	0.045
IG_BH01_LG007	< 5	52	356	4.4	126	2	< 2	< 0.1	1	< 0.2	1.2	583	18.5	33.3	3.22	11.5	1.93	0.61	1.4	0.18	0.9	0.16	0.42	0.057
IG_BH01_LG008	< 5	102	253	4.1	114	3.9	< 2	< 0.1	1	< 0.2	2.5	582	15.8	27.7	2.74	9.19	1.42	0.425	0.92	0.14	0.72	0.13	0.42	0.065
IG_BH01_LG009	< 5	63	357	4.9	127	5.8	< 2	< 0.1	1	< 0.2	2.9	441	16.8	30.1	3.04	10.7	1.87	0.525	1.27	0.17	0.93	0.17	0.48	0.073
IG_BH01_LG010	< 5	82	243	3.5	82	3.3	< 2	< 0.1	1	< 0.2	1	988	55.5	91.5	8.43	25.6	2.97	0.677	1.62	0.16	0.71	0.12	0.35	0.051
IG_BH01_LG011	< 5	56	160	3.3	56	2.5	< 2	< 0.1	1	< 0.2	1.5	390	25.6	42.7	3.99	12.5	1.54	0.422	0.99	0.12	0.59	0.11	0.31	0.048
IG_BH01_LG012	< 5	70	223	3.4	71	3.1	< 2	< 0.1	1	< 0.2	2.2	434	30.6	51.4	4.67	14.5	1.7	0.393	1	0.13	0.62	0.11	0.32	0.045
IG_BH01_LG013	< 5	47	114	2.5	49	2.1	< 2	< 0.1	1	< 0.2	1.4	339	21.9	36.9	3.32	10.7	1.26	0.265	0.79	0.09	0.45	0.08	0.23	0.03
IG_BH01_LG014	< 5	28	1429	18.9	204	6.2	2	< 0.1	1	< 0.2	1.3	216	82.9	168	18.9	69.9	11.7	3.22	7.96	0.88	4.06	0.64	1.65	0.197
IG_BH01_LG015	< 5	70	189	3.5	77	3.7	< 2	< 0.1	1	< 0.2	1.8	392	32.6	55.4	4.95	15.4	1.85	0.521	1.02	0.13	0.63	0.11	0.31	0.047
IG_BH01_LG016	< 5	135	98	3.9	25	2.5	< 2	< 0.1	< 1	< 0.2	2.3	1434	9.12	17.5	1.85	6.75	1.43	0.38	1.19	0.17	0.75	0.13	0.33	0.053
IG_BH01_LG017	< 5	121	66	7.9	36	3	< 2	< 0.1	< 1	< 0.2	1.1	185	5.24	11.3	1.21	4.1	1.28	0.201	1.49	0.24	1.44	0.26	0.8	0.112
IG_BH01_LG018	< 5	179	15	18.8	32	5.8	< 2	< 0.1	1	< 0.2	2.5	50	5.7	12.6	1.5	5.4	1.95	0.048	2.57	0.5	3.06	0.56	1.56	0.217
IG_BH01_LG019	< 5	66	205	3.6	83	3	< 2	< 0.1	1	< 0.2	1.9	377	41.1	67.9	6	18.2	1.97	0.521	0.99	0.13	0.69	0.11	0.32	0.05
IG_BH01_LG020	< 5	44	411	4	132	2.1	< 2	< 0.1	< 1	< 0.2	0.8	447	10.7	19	2.06	7.75	1.54	0.604	1.22	0.15	0.84	0.14	0.37	0.054
IG_BH01_LG021	< 5	47	403	4.2	138	2.3	< 2	< 0.1	1	< 0.2	0.9	467	10.8	19.4	2.03	7.4	1.36	0.555	1.17	0.16	0.78	0.15	0.42	0.063
IG_BH01_LG022	< 5	54	228	3	143	3.3	< 2	< 0.1	1	< 0.2	1.2	423	41.1	67.5	6.09	18	1.83	0.604	0.97	0.11	0.54	0.1	0.29	0.042
IG_BH01_LG023	< 5	60	273	5.6	150	5.3	< 2	< 0.1	1	< 0.2	2.3	466	21.8	40.7	4.24	15.2	2.53	0.773	1.86	0.24	1.19	0.21	0.57	0.072
IG_BH01_LG024	< 5	40	249	3.6	127	3.8	< 2	< 0.1	1	< 0.2	4.5	363	18	32.1	3.22	11.4	1.88	0.563	1.45	0.17	0.78	0.13	0.33	0.045
IG_BH01_LG025	< 5	48	259	4.4	129	3.9	< 2	< 0.1	1	< 0.2	1.2	436	21.7	38.6	3.8	13.8	2.21	0.62	1.61	0.19	0.87	0.15	0.4	0.051
IG_BH01_LG026	< 5	55	224	3	158	3.5	< 2	< 0.1	1	< 0.2	1.4	528	48.3	78.7	6.95	21	2.37	0.67	1.22	0.12	0.59	0.09	0.28	0.039
IG_BH01_LG027	< 5	53	167	4.5	81	2.4	< 2	< 0.1	< 1	< 0.2	1.2	410	9.07	15.7	1.53	4.9	0.99	0.528	0.83	0.13	0.75	0.16	0.42	0.058

IG_BH01_LG028	< 5	68	936	20.8	157	4.9	< 2	0.1	1	< 0.2	2.8	951	47.4	105	12.7	52.6	9.85	2.47	6.96	0.93	4.36	0.8	2.02	0.278
IG_BH01_LG029	< 5	49	168	4.5	62	2.3	< 2	< 0.1	1	< 0.2	1.1	446	9.52	17.9	1.93	7.19	1.7	0.38	1.51	0.2	0.93	0.15	0.36	0.05
IG_BH01_LG030	< 5	56	242	3.1	153	4	< 2	< 0.1	1	< 0.2	1.8	403	38.4	64.2	5.79	17.5	1.99	0.599	1.15	0.12	0.58	0.1	0.33	0.049
IG_BH01_LG031	< 5	145	138	9.4	67	2.2	< 2	< 0.1	1	< 0.2	13	648	18.4	37.6	4.31	16.4	3.05	0.748	2.29	0.31	1.7	0.35	1.07	0.166
IG_BH01_LG032	< 5	59	236	3.2	165	4.2	< 2	< 0.1	1	< 0.2	1.8	447	51.8	85.7	7.61	23.6	2.38	0.623	1.15	0.11	0.59	0.1	0.3	0.046
IG_BH01_LG033	< 5	49	265	6	153	6.3	< 2	< 0.1	1	< 0.2	2.6	414	26.4	47.4	4.77	16.6	2.64	0.741	2.06	0.28	1.34	0.21	0.57	0.076
IG_BH01_LG034	< 5	113	206	12.4	68	2.5	< 2	< 0.1	1	< 0.2	4.8	656	22.1	45.7	5.67	23.6	4.48	1.14	3.49	0.47	2.54	0.47	1.32	0.188
IG_BH01_LG035	< 5	51	653	16.4	87	3.5	< 2	< 0.1	1	0.2	2.8	406	31.9	60.1	7.33	29.8	5.5	1.55	4.2	0.59	3.06	0.59	1.7	0.239
IG_BH01_LG036	< 5	101	200	12	69	2.7	< 2	< 0.1	1	< 0.2	5.4	591	22.1	46.6	5.65	23.6	4.47	1.23	3.47	0.45	2.5	0.47	1.32	0.183
IG_BH01_LG037	< 5	51	258	3.2	170	4.3	< 2	< 0.1	1	< 0.2	1.3	431	26.8	44.8	4.22	13.6	1.71	0.649	1.11	0.13	0.59	0.11	0.3	0.045
IG_BH01_LG038	< 5	59	225	4.5	145	4.7	< 2	< 0.1	1	< 0.2	1.3	387	24	40.4	3.82	12.3	1.87	0.592	1.3	0.17	0.83	0.14	0.42	0.065
IG_BH01_LG039	< 5	52	1137	17.8	154	6.4	< 2	< 0.1	1	< 0.2	3.2	870	70.1	149	17.4	68.7	11.7	3.01	8.03	0.89	4.02	0.65	1.68	0.226
IG_BH01_LG040	< 5	50	250	3.9	185	4.4	< 2	< 0.1	1	< 0.2	1.5	403	25	43.2	4.1	13.9	1.87	0.592	1.3	0.16	0.76	0.14	0.37	0.054
IG_BH01_LG041	< 5	59	194	3.6	135	3.6	< 2	< 0.1	1	< 0.2	1.3	710	22.6	39.4	3.68	12.1	1.73	0.577	1.41	0.17	0.73	0.13	0.34	0.046
IG_BH01_LG042	< 5	94	266	14.6	118	9.3	< 2	< 0.1	1	< 0.2	13.7	622	49.6	112	13.7	56.5	9.76	2.53	6.69	0.74	3.28	0.53	1.32	0.171
IG_BH01_LG043	< 5	71	241	14.7	68	12.5	< 2	< 0.1	< 1	< 0.2	0.5	254	50.3	104	10.8	43.5	7.63	1.67	4.85	0.66	3.09	0.52	1.36	0.187
IG_BH01_LG044	< 5	50	242	3.5	202	4.4	< 2	< 0.1	1	< 0.2	1.2	434	33	55.2	4.98	17	1.99	0.673	1.24	0.13	0.63	0.11	0.31	0.046
IG_BH01_LG045	< 5	43	529	13.7	74	2.7	< 2	< 0.1	1	< 0.2	4.9	344	25	52.5	6.46	26.9	5.29	1.38	4.01	0.53	2.61	0.5	1.41	0.212

Analyte Symbol	Yb	Lu	Hf	Ta	W	Tl	Bi	Th	U	Ni	Cu	Zn	Cd	S	Ag	Pb	LOI
Unit Symbol	ppm	%	ppm	ppm	%												
Detection Limit	0.01	0.002	0.1	0.01	0.5	0.05	0.1	0.05	0.01	1	1	1	0.5	0.001	0.3	3	
Analysis Method	FUS-MS	TD-ICP	GRAV														
IG_BH01_LG001	0.42	0.064	2.6	0.3	< 0.5	0.36	< 0.1	3.41	0.61	4	31	54	< 0.5	0.005	< 0.3	8	0.48
IG_BH01_LG002	0.4	0.061	2.7	0.25	< 0.5	0.34	< 0.1	3.28	1.15	3	17	53	< 0.5	0.002	0.4	6	0.71
IG_BH01_LG003	0.31	0.047	1.7	0.46	0.6	0.51	< 0.1	3.96	1.65	2	46	47	< 0.5	0.004	0.4	19	1.06
IG_BH01_LG004	0.33	0.049	2	0.88	< 0.5	0.42	0.2	8.34	1.66	2	13	38	< 0.5	0.001	< 0.3	8	0.39
IG_BH01_LG005	0.34	0.052	2.3	0.52	< 0.5	0.28	0.1	6.8	2.63	1	10	44	< 0.5	0.002	0.4	8	0.46
IG_BH01_LG006	0.3	0.049	2.6	0.64	< 0.5	0.39	< 0.1	9.04	0.98	2	8	47	< 0.5	0.002	< 0.3	6	0.47
IG_BH01_LG007	0.36	0.054	3.5	0.22	< 0.5	< 0.05	< 0.1	3.53	0.68	3	37	61	< 0.5	0.003	0.3	4	0.4
IG_BH01_LG008	0.46	0.073	3.3	0.72	< 0.5	0.55	< 0.1	3.43	1.67	2	8	66	< 0.5	0.003	0.5	8	1.46
IG_BH01_LG009	0.53	0.074	3.7	1.16	< 0.5	0.44	< 0.1	3.4	0.93	3	18	72	< 0.5	0.004	0.4	5	0.54
IG_BH01_LG010	0.31	0.046	2.5	0.43	< 0.5	0.42	< 0.1	11.9	1.66	2	7	49	< 0.5	0.003	< 0.3	11	0.48
IG_BH01_LG011	0.32	0.048	1.7	0.44	1.2	0.35	0.4	6.5	1.42	2	8	33	< 0.5	0.312	0.4	7	0.93
IG_BH01_LG012	0.35	0.055	2.2	0.72	0.7	0.42	< 0.1	7.44	2.18	1	6	40	< 0.5	0.047	< 0.3	6	1.92
IG_BH01_LG013	0.22	0.038	1.6	0.5	2.9	0.26	0.2	5.23	1.89	1	6	85	< 0.5	0.225	< 0.3	6	1.48
IG_BH01_LG014	1.32	0.216	4.6	0.28	10.1	0.15	0.2	11.4	2.59	171	12	86	< 0.5	0.006	0.4	12	2.72
IG_BH01_LG015	0.32	0.052	2.4	0.62	< 0.5	0.43	0.2	7.6	2.43	2	20	44	< 0.5	0.003	< 0.3	8	0.41
IG_BH01_LG016	0.34	0.046	1.9	0.75	< 0.5	0.72	< 0.1	4.86	4.12	2	3	11	< 0.5	0.009	< 0.3	20	0.17
IG_BH01_LG017	0.77	0.12	2.3	0.4	< 0.5	0.54	< 0.1	3.75	8.83	1	6	14	< 0.5	0.03	< 0.3	18	0.31
IG_BH01_LG018	1.53	0.193	3.3	1.21	2.5	0.96	0.1	4.53	14.6	< 1	5	15	< 0.5	0.006	< 0.3	16	0.19
IG_BH01_LG019	0.33	0.054	2.5	0.55	< 0.5	0.39	0.2	6.94	3.35	2	18	42	< 0.5	0.003	0.4	7	0.38
IG_BH01_LG020	0.34	0.055	3.3	0.2	< 0.5	0.28	< 0.1	1.81	0.68	3	10	60	< 0.5	0.003	< 0.3	3	0.5
IG_BH01_LG021	0.44	0.076	3.3	0.21	< 0.5	0.29	< 0.1	2	1.25	4	7	61	< 0.5	0.003	< 0.3	4	0.4
IG_BH01_LG022	0.28	0.045	3.9	0.58	< 0.5	0.34	< 0.1	7.1	1.85	2	6	47	< 0.5	0.003	0.4	5	0.34
IG_BH01_LG023	0.43	0.069	3.9	0.6	< 0.5	0.38	< 0.1	4.95	1.28	6	4	61	< 0.5	0.002	0.4	7	1.61
IG_BH01_LG024	0.26	0.042	3.4	0.45	< 0.5	0.26	< 0.1	3.63	1.05	3	10	54	< 0.5	0.003	< 0.3	4	0.24
IG_BH01_LG025	0.33	0.051	3.4	0.48	< 0.5	0.29	< 0.1	4.55	1.15	8	17	56	< 0.5	0.004	0.4	5	0.34
IG_BH01_LG026	0.24	0.039	3.8	0.36	< 0.5	0.37	< 0.1	9.53	1.3	3	9	49	< 0.5	0.004	0.3	6	0.42

IG_BH01_LG027	0.36	0.048	3.1	0.44	< 0.5	0.28	< 0.1	2.77	1.32	2	8	25	< 0.5	0.003	< 0.3	9	0.43
IG_BH01_LG028	1.83	0.276	4.6	0.34	< 0.5	0.46	< 0.1	7.07	2.04	143	74	86	< 0.5	0.095	0.3	8	1.97
IG_BH01_LG029	0.3	0.049	2.3	0.36	< 0.5	0.26	< 0.1	5.19	1.49	3	7	23	< 0.5	0.003	< 0.3	10	0.46
IG_BH01_LG030	0.34	0.052	3.9	0.7	< 0.5	0.34	< 0.1	7.44	1.51	4	12	58	< 0.5	0.005	0.4	5	0.52
IG_BH01_LG031	1.14	0.191	1.9	0.14	< 0.5	0.94	< 0.1	2.85	0.75	213	2	84	< 0.5	0.003	< 0.3	< 3	6.64
IG_BH01_LG032	0.31	0.05	4.3	0.57	< 0.5	0.37	< 0.1	9.08	1.62	5	12	62	< 0.5	0.004	0.3	7	0.39
IG_BH01_LG033	0.51	0.074	4	0.68	0.9	0.3	< 0.1	5.74	1.32	6	8	65	< 0.5	0.006	0.3	7	1.24
IG_BH01_LG034	1.26	0.195	1.9	0.14	< 0.5	0.77	0.1	2.84	0.75	229	3	84	< 0.5	0.003	< 0.3	< 3	4.44
IG_BH01_LG035	1.54	0.238	2.4	0.19	0.5	0.32	0.2	3.59	1.17	127	8	75	< 0.5	0.005	< 0.3	19	2.54
IG_BH01_LG036	1.16	0.179	2	0.14	< 0.5	0.7	< 0.1	3.01	0.8	258	4	121	< 0.5	0.003	< 0.3	< 3	2.7
IG_BH01_LG037	0.3	0.049	4.2	0.41	< 0.5	0.32	< 0.1	5.37	0.99	175	20	118	< 0.5	0.006	0.3	8	0.42
IG_BH01_LG038	0.45	0.068	3.8	0.82	< 0.5	0.35	< 0.1	6.09	2.14	7	11	58	< 0.5	0.003	0.3	9	0.38
IG_BH01_LG039	1.33	0.191	3.8	0.3	0.6	0.34	0.1	9.39	2.22	306	60	68	< 0.5	0.071	0.3	8	2.43
IG_BH01_LG040	0.34	0.061	4.7	0.52	< 0.5	0.31	0.1	5.73	1.55	7	18	69	< 0.5	0.005	< 0.3	5	0.33
IG_BH01_LG041	0.33	0.043	3.5	0.38	< 0.5	0.29	< 0.1	5.88	1.32	4	6	46	< 0.5	0.003	0.4	7	0.24
IG_BH01_LG042	1.02	0.156	3.2	0.39	0.6	0.56	0.2	6.03	1.75	419	16	87	< 0.5	0.006	0.3	< 3	4.54
IG_BH01_LG043	1.2	0.182	1.8	0.51	1.2	0.32	< 0.1	2.9	0.77	81	22	91	< 0.5	0.003	< 0.3	< 3	10.54
IG_BH01_LG044	0.26	0.044	4.9	0.32	< 0.5	0.13	< 0.1	6.86	0.83	6	7	68	< 0.5	0.003	0.3	3	0.54
IG_BH01_LG045	1.34	0.203	2.1	0.15	0.5	0.26	0.1	3.26	0.94	185	8	69	< 0.5	0.005	< 0.3	4	3.17

**Appendix C: Geophysical Near and Far
Density Log Correction**

The correction was determined by averaging the difference between each laboratory measurement and the field measurement at the corresponding Position, for the near and far density data sets. Seventy-six laboratory core wet density measurements were considered. This correction was applied to the near and far density logs in WellCAD and the updated logs are exported from WellCAD and updated as .LAS files in the NWMO Acquire database.

Position along borehole	Near Density	Far Density (FD)	Lab Wet Density	Difference ND-Lab	Difference FD-lab	NDCorrection	FDCorrection
m	g/cm ³						
150.115	2.721	2.711	2.655	0.066	0.056	1.025	1.021
150.115	2.721	2.711	2.653	0.068	0.057	1.025	1.022
200.945	2.733	2.750	2.685	0.048	0.065	1.018	1.024
200.945	2.733	2.750	2.689	0.044	0.061	1.016	1.023
249.1	2.703	2.726	2.650	0.053	0.076	1.020	1.029
249.1	2.703	2.726	2.648	0.056	0.078	1.021	1.030
297.91	2.725	2.747	2.677	0.048	0.070	1.018	1.026
297.91	2.725	2.747	2.678	0.047	0.069	1.018	1.026
327.265	2.720	2.738	2.653	0.067	0.084	1.025	1.032
327.265	2.720	2.738	2.653	0.067	0.085	1.025	1.032
388.425	2.753	2.730	2.660	0.093	0.070	1.035	1.026
388.425	2.753	2.730	2.662	0.091	0.069	1.034	1.026
405.22	2.729	2.694	2.647	0.082	0.047	1.031	1.018
405.22	2.729	2.694	2.647	0.082	0.047	1.031	1.018
447.15	2.749	2.766	2.659	0.090	0.107	1.034	1.040
447.15	2.749	2.766	2.662	0.088	0.104	1.033	1.039
464.675	2.739	2.732	2.662	0.076	0.070	1.029	1.026
464.675	2.739	2.732	2.663	0.075	0.069	1.028	1.026
504.48	2.731	2.746	2.671	0.060	0.076	1.023	1.028
504.48	2.731	2.746	2.673	0.057	0.073	1.021	1.027
526.965	2.717	2.763	2.671	0.046	0.092	1.017	1.035
526.965	2.717	2.763	2.673	0.044	0.090	1.016	1.034
553.14	2.747	2.753	2.670	0.077	0.084	1.029	1.031
553.14	2.747	2.753	2.668	0.078	0.085	1.029	1.032
585.745	2.753	2.780	2.666	0.087	0.114	1.033	1.043
585.745	2.753	2.780	2.669	0.084	0.111	1.031	1.042
620.75	2.732	2.751	2.673	0.059	0.078	1.022	1.029
620.75	2.732	2.751	2.670	0.062	0.081	1.023	1.030
666.74	2.730	2.787	2.673	0.057	0.114	1.021	1.043
666.74	2.730	2.787	2.672	0.058	0.115	1.022	1.043
705.53	2.766	2.780	2.678	0.088	0.102	1.033	1.038
705.53	2.766	2.780	2.681	0.085	0.099	1.032	1.037
768.87	2.719	2.776	2.684	0.034	0.091	1.013	1.034
768.87	2.719	2.776	2.685	0.034	0.091	1.013	1.034
800.58	2.797	2.798	2.693	0.104	0.104	1.038	1.039
800.58	2.797	2.798	2.694	0.103	0.104	1.038	1.038
869.95	2.755	2.759	2.695	0.059	0.063	1.022	1.024
869.95	2.755	2.759	2.702	0.053	0.057	1.020	1.021
900.055	2.740	2.775	2.684	0.055	0.090	1.021	1.034

900.055	2.740	2.775	2.688	0.051	0.086	1.019	1.032
201.13	2.767	2.767	2.681	0.087	0.086	1.032	1.032
201.13	2.767	2.767	2.678	0.090	0.089	1.034	1.033
298.045	2.740	2.753	2.661	0.079	0.092	1.030	1.035
298.045	2.740	2.753	2.651	0.088	0.102	1.033	1.038
405.34	2.720	2.720	2.645	0.075	0.075	1.028	1.028
405.34	2.720	2.720	2.635	0.085	0.085	1.032	1.032
446.92	2.736	2.755	2.661	0.075	0.093	1.028	1.035
446.92	2.736	2.755	2.666	0.070	0.088	1.026	1.033
504.59	2.752	2.753	2.646	0.106	0.107	1.040	1.041
504.59	2.752	2.753	2.634	0.117	0.119	1.045	1.045
553.54	2.748	2.742	2.670	0.078	0.072	1.029	1.027
553.54	2.748	2.742	2.659	0.088	0.083	1.033	1.031
585.845	2.747	2.766	2.661	0.086	0.105	1.032	1.039
585.845	2.747	2.766	2.655	0.092	0.111	1.035	1.042
705.975	2.764	2.752	2.660	0.103	0.091	1.039	1.034
705.975	2.764	2.752	2.664	0.099	0.087	1.037	1.033
800.995	2.719	2.740	2.690	0.029	0.050	1.011	1.019
800.995	2.719	2.740	2.690	0.029	0.050	1.011	1.019
900.49	2.767	2.761	2.677	0.090	0.084	1.034	1.031
900.49	2.767	2.761	2.671	0.097	0.090	1.036	1.034
408.61	2.665	2.700	2.652	0.013	0.048	1.005	1.018
468.23	2.759	2.769	2.675	0.084	0.094	1.031	1.035
568.04	2.761	2.726	2.685	0.076	0.042	1.028	1.016
408.4	2.724	2.705	2.661	0.063	0.045	1.024	1.017
468.02	2.750	2.787	2.677	0.073	0.110	1.027	1.041
567.77	2.727	2.744	2.688	0.039	0.056	1.015	1.021
223.3	2.745	2.758	2.670	0.075	0.088	1.028	1.033
321.7	2.744	2.747	2.660	0.084	0.087	1.032	1.033
420.6	2.707	2.704	2.620	0.087	0.084	1.033	1.032
456.6	2.734	2.736	2.640	0.094	0.096	1.036	1.036
531.4	2.722	2.773	2.650	0.072	0.123	1.027	1.046
582.9	2.756	2.769	2.680	0.076	0.089	1.028	1.033
632.7	2.719	2.725	2.680	0.039	0.045	1.014	1.017
721	2.731	2.749	2.670	0.061	0.079	1.023	1.029
820.4	2.734	2.772	2.690	0.044	0.082	1.016	1.031
920.8	2.771	2.734	2.690	0.081	0.044	1.030	1.016
Mean values	2.739	2.750	2.668	0.071	0.082	1.027	1.031
Density correction = 1.03							

Appendix D: Structure log integration methodology

Borehole IG_BH01 - Structure type and position verification and the integration activity to define the azimuth of the arbitrary reference line

Introduction

The orientation of all structures measured during core logging, as described in the WP03 Data Report, are initially defined based on alpha and beta angles relative to (1) the core axis, and (2) an arbitrary reference line drawn along the length of each core run. Since the core was not oriented, these relative orientation angles (alpha/beta for planes; gamma/delta for lineations on planes), for each logged structure need to be corrected to a true orientation in order to produce the final structural log for IG_BH01.

A final structural log was produced by comparing the core logged structures and the televiewer logged structures. This appendix describes the methodology used to compare the structures from core and televiewer logging to (1) assess the nature of the structure type, (2) determine a correct position along borehole of the structure, and (3) identify the angle of each arbitrary reference line traced on each core run relative to low side (reference line correction factor, $\beta_{\text{correction}}$).

The process described in this appendix were the steps taken to develop a *final structure log* that included the final assignment of structure positions, positional discrepancies, structure type (e.g., vein, foliation, etc.), structure dip and dip direction and/or alpha and beta, and structure geological aperture.

Correction and verification Methodology

The following sections describe the steps to *correct* or *verify* individual structures recorded in core logging and televiewer logging activities, which were ultimately used to form the final structural log.

Structure Type and Position Verification

Based on the integration between the two datasets, the structures were classified as being observed in 'both' datasets, in 'core logging only', or in 'televiewer only'. When a structure was observed in both datasets, the position along borehole and structure type recorded from core logging were used as the final structure position and final structure type. For structures only seen in the televiewer survey, a positional correction was applied based on the positional offset calculated from the structures observed in both datasets. Positional corrections were applied to these structures in a way as to preserve structure order. Additional detail relating to the positional corrections applied to structures identified from the televiewer surveys is discussed in WP05 Data Report (Golder, 2019a).

At this stage, each individual structure that was common to both data sets was evaluated, and an integrated structure was carried forward to the *final structure log*. The integration of common structures was as follows:

- a) Position along borehole of the final structure was based on the position of the core logged structure;
- b) Dip and Dip direction of the final structure was based on the orientation of the televiewer logged structure (relative to *low side*);
- c) Structure type was assigned, based on the core logging;
- d) Other characteristics, such as mineral infilling, etc. was assigned based on core logging;

If a structure was identified only in the televiewer logs, core run photographs acquired during core logging were reviewed to aid in evaluating if this structure was present in the core. If it is

determined that this is a real structure and not a drill feature, it was included in the final structural log, along with its interpreted structure type, dip and dip direction, and corrected position.

If a structure was identified only in core logging, this structure was carried forward to the final structural log, along with its structure type, alpha and beta angles, and position.

Structure Orientation

For each core run logged in WP03, an arbitrary reference line was drawn along the length of the core, where the location is initially unknown. Orientations of all structures identified during core logging were described relative to this reference line (beta angles) in each run. The purpose of this section is to describe the process used to define the *true* location, from the 'low side' of the borehole, of this reference line (between 0 – 360°) by integrating the oriented televiewer images.

When a structure was observed in both datasets, the alpha and beta angles from the televiewer survey were used as the final structure orientation.

For structures only observed in core logging, a reference line correction factor was applied to the beta angles in order to locate the arbitrary reference line relative to the bottom of the borehole ('low-side'). The reference line correction factor relies on structures seen in both datasets within the same continuously referenced interval. The correction factor takes an average of the beta angle correction(s), which is the angle from the borehole 'low-side' (identified from the televiewer survey) to the arbitrary reference from core logging, calculated for each structure ($\beta_{\text{correction}} = \beta_{\text{televiewer}} - \beta_{\text{core logging}}$). Figure 1 shows how the beta angle correction relates to the arbitrary reference line and the borehole 'low-side'.

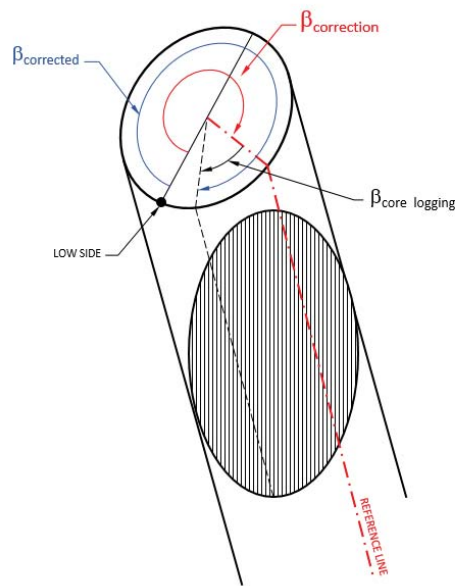


Figure 1: Schematic Showing Beta Angle Correction

$$\beta_{\text{core logging}} + \text{Reference Line Correction Factor(Average)} = \beta_{\text{corrected}}$$

(if $\beta_{corrected} > 360^\circ$, subtract 360°)

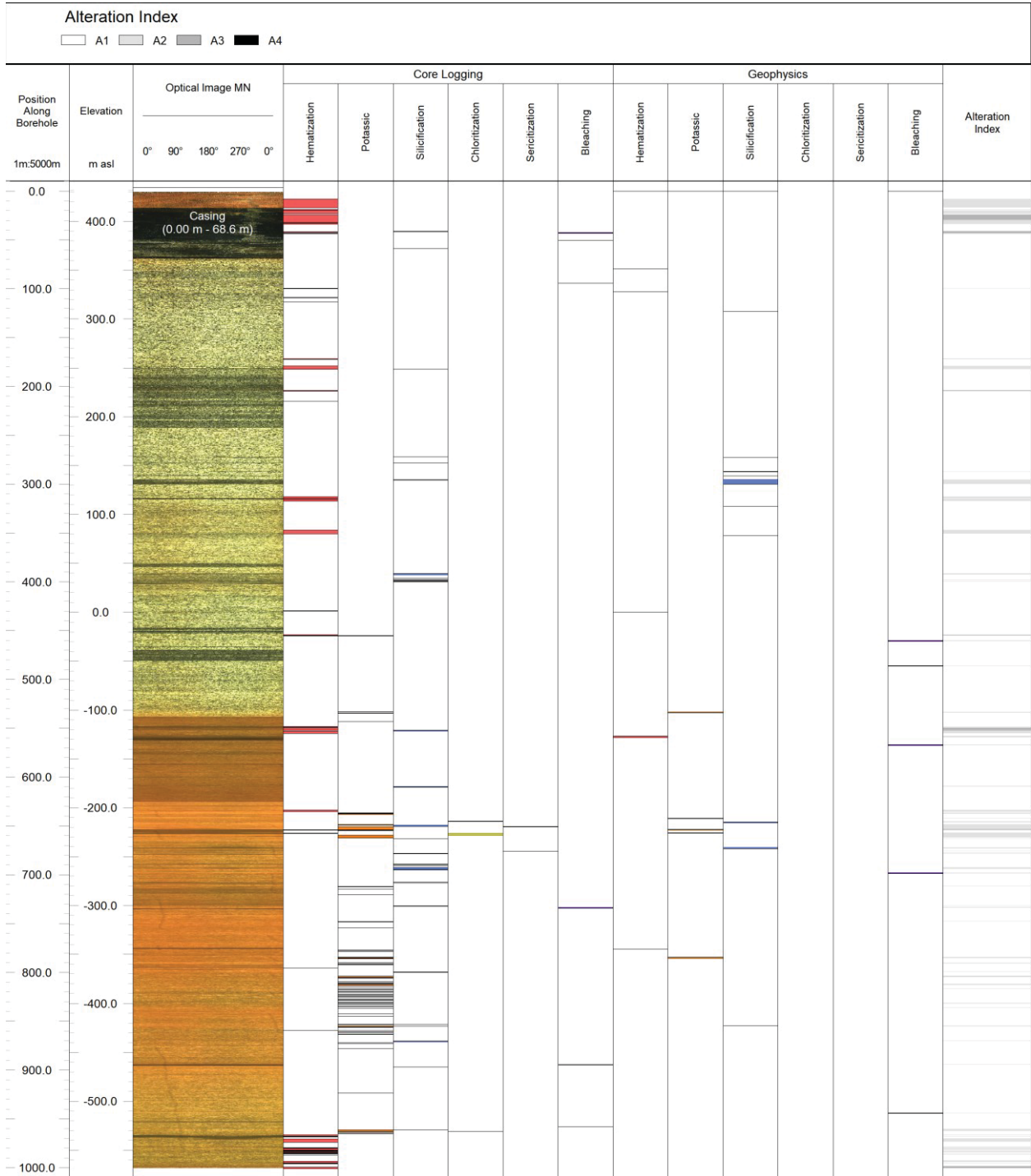
If no core logged structure within a continuously referenced interval was identified in the televiewer logs, then no reference line correction could be developed and orientation of the structure(s) within that interval was not possible.

Dip and dip direction of the structures were calculated using the software DIPS© (Version 7), by Rocscience, which processes the data by using stereographic projections based on the alpha and corrected beta measurements and the borehole deviation survey. The borehole survey file generated from the average of six separate televiewer probe runs using 1 m intervals between survey points was used for the projection of the final structure orientations.

Final Structural Log

The integration of core logged structures and televiewer logged structures resulted in a final structural log. The result of the final structural log includes a table that captures a complete set of attributes of each structure recorded either from core logging, televiewer logging, or a combination of both. Where certain attributes are duplicated between the two logging approaches (i.e., structure type, or position along borehole) decisions were made to carry forward the most accurate value to the final structure log. For example, position values and structure type were obtained from the core logging structures.

**Appendix E: Alteration Log update
based on geophysical image log**



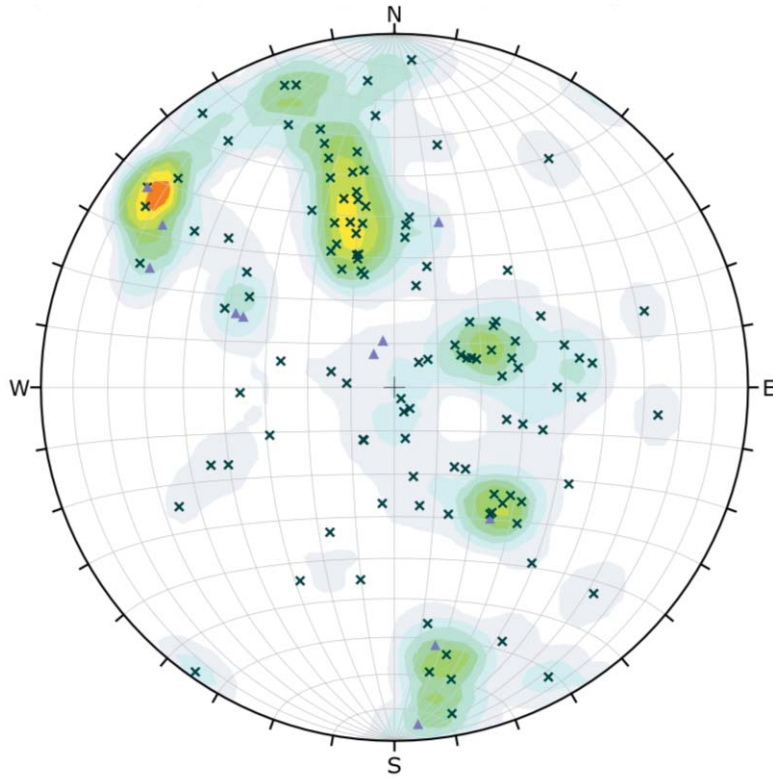
**Appendix F: Summary of Revised
Lineation Orientations**

	WP03-WP05 corrected lineation (trend, plunge) orientations					NWMO summary of Pitch/Rake re-assessment of lineation orientations					QA check and final lineation orientations from Pitch/Rake			
Logged Position Along Borehole (mBGS)	Logged Structure Type	Plane Dip Direction	Plane Dip	Linear Trend	Linear Plunge	Pitch Magnitude (0-90° and in specific direction)	Quadrant/ Direction (e.g., Pitch is measured from SE)	Rake (0-180°, follows Right hand rule)	Rake-corrected Trend	Rake-corrected Plunge	QA check Trend	QA check Plunge	Final Trend	Final Plunge
45.31	Fault	78	53	136	36	42	SE	138	140	32	140	32	140	32
66.55	Fault	2	79	247	36	33	W	33	279	32	279	32	279	32
220.3	Fault	286	80	2	21	* no correction possible, lineation orientation indeterminate upon review								
287.4	Contact - SHR	268	62	1	27	17	N	163	350	15	350	15	350	15
300.3	Contact - SHR	62	76	324	7	12	NW	12	335	12	335	12	335	12
315.2	SHRD	13	38	24	36	67	SE	113	41	35	41	35	41	35
329.3	Fault	42	65	107	36	20	SE	160	123	18	123	18	123	18
394	Fault	53	68	129	19	13	SE	177	138	12	142	3	142	3
395.6	Fault	359	38	22	36	90	W	90	359	38	359	38	359	38
401.4	Contact - SHR	47	73	313	12	25	NW	25	325	24	325	24	325	24
431.6	Fault	7	37	71	12	35	NW	35	306	20	306	20	306	20
533.4	Fault	115	71	60	2	10	W	170	202	9	202	10	202	10
635.3	SHR	16	16	98	7	30	W	30	315	8	315	8	315	8
635.3	SHR	14	16	82	7	20	W	20	303	5	303	5	303	5
654.1	Fault	333	25	332	24	85	SW	85	327	25	328	25	328	25
679.3	Fault	307	32	307	31	85	SW	85	301	32	301	32	301	32
705	Fault	36	81	133	23	10	SE	170	124	10	124	10	124	10
708.1	Fault	277	78	161	14	15	SW	15	190	15	190	15	190	15
732.8	Fault	348	34	295	15	40	SW	40	293	21	293	21	293	21
735	Contact - SHR	4	35	87	5	23	E	157	75	13	75	13	75	13
735	Fault	303	43	217	25	12	SW	12	222	8	222	8	222	8
794.9	Fault	14	21	217	5	* no correction possible, lineation orientation indeterminate upon review								
894.6	Fault	20	58	291	15	* no correction possible, lineation orientation indeterminate upon review								

**yellow highlighted fields indicate revisions made to final dataset during QA check

**Appendix G: Stereonets of Fractures by
Structural Unit**

SU1 (0 – 44.06 m)



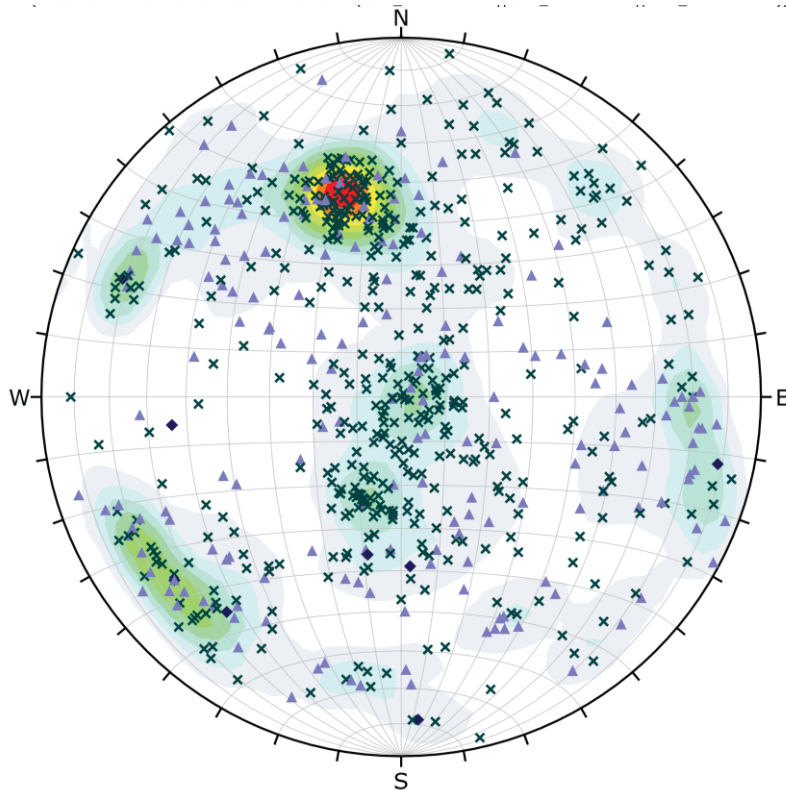
Symbol	STR_TYPE	Quantity
x	JN	117
▲	VN	11

Color	Density Concentrations
	0.00 - 0.80
	0.80 - 1.60
	1.60 - 2.40
	2.40 - 3.20
	3.20 - 4.00
	4.00 - 4.80
	4.80 - 5.60
	5.60 - 6.40
	6.40 - 7.20
	7.20 - 8.00

Contour Data	Pole Vectors
Maximum Density	7.21%
Contour Distribution	Fisher
Counting Circle Size	1.0%

Plot Mode	Pole Vectors
Vector Count (Weighted)	220 (128 Entries)
Terzagli Weighting	Minimum Bias Angle 15°
Hemisphere	Lower
Projection	Equal Area

SU2 (44.06 – 619.45 m)



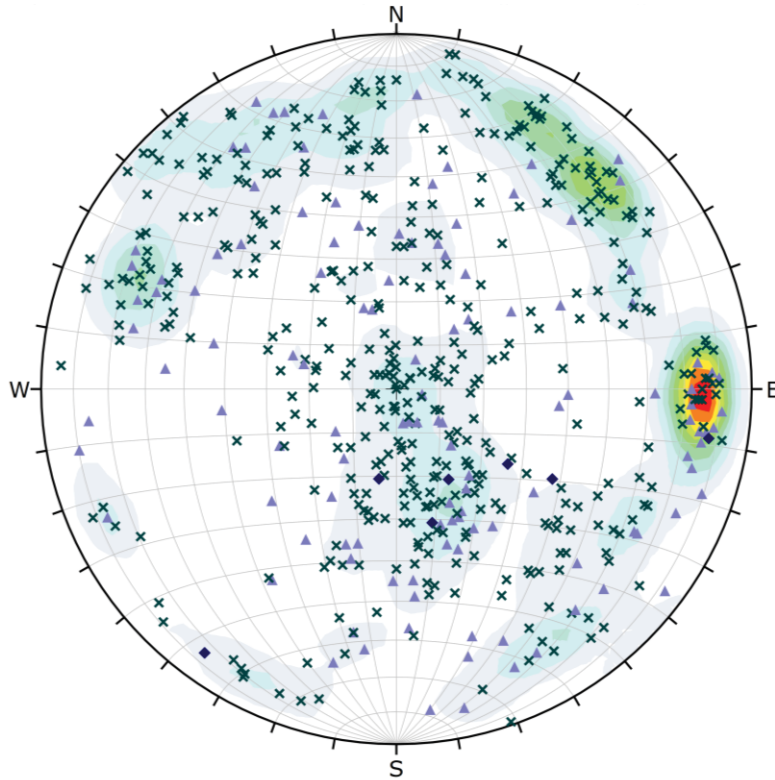
Symbol	STR_TYPE	Quantity
◆	FLT	8
x	JN	477
▲	VN	195

Color	Density Concentrations
	0.00 - 0.70
	0.70 - 1.40
	1.40 - 2.10
	2.10 - 2.80
	2.80 - 3.50
	3.50 - 4.20
	4.20 - 4.90
	4.90 - 5.60
	5.60 - 6.30
	6.30 - 7.00

Contour Data	Pole Vectors
Maximum Density	6.98%
Contour Distribution	Fisher
Counting Circle Size	1.0%

Plot Mode	Pole Vectors
Vector Count (Weighted)	1235 (680 Entries)
Terzagli Weighting	Minimum Bias Angle 15°
Hemisphere	Lower
Projection	Equal Area

SU3 (619.45 – 862.68 m)



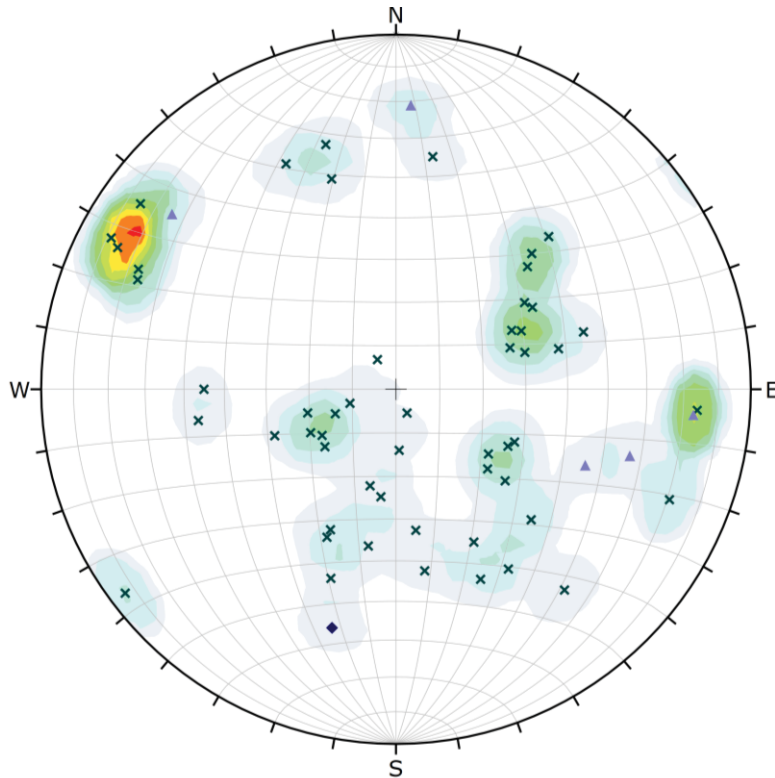
Symbol	STR_TYPE	Quantity
◆	FLT	7
×	JN	436
▲	VN	124

Color	Density Concentrations
	0.00 - 0.80
	0.80 - 1.60
	1.60 - 2.40
	2.40 - 3.20
	3.20 - 4.00
	4.00 - 4.80
	4.80 - 5.60
	5.60 - 6.40
	6.40 - 7.20
	7.20 - 8.00

Contour Data	Pole Vectors
Maximum Density	7.61%
Contour Distribution	Fisher
Counting Circle Size	1.0%

Plot Mode	Pole Vectors
Vector Count (Weighted)	1184 (567 Entries)
Terzaghi Weighting	Minimum Bias Angle 15°
Hemisphere	Lower
Projection	Equal Area

SU4 (862.68 – 961.20 m)



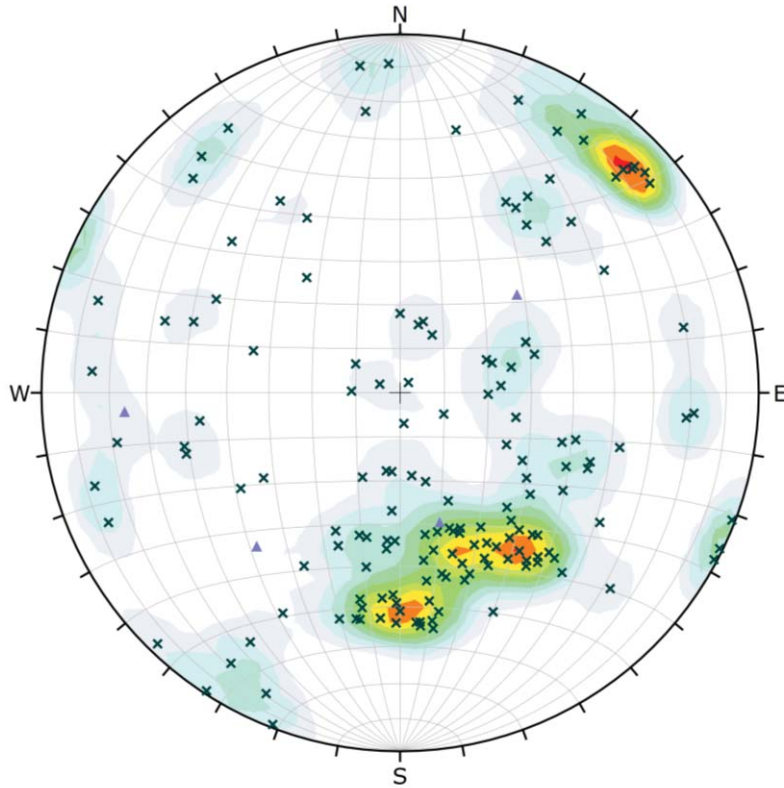
Symbol	STR_TYPE	Quantity
◆	FLT	1
×	JN	55
▲	VN	5

Color	Density Concentrations
	0.00 - 1.20
	1.20 - 2.40
	2.40 - 3.60
	3.60 - 4.80
	4.80 - 6.00
	6.00 - 7.20
	7.20 - 8.40
	8.40 - 9.60
	9.60 - 10.80
	10.80 - 12.00

Contour Data	Pole Vectors
Maximum Density	11.32%
Contour Distribution	Fisher
Counting Circle Size	1.0%

Plot Mode	Pole Vectors
Vector Count (Weighted)	105 (61 Entries)
Terzaghi Weighting	Minimum Bias Angle 15°
Hemisphere	Lower
Projection	Equal Area

SU5 (961.20 – 1001.18 m)



Symbol	STR_TYPE	Quantity
x	JN	164
▲	VN	4

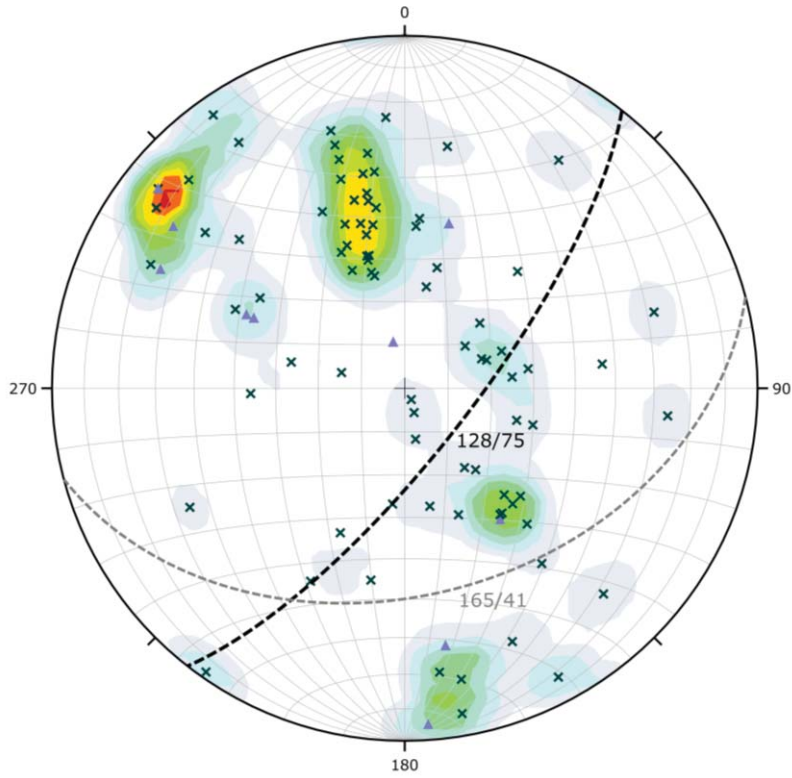
Color	Density Concentrations
	0.00 - 0.80
	0.80 - 1.60
	1.60 - 2.40
	2.40 - 3.20
	3.20 - 4.00
	4.00 - 4.80
	4.80 - 5.60
	5.60 - 6.40
	6.40 - 7.20
	7.20 - 8.00

Contour Data	Pole Vectors
Maximum Density	7.41%
Contour Distribution	Fisher
Counting Circle Size	1.0%

Plot Mode	Pole Vectors
Vector Count (Weighted)	312 (168 Entries)
Terzaghi Weighting	Minimum Bias Angle 15°
Hemisphere	Lower
Projection	Equal Area

**Appendix H: Stereonets of IG_BH01
High Fracture Frequency Intervals
(HFFI)**

IG_BH01 HFFI_1 (18.00 – 40.67 m):



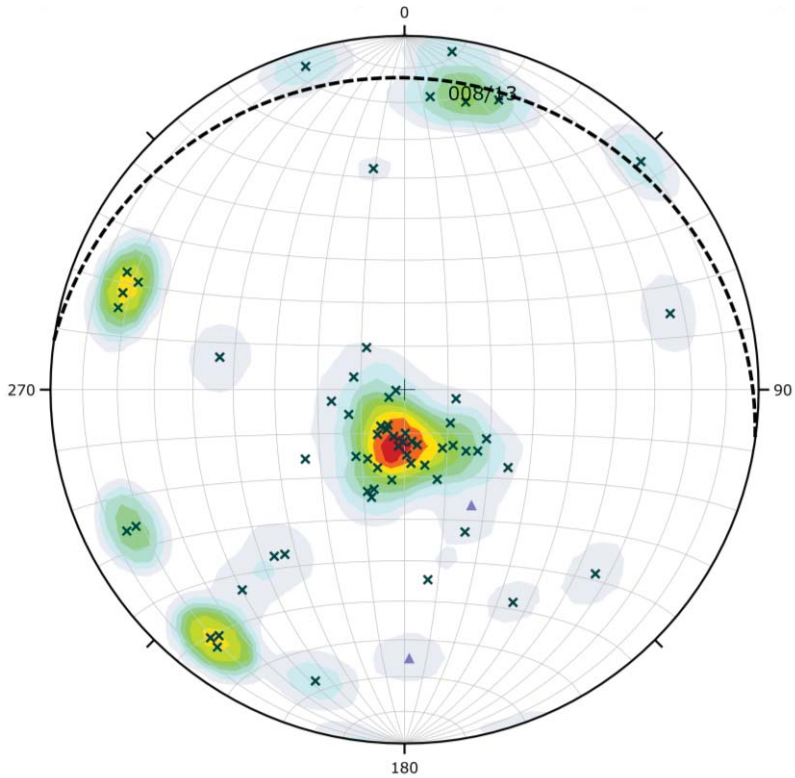
Symbol	STR_TYPE	Quantity
x	JN	84
▲	VN	10

Color	Density Concentrations
	0.00 - 1.00
	1.00 - 2.00
	2.00 - 3.00
	3.00 - 4.00
	4.00 - 5.00
	5.00 - 6.00
	6.00 - 7.00
	7.00 - 8.00
	8.00 - 9.00
	9.00 - 10.00

Contour Data	Pole Vectors
Maximum Density	9.60%
Contour Distribution	Fisher
Counting Circle Size	1.0%

Plot Mode	Pole Vectors
Vector Count (Weighted)	165 (94 Entries)
Terzaghi Weighting	Minimum Bias Angle 15°
Hemisphere	Lower
Projection	Equal Area

IG_BH01 HFFI_2 (541.00 – 557.27 m):



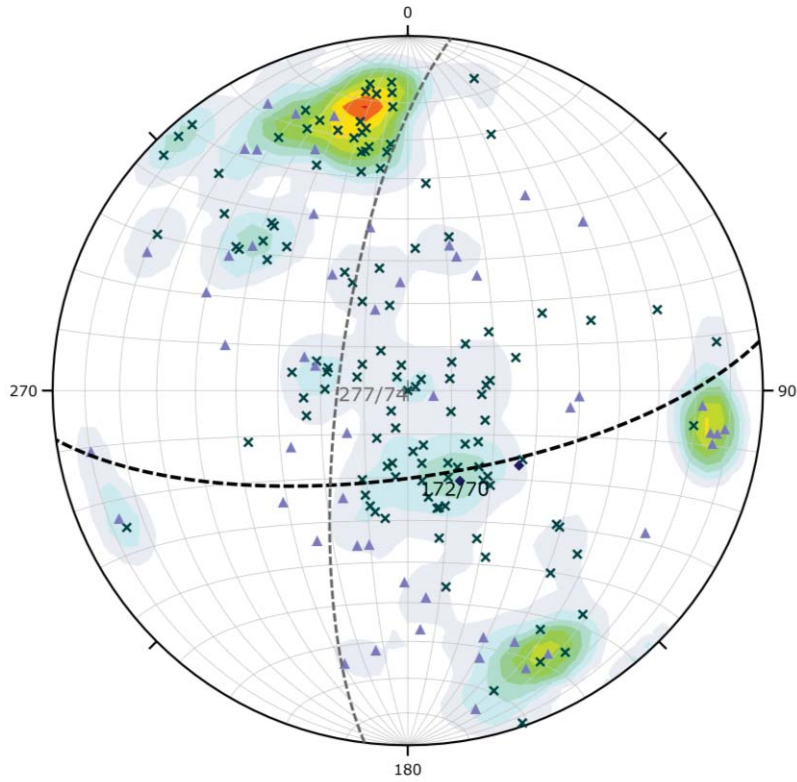
Symbol	STR_TYPE	Quantity
x	JN	66
▲	VN	2

Color	Density Concentrations
	0.00 - 1.30
	1.30 - 2.60
	2.60 - 3.90
	3.90 - 5.20
	5.20 - 6.50
	6.50 - 7.80
	7.80 - 9.10
	9.10 - 10.40
	10.40 - 11.70
	11.70 - 13.00

Contour Data	Pole Vectors
Maximum Density	12.90%
Contour Distribution	Fisher
Counting Circle Size	1.0%

Plot Mode	Pole Vectors
Vector Count (Weighted)	120 (68 Entries)
Terzaghi Weighting	Minimum Bias Angle 15°
Hemisphere	Lower
Projection	Equal Area

IG_BH01 HFFI_3 (627.50 – 679.75 m):



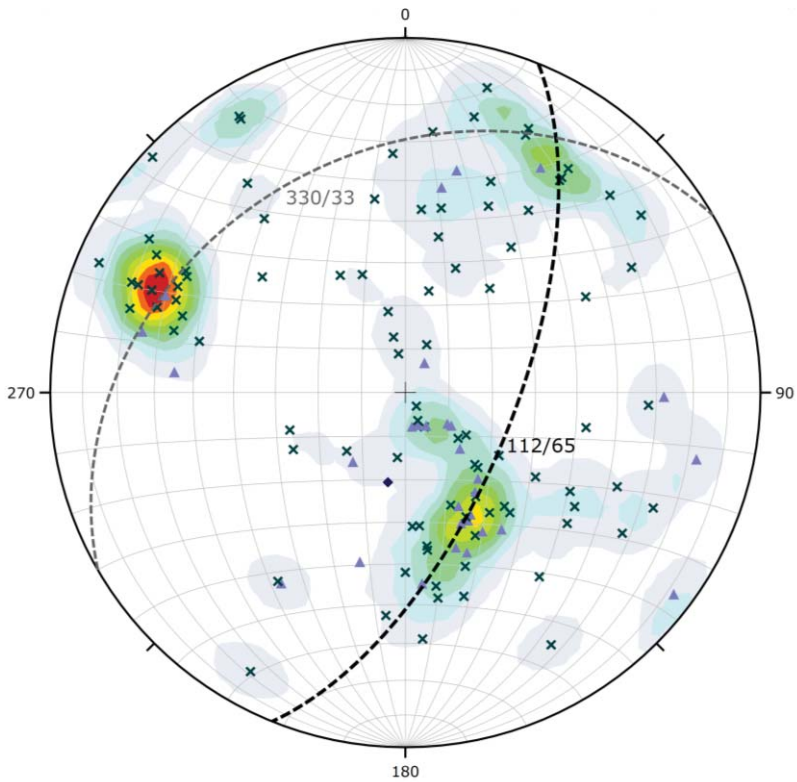
Symbol	STR_TYPE	Quantity
◆	FLT	2
×	JN	124
▲	VN	53

Color	Density Concentrations
	0.00 - 1.00
	1.00 - 2.00
	2.00 - 3.00
	3.00 - 4.00
	4.00 - 5.00
	5.00 - 6.00
	6.00 - 7.00
	7.00 - 8.00
	8.00 - 9.00
	9.00 - 10.00

Contour Data	
Contour Data	Pole Vectors
Maximum Density	9.12%
Contour Distribution	Fisher
Counting Circle Size	1.0%

Plot Mode	
Plot Mode	Pole Vectors
Vector Count (Weighted)	338 (179 Entries)
Terzagli Weighting	Minimum Bias Angle 15°
Hemisphere	Lower
Projection	Equal Area

IG_BH01 HFFI_4 (772.40 – 801.74 m):



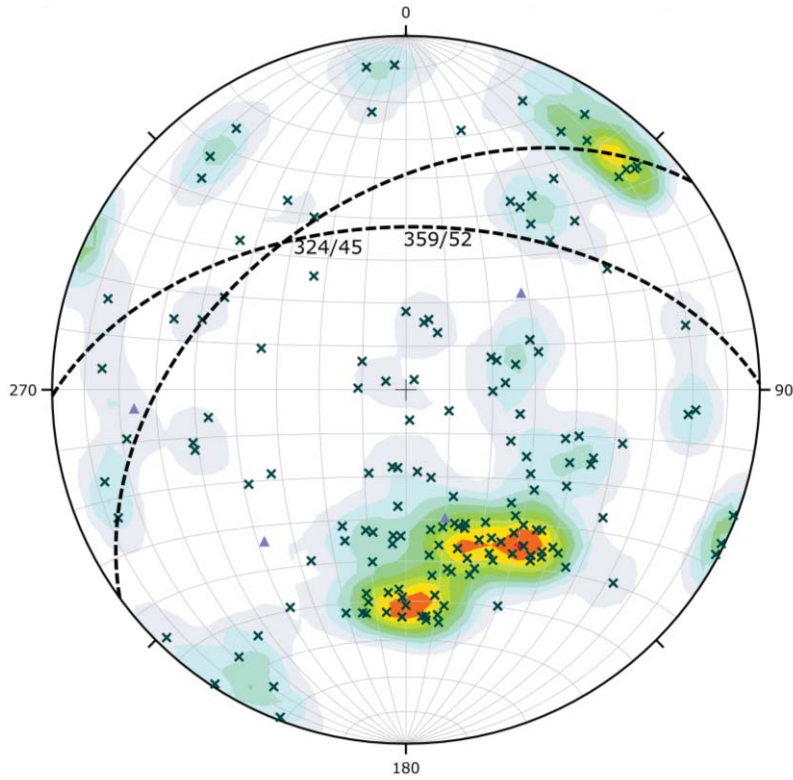
Symbol	STR_TYPE	Quantity
◆	FLT	1
×	JN	95
▲	VN	30

Color	Density Concentrations
	0.00 - 1.00
	1.00 - 2.00
	2.00 - 3.00
	3.00 - 4.00
	4.00 - 5.00
	5.00 - 6.00
	6.00 - 7.00
	7.00 - 8.00
	8.00 - 9.00
	9.00 - 10.00

Contour Data	
Contour Data	Pole Vectors
Maximum Density	9.97%
Contour Distribution	Fisher
Counting Circle Size	1.0%

Plot Mode	
Plot Mode	Pole Vectors
Vector Count (Weighted)	221 (126 Entries)
Terzagli Weighting	Minimum Bias Angle 15°
Hemisphere	Lower
Projection	Equal Area

IG_BH01 HFFI_5 (962.25 – 1001.18 m):



Symbol	STR_TYPE	Quantity
x	JN	162
▲	VN	4

Color	Density Concentrations
	0.00 - 0.80
	0.80 - 1.60
	1.60 - 2.40
	2.40 - 3.20
	3.20 - 4.00
	4.00 - 4.80
	4.80 - 5.60
	5.60 - 6.40
	6.40 - 7.20
	7.20 - 8.00

Contour Data	Pole Vectors
Maximum Density	7.45%
Contour Distribution	Fisher
Counting Circle Size	1.0%

Plot Mode	Pole Vectors
Vector Count (Weighted)	305 (166 Entries)
Terzaghi Weighting	Minimum Bias Angle 15°
Hemisphere	Lower
Projection	Equal Area

**Appendix I: Summary of borehole logs
at 1:1,000 scale**

